2015

Characterisation of Ti-6Al-4V deposits produced by arc-wire based additive manufacture

Nicholas Hoye
University of Wollongong

CHARACTERISATION OF Ti-6Al-4V DEPOSITS PRODUCED BY ARC-WIRE BASED ADDITIVE MANUFACTURE

A thesis submitted in partial fulfilment of the

requirements for the award of the degree

DOCTOR OF PHILOSOPHY

from

UNIVERSITY OF WOLLONGONG

by

NICHOLAS HOYE

B.Eng. (Mechanical), B.Sc. (Materials)

FACULTY OF ENGINEERING AND INFORMATION SCIENCES

2015

Certification

I, Nicholas P. Hoye, declare that this thesis, submitted in partial fulfilment of the requirements for the award of Doctor of Philosophy, in the School of Mechanical, Materials and Mechatronic Engineering, University of Wollongong, is wholly my own work unless otherwise referenced or acknowledged. The document has not been submitted for qualifications at any other academic institution.

Nicholas P. Hoye

2 March 2015

Table of Contents

List of Figures

List of Tables

List of Equations

Nomenclature

Abbreviations

AE	Arc energy
AINSE	Australian Institute of Nuclear Science and Engineering
ANOVA	Analysis of variance
ANSTO	Australian Nuclear Science and Technology Organisation
ASTM	American Society for Testing and Materials
BCC	Body centred cubic crystal structure
BHN	Brinell hardness
BTF	Buy-to-fly ratio
CCT	Continuous cooling transformation
CHM	Cold hearth melting
CMM	Coordinate measuring machine
CMT	Cold metal transfer
CNC	Computer numerical control
CSIRO	Commonwealth Scientific and Industrial Research Organisation
DARPA	Defense Advanced Research Project Agency
DB	Diffusion bonding
DCEN	Direct current electrode negative
DEC	Diffraction elastic constants
DMTC	Defence Materials Technology Centre
DOE	Design of experiment
DOF	Degrees of freedom
DR	Deposition rate
EDM	Electrical discharge machining
ELI	Extra-low interstitial
EMRS	Enhanced roasting and magnetic separation
EPMA	Electron probe micro-analysis
FFC	Fray-Farthing-Chen process
FFT	Fast Fourier Transform
FZ	Fusion zone
GB	Grain boundary

GMAW	Gas metal arc (MIG) welding
GTAW	Gas tungsten arc (TIG) welding
HACC	Hydrogen assisted cold cracking
HAZ	Heat affected zone
HCF	High cycle fatigue
HCP	Hexagonal close packed crystal structure
HI	Heat input
HIP	Hot isostatic pressing
JSF	F-35 Lightning II Joint Strike Fighter military aircraft
LAM	Laser additive manufacturing
LCB	Low cost (metastable) beta titanium alloys
LCF	Low cycle fatigue
MER	Materials and Electrochemical Research Corporation
MRR	Material removal rate
MLI	Mean linear intercept
MLT	Machining layer thickness
ND	Neutron diffraction
OEM	Original equipment manufacturer
OP-S	OP-S colloidal silica
PM	Powder metallurgy
PAW	Plasma arc welding
PWHT	Post-weld heat treatment
Ra	Surface roughness
SD	Standard deviation
SEI	Secondary electron imaging
SEM	Scanning electron microscope/microscopy
SiC	Silicon carbide
SIMS	Secondary ion mass spectrometry
SLM	Selective laser melting
SPD	Superplastic deformation
TAM	Thermally assisted machining
TMP	Thermomechanical processing
TOF	Time-of-flight

TTT	Time-temperature transformation
UC	Ultrasonic consolidation
UMIS	Ultra-micro indentation system, also referred to as nano-indentation
VAR	Vacuum arc remelting
WFSR	Wire feed speed ratio
XRD	X-ray diffraction

Symbols

%EL	Percent elongation, as a measure of ductility
%RA	Relative error
95% CI	Ninety-five percent confidence interval
α	the alpha phase of titanium or titanium alloys
α'	the alpha prime martensite phase of titanium or titanium alloys
α''	the alpha double prime martensite phase of titanium or titanium alloys
α_2	Ti_3Al intermetallic compound
β	the beta phase of titanium or titanium alloys
d_0	unstressed inter-planar spacing
d_{hkl}	inter-planar spacing for the *hkl* crystallographic planes
E	Modulus of elasticity
ε	Engineering strain
$\dot{\varepsilon}$	Engineering strain rate
ω	the omega phase of titanium or titanium alloys
λ	neutron wavelength
ν	Poisson's ratio
σ^{I}	Type I (macro) stresses
σ^{II}	Type II (intergranular) stresses
σ^{III}	Type III (intragranular) stresses
σ_H	Hydrostatic stress
σ'	von-Mises equivalent stress
σ_{ts}	Ultimate tensile strength
σ_y	Yield strength
θ	Bragg scattering angle
wt%	composition by weight percent

Abstract

Significant efforts have been made in recent times to reduce the relatively high cost associated with titanium alloys and hence allow for greater utilisation of the unique properties offered by these materials. One such area of interest is additive manufacturing of components through arc-wire based fusion welding processes. The present thesis details research conducted to characterise aspects of weldability of the Ti-6Al-4V titanium alloy related to this emerging manufacturing process. The resulting properties of the final deposit were also evaluated, with conclusions drawn on the suitability of the arc-wire deposition technique for the additive manufacture of large scale titanium components.

Initial research was conducted to investigate the current primary and secondary production and manufacturing methods for titanium alloys. Particular emphasis is given to the shortcomings of these which contribute to the high final component costs currently seen in industry. Methods to address these shortcomings were investigated with the so-called 'near net shape' and additive manufacturing methods discussed in depth.

Aspects of weldability associated with the additive manufacture of Ti-6Al-4V using gat tungsten arc welding (GTAW) were investigated both qualitatively and quantitatively, with the aim of characterising relationships between processing parameters and the resulting material properties. Initial experiments were used to develop empirical models which related key processing parameters to the geometry and microstructure of additively manufactured Ti-6Al-4V. Results show that the geometry of additively manufactured structures could be well predicted from knowledge of the arc current, weld travel speed and wire feed speed. Key microstructural features appeared to show some dependence on the process parameters considered, but are more likely related to cooling rate through the β-transus. Qualitative observations of deposits suggest an effective process operating envelope exists in terms of specific deposition energy, which is based on arc energy and deposition rate.

Mechanical properties of additively manufactured Ti-6Al-4V were evaluated through tensile testing, Charpy impact testing and hardness testing. Ultimate tensile strength, ductility and hardness of additively manufactured material was found to comply with relevant industry standards, with measured values of yield strength marginally less than

the minimum specified limits. Impact toughness of additively manufactured Ti-6Al-4V was seen to exceed that of equivalent wrought plate samples.

Machinability of additively manufactured Ti-6Al-4V was characterised through milling and drill life trials. Cutting force during milling trials was lower in additively manufactured materials compared to conventionally manufactured wrought materials due to their lower strength and hardness. In contrast, the force during drilling operations conducted on additively manufactured Ti-6Al-4V was seen to be higher, despite drills used in this material showing less tool wear.

Residual stresses within representative thin-walled samples of additively manufactured Ti-6Al-4V produced by the GTAW method were characterised through neutron diffraction. Residual stresses in additively manufactured structures were found to be considerably higher than in an equivalent sample produced from wrought billet by material removal processes, but more favourable than those measured in a T-fillet sample manufactured by welded fabrication. The use of pulsed welding current was seen to broaden the region over which tensile residual stresses were found in the base plate and also reduce the magnitude of peak stress. Results also show that residual stresses within the additively manufactured structure can be significantly reduced through post-weld heat treatment.

Atmospheric contamination of Ti-6Al-4V during the GTAW based additive manufacturing process was investigated through bead-on-plate welding trials and atmospheric exposure. Results indicate that the vast majority of atmospheric contamination of fusion welds in Ti-6Al-4V takes place post-weld, in the solid state. Contamination of this type during the additive manufacturing process would be negated by removal of affected material during subsequent finish machining processes. The current means of contamination assessment by observation of surface colour was shown to be highly subjective in nature and not representative of any bulk contamination.

The findings of the present study will contribute to the development of arc-wire based additive manufacture as an industrially viable means of producing structural titanium components. Further, it is hoped that this body of work will assist in the development of technical know-how which reduces the costs associated with manufacturing titanium components, particularly for the defence and aerospace sectors.

Acknowledgements

The author would like to acknowledge and thank the following parties for their contributions to this research project. Without their help and input, much of the work presented would not have been possible.

- Professor Huijun Li, Professor John Norrish and Professor Rian Dippenaar for their supervision, guidance and general assistance throughout the project;
- Dr Dominic Cuiuri for his assistance throughout the project, particularly in the development of welding equipment, completion of welding experiments and general discussions which helped to retain perspective;
- Dr Anna Paradowska for her considerable assistance with neutron residual stress measurements;
- Mr Greg Tillman for his assistance with metallographic sample preparation;
- Mr Nathan Larkin and Dr Zengxi Pan for their assistance with automation aspects of experimental procedures;
- Mr David Morr of SECO Tools and Dr Steve Dowey of RMIT and Sutton Tools for the supply of cutting tools and assistance in machining trials. Also Dr Suresh Palanisamy and Mr Theo Sinkovits for their assistance in machining trials;
- The staff of the Faculty of Engineering and Information Sciences workshop at the University of Wollongong, in particular Mr Stuart Rodd and Mr Mick Grantham for their continual assistance with sample preparation;
- The Australian Nuclear Science and Technology Organisation (ANSTO) for the provision of beam time at the OPAL research reactor facility operated by the Bragg Institute, as well as the Australian Institute of Nuclear Science and Engineering (AINSE) for funding assistance during these experiments;
- The Defence Materials Technology Centre (DMTC) for funding the research project through Project 1.3 – Evaluation of Titanium Direct/Additive Manufacturing. The DMTC is supported by the Defence Materiel Organisation (DMO);
- The University of Wollongong (UOW) and Welding Technology Institute of Australia (WTIA) for their contributions in funding the project.

Finally the author must thank his family, friends and partner for their continual support, patience and motivation, without which this undertaking would have seemed insurmountable.

CHAPTER 1 - INTRODUCTION

1.1 General

It is broadly understood that the properties of metallic materials are primarily a function of the material's microstructure and that these properties, in turn, dictate the material's ability to perform as required in a particular application or environment. It follows then that a thorough understanding of a material's microstructure and how this may be affected or manipulated during processing and manufacture is highly advantageous. Such knowledge gives the ability to assess the material's suitability for a given application, or indeed, to adapt processing and manufacturing methods such that the desired microstructure, and hence properties, are obtained.

Titanium alloys possess a wide range of desirable mechanical and physical properties including high strength-to-weight ratios, moderate ductility, good fatigue and fracture resistance and excellent corrosion resistance in a wide range of environments [1]. It is this remarkable combination of properties that has seen increased interest in the family of titanium alloys from both research and industry over recent decades. The main drawback of these materials at present is their comparatively high cost, due to difficulties in primary and secondary processing. Given this, the widespread use of these materials is not considered to be economically viable when compared to competitive materials including stainless and high strength steels and aluminium alloys. As such, the unique and attractive properties possessed by titanium alloys tend only to be utilised in substantial quantities by a limited number of specialist industries, namely aerospace, military, power generation, chemical/petrochemical processing and biomedicine [2, 3]. Of these, aerospace is the largest user, accounting for upwards of 60 % of metallic titanium utilisation by mass [1, 4].

With the increased interest in, and use of titanium and its alloys, significant efforts are being made to reduce the costs associated with these materials by development of new novel production and manufacturing techniques. One area of particular interest is the use of near net shape forming and additive manufacturing techniques which have seen a rapid emergence in recent years [5, 6]. Using these, three dimensional free-form structures can be produced by deposition and bonding of successive layers of material, giving increased material utilisation and enhanced design flexibility. Key to the use of

such manufacturing methods as a means of cost reduction, thereby increasing the use of metallic titanium, is a sound knowledge and understanding of the material properties obtained through these new forming processes. This includes the investigation of mechanical and physical properties of the materials or components, as well as how these are related to the observed microstructure and ultimately how they are related to, and so may be manipulated by, the forming process and processing parameters.

While the use of fusion welding processes in fabrication of components and structures from titanium alloys is well established, the use of such arc-based methods for additive manufacture of these items is relatively new and undeveloped. The welding of titanium alloys presents a number of unique weldability issues. These include porosity, contamination cracking, particularly from iron rich particles, and atmospheric contamination leading to embrittlement of the fusion and heat affected zones [7-9]. Contamination by the pick-up of impurity species during welding, particularly iron, causes a reduction in corrosion resistance for low alloy compositions [10]. It is also seen that the weldability of titanium alloys varies significantly with alloy composition and thermomechanical processing history, with low alloy compositions typically exhibiting the best weldability [1, 2]. It follows then that for any new additive manufacturing process which relies on fusion of successive layer deposits to be considered for industrial production of structural components from titanium alloys, these aspects of weldability must be investigated. In addition, any new weldability concerns associated with the process must be identified and investigated in such a way that means to counter the adverse effects of these are developed. Possible measures may include variations in process parameters, alternative gas shielding arrangements, pre- and post-weld thermal treatments or alternative welding processes.

With the field of additive manufacturing itself only being a relatively recent development [11], it can be understood that the use of arc-wire based fusion welding as a near net shape manufacturing technique for titanium components may be considered to be in its infancy. As such, there are still significant research efforts being undertaken to characterise and optimise this process, and so deliver a final product that is able to compete commercially with more conventional subtractive manufacturing methods currently used for titanium alloys [12-17], where more than ninety percent of raw material is reduced to scrap during manufacture [18]. One primary area of interest is the

ability to produce large scale aerospace components from titanium alloys with suitable mechanical and physical properties while reducing raw material usage and hence cost.

It is clear then that an in depth study considering the use of arc-wire based additive manufacturing for the production of structural aerospace components from titanium alloys is essential to validate the manufacturing process for commercial use. Such a study should assess the weldability issues of porosity, cracking and atmospheric contamination previously identified in addition to an assessment of the microstructure and mechanical properties of the materials and components produced. Further, perceived weldability issues unique to the arc-wire additive manufacturing process such as residual stress evolution and thermally activated recrystallisation and grain growth must be investigated. While the initial study should focus on the fusion welding process most commonly used on titanium alloys, namely gas tungsten arc welding, it should be conducted in such a manner as to be compared to, or expanded to include, other suitable fusion welding processes including cold metal transfer, plasma arc, laser and electron beam welding.

1.2 Aims and Objectives

The primary aim of this research project was to conduct an investigation into the aspects of weldability associated with the additive manufacture of freeform structures from the Ti-6Al-4V titanium alloy using arc-wire deposition techniques based on the gas tungsten arc welding (GTAW) process. This was to be done by both qualitative and quantitative means with consideration of key mechanical and physical properties and their relation to the additive manufacture process and parameters. Further, the influence of welding conditions on material properties was to be related to observations of microstructure evolution due to the fusion welding process. Based on these results, it was intended that the viability of the arc-wire based additive manufacture method for the manufacture of large scale titanium aerospace components could be assessed.

The objectives of this research project were:

i. to produce a concise and inclusive literature review covering key aspects of the present research project related to titanium alloys, and more specifically Ti-6Al-4V, including current manufacturing methods and emerging cost

reduction technologies with an emphasis on near net shape additive manufacturing methods;

ii. to develop and commission a basic arc-wire additive manufacturing system capable of producing simple freeform geometries using GTAW combined with automated wire addition, without the need for a dedicated welding environment or controlled atmosphere;

iii. to investigate and characterise the microstructure of additively manufactured Ti-6Al-4V deposits produced using the established arc-wire process, and subsequently establish empirical relationships between these features and welding process parameters;

iv. to investigate and quantify the mechanical properties of additively manufactured Ti-6Al-4V deposits produced using the established arc-wire process, and compare to those of commercially produced wrought product;

v. to investigate aspects of machinability of additively manufactured Ti-6Al-4V deposits produced using the established arc-wire process, and compare to those of commercially produced wrought product;

vi. to investigate and quantify the residual stresses within additively manufactured Ti-6Al-4V components resulting from production by the established arc-wire process and compare to those resulting from competing conventional manufacturing methods;

vii. to investigate and characterise the atmospheric contamination of Ti-6Al-4V during arc-wire based additive manufacture with particular reference the effect on the mechanical properties of the final component;

viii. to suggest, and if possible prove, techniques for controlling any potentially adverse weldability effects during the arc-wire process.

This research project was also aligned to a project (1.3) within the Air Platforms program of the Defence Materials Technology Centre (DMTC) titled ‘Evaluation of Titanium Direct/Additive Manufacturing’. The primary objective of the DMTC project was to develop and evaluate methods for the manufacture of titanium components using arc welding processes for either joining sub-components or direct deposition of titanium weld metal onto a base component. This was done with the intention of reducing manufacturing costs associated with titanium components by increasing material utilisation. Any such method(s) developed were to be assessed for cost effectiveness

and viability as alternative approaches for defence platform fabrication. The outcomes of the project were also considered to be a key foundation in the development of knowledge and enabling technologies for defence OEMs and supply chain manufacturers within Australian industry.

1.3 Rationale

The primary purpose of this research project was to investigate the viability of producing large scale structural titanium components using GTAW additive manufacturing techniques. It can be understood that for new technologies, such as arc-wire based additive manufacturing, to be industrially competitive they must offer some form of advantage over the current manufacturing processes. This may include some enhancement of physical or mechanical properties such as corrosion resistance, or more typically some form of perceived financial benefit through, for example, reduced material usage, faster processing and manufacturing times or increased quality with reduced reworking. Further, these advantages must readily negate any shortcomings of the new technology.

The results of this study are expected to build on existing knowledge of fusion welding of titanium alloys and provide new insights into the response these materials to repeated localised thermal cycling. Of particular interest was the Ti-6Al-4V alloy and the microstructural changes that occur during the process, along with their flow on effects on the physical and mechanical properties of the weldment which forms the final freeform structure or component. This in turn may be used to optimise the arc-wire based additive manufacturing process for not only Ti-6Al-4V, but titanium alloys in general, as well as the fusion welding of titanium alloys for more conventional non-additive manufacturing methods. The results may also prove useful in the additive manufacture of other metallic materials by arc-wire methods, as well as by alternative fusion based additive manufacturing processes.

By encompassing a wide range of weldability aspects including mechanical properties, residual stresses and atmospheric contamination as well as process control, it is anticipated that the present study will aid in the development of arc-wire based additive manufacture as an industrially viable means of producing structural titanium components. In addition, the findings obtained from this research project will contribute

to a greater scientific understanding of the arc-wire based additive manufacturing process and its influence on material properties. Finally, it is hoped that the present study will develop technical know-how which assists Australian manufactures to compete globally in the supply of structural titanium components, particularly for the defence and aerospace sectors.

1.4 Outline of Thesis

This thesis is initiated with a literature review, followed by the presentation of information relating to each of the aspects of weldability investigated. Finally, conclusions are drawn and suggestions for future work presented. The literature review presented in chapter two describes the current knowledge within the field of titanium alloys, with an overview of current processing and manufacturing methods presented to emphasise the perceived shortcomings. This is followed by a brief summary of welding aspects related to titanium alloys and current research in this area. The literature review is concluded by a discussion of current and emerging cost reduction technologies based around near net shape and additive manufacturing.

This literature review leads into the subsequent chapters which address the experimental work conducted during the course of this research project. Each chapter begins with an initial introduction and overview of the research area, followed by the experimental procedures undertaken and the results obtained. Results are analysed and discussed before conclusions are drawn. Chapter three addresses the relationships between fundamental process parameters of the GTAW based additive manufacturing process and the geometry and microstructure of the resulting build-up. The application of these results to process optimisation and process control is considered. Chapter four extends the characterisation of the additively manufactured Ti-6Al-4V material with in depth investigations of mechanical properties through tensile and Charpy impact testing with observations linked to microstructure and processing history. Further material characterisation is presented in the form of machinability, with results of milling and drilling operations evaluated against equivalent wrought materials. Chapter five relates to the evaluation of residual stresses within additively manufactured Ti-6Al-4V components by neutron diffraction methods. The influence of various processing parameters including deposition rate, pulsed welding current and post-weld heat

treatment are investigated and compared to other competitive manufacturing processes. The aspects of atmospheric contamination and its subsequent effects on deposit mechanical properties are presented in chapter six and used to assess the ability to perform fusion based additive manufacturing without the use of a dedicated welding environment or stringently controlled atmosphere.

The thesis is concluded with a summary of the primary findings followed by implications of the results and recommendations for their application in industrial manufacturing processes. Further recommendations relating to future work required in each of the four main focus areas are also given.

CHAPTER 2 - LITERATURE REVIEW

2.1 Titanium and its Alloys

Titanium and its alloys make up a relatively new set of engineering materials that, due to the wide range of desirable properties they offer, are becoming increasingly popular in numerous engineering applications. These properties include high corrosion resistance, high mechanical strength that may be retained at moderate temperatures and relatively low density. While titanium was originally identified in the late 18th century, it wasn't until the 1940's that the Kroll process for titanium extraction was developed allowing the industrial production of high quality grades [19]. Since this time, technological advances in titanium and its alloys have been driven primarily by the aerospace and military sectors, with subsequent use in more 'conventional' applications such as chemical processing equipment, biomedical implants and automotive components following on. Despite being the fourth most abundant structural metal in the earth's crust, behind aluminium, iron and magnesium, the cost of raw titanium remains relatively high. This is primarily due to its highly reactive nature which makes extraction from its ores difficult, requiring strict, well controlled and energy intensive processing [1, 20].

Pure titanium is understood to exhibit one of two crystal structures, also referred to as *phases*, depending on the temperature and pressure. The alpha (α) phase, with its hexagonal close packed (HCP) crystal structure is stable at low temperatures while the beta (β) phase has a body centred cubic (BCC) crystal structure and is stable at elevated temperatures up to melting. Under standard conditions this allotropic transformation takes place at 883 °C [2]. It should also be noted that a number of metastable phases are possible in titanium alloys depending on composition, processing and environmental conditions, including the athermal omega (ω) phase, a number of martensitic phases and various intermetallic compounds [21]. Titanium alloys also show desirable high temperature capabilities with the melting temperature of the pure material being 1668 °C [2]. Considering the mechanical properties of titanium alloys, their modulus of elasticity is approximately 107 GPa [22, 23] with an ultimate tensile strength (σ_{ts}) of 400 MPa in the pure state, which may be increased to in excess of 1400 MPa with suitable alloying and thermomechanical processing (TMP) [19]. These, coupled with the relatively low density of 4500 kg/m^3 [22], give a stiffness-to-weight ratio similar to

that of steels but with strength-to-weight ratios superior to both steels and aluminium alloys. The addition of alloying elements is also used to improve creep resistance, fatigue behaviour, fracture toughness and stress corrosion cracking resistance [2]. The desirable mechanical properties of titanium alloys are clearly shown in Table 2.1 where the most widely used alloy, Ti-6Al-4V [24] (also referred to as ASTM Grade 5), is compared to common structural engineering alloys in terms of strength and stiffness. From this it is clear that the titanium alloys are very competitive based on mechanical behaviour, especially specific fatigue strength, with cost being the major drawback limiting their broader use in more mainstream engineering applications.

Table 2.1 Mechanical properties of common structural engineering alloys. Compiled from CES EduPack 2012, Granta Design Limited [25].

Property	Alloy					
	7075-T6	Grade 2 Ti	Ti-6Al-4V[a]	4340 Steel[b]	316L SS	IN 718[a]
Density (kg/m^3)	2795	4515	4430	7830	7970	8220
Ductility (%EL)	2-10	20-26	10-12	8-10	30-50	10-15
Modulus of Elasticity (GPa)	72	103	114	205	198	203
Strength (MPa)						
Ultimate Tensile	507	418	1018	1885	550	1245
Tensile Yield	445	318	949	1575	240	1055
Compressive Yield	462	190	939	1705	240	1040
Fatigue at 10^7 cycles	160	271	626	432	282	411
Specific Stiffness (x10^6 m)	2.58	2.28	2.57	2.62	2.48	2.47
Specific Strength (x10^3 m)						
Ultimate Tensile	18.1	9.3	23.0	24.1	6.9	15.1
Tensile Yield	15.9	7.0	21.4	20.1	3.0	12.8
Compressive Yield	16.5	4.2	21.2	21.8	3.0	12.7
Fatigue at 10^7 cycles	5.7	6.0	14.1	5.5	3.5	5.0
Frac. Toughness (MPa·m$^{0.5}$)	32	58	91	85	63	135
Cost (AUD/kg)[c]	3.10	13.75	27.40	1.12	6.47	28.50

a. Solution treated and aged
b. Quenched and tempered
c. At 2012, approximate only

Despite the reactivity of titanium at elevated temperatures, the corrosion resistance of its alloys under oxidising conditions at relatively low temperatures is excellent making them competitive with stainless steels [22, 26]. The origin of this corrosion resistance is a dense, rapidly forming, stable oxide layer at the surface [27]. At elevated temperatures this corrosion resistance is lost with the protective oxide layer decomposing, readily

allowing the diffusion of oxygen and other interstitial species into the bulk material. Titanium alloys also possess good ductility and have coefficients of thermal expansion that closely match carbon fibre composite materials, and so are well suited to acting as interface materials in aerospace applications. The general characteristics of the main titanium alloys are illustrated in Figure 2.1 relative to Ti-6Al-4V.

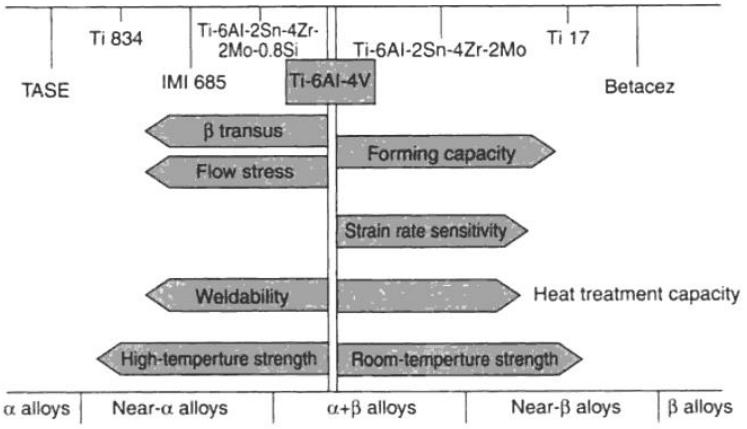

Figure 2.1 General characteristics of the titanium alloys as functions of composition, with both general groupings by constituent phases (bottom) and example alloys (top) shown. From Wessel [1].

From the properties described above it can be readily understood that titanium alloys are suited to a wide range of applications, however their widespread usage is somewhat limited by their relatively high cost. Titanium alloys are used extensively in the aerospace industry, which exploits the high specific strength and excellent fatigue resistance to form, among other things, turbine and compressor components and structural members in landing gear. The chemical processing and energy production industries also use significant volumes of metallic titanium for components where high strength at elevated temperatures combined with excellent corrosion and creep resistance is essential. These include cryogenic storage vessels, heat exchangers, general piping and turbine blades and discs. Other, less prevalent uses for titanium alloys include the biomedical industry where the corrosion resistance, formability, high strength, comparatively low modulus and bone and bio compatibility make them ideally suited to implant devices [28, 29], as well as the automotive and sporting industries. A number of typical applications for titanium alloys are illustrated in Figure 2.2. Long term usage trends for metallic titanium mill products in the United States of America, presented in Figure 2.3, show that titanium usage, and hence development, was initially driven by military aerospace before being taken up by commercial aerospace and other industries. Figure 2.4 shows the greatest demands for metallic titanium mill products

globally are from industrial applications such as chemical processing and energy production, followed by commercial aerospace.

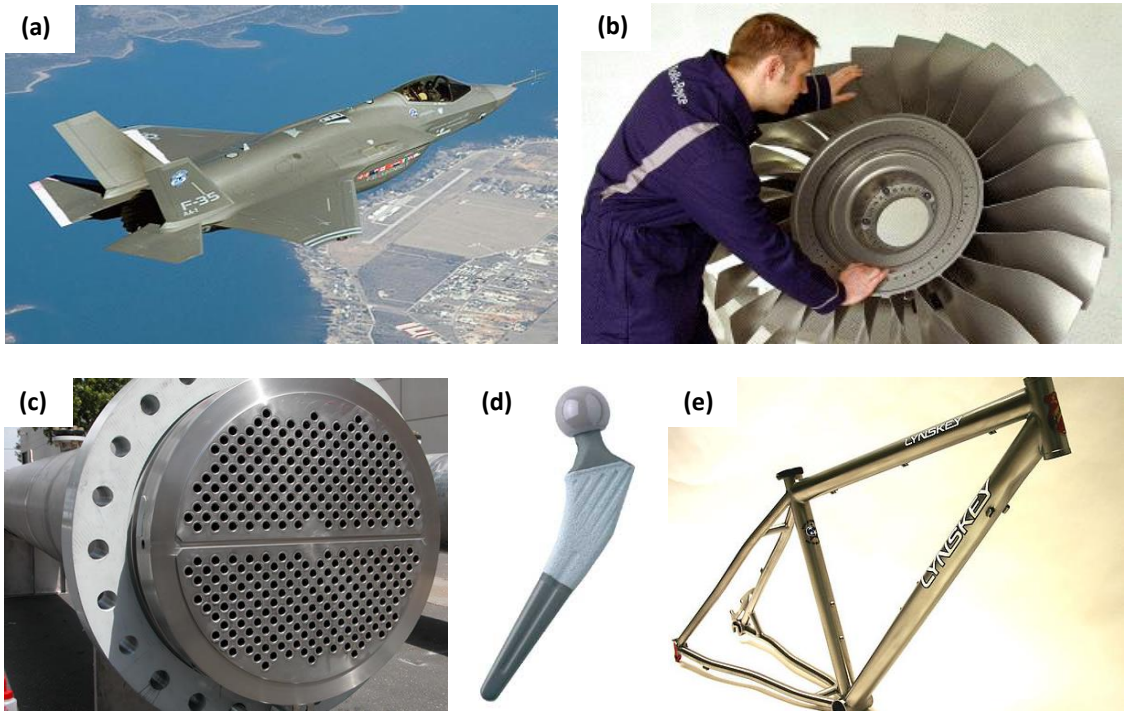

Figure 2.2 Photographs of (a) the F-35 Joint Strike Fighter (JSF) aircraft, (b) blisk (combined blades and disk) manufactured from Ti-6Al-4V and used in the JSF, (c) titanium heat exchanger, (d) Ti-6Al-4V artificial hip joint implant and (e) titanium mountain bike frame. From (a) Lockheed Martin Corporation [30], (b) Bhadeshaia [31], (c) TITAN Metal Fabricators [32], (d) Corin USA [33] and (e) Lynskey [34].

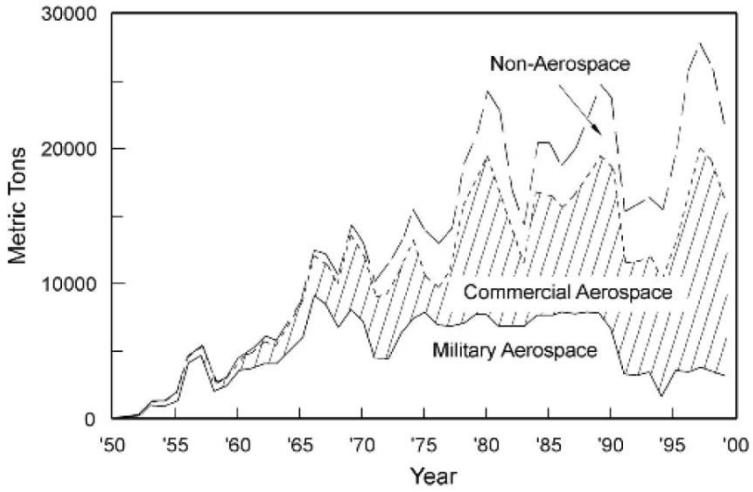

Figure 2.3 Usage trends for USA titanium mill products from 1950 through to 2000. From Lutjering [23].

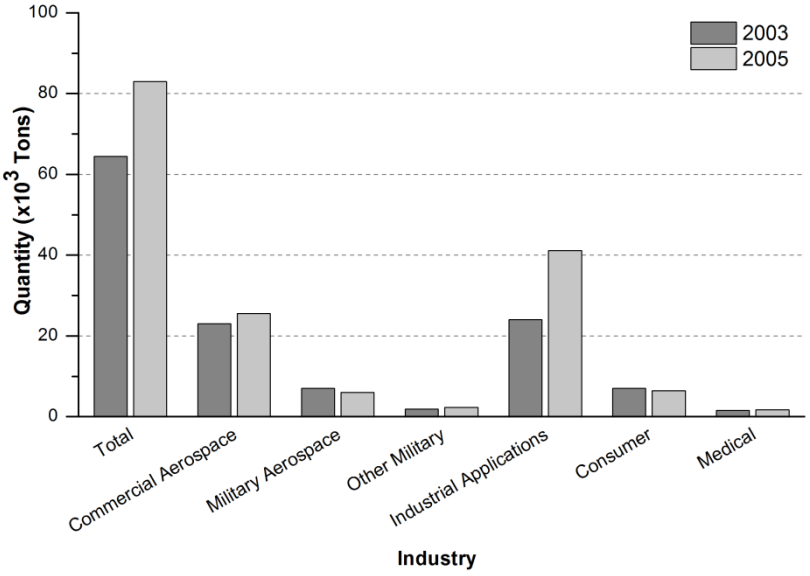

Figure 2.4 Worldwide titanium mill product usage by end-user industry for 2003-2005. Adapted from Hogan *et al.* [35].

2.2 Titanium Alloy Classification

In general, titanium alloys may be divided into two classes based on their primary function: corrosion resistant alloys and structural alloys. The corrosion resistant grades are those that have compositions close to pure titanium or whose primary alloying components are α-stabilisers, and as such so show a microstructure comprised almost entirely of the α-Ti phase. These alloys typically demonstrate excellent corrosion resistance and weldability as well as being easily formed due to their high ductility. The compromise is low strength, which can only be enhanced by work hardening or solid solution strengthening, predominantly by interstitial alloying elements such as hydrogen, oxygen and nitrogen [2]. While increasing strength and hardness, these alloying additions reduce ductility and result in an increase in the allotropic transformation temperature compared to high purity alloy grades [1]. The single phase microstructure means that these α-Ti alloys are not susceptible to precipitate coarsening, as a number of the structural grades may be, and so are able to retain their strength at moderate service temperatures while also offering good creep resistance. As such, these corrosion resistant grades are used for corrosion resistant piping, heat exchangers and valving in industries such as energy production and food, chemical and petrochemical processing. The single phase HCP microstructure also eliminates the possibility of a

ductile-to-brittle transition, making these alloys suitable for cryogenic applications. While the initial capital cost of titanium alloys is much greater than competitive materials such as stainless steels and copper-nickel alloys, their life cycle costs are often seen to be far lower due to their superior durability, virtually eliminating the need for inspection, repair and replacement [36, 37].

Structural titanium alloys are considered to fall into the broad categories of near-α alloys, α+β alloys, metastable β alloys and titanium aluminide intermetallics [1], although it may be argued that the near-α alloys represent a sub-class of the α+β alloys [2]. The classification of alloys is based on the phase composition and hence the inclusion of various alloying elements which interact with the titanium to stabilise either the α or β phase. The effect of alloying elements in terms of α or β stabilisation in binary titanium alloys is summarised in Figure 2.5, which shows the Molchanova classification for titanium alloy phase diagrams.

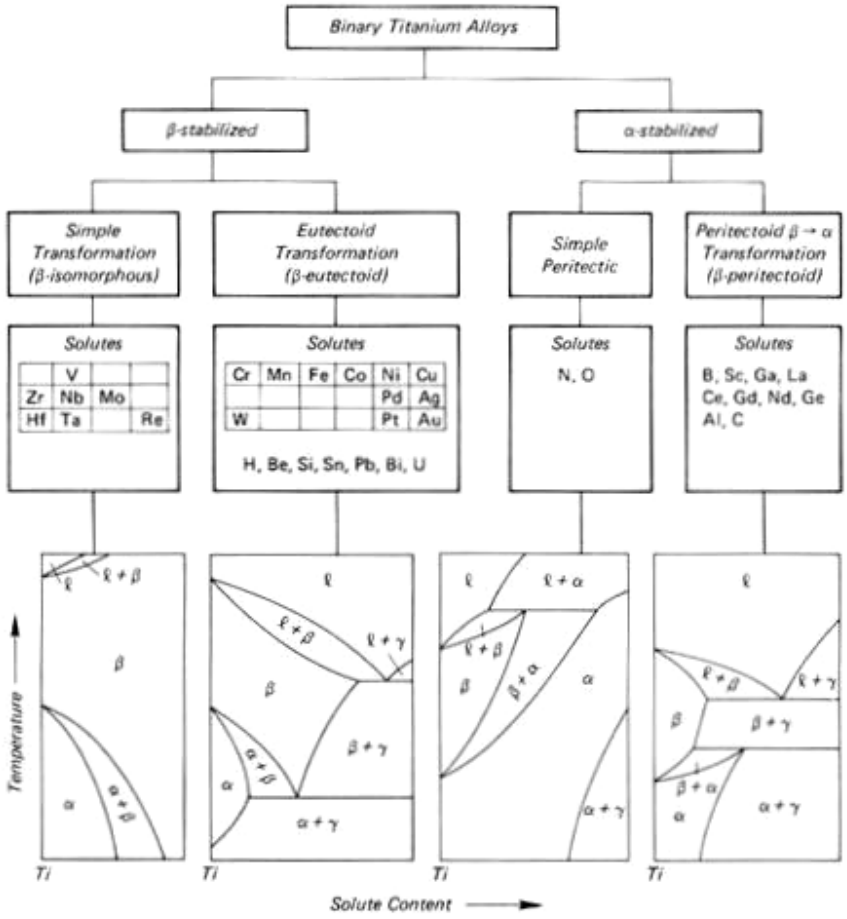

Figure 2.5 The Molchanova classification scheme for binary titanium alloy phase diagrams. From Wessel [1].

Applications for these structural alloys range from structural members in aircraft, space and military devices to biomedical implants and sporting equipment [1]. The duplex α+β grades are also used extensively in applications requiring retained strength at elevated temperature such as gas turbine components for both aircraft and energy production. In these alloys, the presence of a stable secondary (β) phase distributed through the primary (α) matrix acts to restrict thermally activated grain growth of the α-Ti and thereby limit any loss of mechanical strength. Mechanical properties of a number of common titanium alloys are provided in Table 2.2. This illustrates a general trend that the addition of alloying elements leads to an increase in both yield and tensile strengths with a corresponding decrease in ductility. It should be noted however that those elements giving the greatest effect are the β-eutectoid stabilisers such as iron, cobalt and nickel, all of which increase alloy hardenability [1].

Table 2.2 Mechanical properties for several common titanium alloys with compositions provided as weight percentage (wt%). Property data from MatWeb [38].

Alloy Type	Composition	Condition	Yield Strength (MPa)	Tensile Strength (MPa)	Ductility (%EL)
Commercially pure	Ti	Annealed	340	430	28
α	Ti-5Al-2.5Sn	Annealed	827	861	15
Near-α	Ti-8Al-1Mo-1V	Annealed	910	937	18
α+β	Ti-6Al-4V	Annealed	880	950	14
Near-β	Ti-10V-2V-3Al	Solution treated	930	1000	17
β	Ti-15V-3Cr-3Al-3Sn	Solution treated	770	790	22

Of the structural alloys, the most common are the duplex grades whose microstructure, consisting of both α and β phases, is achieved by the addition of both α and β stabilisers. This results in a material that is heat treatable, typically by solution treatment followed by deformation and thermal aging processes, but also readily used in the annealed condition [2]. Within the group of duplex alloys, the Ti-6Al-4V (ASTM Grade 5) alloy is that used most extensively in the aerospace sector and makes up approximately 50 % of all metallic titanium worldwide by mass, as shown in Figure 2.6 [21, 24]. As previously mentioned the inclusion of β-stabilisers into the duplex grades, while in relatively low volumes, gives high strength, good creep and fracture resistance without the high hardenability seen in the metastable β alloys. Typically the duplex alloys contain between 10 % and 50 % β phase at ambient temperature (depending on composition and TMP) and so tend to exhibit good formability and corrosion resistance,

due to the relatively high proportion of α phase, however weldability is considered poor for those alloys containing more than 20 % β-Ti [2].

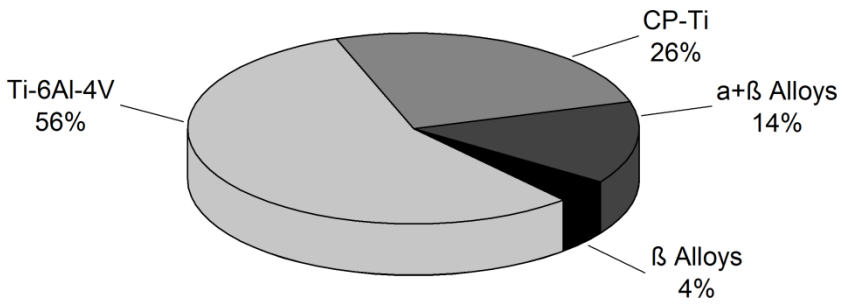

Figure 2.6 Approximate breakdown of metallic titanium usage in the USA market by alloy classification in 1998. While Ti-6Al-4V is classified as an α+β alloy it is shown separately to highlight its dominance. Adapted from Lutjering [23].

The addition of higher levels of β-stabilisers produces microstructures dominated by the β phase that exhibit high strength and high hardenability as well as increased fracture toughness, forging and cold forming abilities compared to the duplex alloys. The trade-off is typically a reduction in creep strength and an increase in crack growth rate [1]. As such there has been, and continues to be, considerable efforts undertaken in the development of high strength metastable β-Ti alloys with improved fatigue properties and good forming characteristics predominantly for use in the aerospace industry. These alloys include Ti-10V-2Fe-3Al (Ti-10-2-3), Ti-15V-3Cr-3Al-3Sn (Ti-15-3) and Ti-3Al-8V-6Cr-4Mo-4Zr (β-C), where designations indicate alloys composition as weight percentage and terms in parentheses represent common industrial names [39]. In general the high alloying contents of these metastable β alloys that deliver their high strength renders their weldability poor, meaning components are largely formed through deformation processes such as forging and rolling. The relatively high cost of β-stabilising elements including vanadium, molybdenum and zirconium has also led to the development of low cost beta (LCB) alloys such as Ti-5Al-5V-5Mo-3Cr (Ti-5553) and Ti-6.8Mo-4.5Fe-1.5Al (TIMETAL LCB) [40, 41], which make use of less expensive alloying additions including iron and chromium. In particular, the Ti-5553 is showing significant promise for structural titanium castings, with high formability by casting and forging as well as increased strength, fracture toughness and fatigue resistance when compared to Ti-6Al-4V [42, 43].

2.3 Production and Manufacture of Titanium and its Alloys

The primary focus of this research project was, as outlined previously in chapter 1, to investigate the viability of producing large scale structural titanium components using GTAW additive manufacturing techniques. The driving force for the development of such new and novel manufacturing processes is the reduction of the costs associated with titanium alloys in order to facilitate more efficient and wide spread utilisation of these unique materials. In order to describe these new processes and their potential in titanium manufacturing, it is necessary to first consider the origins of the relatively high costs associated with titanium alloys. Relating these costs to the current processing methods and technologies allows the identification of shortcomings in present practices and thereby provides context for discussion of technological advancements that may lead to reduced costs through increases in efficiency, productivity and material utilisation.

2.3.1 Cost Structure of Production and Manufacture of Titanium Components

The discussions presented in preceding sections have alluded to the relatively high costs associated with the extraction, production and fabrication of titanium alloys. These costs are clearly illustrated in Figure 2.7, which shows the cost structure for the production of a final metallic component from ore for titanium in comparison to two common competitive engineering alloys, namely steel and aluminium, on a cost per unit mass basis. Machining costs presented have been determined from machinability ratings, based on power requirements and cutting speed, which are taken to represent cost per unit mass of material removed during the machining operation.

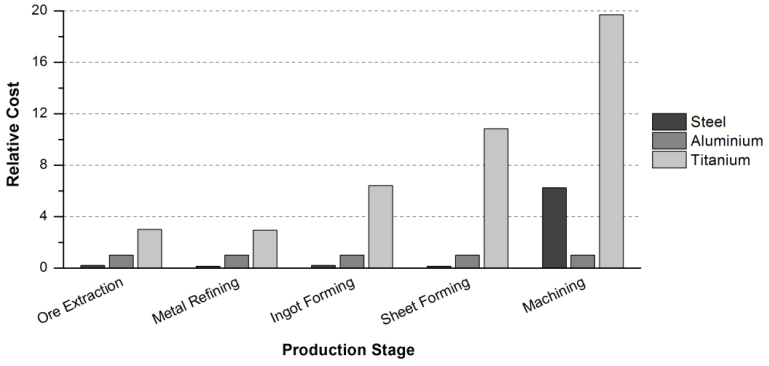

Figure 2.7 Cost structure for the production of a metallic component for steel, aluminium and titanium with relative cost determined from price per unit mass (USD/lb) normalised to the costs for aluminium. Using data from, Hurless and Froes [44], Yang and Liu [45] and [46, 47].

It can be readily seen that at every stage of processing, the costs associated with titanium alloys are many times greater than that of both steel and aluminium and so opportunities for cost reduction exist in all aspects of titanium processing and manufacture. The largest differences within this cost structure are clearly in the machining and sheet forming processes, with ingot forming also showing significant cost reduction potential. It can then be understood that while technological advances in the extraction and refinement of titanium may deliver notable cost savings, greater potential for cost benefits exists in the improvement of current forming processes. Furthermore, massive cost reductions are possible through the reduction or elimination of these forming processes through the development and implementation of near net shape manufacturing processes including powder metallurgy and additive manufacturing methods.

Considering then the production costs associated with a typical aerospace component, such as is expected to appear in the new F-35 Joint Strike Fighter aircraft currently under development as detailed in Figure 2.8, it can be seen that machining makes up approximately 42 % of the total cost with the remainder coming from material cost associated with sponge production and plate manufacture.

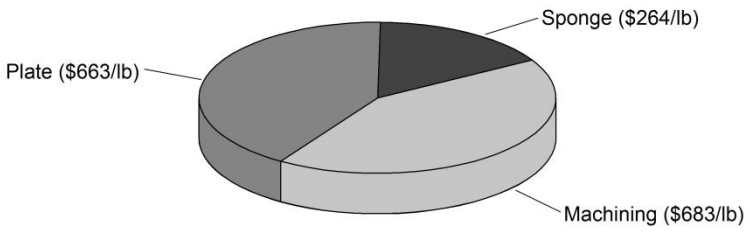

Figure 2.8 Cost breakdown for a typical aerospace component produced from an unspecified titanium alloy in terms of cost per unit mass of final component (USD/lb) for a production run of 200 units per year. Adapted from Barnes, *et al.* [48].

One key factor in the cost of titanium components for aerospace applications is the extremely low utilisation of material with machining based ‘subtractive’ manufacturing processes. This is typically characterised by the so-called ‘buy-to-fly’ ratio (BTF) which relates the mass of the raw material purchased, such as plate or billet, to the mass of the final machined component as in service. Hence this provides an indication of the material lost during manufacture, normally as offcuts or swarf. In the case of the component considered above, the BTF for the machining operations was taken as 10:1, which is a somewhat conservative value for aerospace components, with figures from

15:1 to 35:1 identified in some cases [18, 49]. While most of the scrap can be recovered and recycled, the costs associated with the reprocessing are substantial with a far more economically appealing solution being a reduction or elimination of such scrap generation in the first instance. Clearly a reduction in the BTF for component manufacture would deliver immense savings in terms of both raw material costs and machining requirements with current aerospace industry targets in the order of 5:1 [48, 49]. The most effective means for reducing this BTF is, as previously identified, through the implementation of near net shape manufacturing processes. It is also possible to reduce costs associated with material removal operations, whilst also increasing productivity, through improvements in machining processes such as thermally assisted machining (TAM) and the development of cutting tools with improved wear resistance. Table 2.3 lists several emerging technologies within the metallic titanium industry and identifies the potential cost saving of each as well as their feasibility and expected time frame for commercialisation. A number of these, as well as further technological developments not identified in this table, will be discussed in greater detail in subsequent sections of this chapter.

Table 2.3 Emerging technologies within the supply chain of metallic titanium components and their potential for cost reductions. From Seong, *et al*. [24].

Category	Technology	Time Frame	Feasibility	Cost Savings
Improved Extraction and Refinement	Armstrong Process	Mid	Low	Low
	FFC/Cambridge Process	Mid	Low	Low
	DuPont MER Process	Mid	Mid	Low
	Hydride-Dehydride	Near	Mid	Low
Powder Metallurgy	HIP Casting	Long	High	High
	Mill Product P/M	Long	High	Mid
	Near net-shape P/M	Long	Mid	High
Single Melt Processing	Cold Hearth Melting	Near	High	Low
Solid Freeform Fabrication	Various	Mid	Mid	Mid
Improved Machining	Various	Near	High	High

2.3.2 Current Titanium Production Techniques

One disadvantage of titanium alloys is the relatively high cost of the raw material compared to competitive structural metals, with much of this originating from the primary production methods used to convert ore into metallic products such as billet and plate. Regardless of the processing route taken to form the metallic titanium, the first step is the mining and purification of ores such as rutile (TiO_2) and ilmenite ($FeTiO_3$). As the naturally occurring rutile ore is rarely of sufficient purity to be economically viable for direct use in the production of metallic titanium, synthetic rutile is commonly produced from ilmenite ores via the Becher or Benilite processes and then used as the feed stock for metallic titanium production.

The Becher process consists of four primary steps with the first being oxidation of ilmenite in air to convert all iron in the ore to iron (III) oxide. This iron (III) oxide is then reduced to metallic iron by heating to temperatures in excess of 1100 °C in the presence of coal and sulphur to yield the synthetic rutile. The iron is readily removed in an oxidising 'aeration' process and further purification of the rutile is achieved through a sulphuric acid leach [50, 51]. These four steps are summarised by the chemical reactions presented in Equation 2.1. The primary differences of the Benilite process are the reduction process, which is conducted for a longer time at temperatures close to 800 °C, and the acid leach, which uses hydrochloric acid and calcination. It should be noted that less than 5 % of synthetic rutile produced worldwide is used for the manufacture of metallic titanium, with the vast majority used as white pigment for paints, inks, paper, plastics and household consumables such as cosmetics, toothpastes and sunscreens [50, 52].

i. Oxidation $4\ FeTiO_{3\,(s)} + O_{2\,(g)} \rightarrow 2\ Fe_2O_3 \cdot TiO_{2\,(s)} + 2\ TiO_{2\,(s)}$

ii. Reduction $Fe_2O_3 \cdot TiO_{2\,(s)} + 3CO_{(g)} \rightarrow 2\ Fe_{(s)} + 2\ TiO_{2\,(s)} + 3\ CO_{2\,(g)}$

iii. Aeration $4\ Fe_{(s)} + 3\ O_{2\,(g)} \rightarrow Fe_2O_{3\,(s)}$

iv. Acid Leach *to remove residual iron and other impurities*

Equation 2.1 Chemical reactions describing the production of synthetic rutile from ilmenite by the Becher process.

Usable metallic titanium was first produced on an industrial scale from rutile via the Hunter process, developed in 1910 by Matthew A. Hunter [53]. In this process, rutile is mixed with metallurgical coke in a fluidised bed reactor at elevated temperatures with

chlorine gas injected through the base of the vessel to generate titanium tetrachloride ($TiCl_4$) as described by Equation 2.2. This $TiCl_4$ is then reduced by sodium (Na) at temperatures in the range of 700 °C to 800 °C to yield metallic titanium 'sponge' with 99.9 % purity [54]. It is this second step, involving the reduction of $TiCl_4$ by Na, which constitutes the actual Hunter process. This chemical reaction for this process is presented in Equation 2.3.

$$TiO_{2\,(s)} + 2\,Cl_{2\,(g)} + C_{(s)} \rightarrow TiCl_{4\,(g)} + CO_{2\,(g)}$$

$$TiO_{2\,(s)} + 2\,Cl_{2\,(g)} + 2C_{(s)} \rightarrow TiCl_{4\,(g)} + 2CO_{\,(g)}$$

Equation 2.2 Chemical reactions for the chlorination of rutile to yield titanium tetrachloride.

$$TiCl_{4\,(g)} + 4\,Na_{(l)} \rightarrow Ti_{(s)} + 4\,NaCl_{(l)}$$

Equation 2.3 Chemical reactions describing the formation of metallic titanium by the Hunter process.

A similar procedure to the Hunter process was developed during the 1930's by William J. Kroll, with his work on "The Production of Ductile Titanium" published in 1940 [55]. The Kroll process differs from the Hunter process in that the reduction of $TiCl_4$ is performed using magnesium in preference to sodium. The use of magnesium is seen to be more economical and so the Kroll process has essentially replaced the Hunter process, making it the most common industrial method for the production of metallic titanium [54]. Prior to the reduction stage, the $TiCl_4$ is purified in a two-stage fractional distillation process to remove impurities such as carbon oxides and silicon chlorides. The purified $TiCl_4$ may then be reduced by magnesium in a batch process via a two-step reaction, described by Equation 2.4, to yield the titanium sponge product which is further purified by a vacuum distillation process to remove residual magnesium chloride ($MgCl_2$) before being crushed and sized. The Kroll process is illustrated schematically in Figure 2.9, which also shows the recovery of both magnesium and chlorine through electrolysis of the $MgCl_2$ by-product.

$$TiCl_{4\,(g)} + Mg_{(l)} \rightarrow TiCl_{2\,(g)} + MgCl_{2\,(l)}$$

$$TiCl_{2\,(g)} + Mg_{(l)} \rightarrow Ti_{(s)} + MgCl_{2\,(l)}$$

Equation 2.4 Chemical reactions for the reduction of titanium tetrachloride by magnesium in the Kroll process.

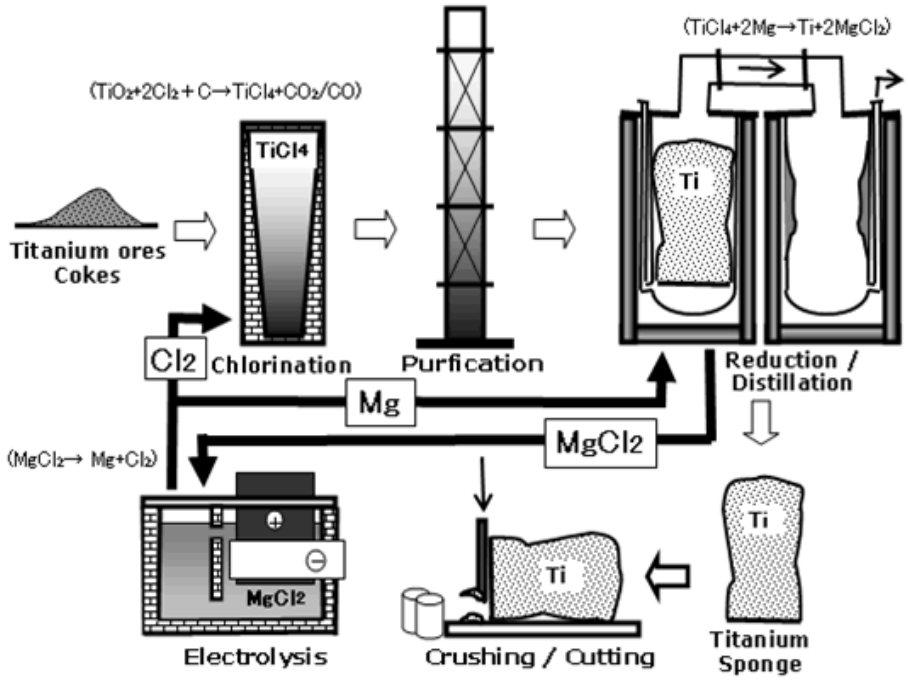

Figure 2.9 Process diagram illustrating the production of titanium sponge by the Kroll process. From TOHO Titanium [56].

The high purity sponge, as implied by the name and as shown in Figure 2.10, is a highly porous solid not suitable for use in any engineering application without further processing. Following its production, the titanium sponge is cut or crushed into a coarse powder, as shown in Figure 2.10(b), which can be mechanically mixed with recycled materials, known as 'revert', or master alloys to introduce alloying elements such as aluminium and vanadium to produce a bulk of the desired composition. The inclusion of revert must be carefully controlled to eliminate the introduction of undesirable contaminants such as heavily oxidised sections or tungsten carbide inclusions from machining swarf. This bulk is mechanically compacted and formed into feed electrodes which are melted in a vacuum arc remelting (VAR) furnace to produce an intermediate ingot with poor compositional homogeneity and unacceptably high levels of contaminants, particularly oxygen and nitrogen [54]. As such, these ingots undergo a conditioning procedure to remove surface defects before being remelted in a second vacuum melting process where strict process control yields a final ingot of the alloy with the required composition and purity. For critical applications where very high purity is needed to achieve the required fatigue or reliability properties a third vacuum melting process may be employed [27]. Following further surface conditioning, these ingots may then undergo TMP to produce mill products such as slabs, bar and plate

which can then be further fabricated to produce the final component as required. The cost structure for the production of plate products via the Kroll process and vacuum are remelting is illustrated in Figure 2.11.

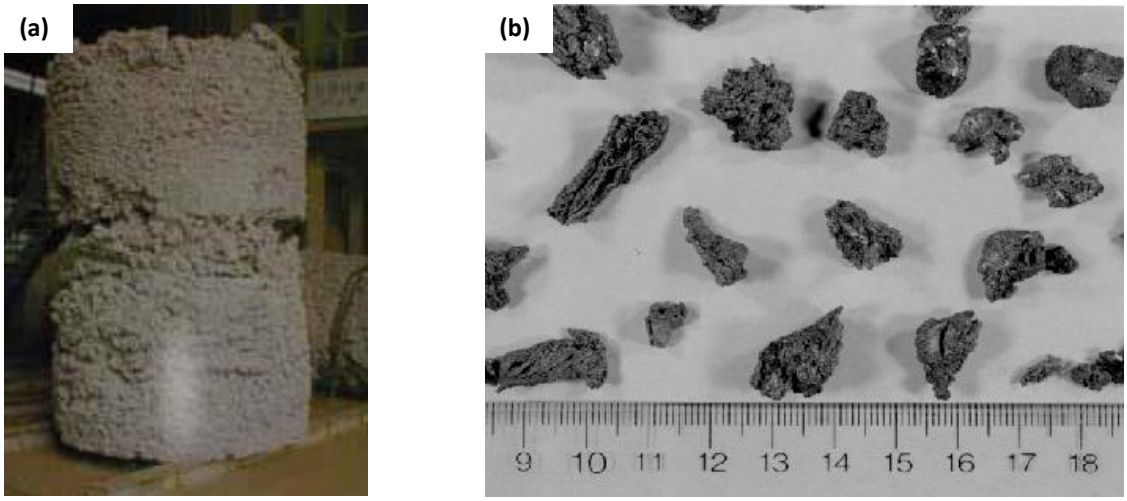

Figure 2.10 Photographs showing the morphology and porous nature of metallic titanium sponge (a) before and (b) after crushing. From (a) Sumitomo Corporation [57] and (b) Lutjering [54].

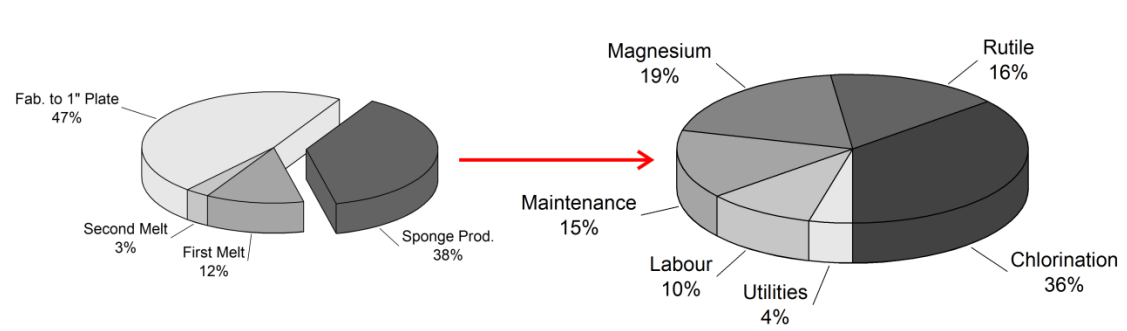

Figure 2.11 Relative cost factors for conventional mill processing of titanium plate 1 inch in thickness with emphasis on costs associated with sponge production by the Kroll process. Adapted from Lutjering [54] and Kraft [58].

Other melting processes such as cold hearth melting (CHM) and electroslag remelting have recently been used instead of or in conjunction with the typical VAR to produce titanium alloys. These methods present a number of advantages compared to the VAR process with the first being the ability to produce non-axisymmetric profiles such as rectangular slabs and billets, which may be more readily and economically processed to flat mill products. CHM also has a higher tolerance for inclusion of revert with residence of the melt facilitating gravity separation of contaminants such as tungsten from machining, as well as allowing the dissolution of oxygen and nitrogen rich defects

[54]. Finally, these processes tend to be better suited to real-time process control, yielding a higher quality final product.

2.3.3 Emerging Production Processes

The high chemical affinity of titanium for interstitial ‘contaminants’ such as oxygen and nitrogen, particularly at elevated temperatures, necessitates the highly controlled energy intensive production route and also leads to significant material waste, increasing the cost of the final product. The cost structure presented in Figure 2.11 clearly shows that the two major cost centres in the production of mill products are the initial sponge production and the multi-step TMP used to form the desired section profile. Considering the latter, a large portion of this cost is due to the significant loss of material during surface conditioning procedures between TMP steps which are required to remove surface defects such as cracks and heavily contaminated material. The poor operating and conversion efficiencies of the Kroll process in sponge production have been acknowledged since its inception, with Kroll himself predicting his pyrometallurgical process would be readily superseded by a more efficient electrochemical process [59]. While no such replacement has been successfully implemented in industry, numerous processes are currently under development with the aim of reducing the cost of titanium production.

One of the primary shortcomings of both the Hunter and Kroll processes in titanium sponge production is their batch mode operation which is labour intensive and has significantly lower efficiency than an equivalent continuous process [59]. As such, a number of technologies are being investigated and developed to adapt the same chemistry as these proven processes into a more efficient continuous process. The first of these is the Armstrong process developed by International Titanium Powder which uses the same chemistry as the Hunter process. $TiCl_4$ vapour is injected continuously into a stream of molten sodium where it is reduced with 100 % efficiency to yield fine metallic titanium particles which are separated from the excess sodium and sodium chloride by-product through filtration and distillation [58, 60]. Aside from the inherent increases in efficiency due to continuous operation, the Armstrong process gives a great deal of control making it possible to consistently produce high purity powders with chlorine, sodium, iron and oxygen contents less than 10 ppm, 30 ppm, 270 ppm and 1000 ppm respectively [58, 60]. The powder produced is found to be suitable for near

net shape powder metallurgy forming methods such as hot isostatic pressing (HIP) as well as conventional melt processing to form mill products [61]. The process is also capable of producing pre-alloyed powders such as Ti-6Al-4V by inclusion of suitable metal chlorides in the $TiCl_4$ feed stream [62]. A full-scale production facility using the Armstrong process has recently finished commissioning with an annual production capacity of two million kilograms; however the cost of the final powder is yet to be ascertained.

The TiRO process currently under development by the Commonwealth Scientific and Industrial Research Organisation (CSIRO) in Australia uses the chemistry of the Kroll process for the continuous production of metallic titanium using a fluidised bed formed by argon gas [63]. Currently operating as a pilot plant with capacity of two kilograms per hour, the process shows potential with high conversion efficiency and control over the size and shape of the powder product by varying process parameters [64]. While this process offers increased efficiency with reduced labour and energy requirements, it is yet to be proven on an industrial scale and contaminant levels, particularly chlorine, remain relatively high compared to Armstrong powders.

In contrast to the pyrometallugy based Armstrong and TiRO processes, the Fray-Farthing-Chen (FFC) process is based on electrolysis with synthetic rutile being converted directly to metallic titanium by electrochemical deoxygenation in a bath of calcium chloride ($CaCl_2$) at elevated temperature [65, 66]. The product of this batch process is a metallic titanium sponge like that obtained through the Kroll process, which is suitable for both powder metallurgical and conventional melt forming processes. One of the key benefits of the FFC process is the direct use of rutile, eliminating the intermediate $TiCl_4$ and hence costs associated with its production. However, this also presents difficulties as the purity of the final titanium depends heavily on the purity of the rutile feed stock, with iron impurities from ilmenite processing of greatest concern. Under normal processing conditions the final oxygen levels are below 1000 ppm with longer processing times able to reduce this to as low as 60 ppm [58]. Compared to the Kroll process, the FFC process is said to be five times faster with capital expenses, operating costs and carbon emissions reduced by at least 50 % [44, 65, 67]. It has also been shown that the electrochemical deoxygenation process is suitable for a number of metal oxides including zirconium, vanadium, aluminium and chromium meaning there is the possibility to directly produce pre-alloyed powders as in the Armstrong process

[68, 69]. The process is currently run by the UK based company Metalysis, and while not yet operating at a full industrial scale, significant quantities of both titanium and tantalum have been produced with a small scale production facility currently being commissioned [70].

Another electrochemical based extraction method is currently being developed by collaboration between Materials and Electrochemical Research (MER) Corporation and DuPont Titanium technologies. Titanium is extracted in a two-stage process by first mixing the TiO_2 rich feed stock with carbon rich material and binder under high temperature and pressure to produce a composite anode which is then used in an electrowinning process with various electrolyte salt solutions [71]. The principal advantage of this process is the ability to utilise a wide range of TiO_2 containing feed stocks from raw ilmenite and titania slags to synthetic rutile, however, as with the FCC process, the purity of the final product is highly dependent on that of the initial feed. Titanium powders produced using this process exhibit oxygen levels of less than 500 ppm with other impurity levels not yet released. Current production is being scaled up to a demonstration facility capable of 225 kg/day with significant funding from the Defense Advanced Research Project Agency (DARPA) to further develop the process [71-73].

One further development worth discussing is the enhanced roasting and magnetic separation (EMRS) process being developed by Auspac Resources in Australia for the production of synthetic rutile. The three stage process begins with magnetic purification of ilmenite, which is then roasted in a two stage fluidised bed before acid leaching to yield the rutile [74]. In addition to the competitive costs and higher TiO_2 yield detailed in Table 2.4, the ERMS process is able to convert a wider range of ilmenite ores that would not be deemed economically viable for either the Becher of Benilite processes.

Table 2.4 Comparison of the ERMS process to conventional synthetic rutile production methods in terms of product purity and cost. From Veldhuizen [51].

Process	TiO_2 Content (%)	Capital Cost (USD/tonne)	Operating Cost (USD/tonne)
Becher	88-93	400	110-140
Benilite	90-95	620	180
ERMS	96-98	400	120

The preceding discussions describe only the more advanced or promising processes for primary production of metallic titanium and are in no way a complete assessment of all new processes and technologies with some twenty organisations worldwide understood to be conducting similar research and development projects [35]. A more comprehensive assessment of emerging cost reduction technologies for metallic titanium, such as that presented by Kraft [58], is beyond the scope of this literature review.

2.3.4 Fabrication of Titanium and its Alloys

While the unique properties of titanium and it alloys make them highly sought after for mechanically and physically demanding applications, it is the same properties that present significant challenges in component fabrication. The conversion of mill products to a final usable form is seen to be the greatest cost for engineering components manufactured from titanium alloys, and so represents an area where significant cost reductions could be achieved. The process of value adding typically begins with mechanical deformation, by forging or rolling for example, to generate a preform which is then finished by a series of material removal steps such as milling, turning and drilling. The high mechanical strength of titanium alloys requires high flow stresses, and hence substantial upsetting forces, during the forging or rolling processes, with very few facilities worldwide capable of producing the large preforms required for typical applications such as aircraft superstructures and turbines for power generation [54]. In order to reduce the upsetting forces required, as well as deliver the desired microstructure, these deformation processes are often conducted at elevated temperatures, requiring expensive dies and tooling as well as consuming large quantities of energy. Given the scale of these high temperature deformation processes, it is impractical for them to be performed under inert atmospheric conditions leading to significant atmospheric contamination of the surface layers, which must be removed prior to subsequent processing giving considerable loss of material.

Material removal by machining processes is used extensively in the manufacture of engineering components from titanium alloys. However, as the information presented in Figures 2.7 and 2.8 clearly shows, the majority of component manufacture costs originate from these machining processes. The process of metal removal during machining is achieved by controlled shearing of unwanted material from the bulk work-

piece using a sharpened cutting tool. Typically this is accompanied by a significant temperature increase in the shear zone due to localised severe plastic deformation and friction between the cutting tool, work-piece and removed material. This localised increase in temperature is exacerbated when machining titanium alloys due to their relatively low thermal conductivity, shown in Table 2.5, which clearly limits their ability to dissipate thermal energy through the bulk. At these elevated temperatures the titanium work-piece becomes highly reactive with its surrounds, with atmospheric contamination by oxygen and nitrogen not only increasing the strength and hardness of the exposed surface but also stabilising the HCP α-Ti phase giving rise to a so-called 'alpha case'. This oxygen rich surface layer has dramatically reduced ductility and readily forms micro-cracks that then compromise mechanical properties of the component as a whole, particularly fatigue behaviour [75-78]. Finishing operation such as final machining and grinding must be carefully executed to remove any such surface defects which are most common in roughing operations where material removal rates (MRR) are comparatively high. While machining in argon can reduce atmospheric contamination of the work-piece, tool life is significantly compromised due to the poor lubrication properties and low thermal conductivity of argon [79].

Table 2.5 Thermal conductivity values for various engineering alloys. Compiled from Granta Design Limited [25].

Alloy Designation	Condition	Thermal Conductivity (W/m.K)
6061 Aluminium	T651	161-174
7050 Aluminium	T7651	154-167
AISI 1040 Low Carbon Steel	Annealed	50-54
AISI 4340 Low Alloy Steel	Annealed	35-50
AISI 430 Stainless Steel	Annealed	23-27
AISI 316 Stainless Steel	Annealed	13-17
Grade 2 Titanium	Annealed	16.3-18.0
Ti-6Al-4V	Solution treated + aged	7.1-7.3
Ti-10V-2Fe-3Al	Solution treated + aged	8.0-8.7

One common method for increasing cutting tool life is the use of ceramic surface coatings, with the most common being titanium based including TiN, TiCN and $TiAlN_2$ as well as various zirconium and chromium nitrides [80]. At the elevated temperatures found in the cutting zone the titanium work-piece readily reacts with such surface coatings, degrading the cutting tool and so severely shortening tool life while also

contaminating the work-piece with hard, brittle ceramic particles. It is also seen that titanium interacts unfavourably with cobalt based binding agents in cutting tools, further reducing tool life.

In addition to the chemical reactivity of titanium alloys reducing tool life, the high strength and hardness of these materials requires comparatively high cutting forces which in turn increases tool wear. To compound this, the chips of titanium alloys tend to be considerably thinner than those formed when machining other engineering materials and so the tool-chip contact area is significantly reduced generating high localised stress levels in the cutting zone and the tip of the cutting tool [45, 48]. This high contact pressure, combined with high surface friction and heat build-up in the cutting zone can cause localised pressure welding and galling, damaging both the cutting tool and work-piece [81, 82].

Titanium and its alloys are considered to exhibit moderate stiffness with values of Young's modulus in the range of 100 GPa to 120 GPa, as presented in Table 2.1. This moderate stiffness, combined with the high cutting forces described previously, gives rise to cutting induced vibrations even under low cutting speeds and shallow depths of cut [83, 84]. This is of particular concern in the manufacture of aerospace components, such as the strut shown in Figure 2.12, where deep pockets with thin walls or webs are used to minimise mass while maintaining component stiffness and strength. Such thin profiles readily deflect while being machined causing chatter and poor surface finish which can degrade the fatigue performance of the component, as well as further reducing tool life through rubbing contact. This is particularly apparent during milling operations where contact between the cutting tool and work-pieces is intermittent rather than continuous [85].

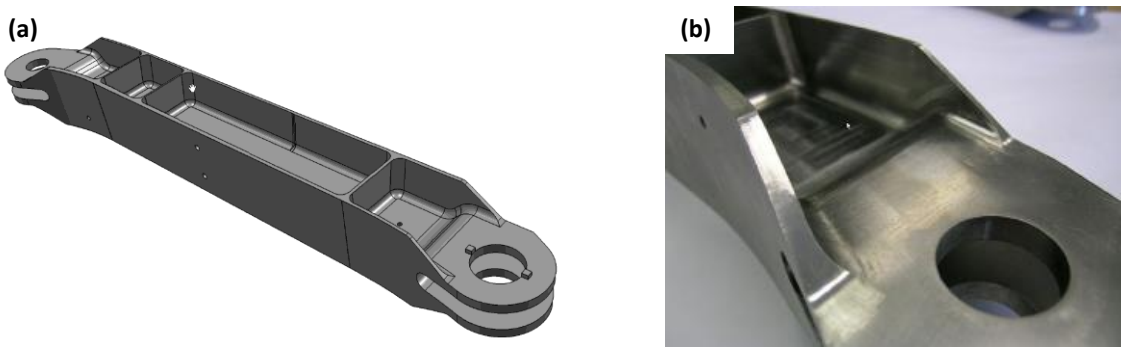

Figure 2.12 (a) Three dimensional model, and (b) final machined profile of a typical aerospace strut component featuring deep pocket and thin wall features. From Scherrer *et al*. [86].

Further difficulties encountered during the machining of titanium alloys may include microstructural alterations due to severe plastic deformation and localised heating, work hardening of the machined surface and auto-ignition of swarf [45].

In light of the difficulties described above, a great deal of research and development is being undertaken to reduce the costs associated with the machining of titanium alloys. The primary objective of these efforts is to increase the efficiency of titanium machining processes by increasing both tool life and MRR. As the greatest volumes of material removal take place during roughing operations it follows that these are where the greatest savings in terms of time, and hence money are to be made.

In many instances it is recommended that titanium alloys be machined with low cutting speeds, high feed rates and generous application of coolant to the cutting zone [10, 87, 88]. This coolant is typically applied at pressures below 0.8 MPa in an effort to lubricate the contacting interfaces and remove heat generated, however this is seldom realised with the loss of the fluid through boiling off due to the extreme temperatures in the cutting zone. High pressure coolant application, in the order of 7-20 MPa, forces greater penetration into the cutting zone giving enhanced cooling as well as reduced friction by acting as a hydraulic wedge between the cutting tool and chip. This is seen to result in increased cutting tool life and MRR as well as improved surface finish quality, attributed to the reduced tool wear [89-92].

The application of cryogenic cooling in machining of titanium alloys, through liquid nitrogen [93] or carbon dioxide ‘snow’ [94], has also been shown to reduce tool wear and improve surface quality by reducing heat build-up in the cutting zone. While such methods do have the potential for atmospheric contamination of the work-piece surface, the depth of these effects are very shallow and so are acceptable in roughing operations with the effected material removed during subsequent finishing processes.

An alternative approach to reducing tool wear and increasing MRR is to reduce the cutting forces required by thermal ‘softening’ of the material to be removed selectively preheating the material ahead of the cutting tool. This process of thermally assisted machining (TAM) is most commonly performed using lasers and has been shown to give reductions in machining time as high as 40 %, translating to a cost saving of between 20 % and 30 % [48]. An extension of this work is a hybrid process using both selective laser preheating of the work-piece and cryogenic cooling of the cutting tool

which is seen to give a 30 % increase in MRR compared to TAM alone, without compromising tool life [95]. Since such processes have the potential to cause thermal damage to the microstructure within the work-piece they are again best suited to roughing operations, with subsequent finish machining used to remove the heat affected surface layer. Additional methods for improved machining of titanium alloys relate to the cutting tool itself with development of new tool materials, tool geometry and surface coatings.

Clearly another more desirable option is to significantly reduce or eliminate the need for material removal processes by employing net shape and near net shape fabrication techniques. The cost benefit of such methods is twofold, with reduced machining requirements and reduced raw material costs through improved material utilisation. Whilst it is possible, the casting of titanium alloys poses numerous challenges, the first of which it the high temperature reactivity of these materials which typically limits manufacture to investment casting using refractory materials as forming dies. In addition to the high cost of the single use die, there is limited ability to manipulate microstructures through control of cooling rates and an increased potential for non-metallic inclusions as well as alpha case formation [44]. Other difficulties with casting of metallic titanium components include porosity, shrinkage and void formation. Hot isostatic pressing has been successfully used as a post-casting treatment to 'heal' internal porosity and generate a near to fully dense final component with improved fatigue properties.

Another net shape process used for component fabrication is superplastic deformation (SPD), typically combined with diffusion bonding (DB) processes to form complex profiles from sheet sections that would otherwise require extensive forming and joining processes including forging, machining, welding and mechanical fastening. It follows then that combined SPD/DB processes deliver significant benefits in terms of increased material utilisation, reduced labour costs and minimal alteration of microstructure and hence properties. However, as alluded to, these fabrication techniques are limited to the development of sheet type profiles with various contour features and integral stiffening such as aircraft panels and internally stiffened pipe sections as shown in Figure 2.13.

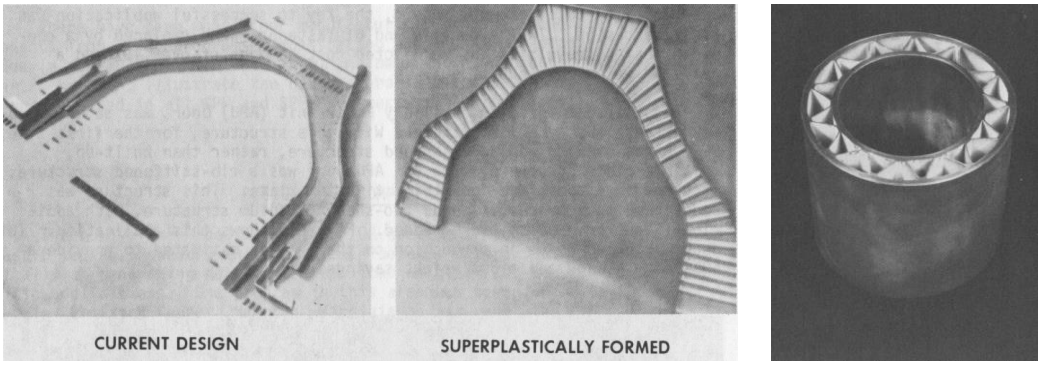

Figure 2.13 Examples of components with composite profile fabricated using combined superplastic forming and diffusion bonding methods. From Weisert and Stacher [96].

Additional near net shape processes are those based on powder metallurgy (PM) methods such as conventional press and sinter or HIP of components. While these methods are capable of accurately producing near net shape profiles with intricate geometries, concerns still exist over the properties of these parts with full density rarely achieved and high potential for inclusions. In particular the presence of residual chlorine from sponge production is seen to cause internal porosity during thermal processing and so adversely affect fatigue and other mechanical properties [44, 97]. The high capital cost of PM processing equipment also makes low production volumes, such as would be expected in aerospace applications, very costly. It has also been observed that abrasive tool wear is higher during finish machining of PM near net shape profiles compared to equivalent wrought sections [98]. Recent work has highlighted the potential for roll forming of continuous mill profiles from blended and pre-alloyed titanium powder feed stocks with studies showing mechanical properties approaching, if not exceeding those of conventional wrought sections [99, 100]. A key drawback to the use of PM methods is the high cost of suitable titanium powders, which are at present produced from wrought products through gas atomisation, plasma rotating electrode or hydride-dehydride processes. It follows then that the development of direct powder producing methods, such as the Armstrong and TiRO processes, will make component manufacture by PM techniques more economically viable.

2.3.5 Welding of Titanium and its Alloys

Welding is widely recognised as an industrially important joining process, allowing the fabrication of components and engineered systems by forming a permanent and rigid connection between assembled preformed profiles. The process of fusion welding may be considered as a combined process involving casting like behaviour in the fusion zone

(FZ) and TMP in the adjacent heat affected zones (HAZ). The sensitivity of titanium alloys to such thermal processes is well documented and so it can be concluded that the fusion welding of titanium alloys presents a number of challenges. Considering then the weldability of titanium alloys, it is generally accepted that those grades with low alloying contents such as the alpha and near-alpha alloys are readily welded while the duplex and beta rich alloys react less favourably to fusion welding. The addition of alloying elements to achieve a desired response to controlled TMP, such as rolling or forging, also has the potential to give unwanted changes to microstructure and properties during the welding process. The most common defects encountered in the welding of titanium alloys are porosity, atmospheric contamination of the FZ and HAZ, embrittlement of the weld area and cracking due to contamination.

Porosity is characterised by the presence of pores within the FZ giving a discontinuous solid which then has compromised mechanical properties due to the pores acting as stress concentrators and so facilitating crack formation and propagation. In fusion welds of titanium alloys, porosity often results from poor joint preparation where contaminants such as surface moisture or oil and grease liberate gaseous species upon heating. These gases are highly soluble in the liquid titanium in the molten pool, but have reduced solubility in the solid titanium alloy and so are ejected during solidification to give retained bubbles in the FZ. Porosity may also be attributed to the presence of chloride ions in the bulk metal (typically residual contaminants from the decomposition of $TiCl_4$ during the Kroll process) which then evolve into trapped gas bubbles during the weld solidification process. This chloride based porosity has also been observed during HIP of titanium alloys, with the addition of rare earth elements found to supress the pore formation [97]. Further, chlorine is seen to compromise fatigue behaviour as well as severely degrade the tungsten electrode in GTAW, reducing arc stability [44, 101-103].

The high affinity of titanium with atmospheric species such as oxygen and nitrogen at elevated temperatures presents difficulties during fusion welding processes, with contamination of the weldment by interstitial species also possible from moisture or hydrocarbon based contaminants in the weld zone. Such interstitial contamination is seen to reduce ductility and cause embrittlement by distorting the HCP crystal lattice structure in such a way that the number of active slip planes for dislocation movement is reduced from three to one [104]. The effect of oxygen content on mechanical behaviour

of commercially pure titanium is presented in Table 2.6. Further to this, it is seen that a 0.05 wt% increase in oxygen, nitrogen or carbon increases the strength of commercially pure titanium by 60 MPa, 135 MPa and 35 MPa respectively [105]. Such contamination is best avoided with extensive shielding of the entire weld zone with inert gases using non-conventional nozzles and trailing shield devices, or by completing welding processes in a controlled atmosphere such as a purged glove box or vacuum chamber. Welding guidelines for titanium and its alloys published by the Welding Technology Institute of Australia [8] suggest that alloys with high alloying contents are best welded using filler metal of lower strength to provide adequate joint ductility implying embrittlement of the weld zone is unavoidable in many titanium alloys. Atmospheric contamination of titanium causes discolouration of the surface, and while a number of welding standards [8, 106] use colour as an indication of weld quality it is understood that interstitial contamination can take place without surface discolouration occurring [104]. Atmospheric contamination by hydrogen can also lead to hydrogen assisted cold cracking (HACC) which originates in regions of high triaxial stress [107, 108].

Table 2.6 Chemical composition of the ASTM commercially pure titanium grades with β transus temperatures and mechanical properties included to illustrate the effect of oxygen and nitrogen on phase transformations and mechanical behaviour. Compiled from Aerospace Specification Metals, Inc. [109-112].

ASTM Grade	Composition, maximum allowable (wt%)						Beta Transus (°C)	Ductility (%EL)	σ_{ts} (MPa)	Hardness, Vickers
	Ti	C	Fe	H	N	O				
1	99.5	0.1	0.2	0.015	0.03	0.18	888	24	240	122
2	99.2	0.1	0.3	0.015	0.03	0.25	913	20	344	145
3	99.1	0.1	0.3	0.015	0.05	0.35	920	18	440	225
4	99.0	0.1	0.5	0.015	0.05	0.40	950	15	550	280

Another source of embrittlement within the weld zone is contamination by species such as silicon and iron from dust particles that may be present on in the weld zone due to poor preparation. While severe iron contamination can result from poor preparation of the weld joint, it is more commonly from residual contaminants from the ilmenite ore as well as reactor vessels used in the Kroll process. In these cases, segregation of iron within the fusion zone allows the formation of a titanium-iron eutectic that can cause cracking and act as initiation sites for corrosion [113].

The welding of titanium alloys also leads to significant changes in microstructure with the most apparent of these being significant grain growth of the β phase at elevated

temperatures. During fusion welding, the parent material in the near-HAZ adjacent to the fusion line is heated beyond the beta transus allowing recrystallisation to take place and giving rise to a coarser β grain structure. Along the solid-liquid interface of the molten pool these β grains are partially melted and so act as nucleation sites for epitaxial grain growth during solidification of the molten pool, with the crystallographic orientation of the solidifying titanium being identical to that of the parent β grain at the fusion line [114]. A process of competitive grain growth ensues where those grains oriented more favourably with respect to the heat source and thermal gradient become dominant with the result being large columnar like β grains. In metals with BCC crystal structures such as β-Ti, grain growth is most favourable for those grains where the <100> direction is aligned with the greatest thermal gradient [115]. This process is illustrated schematically in Figure 2.14.

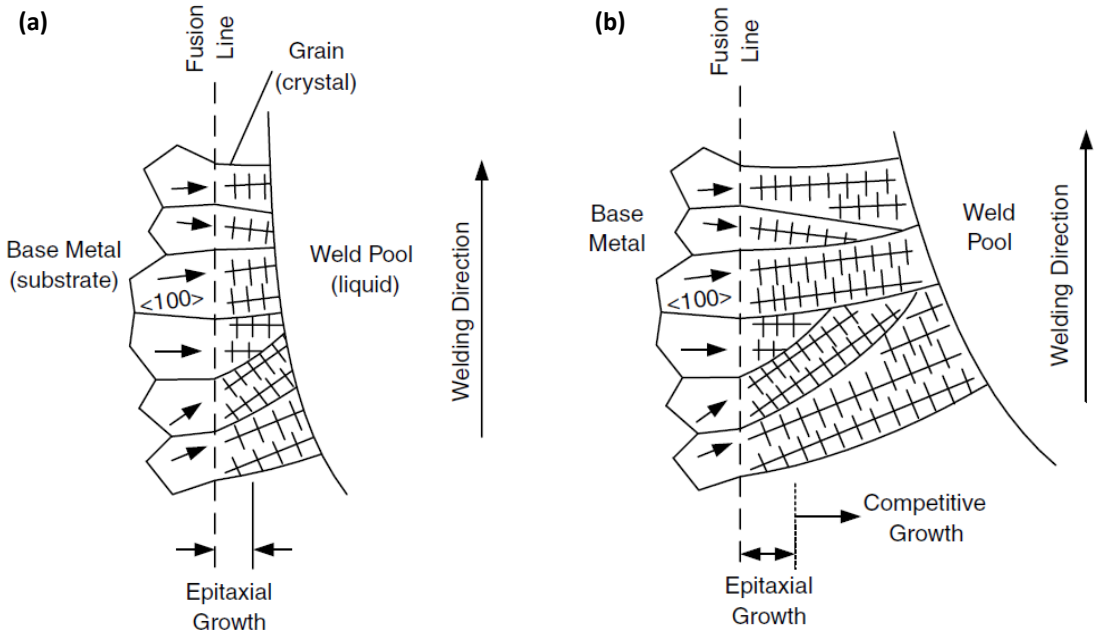

Figure 2.14 Schematic illustration of (a) epitaxial grain growth from partially melted β grains, and (b) competitive grain growth, during weld pool solidification. Adapted from Kou [115].

Upon cooling, the HAZ and FZ again pass through the beta transus, leading to nucleation and growth of the α phase within these large prior β grain boundaries. This prior β-Ti grain size, along with cooling rate, greatly influences the resulting microstructure of α or α+β grains and hence the mechanical properties of the weldment, giving a microstructural and mechanical behaviour discontinuity across the welded joint [54]. Grain coarsening of this type is often seen to reduce mechanical strength and hardness as well as generate anisotropy in material properties. A number of methods

have been proposed to limit grain growth during solidification of titanium welds including the use of inoculants to provide additional nucleation sites [116], pulsing of the heat source to produce instability in the solidification interface [114, 117-119] and addition of alloying elements to produce constitutional undercooling, again de-stabilising the solid-liquid interface [120]. Figures 2.15 and 2.16 illustrate grain coarsening within commercially pure titanium due to fusion welding.

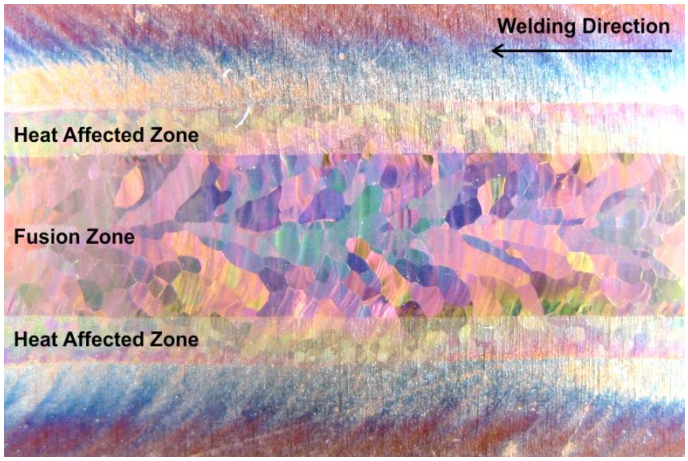

Figure 2.15 Macro photograph showing (in plan view) large prior β grains formed during bead-on-plate welding of commercially pure ASTM grade 2 titanium by GTAW. Colouration of the weld area is due to post-weld atmospheric contamination due to insufficient inert gas shielding upon cooling.

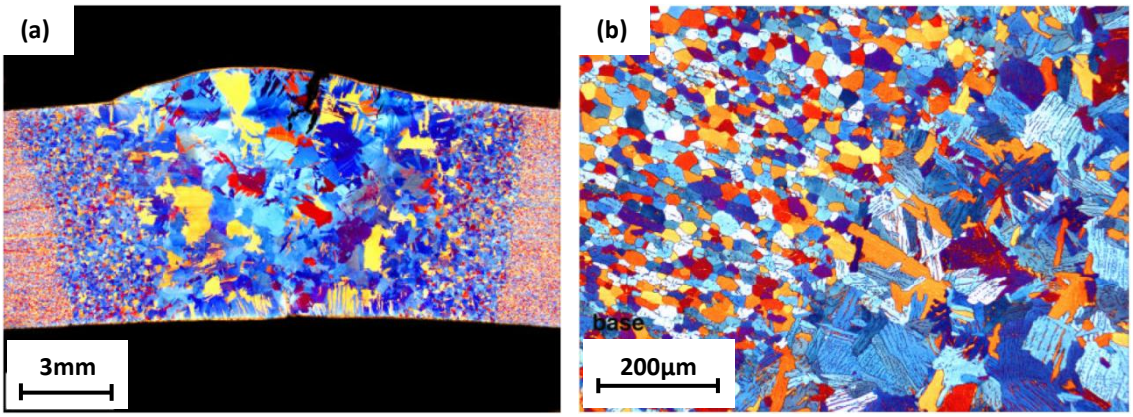

Figure 2.16 Optical micrographs showing grain coarsening in (a) FZ, and (b) HAZ, resulting from a multiple pass butt weld in commercially pure titanium plate by GTAW. From Danielson [7].

As with most metals, the thermal cycling associated with fusion welding of titanium alloys is unevenly distributed across the weldment giving rise to thermally induced residual stress in the final component. Whilst causing distortion and dimensional inaccuracies, the main problem with these internal stresses is the severe degradation of fatigue performance, which is one of the most desirable properties of titanium alloys.

Post weld heat treatments have been shown to be effective in reducing such stresses, however care needs to be taken to limit thermally activated grain growth as well as embrittlement of the weld zone, particularly in the metastable β alloys [121].

Titanium alloys with high alloying contents, particularly those high in β stabilisers, are susceptible to segregation of alloying elements during solidification due to the limited back diffusion of solute atoms in the solid [104, 122]. The resulting non-homogeneous composition of the FZ gives discontinuities in mechanical properties and may also lead to cracking in the weld zone. Alloys with high levels of β stabilisers also tend to show higher hardenability compared to the near-α and duplex grades. When combined with the relatively high cooling rates associated with fusion welding, this gives increased likelihood of forming the α′ martensite and athermal ω phases which are detrimental to mechanical properties. This problem is greatest for welding processes with high energy densities such as the electron beam and laser welding, and may be countered through the use of pre-heating and process control to manipulate cooling rates.

Of the conventional welding processes, gas tungsten arc is the most widely used for manual operations with titanium alloys due to its high level of cleanliness, reducing the likelihood of atmospheric contamination, as well as low capital investment. Advanced processes such as plasma arc welding, laser welding and electron beam welding are utilised for automated procedures and large production runs where their high capital costs can be justified [104]. These processes also offer high energy densities increasing welding productivity for thick sections with atmospheric control either inherent in their operation or readily implemented. Both friction stir welding and linear friction welding are seeing increased use in automated joining of titanium alloys with applications including fabrication of aerospace components and gas turbine assemblies for energy generation.

2.4 Additive Manufacturing of Titanium

The analysis provided above relating to the economic impediments and technical difficulties associated with the production of titanium alloys and the manufacture of structural engineering components from these materials leads to the conclusion that one effective means of reducing a large portion of such costs is through near net shape forming. While casting and powder metallurgical techniques have been shown to be

viable for some applications, they are seen to have a number of shortcomings including limitations on component size, restrictions on which alloys may be used and the concerns over mechanical properties. An alternative class of near net shape forming methods is that those based on the concepts of solid freeform fabrication, commonly referred to as ‘additive manufacture’. The underlying principle of these methods is that any three dimensional solid body may be considered to comprise of a series of planar sections that combine to form the full component profile. Using this concept, a desired component may be manufactured by the sequential build-up of these sections or ‘layers’, as determined from the computer model of the component, yielding an intermediate part which is near net shape to the final component. Finishing procedures such as thermal treatments and material removal processes can then be conducted as required to produce the final component. Advantages of these additive manufacturing techniques include reduced raw material requirements, increased materials utilisation, reduced material removal requirements and shorter lead-times between design and manufacture. In addition, this layer-wise approach to manufacturing facilitates new and optimised component designs that were previously considered impossible or not economically viable using conventional subtractive manufacturing methods. Many of these processes also lend themselves to creation of ‘functionally graded’ components where alloy composition is intentionally altered during the build-up process to give a final part which has mechanical and physical properties that are inhomogeneous by design. Further, a number of these techniques can be used in repair applications to re-build or repair worn and damaged components and so reclaim items that would otherwise be scrapped, reducing wastage and expenditure. With titanium being extremely energy intensive to produce and with increasing global demand for titanium alloys it is clear that additive manufacturing methods also stand to deliver significant environmental benefits [24].

Additive manufacturing processes used for the production of metallic components typically rely on a point heat source to bind the consumable material to itself and to successive layers to produce the near net shape freeform. It follows that these techniques may be broadly categorised according to the heat source and consumable used [123]. Consumable materials can be in either wire or powder form, with powders being further subdivided according to the delivery method as powder bed or blown powder. The heat source used may be a power beam such as laser or electron beam or

an electric arc as would be commonly seen in fusion welding processes. As shown in Table 2.7, many combinations of consumable and heat source are possible, each with their own strengths and weaknesses with respect to the additive manufacture of titanium alloys.

Those processes identified as using a 'powder bed' consumable achieve the layer-wise build-up of profiles by selectively heating regions on the top surface of a contained powder bed using a highly focused heat source such as laser or electron beam. The localised heating causes fusion or sintering of the metallic powder particles, binding them together to form a rigid slice of the final component. A new layer of powder is then spread across the powder bed and the controlled heating process repeated to generate the new layer and bond it to previous layers. Due to the highly focused nature of the power beams used in these powder bed processes, high levels of resolution are possible with wall thicknesses of 100 μm, and layer thicknesses as low as 10 μm [124]. The processes are also conducted within a chamber, reducing the likelihood of atmospheric contamination by use of inert atmospheres or vacuum conditions. The contained nature of the processes also presents a drawback with limitations on the possible build envelope, and hence component size. It is also seen that in some instances there is incomplete fusion of powder particles, resulting in angular internal porosity which severely degrades mechanical performance and requires additional processing such as HIP. It can also be understood that the volume of powder required to fill the build chamber far exceeds the volume of the part(s) being produced and can present an economic barrier to development of large scale powder beds. While this excess powder may be recovered and reused, doing so introduces additional processes and costs on top of the already high price of titanium powders. Further, the recovery of excess powder places design constraints on parts with hollow profiles where some means of extracting the un-fused powder must be present. Processes of this type have been developed using either electron beam or laser heating sources, with a number of companies offering commercially available machines as listed in Table 2.7. These are particularly suited to the manufacture of small intricate components in limited production runs such as customised biomedical implants as shown in Figure 2.17.

Table 2.7 Summary of additive manufacturing technologies either in use or under development for the production of metallic titanium components. Key industrial or research organisations and process status are also given for each process.

Consumable	Heat Source	Process *Organisation*	Status
Powder Bed	Electron Beam	Electron Beam Melting (EBM) *Arcam [125]*	Commercialised
Powder Bed	Laser	Selective Laser Melting (SLM™) *ReaLizer [126] and Renishaw [127]*	Commercialised
Powder Bed	Laser	Selective Laser Sintering (SLS) *EOS [128]*	Commercialised
Powder Bed	Laser	Direct Metal Sintering (DMS) *3DSystems [124]*	Commercialised
Blown Powder	Laser	Laser Engineered Net Shaping (LENS™) Technology *Optomec [129]*	Commercialised
Blown Powder	Laser	Laser Additive Manufacturing (LAM℠) *AeroMet [130]*	Ceased operations
Blown Powder	Laser	Laser Free-Form Fabrication (LF3™) *Triton Systems Inc. [131]*	unknown
Blown Powder	Laser	Laser Metal Deposition *SAUER LASERTEC [132]*	Commercialised
Blown Powder	Electric Arc (Plasma)	Plasma Transferred Arc Solid Free Form Fabrication *MER Corp. [133]*	unknown
Wire	Electron Beam	Electron Beam Freeform Fabrication (EBF^3) *NASA Langley Research Centre [134]*	Proprietary
Wire	Electron Beam	Electron Beam Additive Manufacturing (EBAM) *Sciaky Inc. [135]*	Commercialised
Wire	Laser	LaserForge™ *H&R Technology [136]*	Commercialised
Wire	Laser	Laser-beam deposition *Katholieke Universiteit Leuven [12]*	Research
Wire	Electric Arc (GTAW/CMT)	Wire Arc Additive Layer Manufacture (WAALM) *Cranfield University [137]*	Research
Wire	Electric Arc (GTAW)	Robotised TIG Metal wire Deposition (RTMwD) *Luleå University of Technology [17]*	Research
Wire	Electric Arc (GTAW)	Shaped Metal Deposition (SMD) *Rolls Royce/University of Sheffield [14]*	Research
Wire	Electric Arc (PAW)	Plasma arc welding based additive manufacture *Montana Tech [138]*	Research

The next group of processes are those making use of the so-called ‘blown powder’ consumable. In these, a localised heating source such as a laser or electric arc is used to selectively melt a substrate material while a directed nozzle introduces metallic powder into the molten pool. This process is repeated to build-up each layer of the freeform structure in a near net shape manner. Typically this approach offers increased deposition rates, and hence productivity, with a compromise in spatial resolution compared to the powder bed methods. Deposits can be up to 12 mm in width with build-ups in excess of 3mm per layer [130]. As such, build-ups produced in this way require finishing material removal processes to give the final component profile. Like the powder bed methods, blown powder processes are most commonly performed under controlled atmospheric conditions within a processing chamber to prevent atmospheric contamination, however the build envelope is less restricted in size as the amount of excess powder required is far less. Laser Additive Manufacturing (LAM℠) was developed by AeroMet in the late 1990’s using the combination of laser melting and blown powder to manufacture parts for the aerospace industry, however, the company ceased operation in 2005 citing a lack of profitability in the process [11]. A number of companies have since manufactured commercially available machines including the new LASERTEC 65 unit from SAUER LASERTEC and DMG MORI USA [132]. This machine incorporates blown powder laser additive manufacturing abilities into a 5-axis computer numerically controlled (CNC) machining centre to provide a single machine centre for additive manufacture and finish machining metallic components from a number of alloys including titanium.

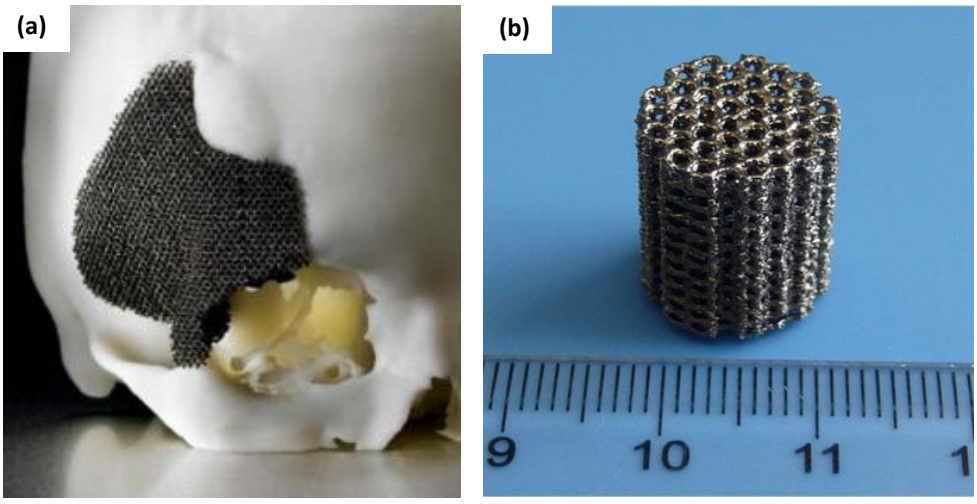

Figure 2.17 Examples of a customised biomedical implants produced by electron beam melting of titanium powder. From Hanlon [139] and Li [140].

At present one of the main drawbacks of the powder based methods for manufacture of titanium components is the high cost of powder consumables which are generally produced from wrought mill products through gas atomisation or plasma rotating electrode processes. An alternative approach is to make use of a more readily available consumable in the form of solid wire, combined with a suitable heat source to effectively give a fusion welding process with controlled addition of filler material. Deposition of successive beads on top of one another then gives the layer-wise build-up of a near net shape freeform commonly referred to as additive manufacturing. Processes have been investigated using both power beams and electric arcs as the point heat source, with a number going on to be commercialised as indicated in Table 2.7. It must be noted that the LaserForge™ process of H&R Technologies is not a fusion welding process, rather a laser is used to give metallurgical bonding between the layers of deposited flat wire without melting [136]. As with the blown powder processes, these wire fed approaches offer high productivity with reduced spatial resolution and so are best suited to manufacture of near net shapes for large structures including aerospace components similar to that in Figure 2.18. Electron beam processes must be conducted in vacuum chambers and so have inherent resistance to atmospheric contamination, while laser and electric arc processes can be protected by inert gas shielding. In addition to the size constraints associated with operating in a vacuum chamber, electron beam processes are seen to suffer from difficulties in composition control when working with titanium alloys due to vaporisation of high vapour pressure elements such as aluminium [141]. With the development of localised inert gas shielding, both the laser and electric arc-based processes may be readily installed on industrial robotic manipulators to give large scale flexible additive manufacturing capabilities without the need for specialised equipment, which would typically have high capital costs and limited flexibility. Further, the low capital costs of conventional fusion welding equipment makes the electric arc-wire based additive manufacturing methods an attractive prospect for industry.

As with all engineered materials, the microstructure, and hence mechanical and physical properties, of additively manufactured metallic structures is strongly dependent on the processing parameters used. At present, a large portion of the research activities related to additive manufacturing are dedicated to identifying and understanding these property-processing relationships for each of the various additive manufacturing approaches

[142]. Such knowledge is essential and can be used to develop processing ‘maps’, such as those suggested by Gockel and Bueth [143], which then assist in the development and validation of the processes for use in commercial applications.

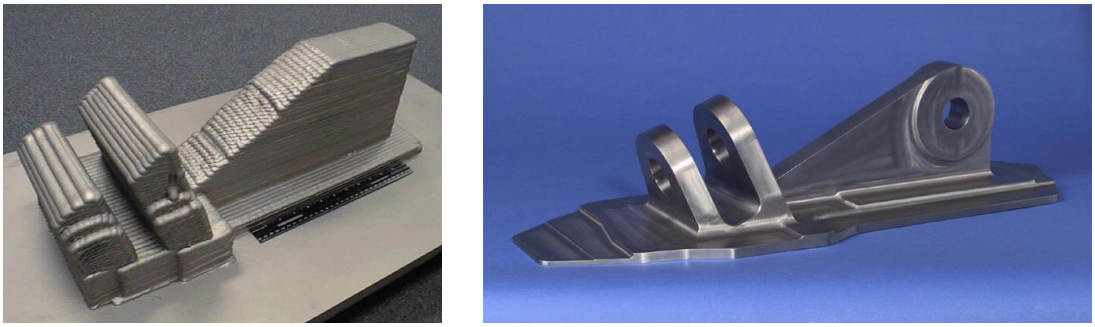

Figure 2.18 A typical aerospace component formed by electron beam wire deposition followed by finishing material removal processes. From Rosenberger [49].

From the above summary it can be seen that in general those processes using power beam heat sources are well advanced with many ‘turn-key’ systems commercially available. In contrast, the electric arc-based processes, while showing promise, tend to be less developed with research taking place in many locations worldwide. It is also worth noting that with the three different consumable delivery methods and three heat sources identified, there are two possible combinations which appear to have been left unexplored, namely electron beam with blown powder and electric arc with powder bed. The fabrication of components through conventional techniques such as joining of preformed units by fusion welding is also possible but in many cases it is considered undesirable due to the inherent variability of the processes as well as the effects of microstructural alterations on mechanical properties.

In addition to the solid-state near net shape fabrication methods of superplastic forming and diffusion bonding discussed in Section 2.3.4, the layer-wise build-up of three dimensional freeform structures can be done in the solid state by methods such as ultrasonic consolidation (UC). In this, the layers of the near net shape profile consist of thin metallic foils, approximately 150 μm thick, which are successively bonded to the substrate and one another using a ultrasonic welding process [144, 145]. The process can be readily combined with CNC milling equipment to allow profile machining during the build-up process [146], and are particularly well suited to aluminium alloys.

2.5 Arc-wire Based Additive Manufacture of Ti-6Al-4V

Titanium alloys offer a unique and desirable combination of physical and mechanical properties, with their current high costs limiting their use to select applications in the aerospace, chemical processing and biomedical sectors. It is evident that there exists a number of possible means for reducing the costs associated with the use of the these materials, with additive manufacturing methods giving a two-fold benefit through reduced raw material and machining requirements. Due to their increased flexibility through robotic and out-of-chamber operation, moderate deposition rates and low capital costs, the arc-wire based methods are considered to be ideally suited to the manufacture of structural components from titanium alloys [13, 14]. The ability to independently control heat input and deposition rate in the gas tungsten arc welding (GTAW) process presents a significant advantage over other arc-wire fusion welding processes such as gas metal arc welding (GMAW) and controlled dip transfer/cold metal transfer (CMT). The largest barrier to the adoption of such methods in the manufacture of titanium components for aerospace applications is the certification process [24]. Clearly then all research efforts into assessing the industrial viability of such a process must in some way address aspects of this qualification such as process control, mechanical properties, residual stress and atmospheric contamination.

As described in the preceding discussion, the Ti-6Al-4V alloy is used extensively, not only in aerospace applications, but all industries, and is clearly the most dominant titanium alloy at present. Ti-6Al-4V is considered the benchmark alloy for comparing all others [104] with a great deal of information available regarding its physical metallurgy, mechanical properties and response to TMP. Ti-6Al-4V shows good weldability, especially by GTAW, due to its low hardenability and the ductile nature of its α′ martensite phase. These, combined with its relatively high cost and difficulties in forming processes, make the Ti-6Al-4V alloy the ideal candidate alloy for the investigation of arc-wire based additive manufacture of structural titanium components. While β alloys such as Ti-10-2-3 are seeing increased popularity in aerospace, their low weldability and susceptibility to element segregation on solidification [54] makes them not suitable for arc-wire based additive manufacturing. Another promising β alloy for use in structural aerospace components is Ti-5553, however this alloy, while relatively

new and less established, is easily cast and forged and so there is little need for components to be formed from it by additive manufacturing methods [147].

Considering this, the current research topic was focused on investigating aspects of weldability associated with the additive manufacture of freeform structures, predominantly for the defence and aerospace sectors, from the Ti-6Al-4V titanium alloy using arc-wire deposition techniques based on the gas tungsten arc welding (GTAW) process.

CHAPTER 3 – PROCESS CHARACTERISATION

3.1 Introduction

The use of gas tungsten arc welding with automated wire feed for the additive manufacture of titanium components is a repeated process of melting, metal addition and solidification. Each of these thermal cycles is a function of the welding process parameters used and clearly influences the development of microstructure in both the fusion zone and the adjacent heat affected zones, and hence the properties of the final additively manufactured deposit. It is also widely known that these welding process parameters have a great influence over the geometry of the resulting weld beads, with these geometries in turn influencing the properties of the welded structure. The importance of these weld bead geometries may be regarded as especially significant during additive manufacturing processes, such as the one considered in this study, where each bead combines to yield a final near net shape free form with a predefined desired profile. Any significant deviation from this profile may be thought of as inefficiency in the process, requiring increased material removal and wastage or re-working, which would contribute unnecessary costs. It is clear then that a thorough understanding of the relation between process parameters and the resulting weld bead geometries and material microstructures is crucial for the optimisation of fusion welding based additive manufacturing processes.

Often welding procedures are developed by a method of trial and error where process parameters are varied until an acceptable outcome, in terms of weld bead geometry and properties, is achieved. While such methods can deliver adequate results, they are time consuming and rarely yield an optimised solution. In contrast, the development of mathematical models relating input parameters to output variables allows for process optimisation across a range of scenarios as well as facilitating process automation to further increase efficiency [148, 149]. The aim of this component of the research project was to establish a comprehensive understanding of the relationship between common process parameters and resulting weld deposit geometries and microstructures in the additive manufacture of Ti-6Al-4V using GTAW. This was done initially through experimentation with the effect of various input parameters on deposit geometry and microstructures observed and quantified. Using this data, a series of mathematical models for the subsequent build-up properties were generated through analysis of

variance (ANOVA) and multiple regression techniques. It is intended that such models will allow for the optimisation of process parameters during the additive manufacture of titanium alloys by GTAW and so assist in validating the technique as a possible low cost alternative to more conventional manufacturing methods.

3.1.1 Physical Metallurgy of Ti-6Al-4V

In order to relate microstructure evolution in Ti-6Al-4V deposited by arc-wire based additive manufacture to the process parameters used, it is first necessary to understand the physical metallurgy of the Ti-6Al-4V alloy. Due to the inclusion of both aluminium and vanadium, which act as α and β stabilising elements respectively, Ti-6Al-4V exhibits a duplex microstructure with both the α-Ti and β-Ti phases present under standard service conditions. The relative fractions of each of these phases, as well as their morphologies, are a function of both thermal processing and alloying (predominantly interstitial) contents. For the Ti-6Al-4V alloy, the β transus is observed at 995 °C ± 15 °C with the β-Ti single phase field extending up to the liquidius temperature of 1655 °C ± 15 °C. Upon cooling from the molten state, solidification is seen to initiate at 1605 °C ± 10 °C [21]. Oxygen and other interstitial species such as carbon and nitrogen are seen to have a significant effect on transformation behaviour of titanium alloys with the β transus of extra-low interstitial (ELI) Ti-6Al-4V (containing 0.13 wt% O) reported at 975 °C, some 20 °C lower than the standard grade with 0.20 wt% O. The effect of oxygen on the β transus temperature was also shown for commercially pure titanium in Table 2.6.

While the presence and morphology of β grains at ambient or operating temperature is critical in determining the final properties of the material, it is the morphology of the β-Ti at temperatures greater than service conditions that is of interest, particularly above the β transus where the α phase is no longer stable. The super-transus β morphology has a significant impact on the evolution of the α-Ti phase upon cooling from processing or forming temperatures. These β-Ti grains are generally in the order of several hundred micrometres in size and form through recrystallisation and grain growth in the solid state to relieve lattice strains from prior forming processes, or due to grain competitive growth during solidification as described in Chapter 2. Upon cooling through the β transus, the transformation to α-Ti can take place either martensitically or by heterogeneous nucleation from the high temperature β grain boundaries in a diffusion

controlled manner as shown in Figure 3.1, depending on cooling rate [150]. The crystallographic orientation relationship between the prior β-Ti and the new α-Ti is described by Burgers relationship given in Equation 3.1. Clearly the super-transus β grain boundary density, and hence grain size, will significantly influence the resulting morphology of the α-Ti phase. Another factor to be considered is the formation of a preferred crystallographic direction or 'texture' within the β-Ti microstructure due to TMP or cooling conditions during solidification which, given the Burgers relationship, would impart such texturing effects onto the α-Ti grains and potentially create anisotropy in mechanical properties such as strength and elastic modulus.

$$(110)_\beta || (0002)_\alpha$$

$$[1\bar{1}1]_\beta || [11\bar{2}0]_\alpha$$

Equation 3.1 The Burgers relationship between the BCC β-Ti and HCP α-Ti crystal structures in titanium alloys.

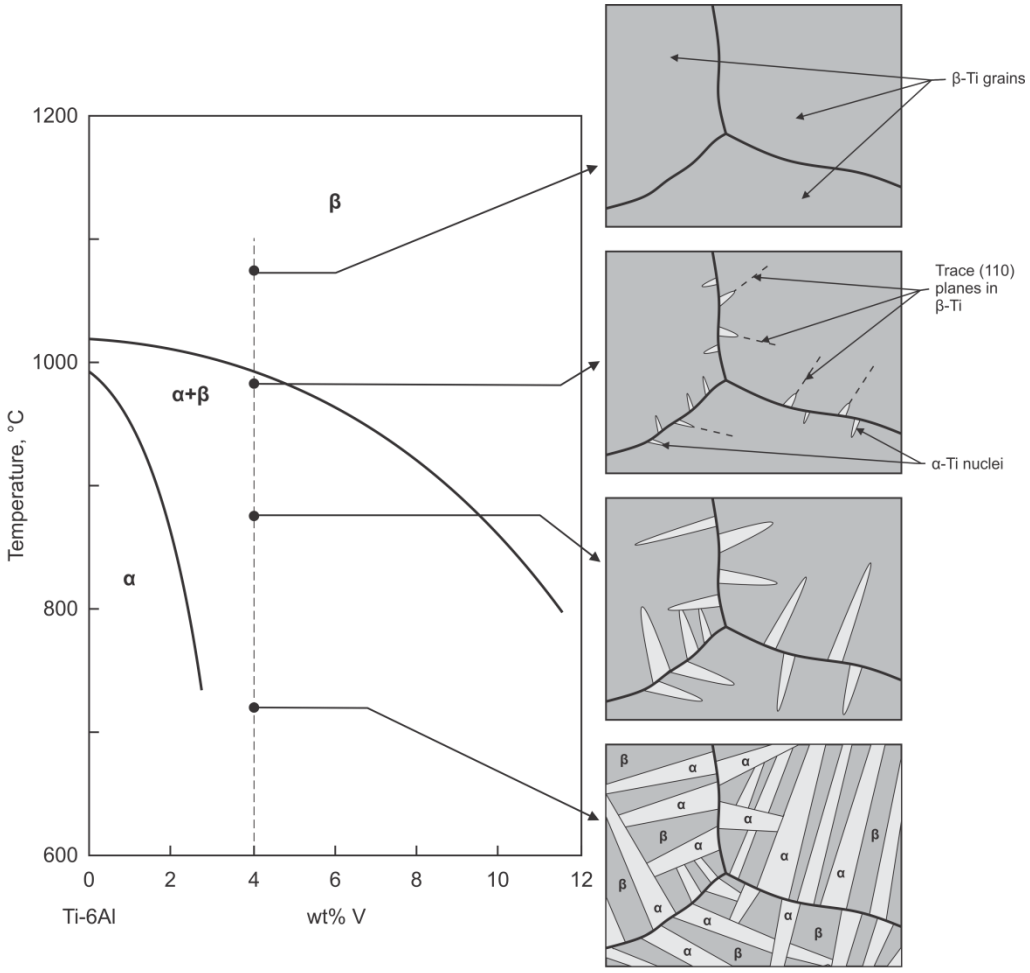

Figure 3.1 Schematic illustration of the formation of Widmanstätten laths in Ti-6Al-4V achieved by slow cooling through the β transus. Adapted from Donachie [121].

Cooling of Ti-6Al-4V to below the β transus temperature gives rise to the α-Ti phase, with the morphology of the low temperature phases dependent on the TMP history and the cooling rate through the β transus. The α-Ti morphologies resulting from heterogeneous nucleation and diffusion controlled growth may be broadly classified as fully lamellar, fully equiaxed or a mixture of both lamellar and equiaxed structures commonly referred to as 'bi-modal'.

The lamellar morphology is observed as a layered plate like arrangement of α-Ti laths surrounded by retained β-Ti and is readily obtained; however the actual morphology is dependent on both the cooling rate and prior holding temperature. The structure is also known as 'β annealed' as it is commonly developed by an annealing treatment above the β transus. The key parameter in the formation of this microstructure is the cooling rate through the β transus, with increasing cooling rates giving decreased α lath size and thickness as well as α-Ti colony size. Slow controlled cooling across the β transus gives nucleation along the high temperature β-Ti grain boundaries with subsequent growth of coarse plate like α structures. It is also possible for an alternating α+β Widmanstätten structure to develop with this cooling, or by annealing at high temperatures within the two phase region [21]. In contrast, a structure of fine needle like α-Ti termed acicular α is obtained by faster cooling such as in air, while severe cooling by water quenching followed by annealing in the two phase region is recognised as producing a fine lamellar structure [1]. These cooling rate effects are clearly illustrated in for Ti-6Al-4V in Figure 3.2. Due to the heterogeneous nucleation of Widmanstätten α-Ti laths, grain boundaries of the super-transus β-Ti are commonly evident in the final fully lamellar microstructures, with layers of α-Ti also seen along these prior grain boundaries. As with the primary α-Ti laths, the thickness of these grain boundary layers decreases with increasing cooling rates. In addition to cooling rate, prior β grain size influences the morphology of lamellar structures in Ti-6Al-4V with these β-Ti grain boundaries limiting the maximum possible α colony size. Smaller super-transus β-Ti grain size also corresponds to an increased grain boundary density and so an increased number of sites available for heterogeneous nucleation of α-Ti laths, leading to a more refined lamellar structure.

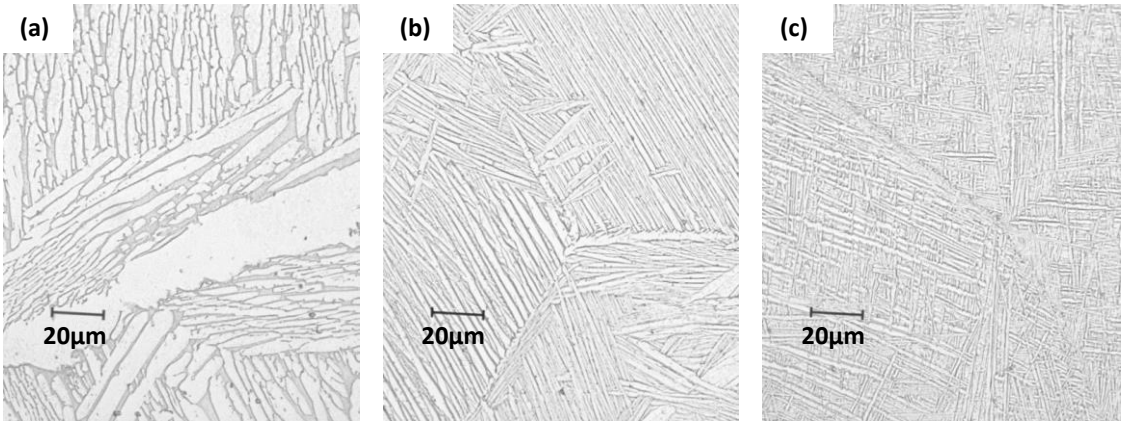

Figure 3.2 Optical micrographs showing the effect of cooling rate on α lamellae morphology in the α+β Ti-6Al-4V alloy: (a) 10 °C/min, (b) 100 °C/min and (c) 1000 °C/min. From Hoye [151].

In terms of mechanical properties, the size of the α lamellae and α-Ti colonies corresponds to the effective slip length for dislocations, whose movement is hindered by the incoherent interface which exists between the α-Ti laths and retained β-Ti. It follows then that reduced lath and colony dimensions, achieved through increased cooling rates, have the effect of increasing yield strength and ductility as shown in Figure 3.3. A dramatic increase in strength occurs at cooling rates in excess of 1000 °C/min where the martensitic transformation takes place, however this is accompanied by a loss of ductility with fracture taking place along the continuous layers of grain boundary α-Ti. Reductions in the size of α lamellae and α-Ti colonies also improve both high cycle fatigue (HCF) as shown in Figure 3.4, through improved resistance to crack nucleation, and low cycle fatigue (LCF) by decreasing micro-crack propagation rates [152]. Lamellar microstructures tend to exhibit desirable damage tolerance behaviour with good fracture toughness as well as good resistance to failure by creep and stress corrosion cracking [21].

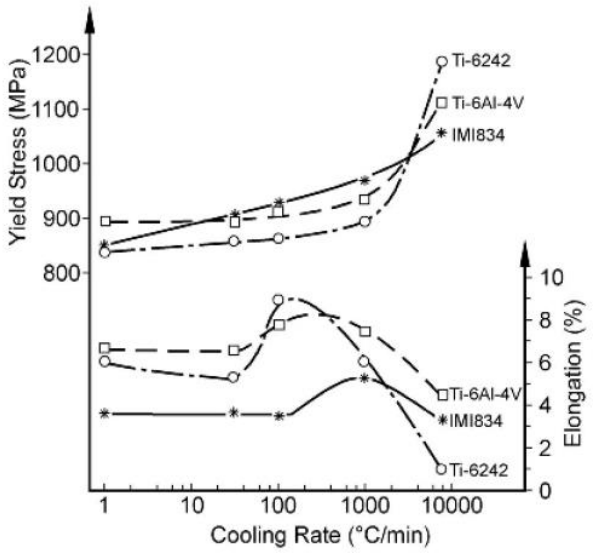

Figure 3.3 Effect of cooling rate from the β phase field on yield strength and ductility of fully lamellar structures in α+β titanium alloys including Ti-6Al-4V. From Lutjering [153].

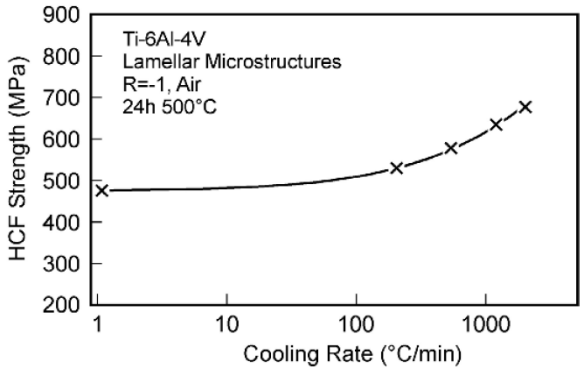

Figure 3.4 HCF strength of lamellar microstructures in Ti-6Al-4V and its dependence on cooling rate through the β transus. From Lutjering [153].

Fully equiaxed microstructures are formed in Ti-6Al-4V alloys through a four stage process of homogenisation, deformation, recrystallisation and annealing. Homogenisation is conducted at temperatures above the β transus with the cooling rate controlled to produce a lamellar microstructure that is subsequently plastically deformed at temperatures high in the dual phase region. Once cooled from the deformation process the alloy is re-heated to a moderate temperature within the dual phase region to give recrystallisation of the highly strained lamellae, yielding a microstructure dominated by equiaxed primary α-Ti grains. The final low temperature anneal is used to increase strength through precipitation of secondary α-Ti and Ti_3Al.

Similarly to the lamellar microstructures, the mechanical properties of equiaxed microstructures depend on the effective slip length for dislocations and so the α-Ti grain

size is of prime importance. As such, trends between mechanical properties and α grain size in equiaxed structures are similar to those for α lamellae and α colony size in lamellar microstructures. Equiaxed microstructures are seen to exhibit greater ductility than lamellar microstructures as well as enhanced HCF strength as shown in Figure 3.5.

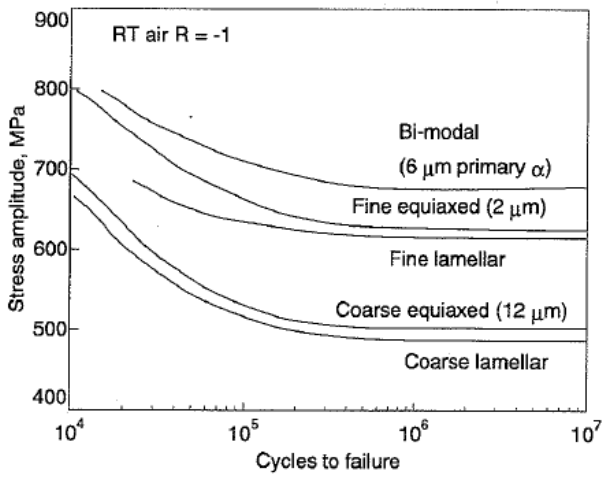

Figure 3.5 Comparison of HCF behaviour in Ti-6Al-4V alloys with different microstructures. From Boyer [21].

Another important microstructure is the so-called 'mill annealed' condition, in which a large portion of wrought titanium alloys are supplied and used. This is an equiaxed microstructure formed in a similar manner to the fully equiaxed structures previously described with the key difference being the omission of the recrystallisation process. Severe deformation is conducted in the two phase region, forming sub-grain structures within the plate like lamellar α which formed on cooling from homogenising, and ultimately breaking these up into more equiaxed grains. Annealing is then conducted to produce a fully equiaxed microstructure that is heavily dependent on the deformation imposed [21].

Bi-modal microstructures consist of both lamellar and equiaxed grain morphologies and are generally obtained through a similar four stage process to the fully equiaxed microstructures. The primary difference in the processing routes is the cooling rate from the recrystallisation stage where equiaxed grains of both α-Ti and β-Ti are formed. More rapid cooling hinders further development of primary α-Ti grains and leads to formation of lamellar structures within the recrystallised β-Ti grains, producing the mixed microstructure of equiaxed primary α-Ti grains separated by regions of alternating α+β Widmanstätten laths.

The important microstructural feature for mechanical properties in bi-modal microstructures is the size of the β-Ti grains which transform into the lamellar regions. The size of these grains is determined by the size and separation, and hence volume fraction, of primary α-Ti. These in turn are functions of the cooling rate from the homogenisation process and the recrystallisation temperature. Reducing the prior β grain size generally leads to an increase in yield strength, ductility and resistance to crack growth as well as resistance to crack nucleation as the primary α grains, where such cracks are seen to originate, are refined [153].

During rapid cooling of Ti-6Al-4V from elevated temperatures a number of martensitic structures are possible as indicated in the continuous cooling transformation (CCT) curves presented in Figure 3.6. The first of these martensitic phases is the α' which has HCP crystal structure with lattice parameters similar to the α-Ti phase [21] and is seen to adopt an acicular morphology consisting of fine plate like structures with high dislocation density and twinning. These α' martensite plates are rich in β stabilising elements and so may be annealed to produce a dual phase α+β microstructure through heterogeneous nucleation of β precipitates at dislocations [150]. Quenching from temperatures above the β transus yields a microstructure of α' martensite while quenching from between 900 °C and 1000 °C gives rise to a mixed α'+α structure. Lutjering [153] and Sieniawski *et al*. [154] state that for the formation of α' martensite in Ti-6Al-4V, the critical cooling rate is approximately 18 °C/s, while Ahmed [155] gives a significantly higher value of 410 °C/s.

The second of the martensitic structures is the α" phase which has an orthorhombic crystal structure and is seen to form in conjunction with the α phase on quenching from between 750 °C and 900 °C. Formation of this α" martensite is only possible from these lower temperatures as it is the transformation product of enriched β phase particles, which form at temperatures high in the α+β phase field after nucleation and growth of primary α particles. The α" martensite is also mechanically softer than the other phases observed in Ti-6Al-4V [21].

Each of the martensitic structures contains high residual stresses from the quenching and transformation process, which if not fully relieved may result in distortion of the part or degradation of mechanical properties. Due to this, martensitic microstructures are rarely used in structural components and are instead used as starting microstructures

for further aging processes [156] to produce the lamellar or fine equiaxed and bi-modal morphologies described previously. In the case of fusion welding of Ti-6Al-4V, the cooling rates required to produce these martensitic structures tend only to occur on initial cooling or in power beam processes [104].

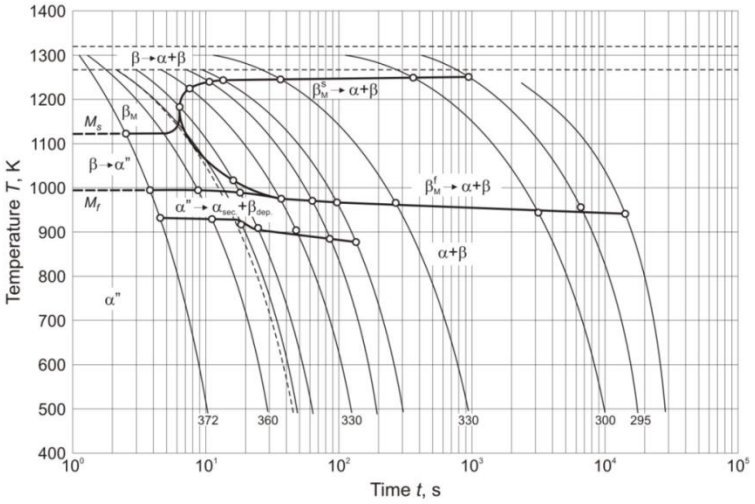

Figure 3.6 CCT diagram for Ti-6Al-4V alloy. From Sieniawski *et al*. [154].

Two other phases possible in the Ti-6Al-4V alloy are the omega (ω) phase and the intermetallic compound Ti_3Al (α_2). The athermal ω phase is metastable and precipitates during low temperature aging however its formation is supressed by oxygen and so tends only to be of concern in the extra-low interstitial (ELI) grades. In contrast, the presence of oxygen promotes the precipitation of the Ti_3Al intermetallic within the α-Ti phase as oxygen acts to reduce the solubility of aluminium in Ti-Al-x alloys. Ti_3Al, generally formed during artificial aging at temperatures around 500 °C, is understood to have an ordered hexagonal structure that is coherent with the α-Ti matrix and so increases mechanical strength by impeding dislocation movement [150].

3.1.2 Ti-6Al-4V Weld Microstructure

The microstructure of fusion welds in a section of Ti-6Al-4V, initially in the mill annealed condition, can be broadly divided into four regions based on the thermal cycling undergone as shown in Figure 3.7. At locations well removed from the weld zone, the parent material may be expected to see some increase in temperature during welding but this is insufficient to cause any alteration to the initial microstructure. Closer to the fusion line temperatures rise high into the dual phase region giving an increased volume fraction of the β phase which is transformed on cooling into fine lamellar regions that separate the retained primary α-Ti [21] as would be achieved by a

standard α+β (duplex) annealing process. Closer still to the fusion line temperatures readily exceed the β-transus. With no α-Ti present to restrict their growth, β-Ti grains grow rapidly and significantly, up to many hundreds of micrometres in diameter depending on the peak temperature and cooling rate, before transforming to a mixture of Widmanstätten α-Ti and retained β-Ti on cooling. Finally, the fusion zone is defined by the region where the parent material is heated beyond the effective liquidus temperature to produce a molten pool. On cooling, grains of β-Ti nucleate heterogeneously at the solid-liquid interface and grow epitaxially into the solidifying molten pool as described in Chapter 2. Further cooling through the β-transus brings about heterogenous nucleation of α-Ti laths from β grain boundaries, yielding a mixture of Widmanstätten α-Ti and retained β-Ti as in the super-transus HAZ. It follows then that the microstructure of the FZ and super-transus HAZ are comparable to that produced during a standard β annealing process.

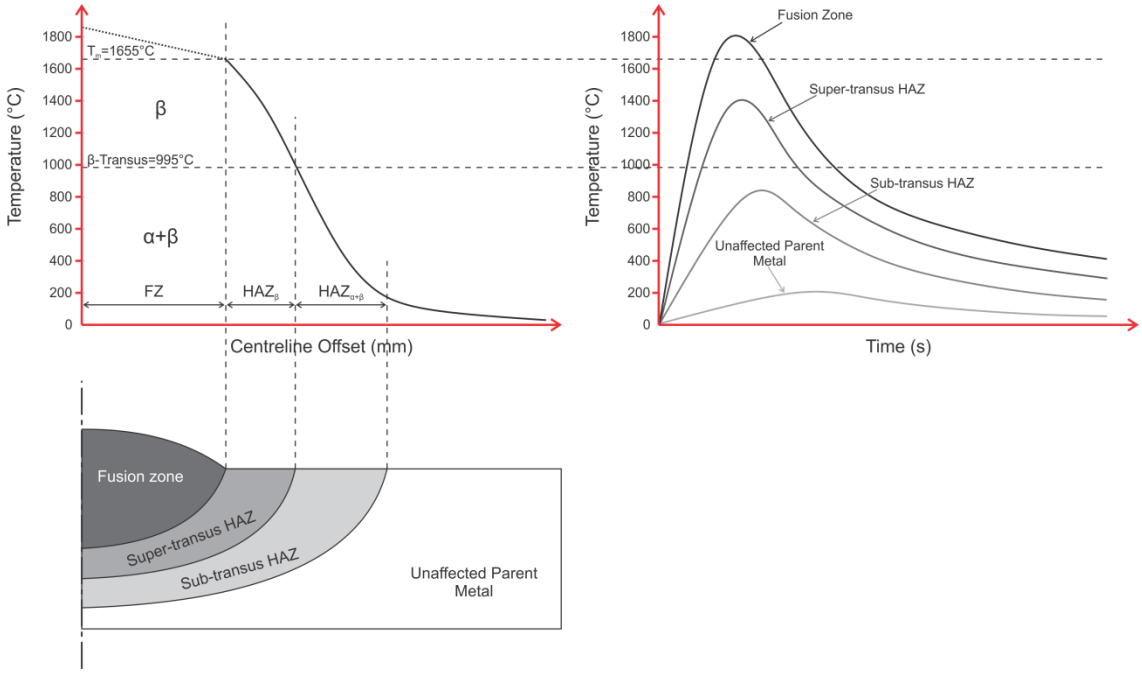

Figure 3.7 Schematic illustration of the thermal profile and thermal cycle associated with the fusion welding of Ti-6Al-4V.

The additive manufacture of components from Ti-6Al-4V using GTAW involves repeated fusion welding with deposited material being subjected to numerous thermal cycles during the build-up process analogous to repeated β and α+β annealing. The microstructure of the deposited freeform would be expected to consist of Widmanstätten α-Ti laths and retained β-Ti bounded by large prior β-Ti grain boundaries and so would

be classified as lamellar. The lack of mechanical deformation during the additive manufacturing process means that equiaxed structures are unlikely while duplex structures may only exist in the sub-transus HAZ of the parent metal. For arc-wire additive manufacturing, the low thermal conductivity of Ti-6Al-4V and repeated thermal cycling would be expected to heat the structure sufficiently to limit the effective cooling rates and so supress the formation of martensites. Further, if martensites were to form with rapid cooling during the initial weld passes, where there is insufficient thermal build-up in the weld deposit to limit cooling rates, these would be tempered in the HAZ of subsequent weld passes to produce the lamellar structure typical of welded deposits.

Considering then the relationship between microstructure and mechanical properties in in Ti-6Al-4V components produced by arc-wire based additive manufacture, the main features of interest in the lamellar microstructure expected are considered to be:

a) Volume fraction of each of the α-Ti and β-Ti phases
b) Prior β-Ti grain size
c) α-Ti colony size, and
d) α-Ti lath width

While it is clearly understood that these microstructural features are influenced by welding process parameters such as heat input and cooling rate, no direct model relating the two is evident for arc-wired based additive manufacture of Ti-6Al-4V. Numerous studies have been conducted to characterise the mechanical properties of fusion welded titanium alloys, including correlations to microstructure [118, 157-160], however these are predominantly related to joining processes rather than repeated deposition as in additive manufacture. For the particular case of arc-wire based additive manufacturing of titanium, Mitzner [120] and Wang *et al*. [114] have investigated the use of pulsed current for grain refinement with consideration of microstructure and mechanical properties. These studies are relatively limited in scope with only a small number of parameter sets used and no model relating processing parameters to microstructural features explicitly given. The work of Charles [17] related to the development of finite element based models for the prediction of microstructural evolution in the additive manufacture of Ti-6Al-4V by GTAW with controlled wire addition. This modelling uses thermal profiles of the fusion welding process in conjunction with time-

temperature transformation (TTT) curves and additional data from previous studies for laser based additive manufacturing [161-163], but again the processing window investigated is narrow and no direct mathematical relation was offered. It is apparent that the development of empirical relations between process parameters and microstructural features presents a number of advantages in the production of parts from titanium alloys [164] and particularly for the arc-wire based additive manufacture of Ti-6Al-4V.

3.1.3 Weld Bead Geometry

As previously identified, the geometry of weld beads produced by GTAW, as with all fusion welding processes, is essentially a function of the various process parameters such as arc current, arc voltage, travel speed and deposition rate. Much literature exists describing models for various aspects of the GTAW process including weld pool and weld bead geometries [165-170], however these studies are primarily concerned with conventional joint configurations such as butt and fillet welds and are not specific to titanium alloys. As such, these models may not be well suited for predicting the geometries of multi-layer weld deposits used for additive manufacture of components from Ti-6Al-4V. For the specific case of additive manufacture with titanium alloys, Martina *et al.* [171] show the development of empirical models relating deposit geometry to processing parameters for the plasma arc welding (PAW) based additive manufacture process, while Beuth and Klingbeil [172] have developed models to predict weld pool geometry, thermal gradients and residual stresses in the laser based processes. Further, the work of Sequeira Almeida and Williams [15] considers the development of process models for modified GTAW and gas metal arc welding (GMAW) processes. While this study covered a number of welding processes and investigated the effect of process variables on the resulting titanium weld bead, there was no focused investigation of the fundamental GTAW process. It is for this reason that an exercise of characterisation of additively manufactured deposits of Ti-6Al-4V, produced by GTAW with controlled wire addition, was undertaken as part of the current research project.

3.2 Methods and Methodology

Samples of commercially sourced Ti-6Al-4V plate with dimensions 100 mm x 16 mm x 9.65 mm were used to form the substrate onto which weld beads were deposited using Ti-6Al-4V wire with a diameter of 1.0 mm. The nominal chemical composition of these materials (in wt%) is provided in Table 3.1.

Table 3.1 Chemical composition of Ti-6Al-4V alloy.

Alloy	Composition (wt%)							
	Ti	C	Fe	H	N	O	Al	V
Ti-6Al-4V	99.2	0.1	0.3	0.015	0.03	0.25	6.1	4.0

Welding was conducted using a water cooled Conley & Kleppen (CK) machine mount torch coupled to a Kemppi MasterTIG MLS 2000 inverter power supply with independent wire feed provided through a CK WF3 dedicated wire feed unit. Inert gas shielding of the weld zone was achieved with welding grade pure argon using pre and post flow options. Additionally, a custom fabricated trailing shield was used to ensure a sufficiently large shielding envelope was generated to the rear of the fusion zone to prevent post weld atmospheric contamination of the successive weld beads. Shielding gas flow rates and other common process parameters are detailed in Table 3.2.

Table 3.2 Summary of GTA welding parameters.

Polarity	DCEN
Electrode	2% Ceriated, 2.4 mm Ø
Shielding gas	Welding Grade Argon
Flow rate – torch nozzle	8 L/min
Flow rate – trailing shield front	10 L/min
Flow rate – trailing shield rear	7 L/min
Pre-flow duration	3 seconds
Up slope duration	2 seconds
Down slope duration	1 second
Post flow duration	30 seconds

For the present study, five common input parameters of the GTA welding process, namely arc length (L), arc current (I), travel speed (TS), wire feed speed ratio (WFSR) and interpass temperature (IT), were selected to be varied in order to characterise the physical geometry and microstructure of deposited weld beads. Wire feed speed ratio was defined as the ratio of the wire feed speed to the welding travel speed. This was

used in preference to the wire feed speed alone in order to eliminate impractical combinations of the two which would inevitably produce unstable deposition conditions. Each parameter was examined at four different levels, selected based on previous experimental procedures, in order to cover a broad operating envelope. This approach gave three degrees of freedom (DOF) per parameter; totalling fifteen DOF's for the five input parameters. The levels for each parameter are given in Table 3.3. Using the design of experiment (DOE) methods of Taguchi, a total of sixteen experiments were conducted with the L'16 orthogonal array used to determine the combination of input parameters for each experiment. Actual parameter sets used for each experiment are shown in Appendix A.

Table 3.3 Definition of input parameters and levels used in experiments to characterise the GTAW additive manufacture process.

Parameter (units)	Arc Length (mm)	Arc Current (amperes)	Wire Feed (ratio to TS)	Travel Speed (mm/min)	Interpass Temp (°C)
Level 1	3.0	100	5	100	40
Level 2	3.5	120	7	150	90
Level 3	4.0	140	9	200	150
Level 4	5.0	80	11	250	200

Samples were held 'on edge' in a steel clamping arrangement to simulate the beginning of a wall-like build-up, with the entire fixture attached to a lathe bed modified to serve as a linear actuator, above which the torch and wire feed were held stationary. Experiments were performed with ten successive passes conducted for each parameter set to yield a small vertical wall. This geometry was selected to mimic the type of build-up that would be required to manufacture thin-walled, pocketed sections commonly found in structural aerospace applications. Arc current and voltage (V) were monitored for each welding pass using a Triton Electronics AMV4000 weld monitor, allowing the determination of arc energies (AE) and heat inputs (HI) using Equations 3.2 and 3.3. Temperature profiles for each pass were recorded through NI LabVIEW software using K-type thermocouples attached to each end of the sample.

$$Arc\ Energy\ \left(\frac{J}{mm}\right) = \frac{Current\ (A) \times Voltage(V) \times 60}{Travel\ Speed\ (mm/min)}$$

Equation 3.2 Calculation of arc energy from arc current, arc voltage and travel speed with units for each term shown in parentheses.

$$Heat\ Input\ \left(\frac{J}{mm}\right) = Arc\ Energy\ \left(\frac{J}{mm}\right) \times 0.6$$

Equation 3.3 Calculation of heat input from arc energy using an assumed efficiency factor of 0.6.

Factors of interest in terms of weld bead geometry were the build-up height per pass (H) and average wall width (W) as well as the apparent surface roughness of the build-up which was characterised in terms of machining layer thickness (MLT). This was defined as the maximum thickness of material required to be removed (by a machining process or similar) to bring the surface of the deposit back to a solid, continuous planar vertical surface. This was used in preference to other measures of surface profile such as Ra or standard deviations since it relates directly to the amount of tool engagement required in finishing processes and also represents the potential extent of material wastage. Height per pass was measured at the completion of each pass using a Micro-Epsilon scanCONTROL 2710-50 laser profile scanner held stationary adjacent to the welding torch. Following welding, each sample was sectioned in two places, removing the start and end portions to leave the central steady state region approximately 40 mm in length. The sides of each of these steady state sections were laser profiled, with measurements used to determine wall width and machining layer thickness. These geometry factors, illustrated in Figure 3.8, were used as output variables in the modelling process. Deposition rates (DR) were also determined for each experiment with knowledge of both the wire feed speed and actual mass deposited in this steady state section.

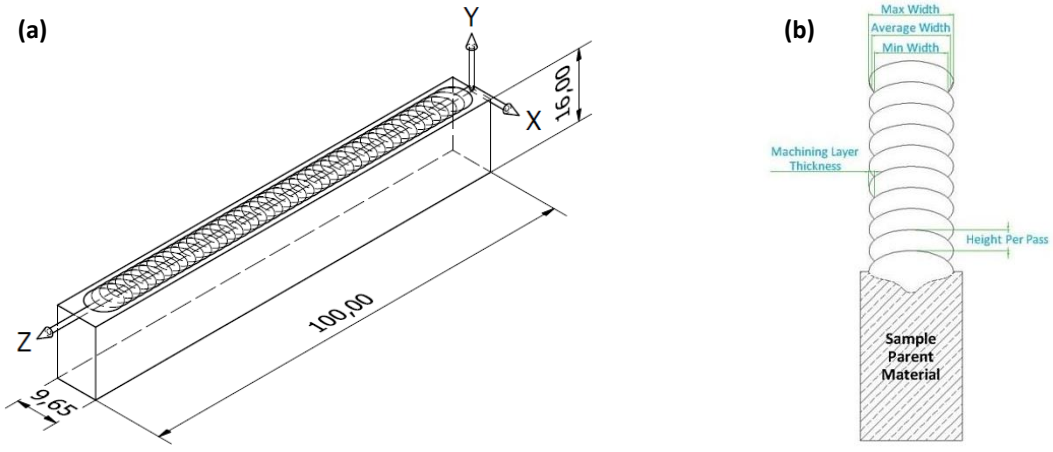

Figure 3.8 Sample geometry with (a) coordinate system and (b) geometry factors defined.

Further analysis of microstructure and mechanical hardness for each sample was performed by first removing a thin slice from the steady state region which was then hot compression mounted in phenolic powder. Mounted samples were plane ground using

silicon carbide (SiC) and chemically-mechanically polished using modified a colloidal silica solution (1 part H_2O_2, 2 parts NH_3 and 25 parts 0.25 μm OP-S) as per Struers application notes for titanium [27]. The microstructure of samples was examined in this un-etched condition using a JEOL 7001F scanning electron microscope. Samples were etched using Kroll's reagent (2 vol% HF, 6 vol% HNO_3 with balance H_2O) for optical microscopy using a Leica DMRM compound microscope and macro imaging with a Leica M205A stereo microscope.

In addition to the four key microstructural features previously identified, the α-Ti lath length, and hence lath aspect ratio, was measured as were the mechanical hardness of the deposited material and the extent of the HAZ into the parent material. Representative micrographs and macro images were used in conjunction with manual and automated image analysis methods to characterise the microstructural features of interest. Firstly the volume fraction of α-Ti was determined from representative back-scattered electron images from the steady state region of the build-up using the ImageJ software as shown in Figure 3.9. A bandpass fast Fourier transform (FFT) filter was applied to the image to enhance the contrast between the α-Ti laths and the β-Ti which lies at their boundaries. The 'find edges' sub-routine was then used to identify the β-Ti before the image was converted to binary using a threshold, allowing the determination of the relative proportions of the α and β phases. This process was repeated across ten micrographs for each sample and the mean obtained. This method was used to determine volume fraction of each phase in preference to point counting due to the fine grain boundary nature of the β-Ti phase and the ease with which the process could be automated.

The mean width and length of the α-Ti laths were determined for each sample using the back-scattered micrographs and ImageJ with ellipses fitted to ten laths per micrograph as shown in Figure 3.10. The major and minor axes of each ellipse were measured and taken to represent the length and width of the lath respectively. This process was repeated across ten micrographs for each sample and the mean obtained. It must be noted that any lath which intersected the edge of the micrograph was excluded from these measurements as their true length could not be accurately determined.

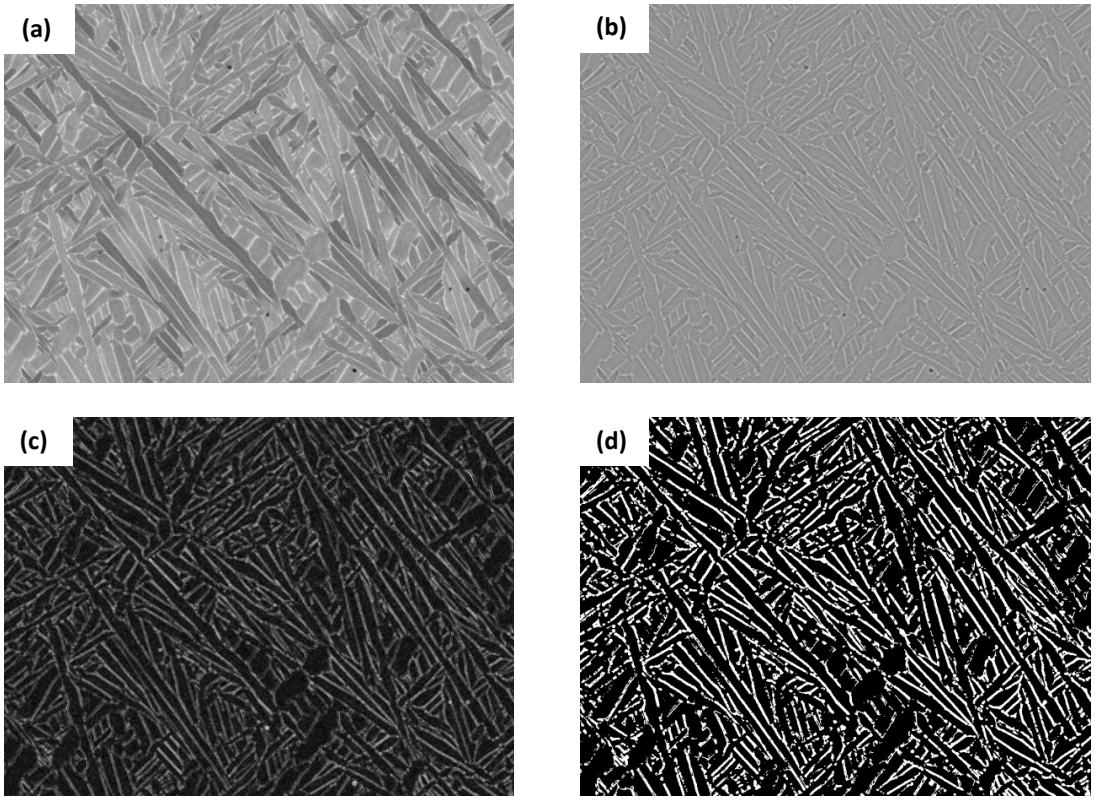

Figure 3.9 Procedure for determining volume faction α-Ti: (a) Original back-scattered image, (b) after application of FFT bandpass filter, (c) after running the 'find edges' sub-routine and (d) final binary image used to determine volume fraction.

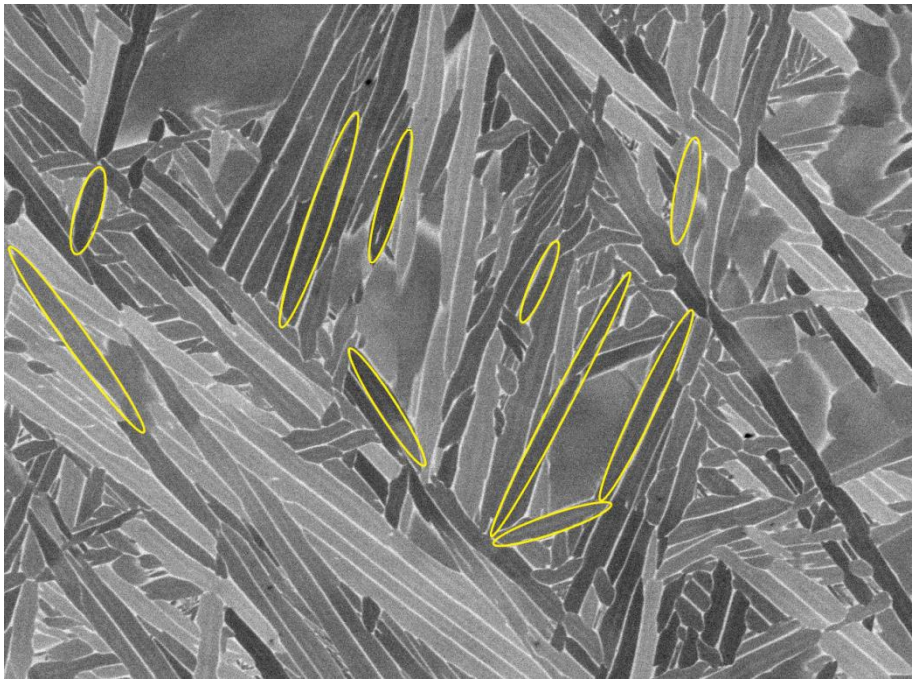

Figure 3.10 Measurement of α-Ti lath width and length using ellipses.

Note: Scale bars were removed from images to prevent errors during automated area-based analyses. Images were taken at 3000x magnification and scale bars are as for Figure 3.11.

Alpha colony size was determined using the mean linear intercept (MLI) method where the size of a microstructural feature may be related to the mean linear intercept of the feature with randomly placed straight line sections projected onto the micrograph. As the projection of a group of random lines is difficult, it is assumed that the microstructure is random and so a regular arrangement of lines may be used [173]. In the present study circles of known circumference were used in preference to straight lines since the intersection of a line with the edge of the micrograph creates ambiguity by effectively being counted as a boundary intercept where it may not be. Circles also automatically compensate for non-equiaxed profiles, eliminating the need to measure intercepts in two orientations [174]. By counting the number of colony boundaries which intersect each circle as shown in Figure 3.11, the MLI of the α-Ti colonies can be quantified. Again this process was repeated across ten micrographs for each sample and the mean obtained. A similar approach was applied to determine the size of the prior β-Ti grains with circles of known circumference projected onto the fusion zone of macro images obtained from stereo microscopy as shown in Figure 3.12a. The depth of the HAZ into the parent material was taken as a single measurement on each sample using a single macro image as shown in Figure 3.12b.

Finally, the mean Vickers microhardness of each sample was determined using automated testing with a Struers Durascan 70 equipped with Ecos Workflow software. Using a load of 0.5 kg and a dwell time of ten seconds, indents were placed in a grid arrangement at intervals of 1.0 mm perpendicular to the build direction and 0.5 mm in the build direction. This array measured 2.0 mm in width and was centred about the centreline of the build-up. As measurements were taken only in the deposited material, the height of the array varied between samples with the total number of indents ranging from 33 to 69. These hardness values, along with the seven microstructural features were used as further outputs of the welding process that were mathematically related to the input process parameters.

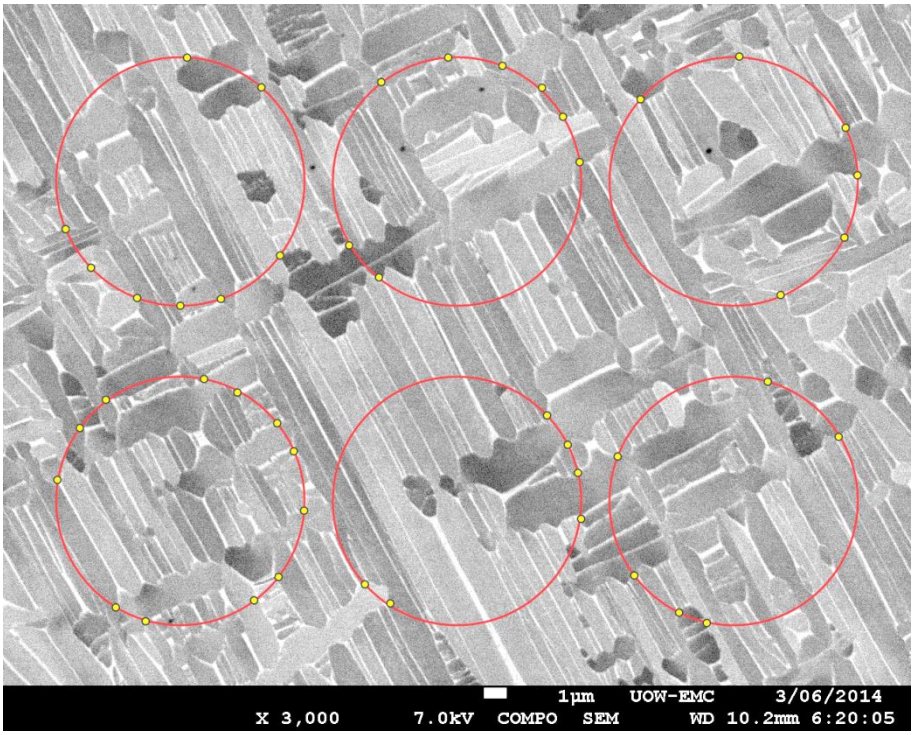

Figure 3.11 Measurement of α-Ti colonies using overlayed circles to determine mean linear intercepts.

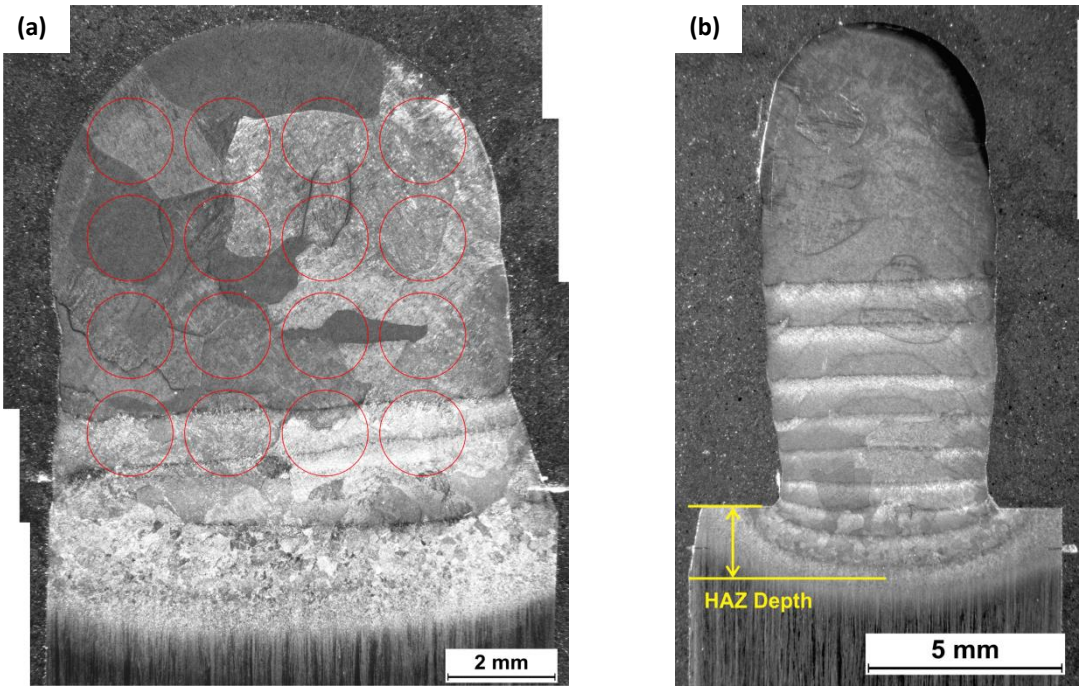

Figure 3.12 Macro images showing (a) measurement of prior β-Ti grain size by the MLI method using overlayed circles, and (b) measurement of HAZ depth.

For each of the microstructural features characterised by more than one measurement the mean value, $\bar{X}$, and standard deviation, S, of the measurements were determined. In order to determine a confidence interval for each feature the method of Student's t distribution was employed since the true mean, μ, and true standard deviation, σ, of each

sample set are unknown, making use of the normal distribution inappropriate. This method shows that the $100(1-\alpha)$ % confidence interval for the true mean is given by the relation shown in Equation 3.4 where *n* is the sample size. In each case the 95 % confidence interval (*95% CI*) was calculated, giving $\alpha = 0.05$.

$$\bar{X} - t_{n-1,\frac{\alpha}{2}}\frac{S}{\sqrt{n}} < \mu < \bar{X} + t_{n-1,\frac{\alpha}{2}}\frac{S}{\sqrt{n}}$$

Equation 3.4 Confidence interval for true mean value using the Student's t distribution.

The relative error, *%RA*, for each feature was calculated from this *95% CI* using the method outlined in ASTM E112 for statistical analysis related to measurements of grain size. This is shown in Equation 3.5.

$$\%RA = \frac{95\%\ CI}{\bar{X}} \times 100\%$$

Equation 3.5 Calculation of relative error from mean value and confidence intervals.

It is stated in ASTM E112 that measurements with relative error of 10 % or less are considered to be accurate enough for most applications. Considering the values for relative error presented in Table 3.4 it is seen that the only set of measurements which can be thought of as inaccurate are those of the prior β-Ti grain size where the relative error exceeds 30 %. This large error is thought to come from poor selection of circle size which was too close to the mean grain size and so produced great variation in results.

Table 3.4 Summary of relative errors for characterisation of microstructure features.

Feature	Average Relative Error (%)
Microhardness (HV0.5)	0.97
Prior β-Ti Grain Size (L_{beta})	33.12
α-Ti Volume Fraction (V_{alpha})	1.72
α-Ti Colony Size (L_{colony})	8.88
α-Ti Lath Length (L_{alpha})	10.52
α-Ti Lath Width (W_{alpha})	6.38
α-Ti Lath Aspect Ratio (AR)	10.46

3.3 Results and Discussion

3.3.1 Qualitative Observations

Considering firstly general observations of additively manufactured build-up structures, it was noted that for a number of parameter sets the bead featured a bulge in terms of both height and width at the start which was followed by a narrowing before steady state geometry was achieved. This can be seen in Figure 3.13. The initial bulge is attributed to slight discrepancies in the timing for the start of wire feed and travel with respect to arc initiation and formation of the molten pool. Due to the nature of control used, both wire feed and travel speed do not instantaneously achieve their pre-set values but rather 'ramp up' to this value over a short period of time. As the ramp time is shorter for the wire feed than the travel speed, wire is added to the molten pool before a constant travel speed is achieved, depositing a greater volume of material at the start. The narrowing of the weld bead adjacent to the start region may also be explained in terms of the control of the linear actuator which represents an under-damped system. In this case there is an 'overshoot' in the velocity of the linear actuator, with this localised region of higher travel speed corresponding to reduced wall thickness. It is clear then that such features could be reduced or eliminated in future developments by refinement of the various control systems.

Figure 3.13 Top view of all samples (numbered R to L from 1 to 16) with welding direction indicated to highlight bulge and narrowing features observed near the start point for certain parameter sets.

The general microstructure of the additively manufactured samples shows that there are three distinct regions which can be identified, as shown in Figure 3.14. The parent material shows a typical rolled microstructure with elongated grains of primary α-Ti surrounded by retained β-Ti. In the HAZ this is transformed to give irregular Widmanstätten laths of α-Ti separated by retained β-Ti and large angular grains of primary α-Ti. Also of note is the presence of distinct grain boundary (GB) α-Ti which is able to form with the relatively low cooling rates understood to exist in the HAZ. This GB α-Ti is not as prevalent in the deposited material where higher initial cooling rates give rise to the formation of the typical β-annealed structure consisting of more slender, highly oriented α-Ti laths surrounded by retained β-Ti. Of note is the apparent equiaxed morphology of the prior β-Ti grains in the deposited material, which differs to the columnar structure reported in other studies of the GTAW based additive manufacturing process [14, 16, 17]. As described in Section 2.3.5, the transition from equiaxed to columnar morphologies is related to thermal gradients and solidification rates during the welding process. It is thought that lack of columnar prior β-Ti grains in the present samples may be related to the small sample volume and limited number of weld passes performed being insufficient to produce the thermal conditions which lead to columnar grain formation.

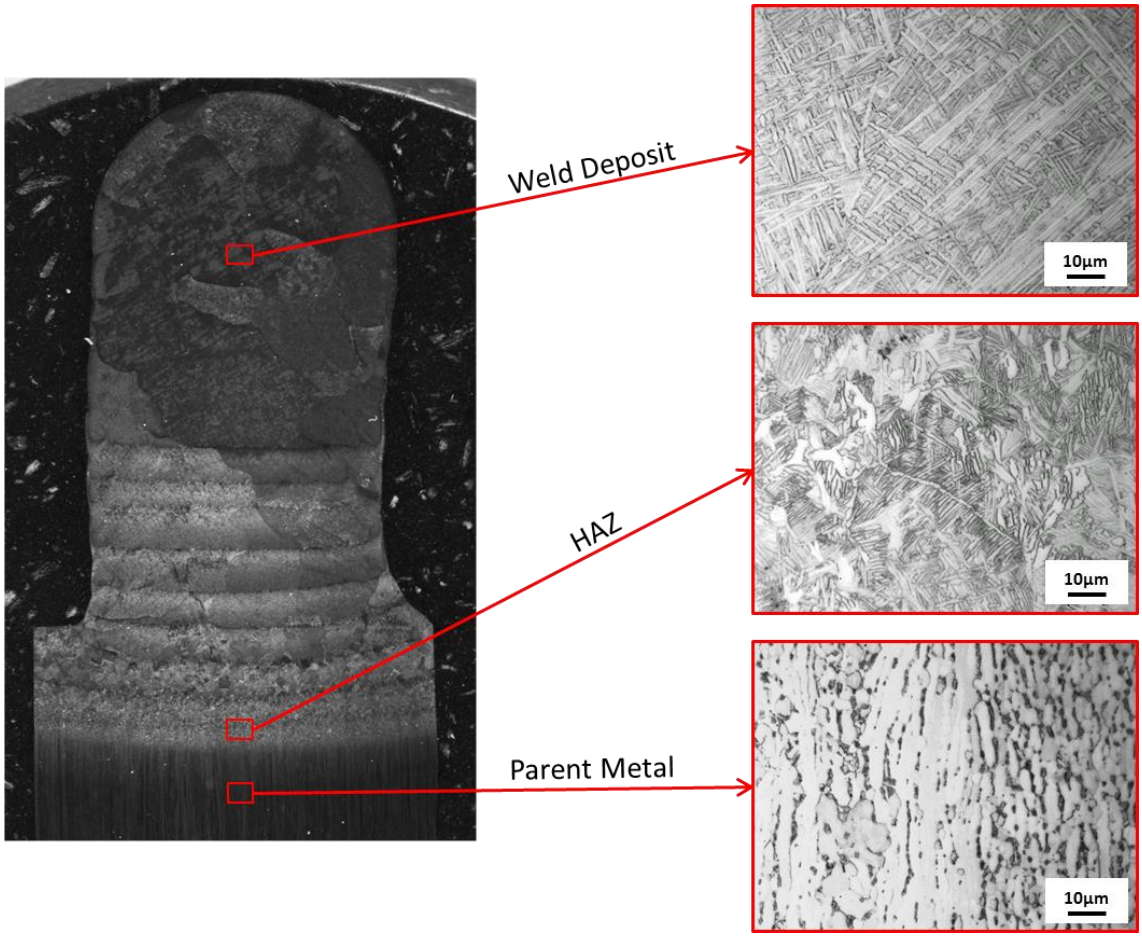

Figure 3.14 Typical microstructures observed in the deposited material, HAZ and parent metal of a sample of additively manufactured Ti-6Al-4V.

In essence the primary aim of any manufacturing process is the production of value added components of suitable quality at minimal cost. Applying this logic to the process of GTA-wire based additive manufacturing it becomes apparent that the process efficiency is proportional to the wire deposition rate and material utilisation, and inversely proportional to arc energy. It is clear then that a key parameter in characterising the efficiency of the process is some measure of the energy consumed per unit mass of deposited material. In the present study this has been termed 'specific deposition energy' representing the arc energy per unit mass of deposited material. Equation 3.6 shows the calculation of specific deposition energy based on initial input parameters while Equation 3.7 shows the calculation based on measured values of arc energy and deposition rate. In either case the same value should be obtained. The calculation of specific deposition energy is based on arc energy rather than heat input as it is a more direct measure of energy consumption in the welding process.

$$Specific\ Deposition\ Energy\ \left(\frac{kJ}{g}\right) = \frac{Current\ (A) \times Voltage\ (V) \times 60 \times 1000}{Wire\ Speed\ (mm/min) \times Wire\ Area\ (mm^2) \times Density\ (kg/m^3)}$$

Equation 3.6 Calculation of specific deposition energy from known variables with units for each term shown in parentheses.

$$Specific\ Deposition\ Energy\ \left(\frac{kJ}{g}\right) = \frac{Arc\ Energy\ \left(\frac{J}{mm}\right) \times Travel\ Speed\ \left(\frac{mm}{min}\right) \times 60}{1 \times 10^6 \times Deposition\ Rate\ (kg/\mathrm{hr})}$$

Equation 3.7 Calculation of specific deposition energy from measured process parameters with units for each term shown in parentheses.

General observations of wall profile and microstructure suggests that there exists an optimum processing window in terms of this specific deposition energy to produce defect free build-up structures of uniform profile. Samples prepared using high deposition rate and low arc energy, corresponding to low specific deposition energy, tended to exhibit poor surface quality and irregular profile as well as internal defects such as porosity and lack of fusion. Conversely, samples prepared with low deposition rate and high arc energy produced excessively large weld beads with slow build rates representing inefficiencies in terms of both material waste and energy consumption. Initial consideration suggests operation between 10 kJ/g and 20 kJ/g produces acceptable additively manufactured deposits. While such observations are purely qualitative and require further analysis to be verified and characterised, they are in agreement with the work of Kobryn *et al*. [130, 175] which relates to specific energy input during laser additive manufacturing (LAM) of titanium alloys.

3.3.2 Analysis of Variance

Before mathematical models were developed to relate input process parameters to each of the various geometric and microstructural output variables characterised, analysis of variance (ANOVA) was conducted using MATLAB to assess the relative influence or significance of each of the input parameters considered. This relative significance was determined from the F-statistics associated with each input parameter expressed as a fraction to clearly illustrate which parameters were dominant. As such, the sum of all the values of relative significance for a single output variable is one. The larger the value of relative significance for any given input process parameter, the greater the influence that parameter has on the particular output variable *relative* to the other input

process parameters. These results are summarised in Table 3.5 with arc voltage, wall thickness-to-height ratio and standard deviation of side wall surface profiles included.

From these relative significance values it is clear that the arc voltage is primarily a function of arc current and to a lesser extent arc length. While this relationship is well known and understood it serves as an initial check to ensure that the experimental approach and analysis methods used were sound. Further, an understanding of the relationship between arc voltage and arc length during the GTAW additive manufacturing process may be implemented into a feedback control system for process automation where monitoring of arc voltage can be used to adjust and maintain the arc length 'on the fly'.

Table 3.5 Relative significance of process input parameters on characterised outputs.

			Input Parameters				
			Arc Length L	Arc Current I	Wire Feed Speed Ratio WFSR	Travel Speed TS	Interpass Temperature IT
Output Variables	Arc Voltage	V	0.282	0.629	0.061	0.018	0.010
	Build-Up Per Pass	H	0.050	0.213	0.533	0.191	0.013
	Wall Thickness	W	0.021	0.448	0.010	0.473	0.048
	Thickness-to-Height Ratio	W/H	0.043	0.294	0.270	0.345	0.048
	Machining Layer Thickness	MLT	0.143	0.120	0.230	0.263	0.244
	Surface Standard Deviation	SD	0.179	0.101	0.287	0.121	0.312
	Hardness	HV	0.502	0.068	0.286	0.037	0.108
	Prior Beta Grain Size	L_{beta}	0.140	0.110	0.098	0.553	0.098
	HAZ Depth	D_{HAZ}	0.022	0.337	0.060	0.559	0.022
	Alpha Volume Fraction	V_{alpha}	0.571	0.078	0.032	0.272	0.048
	Alpha Lath Width	W_{alpha}	0.121	0.378	0.064	0.259	0.178
	Alpha Lath Length	L_{alpha}	0.125	0.489	0.157	0.162	0.067
	Alpha Lath Aspect Ratio	AR	0.327	0.127	0.290	0.080	0.176
	Alpha Colony Size	L_{colony}	0.341	0.175	0.082	0.100	0.302

Considering then the average wall thickness it can be seen from the high relative significance for arc current and travel speed that these two input parameters appear to have the greatest influence over the thickness of the weld deposit. This may be readily explained as both arc current and travel speed, when combined with arc voltage, relate directly to arc energy and so heat input. As heat input is a measure of the amount of thermal energy delivered to the weldment, it can be clearly understood that for a given

heat input, a molten pool of a given size will be created (assuming other factors such as the thermal properties of the weldment are consistent, as in the present study). The width of the molten pool then acts to limit the width of the deposited bead, and so the thickness of the wall type build-up that forms the basis of this additive manufacturing technique. Figure 3.15 illustrates the relationship between arc energy and wall thickness for the parameter sets examined. This finding is consistent with the models for weld bead width during conventional GTA butt welds developed by Esme *et al*. [167] and Tarng and Yang [169].

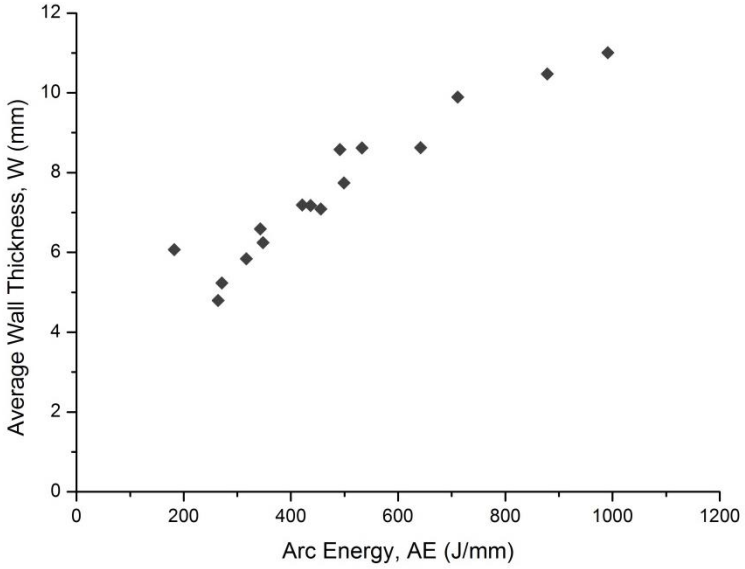

Figure 3.15 Relationship between calculated arc energy and measured values of average wall thickness. While error bars for the 95 % confidence interval are plotted, their values are so small they cannot be resolved from the data markers.

In contrast, the ANOVA results for build-up height per pass shows a strong dependence on wire feed speed, with arc current and travel speed having a lesser influence. This observation is self-evident as wire feed speed is directly related to the material deposition rate during the welding process, as illustrated by Figure 3.16. Deviations of the measured deposition rates from those predicted using pre-set wire feed speeds and material density may be due to irregularities in wire cross section, density values used and actual feed speeds being variable with resistance in the feed line and slip between the wire and drive rolls as well as experimental errors from measurements of mass and wire feed speed. Given that the width of the deposit is effectively controlled by heat input, conservation of volume infers that the addition of filler material will yield a proportional build-up in terms of height per pass. It is this independence of wire feed

from heat input that gives GTA welding a considerable advantage over GMA and other arc-based welding processes, offering precise control of bead geometry and surface quality, and so making it well suited to additive manufacture methods [15]. It is also worth noting that in all parameter sets (here after referred to as trials, corresponding to the information provided in appendix A) it was observed that the build-up per pass was greatest for the first, taking between two and three passes for a steady state value to be achieved. This is assumed to be due to heat being drawn away from the molten pool by raising the temperature of the sample and surrounding material from ambient. In effect this restricts the size of the molten pool during this first welding pass resulting in an increased build height for the same deposition rate. Once this chill effect is removed the steady state build-up condition is achieved and maintained with the relatively low thermal conductivity of Ti-6Al-4V restricting loss of thermal energy to the experimental equipment and surrounds.

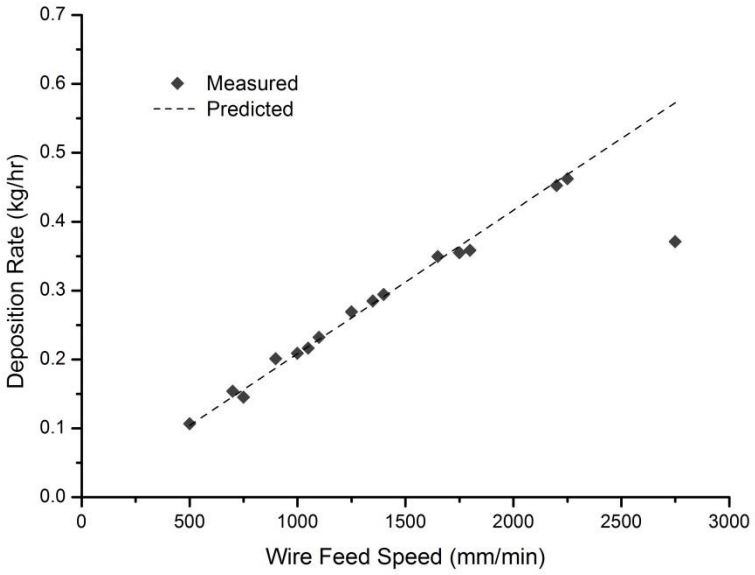

Figure 3.16 Comparison of predicted deposition rates based on wire feed speeds and measured deposition rates determined from mass increase of samples.

While not quantified, results of these trials indicate that there exists a physical limit to the deposition rate possible for a given heat input while maintaining acceptable weld quality. This was particularly evident in trial four where the measured deposition rate deviated significantly from that expected based on the pre-set wire feed speed. In this case the combination of low heat input and high wire feed speed produced ‘stubbing’ of the wire on the solid-liquid interface within the molten pool, causing slip between the wire and the drive rollers, hence reducing the actual wire feed speed well below the pre-

set value. This stubbing is also evident in surface finish as shown in Figure 3.17 where the filler wire has been heated, softened and ‘folded’ under the feeding force rather than being fully absorbed in the molten pool. By comparison, the sidewall profile of trial eight, which was deposited using a more realistic parameter set, is significantly more desirable. Despite these qualitative observations, the results of ANOVA presented in Table 3.5 show no clear correlation between the chosen measure of surface roughness and the input parameters considered. From the schematic illustration of Figure 3.8b it appears the MLT should relate to the bead thickness-to-height ratio and so essentially be dependent on heat input and deposition rate, however additional factors such as melt pool stability and surface tension may also influence the sidewall surface profile. Further investigation is required to test these hypotheses.

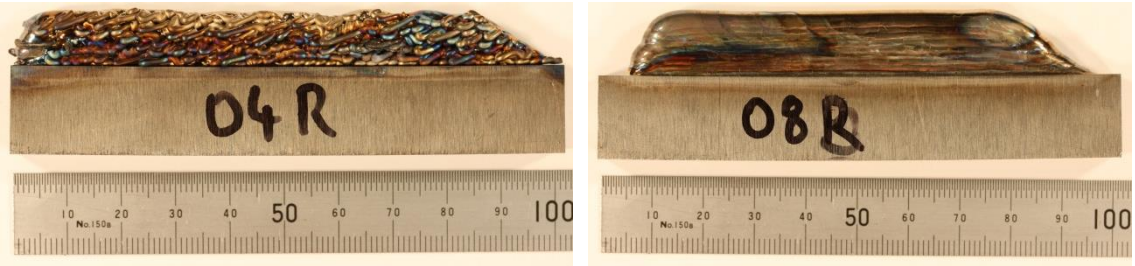

Figure 3.17 Samples from trials four and eight showing variation in sidewall surface profiles.

With respect to the characterised microstructural features, it is apparent that the depth of the HAZ is primarily a result of heat input, with arc current and travel speed being the most influential process parameters. This is not unexpected with the supply of a greater amount of thermal energy meaning a larger region of the sample is heated beyond the temperatures required to cause a change in microstructure. Again, these observations are well understood and readily explained using thermal modelling of the welding process [17, 166, 176, 177].

Growth of β-Ti grains is understood to be a thermally activated process which typically follows parabolic growth laws with respect to time [178]. Form this it would be expected that peak temperature, time above the β-transus and cooling rate from above the β-transus would essentially control the size of prior β-Ti grains in additively manufactured structures, and so arc current and travel speed would be the input process parameters of greatest importance. While the values in Table 3.5 show a high dependence on travel speed, the relative significance of arc current is less than would be expected. The most likely explanation for this is the large error associated with

measured values of prior β-Ti grain size due to the size of circles used in the determination of the mean linear intercepts. Other contributing factors may be size constraints and to a greater extent texture effects, as explained by Ma and Wang [178], which result from epitaxial grain growth during deposition of successive weld beads.

Previous studies [151, 155] have shown that the width and length of the α-Ti laths as well as the size of α-Ti colonies are primarily a function of the cooling rate through the β-transus temperature. This is readily explained with the α-Ti laths forming through a process of heterogeneous nucleation and competitive growth. When cooling rates through the transus are relatively low then there are a few nucleation sites from which laths grow into the prior β-Ti grains. Of this reduced number of nucleated grains, those with a more favourable orientation with relation to the thermal gradient will become dominant resulting in a microstructure with broad and long α-Ti laths grouped in large colonies. The converse is true for relatively high cooling rates where many more heterogeneous nucleation sites become energetically favourable and so greater numbers of laths are nucleated, yielding a more refined structure in terms of lath dimensions. This was clearly shown in the work of Hoye [151] presented in Figure 3.2. While the present study shows a strong relationship between lath dimensions and heat inputs, observations of lath aspect ratios and α-Ti colony size appear to be relatively constant across all trials with no clear dependence on any single input process parameter.

While thermal profiles were recorded for each trial they were considered to be of little value in the analysis of results such as size and shape of the α-Ti phase for a number of reasons. Firstly, only the thermal profile of the first weld pass in each trial would be comparable since each parameter set produced a different bead profile which would clearly influence the thermal profiles of subsequent passes. Secondly, the point at which temperature was measured was far removed from the fusion zone to prevent exposure to high temperatures which would cause the nickel-based thermocouple to detach from the sample. Such detachment may be due to differences in thermal expansion at the joint, but also due to the formation of a eutectic mixture between titanium and nickel which starts to melt at 942 °C. As such critical features of the temperature profile such as peak temperature and cooling rate through the β-transus are not representative of those in the fusion zone and can’t be related to microstructural observations from this region. Further, there is already a great deal of knowledge relating to the heat inputs, thermal properties of materials and thermal cycles in welding processes. As such the recorded

profiles were used primarily to monitor interpass temperatures and don't feature in the analysis of bead geometry and microstructure. Any such investigation would be best attempted through simulations and modelling such as those performed by Charles [17], using experimental observations as means for verification.

From measurements, the volume fraction of α-Ti appears to show a strong dependence on both arc length and travel speed. While initially this seems unreasonable, it is thought that the alpha phase may have been stabilised to some extent by oxygen and nitrogen introduced into the fusion zone by atmospheric contamination. The level of contamination would then depend on the entrainment of air in the shielding envelope at different arc lengths and more rapid exposure of the weld bead to atmosphere at higher travel speed with fusion from subsequent weld passes acting to mix the contamination through the bulk. In order to verify this hypothesis, composition analysis would need to be performed with a technique that is sensitive to light elements such as secondary ion mass spectrometry (SIMS). Another plausible explanation is uncertainty in the measured volume fraction due to the subjective process used, with automated image analyses dependent on the threshold used, the contrast and brightness of the macrograph, the extent of etching during chemical polishing and noise present in the micrograph. As such measurements of the volume fraction of α-Ti, and to a lesser extent α-Ti lath dimensions, are considered representative and not absolute. A more accurate measure of phase proportions could be achieved through bulk diffraction methods such as synchrotron x-ray diffraction or neutron diffraction.

Mechanical properties of the additively manufactured deposits were characterised by microhardness which in essence is a measure of the resistance to plastic deformation. It follows then that hardness would be expected to relate to some measure of effective dislocation slip distance such as α-Ti lath dimensions or α-Ti colony size through the Hall-Petch relation where strength is proportional to the inverse of the square root of the characteristic length. Figure 3.18 plots hardness against the inverse square root of three different characteristic lengths, a, namely α-Ti lath width, α-Ti lath length and α-Ti colony size. In each case no linear relationship is observed and so microhardness of these samples is dependent on some other variable. These results are contrary to that of Mitzner [120] which showed hardness followed a Hall-Petch relation with α-Ti lath width. It must be noted however that the range of each characteristic length in the present study is relatively small and so may not reveal a Hall-Petch relation if such a

trend were to exist. The effect of grain size on hardness may also not be evident in the present results due to atmospheric contamination, particularly by oxygen, which is known to have a strong influence on the hardness of titanium alloys.

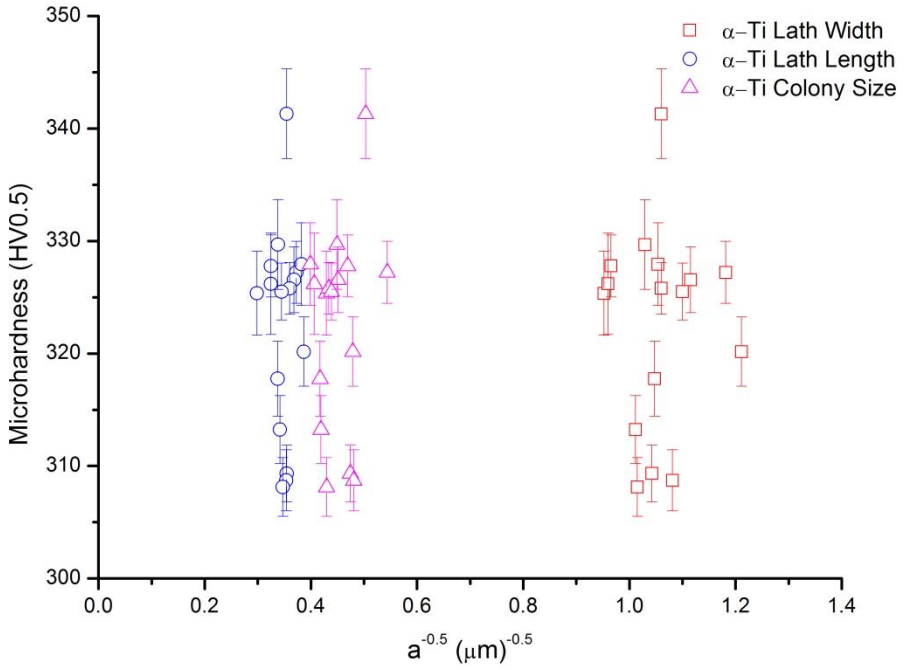

Figure 3.18 Plot of hardness against the inverse square root of three different characteristic lengths, a, namely α-Ti lath width, α-Ti lath length and α-Ti colony size to assess for Hall-Petch type linear relationships. Error bars represent the 95 % confidence interval.

The values relative significance derived from ANOVA suggest that arc length and wire feed speed have the greatest influence on the microhardness of the additively manufactured deposit, with microhardness increasing at shorter arc lengths as shown in Figure 3.19. While at first this may seem erroneous, it may be explained by considering the effect of arc length on the inert gas shielding envelope. Since a constant electrode stick out, defined in Figure 3.20, was used for all trials, increasing arc length was accompanied by an equal increase in the distance between the shielding nozzle and the work-piece. With the use of a gas lens to generate laminar flow of shielding gas it is thought that close to the nozzle exit, the gas flow velocity is relatively high and concentrated while further away the flow becomes divergent with a lower velocity. From this it is predicted that while welding with shorter arc lengths, the high velocity focused gas stream impinges on the work-piece generating turbulence in the welding zone and there-by entraining atmospheric gas into the shielding envelope, allowing interstitial species such as oxygen and nitrogen to contaminate the weld metal. Such

atmospheric contamination is well understood to cause increased hardness in fusion welds in titanium alloys [7, 179-181], with contamination of prior weld passes being mixed effectively into the bulk by subsequent weld passes.

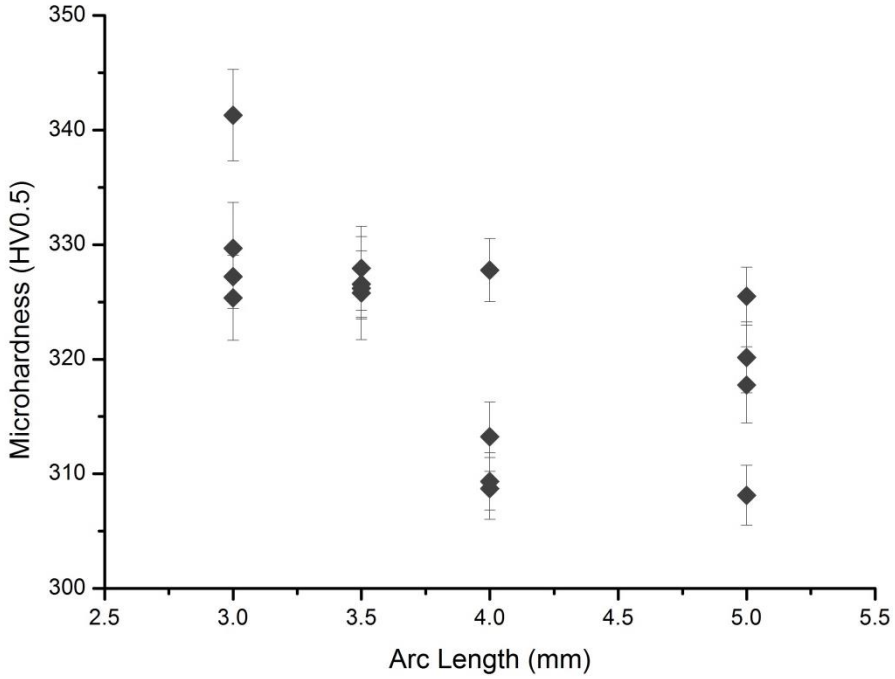

Figure 3.19 Relationship between arc length and measured microhardness values. Error bars represent the 95 % confidence interval.

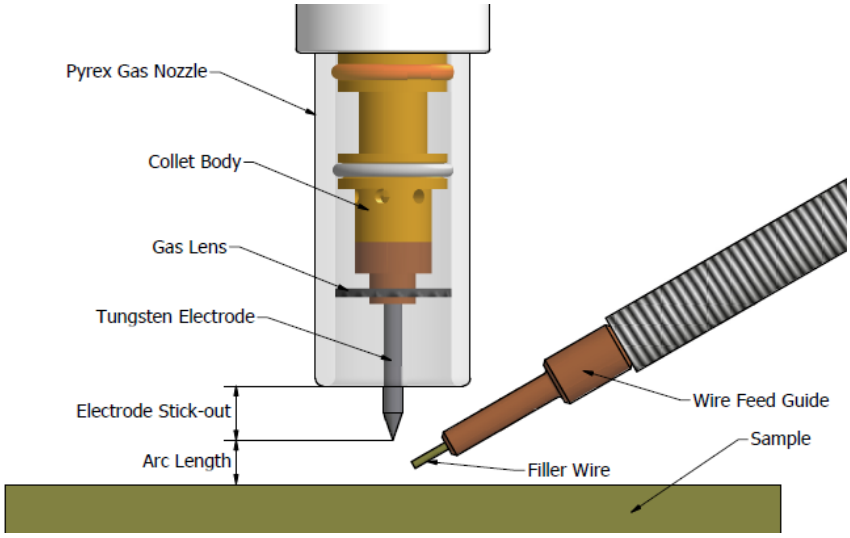

Figure 3.20 Illustration of electrode stick-out in GTAW torch.

It is thought that the observed dependence of microhardness on wire feed speed has similar origins; with higher wire feed speeds generating further turbulence in the shielding envelope due to boundary layer shear about the wire. These hypotheses could be readily verified through the use of computational fluid dynamics, which could then

be used to optimise inert shielding arrangements to minimise atmospheric contamination, however modelling and simulation of this type is beyond the scope of the present study.

3.3.3 Mathematical Models

Using the experimentally obtained values from the characterisation of geometry and microstructural features, mathematical models relating input process parameters to these output variables were developed using empirical curvilinear equations [182]. Each of the geometry and microstructure features were treated as output variables, represented by the response parameter *Y*, which are related to the five input process parameters under the assumption of linear relationships for close ranges. This yielded equations of the form shown in Equation 3.8.

$$Y = kX_1{}^{a}X_2{}^{b}X_3{}^{c}X_4{}^{d}X_5{}^{e}$$

where: *Y* is any output variable such as H, HV or L_{colony}

X_1-X_5 are the input parameters of L, I, WFSR, TS and IT respectively

a, b, c, d, e and *k* are modelling constants

Equation 3.8 General form of empirically derived mathematical models relating characterised output variables to process parameters.

Values of modelling constants for each geometry and microstructural feature, summarised in Table 3.6, were determined using multiple regression techniques with a program run in the MATLAB software. Within these models, the relative influence of each input process parameter on any given output variable may be determined by consideration of the power to which it is raised. The relative error, *e*, associated with each calculation from mathematical models was determined as shown in Equation 3.9. The average error values for each output characterised are given in Table 3.6.

$$e = \left|\frac{m - c}{m}\right| \times 100\ \%$$

where: *m* is the measured value for the geometrical factor of interest

c is the calculated value for the same geometrical factor.

Equation 3.9 Calculation of relative errors from measured and calculated values.

Table 3.6 Modelling constants for geometry and microstructural features.

			Modelling Constant						Average Error (%)
			k	a	b	c	d	e	
Output Variables	Arc Voltage	V	1.871	0.193	0.328	-0.056	0.017	0.008	1.05
	Build-Up Per Pass	H	0.325	0.198	-0.455	0.730	0.282	-0.016	9.57
	Wall Thickness	W	1.980	-0.171	0.751	0.055	-0.462	0.060	4.38
	Thickness-to-Height Ratio	W/H	6.207	-0.369	1.206	-0.675	-0.744	0.076	11.83
	Machining Layer Thickness	MLT	0.315	-0.826	-0.364	0.085	0.547	0.349	25.18
	Surface Standard Deviation	SD	0.058	-0.988	-0.076	0.588	0.297	0.103	40.30
	Hardness	HV	388.790	-0.088	0.021	-0.047	-0.010	-0.005	1.27
	Prior Beta Grain Size	L_{beta}	213.075	0.863	-0.107	-0.175	-0.929	-0.159	19.90
	HAZ Depth	D_{HAZ}	5.008	-0.196	1.004	-0.227	-0.856	0.001	8.14
	Alpha Volume Fraction	V_{alpha}	1.045	-0.082	0.022	-0.013	-0.037	-0.003	1.63
	Alpha Lath Width	W_{alpha}	0.354	-0.127	0.371	0.062	-0.176	0.031	7.39
	Alpha Lath Length	L_{alpha}	2.170	-0.099	0.394	0.114	-0.141	0.024	5.86
	Alpha Lath Aspect Ratio	AR	6.244	0.021	0.018	0.098	0.019	0.000	5.30
	Alpha Colony Size	L_{colony}	1.624	0.202	0.287	0.016	-0.137	0.038	10.62

As a means of comparison, values for each geometric or microstructural output were calculated using the empirically derived mathematical models and then plotted against the corresponding experimental data as shown in the scatter plots of Figures 3.21 and 3.22. Scatter plots for additional output variables are shown in Appendix A. From these plots it is evident that model predictions of wall thickness and thickness-to-height ratio agree closely with measured values. In contrast, the derived model shows poor accuracy when predicting machining layer thickness. There are several sources of error in the determination of the MLT which may contribute to this poor result, the first of which is error in measurement of surface profiles by laser scanning. As this technique relies on reflection of the laser from the surface being scanned, any inclined or rough surface will be poorly mapped due to scattering of the laser. This problem is compounded by highly reflective surfaces such as those of the weld beads in the current experiments. Further, a number of samples showed a constricted root section to the build-up profile where the chill of the sample and surrounding material during the initial weld pass produced a narrower and taller bead profile than once the steady state condition had been achieved. As the MLT is the difference between the widest and narrowest part of the wall, such a constriction at the base will exaggerate the MLT beyond what would be considered the true value for the steady state build region. In practice such constrictions can be easily

avoided by conducting initial passes with higher heat inputs to counter the initial chill effects and so produce a weld bead of the required width from the outset. Once the sample and surrounds have heated sufficiently, the heat input of the GTAW process may be reduced to the desired value and the build process continued under steady state conditions.

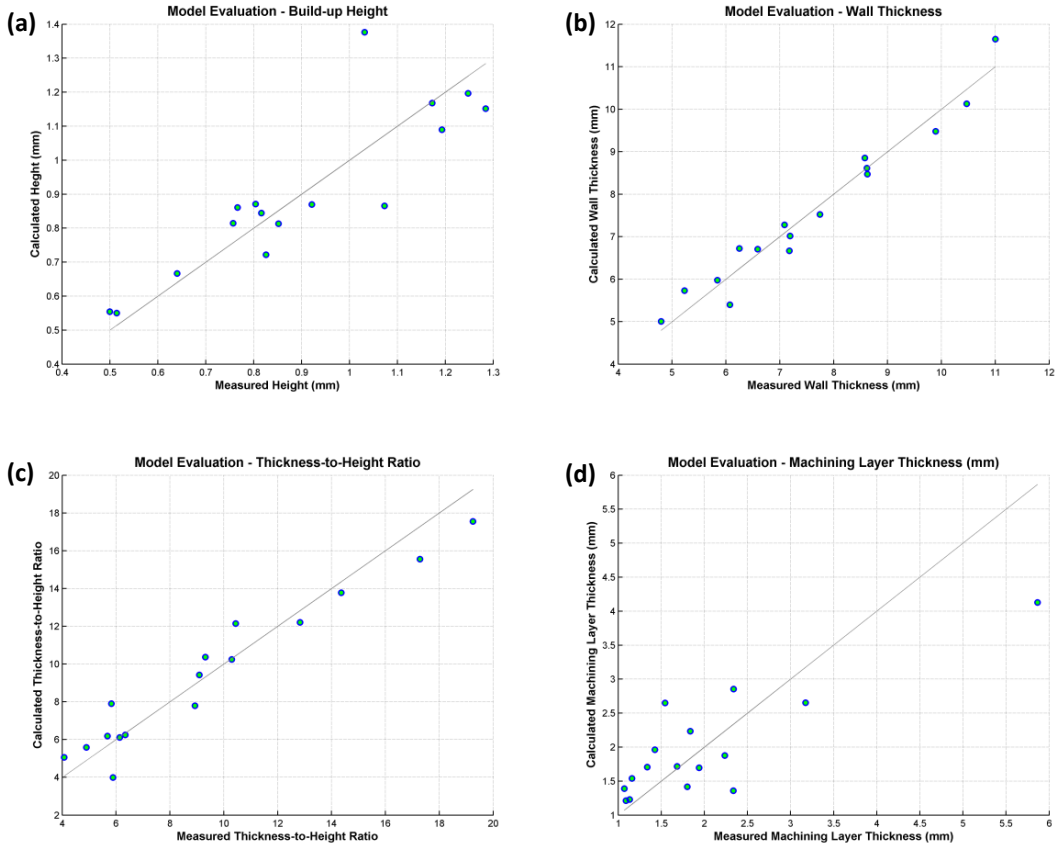

Figure 3.21 Comparison of measured and calculated values for geometry features: (a) build-up height per pass, (b) average wall thickness, (c) thickness-to-height ratio and (d) machining layer thickness.

With the exception of prior β-Ti grain size and α-Ti colony size, the error in agreement between measured and calculated values for characterised microstructural features was less than 10 % on average. While this suggests that the mathematical models provide a reasonable prediction of the observed behaviour, inspection of the scatter plots in Figure 3.22 reveals that there still exist some inaccuracies which may be unacceptable. The sources of uncertainty, as described previously, include variability in measurement methods, particularly those which are reliant on sample preparation and imaging conditions. In the case of prior β-Ti grain size, the errors produced by selection of inappropriate circle overlays are thought to have a significant contribution to the shortcomings of the mathematical model.

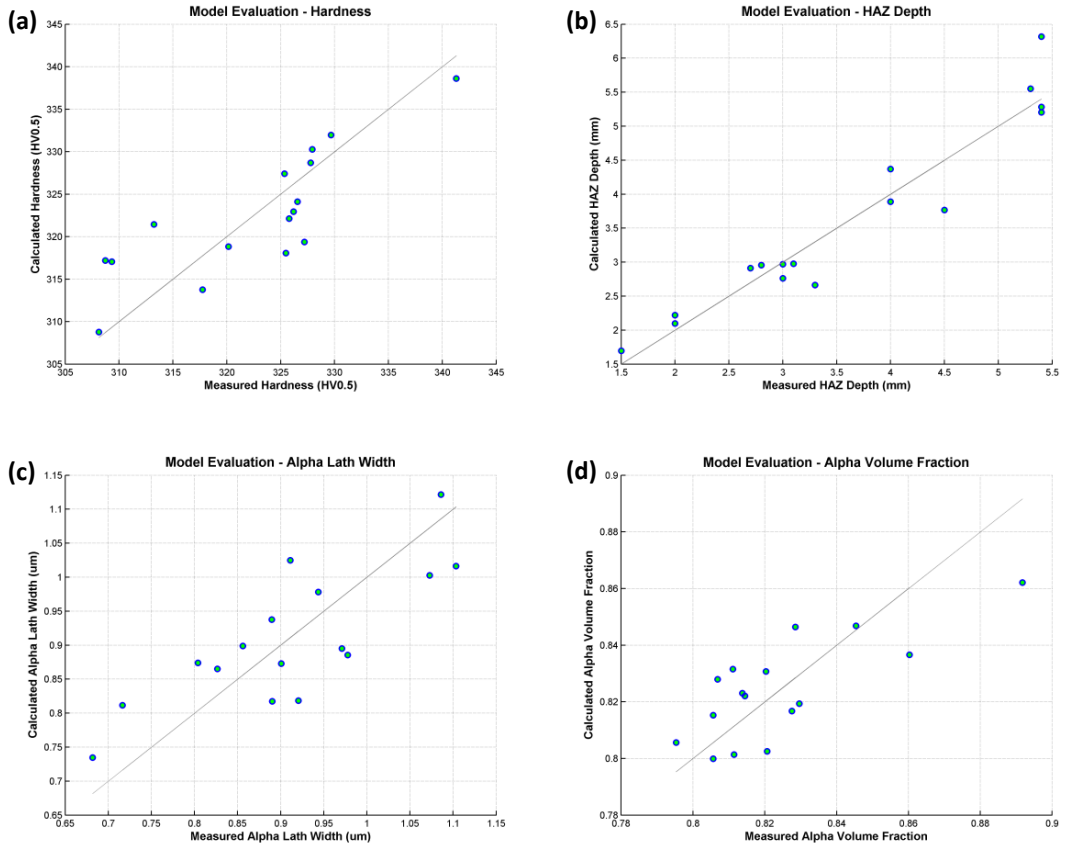

Figure 3.22 Comparison of measured and calculated values for microstructure features: (a) Vickers microhardness, (b) depth of heat affected zone, (c) α-Ti lath width and (d) α-Ti colony size.

The variances (termed ‘errors’) between experimental and calculated values determined using each of the mathematical models are summarised in Figures 3.23 and 3.24. Firstly in terms of geometry features, it is shown that the models used to relate build-up height and wall thickness to the selected input parameters are in close agreement with experimental data with an average accuracy of 91 % and 96 % respectively. The model generated to predict thickness-to-height ratios of weld beads during additive manufacture still show good agreement with experimental data with an average accuracy of 88 %. In contrast, the models for machining layer thickness and standard deviation of surface profile have poor correlation to the experimental data with average accuracies of 75 % and 60 % respectively. These low levels of accuracy are to be expected given the apparent lack of influence of the selected input process parameters. As such, further work is required in this area, be it the investigation of relations to dependent variables such as heat input, deposition rate and thickness-to-height ratio, or the definition of a new measure for sidewall surface roughness.

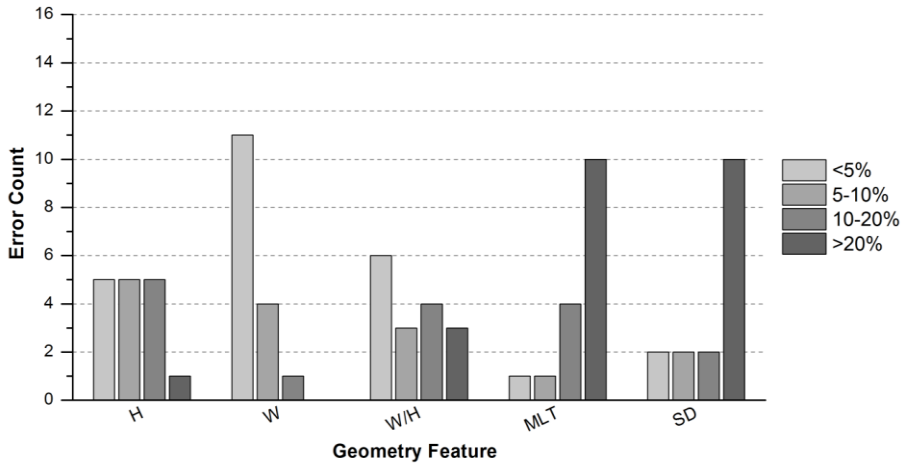

Figure 3.23 Accuracy analysis of models for geometric features showing errors between measured and calculated values.

Of the microstructure features characterised it is clear that models for microhardness and volume fraction α-Ti show the greatest accuracy with average error less than 2 % between measured and calculated values. Mathematical models derived for α-Ti lath geometry and depth of HAZ also show reasonable accuracy with average errors of less than 10 %. As previously stated, models for the prediction of α-Ti colony size and prior β-Ti grain size have low accuracy, primarily due to errors in data collection.

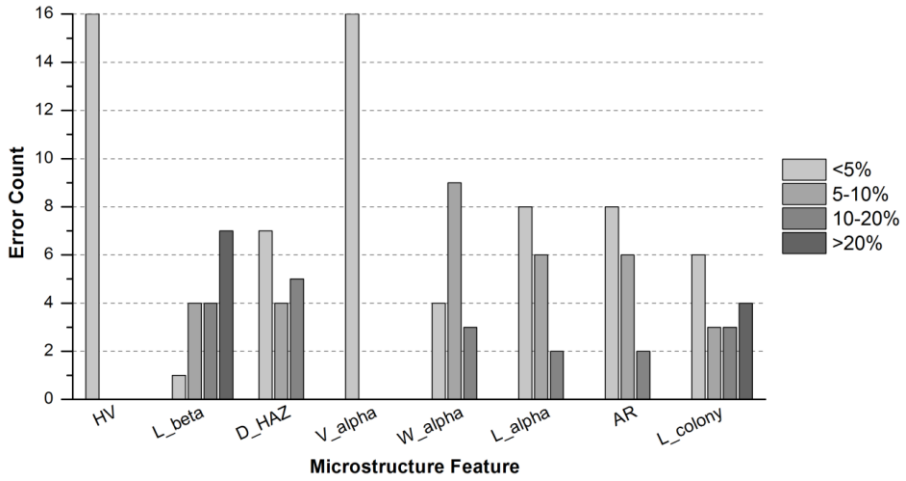

Figure 3.24 Accuracy analysis of models for microstructure features showing errors between measured and calculated values.

It is hoped that empirical relations, such as those developed in the present study, may be used to optimise the GTA welding process for additive manufacture and so allow the process to be competitive on a cost basis with more conventional manufacturing methods, particularly for high cost components such as those fabricated from titanium alloys for use in the aerospace sector. It must be noted however that process models of

this type are of little use without validation using independent experimental data. Escobar-Palafox *et al.* [14] have also shown that with an understanding of process parameters, process models can be used to generate control regimes allowing for more flexible automation of the GTA-wire based additive manufacturing process.

3.4 Conclusions

It has been shown that gas tungsten arc welding can be successfully used in conjunction with an automated wire feed system to generate additively manufactured profiles in the Ti-6Al-4V titanium alloy. Using Taguchi DOE techniques, experiments were conducted to investigate the influence of common welding process parameters on the geometry, microstructure and microhardness of the resulting multi-layer deposit.

Results show that the average thickness of the wall-like build-up is primarily a function of arc current and weld travel speed as is the depth of the heat affected zone. This is readily explained with the combination of arc current and weld travel speed being related to the arc energy and heat input of the welding process. Both the width and length of α-Ti laths are also seen to be influenced by arc energy, however it is thought the origin of these features lies with the cooling rate through the β-transus which was not characterised in the present work. Build height per layer is chiefly related to wire feed speed, and hence deposition rate, with surface roughness of the build-up and aspect ratio of the α-Ti laths also showing some dependence on deposition rate. The α-Ti colony size and volume fraction of α-Ti phase both appear to be influenced by arc length, however the origins of these are unclear and erroneous results may have arisen from uncertainty in characterised values. Where prior β-Ti grain size would be expected to be a function of peak temperature and so heat input, measured values suggest a strong correlation with weld travel speed but very little dependence on arc current. Mechanical properties of the deposited materials were characterised through microhardness testing, with results indicating a surprisingly strong dependence on arc length but no evident relationship to the width of α-Ti laths as would be expected from the Hall-Petch equation. It is thought that the changes in arc length alter the inert gas shielding of the process promoting atmospheric contamination of the deposited material and so altering the microhardness.

Empirical curvilinear models were generated using multiple regression techniques to relate the process parameters considered to the geometry and microstructure features characterised. Models for wall thickness, build-up height per pass, HAZ depth, α-Ti lath length and microhardness show high accuracy with excellent agreement between measured and calculated data. Conversely, machining layer thickness, used to characterise sidewall surface roughness, showed very little dependence on any of the welding process parameters considered, with this being reflected in the relatively poor accuracy of the mathematical model. Models for prior β-Ti grain and α-Ti colony size also show low accuracy when compared to experimental results.

Qualitative observations suggest an effective process operating envelope exists in terms of specific deposition energy based on arc energy and deposition rate. The empirically derived models for microstructural features could be further refined and improved through incorporation of finite element or phase field modelling approaches. The current models must be validated with independent experimental data to ensure their accuracy. Overall it is considered that the mathematical models developed, particularly those relating to geometry of deposits, show considerable promise for both process optimisation and control in process automation.

CHAPTER 4 – MECHANICAL PROPERTIES

4.1 Introduction

It is well understood that the mechanical and physical properties of a material are heavily influenced by its microstructure, which in turn is dependent on the thermal and mechanical processing used to form the material. The experimental work presented in Chapter 3 is not alone in showing that process parameters in GTAW-wire based additive manufacture have a significant effect on both the geometry and microstructure of weld deposited Ti-6Al-4V. In order for GTAW-wire based additive manufacturing to be considered a viable process for the production of structural engineering components from Ti-6Al-4V, the mechanical properties of deposits produced in this way must be evaluated and compared to those of materials formed by more conventional processing methods.

Being a fusion welding based process, arc-wire based additive manufacturing of titanium alloys would be expected to encounter similar difficulties to those described in Chapter 2. These are porosity within the fusion zone and, to a greater extent, embrittlement and cracking due to contamination, particularly by interstitial elements from the surrounding atmosphere. Also of concern is potential anisotropy of mechanical properties across the additively manufactured part. Orientation dependencies of this type would be expected to stem from the highly oriented grain structures which develop through epitaxial grain growth during the deposition process. By conducting suitable tests on representative samples of additively manufactured Ti-6Al-4V, the mechanical properties of these materials may be readily evaluated and compared to those of equivalent materials produced by conventional processing methods, or to relevant industrial standards and guidelines. Any discrepancies or shortcomings of the additively manufactured materials could then be further investigated and related to microstructure and processing.

Numerous studies have previously been conducted to evaluate the mechanical properties of Ti-6Al-4V resulting from various additive manufacturing techniques including arc-wire [12, 13, 16, 183-186], laser-wire [12, 13, 185, 187, 188], laser-powder [131, 185, 189, 190] electron beam-powder [185, 187] and electron beam-wire [191]. The results of these are summarised in Table 4.1, with the requirements for complying with ASTM

standards for Ti-6Al-4V given in Table 4.2. The coordinate system used in describing this data is illustrated in Figure 4.1. The longitudinal direction is that running parallel to the direction of weld travel, the transverse is that running perpendicular to the plane of the additively manufactured build-up and the normal is that perpendicular to the plane of the base plate and hence aligned with the build direction. The same coordinate system is used throughout the remainder of this thesis.

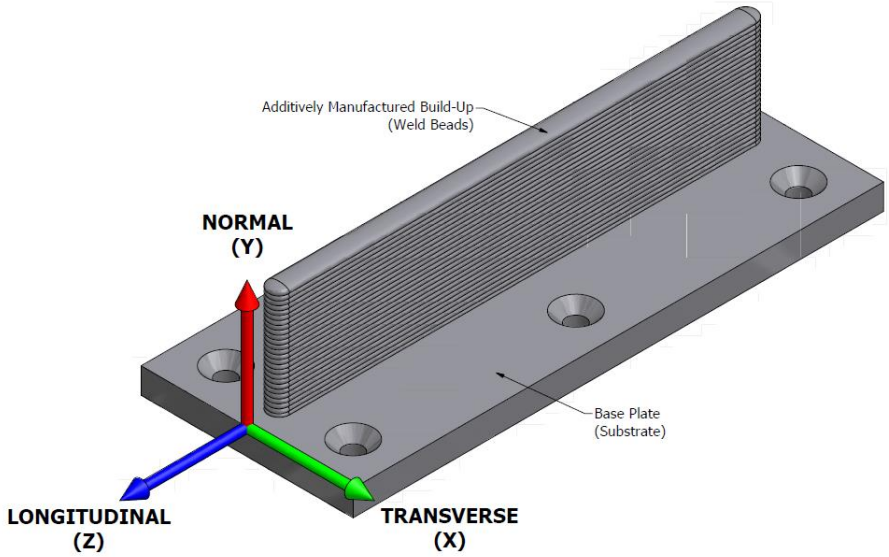

Figure 4.1 Coordinate system used in reference to additive manufactured structures.

Two conclusions can be drawn from the data presented in Tables 4.1 and 4.2. Firstly, anisotropy is evident in most studies, with the longitudinal direction typically exhibiting higher strength and lower ductility compared to the normal direction for samples processed by the same methods. Secondly, the minimum requirements of strength and ductility, as set out in relevant ASTM standards, may be achieved in the as- deposited condition or through additional thermal processing such as annealing and stress relieving heat treatments or hot isostatic pressing. Strength and ductility measurements of this type are considered to form the base level needed for evaluation of Ti-6Al-4V produced by additive manufacture. More in-depth evaluation would include analysis of fatigue and fracture properties since these are critical in typical structural applications where titanium alloys are used. Additional testing may include creep and stress rupture behaviour or characterisation of physical properties such as corrosion resistance.

Table 4.1 Published tensile test data for various additive manufacturing methods. Where used, details of heat treatments (HT) and hot isostatic pressing (HIP) processes are given.

Author	Process	Heat Source	Consumable	Sample Condition	Yield Strength (MPa)		Tensile Strength (MPa)		Ductility (%EL)	
					Longitudinal (Z)	Normal (Y)	Longitudinal (Z)	Normal (Y)	Longitudinal (Z)	Normal (Y)
Wang (2013) [16]	WAALM	GTA	Wire	as-deposited	860 [a]	803	969 [a]	918	8.7 [a]	14.5 [a]
Brandl (2010) [13]	WF-A-Beam	GTA	Wire	as-deposited	890	860	969	938	7.9	16.5
				HT 600°C, 4hr, FC	915	890	982	977	6.6	11.6
				HT 843°C, 2hr, FC	898	855	960	930	13.6	20.5
	WF-L-Beam	Laser	Wire	as-deposited	818	791	895	872	4.1	11.2
				HT 600°C, 4hr, FC	874	847	940	927	7.5	11.0
				HT 843°C, 2hr, FC	822	812	893	883	12.5	10.7
Baufeld (2010) [183]	SMD	GTA	Wire	as-deposited	*n/a*	*n/a*	998 [a]	940 [a]	9.5 [a]	17.5 [a]
Baufeld (2009) [184]	SMD	GTA	Wire	as-deposited	*n/a*	*n/a*	983	953	8.5	16.3
				HT 900°C, 2hr, FC	*n/a*	*n/a*	*n/a*	940	*n/a*	18.0
				HT 1040°C, 2hr, FC	*n/a*	*n/a*	*n/a*	980	*n/a*	9.0
Brandl (2011) [187]	WF-L-Beam	Laser	Wire	as-deposited	984	859	1054	930	4.1	9.5
				HT 843°C, 2hr, FC	918	872	987	940	9.8	11.4
	Arcam	Electron Beam	Powder Bed	as-deposited	897	877	971	955	12.1	14.2
				HT 843°C, 2hr, FC	830	811	920	859	17.7	15.3
Alcisto (2009) [131]	LF3™	Laser	Powder Feed	as-deposited	994	964	1068	1044	5.4	3.0
				HT 980°C, 1hr, FC	861	823	962	936	11.7	11.7
Kobryn (2001) [189]	LENS™	Laser	Powder Feed	HT 715°C, 2hr	1065	832	1109	832	4.9	0.8
				HIP 900°C, 2hr, 100MPa	946	899	1005	1002	13.1	11.8
Taminger (2010) [191]	EBF[3]	Electron Beam	Wire	as-deposited	839 [b]		910 [b]		11.5 [b]	
Facchini (2009) [190]	SLM	Laser	Powder Bed	as-deposited	990 [b]		1095 [b]		8.1 [b]	
				HT 1 [c]	835 [b]		915 [b]		10.6 [b]	
				HT 2 [c]	870 [b]		990 [b]		11.0 [b]	

[a] Values estimated from published graphical data
[b] Sample orientation not specified
[c] Heat treatment details not specified

Table 4.2 ASTM requirements for mechanical properties of Ti-6Al-4V alloys

Standard	Product Form	Grade	Minimum Yield Strength (MPa)	Minimum Tensile Strength (MPa)	Minimum Ductility (%EL)	Maximum Hardness (BHN)
ASTM B265	Strip, Sheet & Plate	5 (Ti-6Al-4V)	828	895	10	n/a
		23 (Ti-6Al-4V ELI)	759	828	10	n/a
ASTM B348	Bars & Billets	5 (Ti-6Al-4V)	828	895	10	n/a
		23 (Ti-6Al-4V ELI)	759	828	10	n/a
ASTM B367	Castings	C5 (Ti-6Al-4V)	825	895	6	365

In its present form, GTAW-wire based additive manufacture is a near net shape method of producing structural engineering components from Ti-6Al-4V, with subsequent machining required to remove material and generate the final desired profile. These operations would most likely be milling and drilling processes, with other forms of material removal such as turning and grinding less likely to be used. As identified in Chapter 2, the machining of titanium alloys presents a number of challenges due to their high strength, low stiffness, high chemical reactivity and low thermal conductivity. These properties are often seen to contribute to reduced tool life, poor surface finish and alteration of microstructure, particularly 'alpha case' formation. Since machinability is inextricably linked to material properties, it is apparent that the machining response of Ti-6Al-4V produced by GTAW-wire based additive manufacturing may differ from that of conventional wrought material and must be characterised.

The present body of work was aimed at evaluating both the mechanical properties and machinability of additively manufactured samples of Ti-6Al-4V produced by the GTAW-wire based method. Due to the exploratory nature of the present research project, mechanical testing was limited to static tensile and Charpy impact testing of representative samples from additively manufactured components. Equivalent testing was conducted on samples from commercially sourced wrought products including rolled plate and billet sections. Results obtained relating to strength, ductility and impact toughness could then be referenced to additively manufactured materials from independent research activities, such as those listed in Table 4.1. Additionally, these initial results are considered to form a benchmark for future work in which process and material property optimisation may be assessed. Basic aspects of machinability were

addressed through milling trials to assess cutting force and drilling trials which characterised cutting forces and tool wear.

4.2 Methods and Methodology

4.2.1 Mechanical Properties

Mechanical properties of Ti-6Al-4V produced by GTAW-wire based additive manufacture were evaluated by static tensile testing and Charpy impact testing. A single additively manufactured build-up was produced by sequential deposition of weld beads onto a commercially sourced Ti-6Al-4V base plate measuring 250 mm x 100 mm x 12 mm. This base plate was fastened to a 25 mm thick mild steel adaptor plate which in turn was mounted to the modified lathe linear actuator system. Welding was conducted using a water cooled Conley & Kleppen (CK) machine mount torch coupled to a Kemppi MasterTIG MLS 2000 inverter power supply. Independent wire feed of diameter 1.0 mm Ti-6Al-4V wire was provided through a CK WF3 dedicated wire feed unit. The combined torch and wire feed arrangement was mounted above the linear actuator with height adjustment possible through a manually operated rack-and-pinion. The general arrangement of this equipment is illustrated in Figure 4.2. Process parameters of arc current, arc length, travel speed and wire feed speed are detailed in Table 4.3. These were selected based on the results of process characterisation studies with the aim of maximising deposition rate while operating with suitable specific deposition energy (between 10 kJ/g and 20 kJ/g) and producing a build-up approximately 8 mm in thickness. It should be noted that arc current was set at 160 A for the first weld pass and 150 A for the following three passes to counter chill from the base plate which was seen to cause narrowing of the weld bead during the initial stages of the build. A total of 48 weld beads were deposited, yielding a total build height of approximately 60 mm as shown in Figure 4.3.

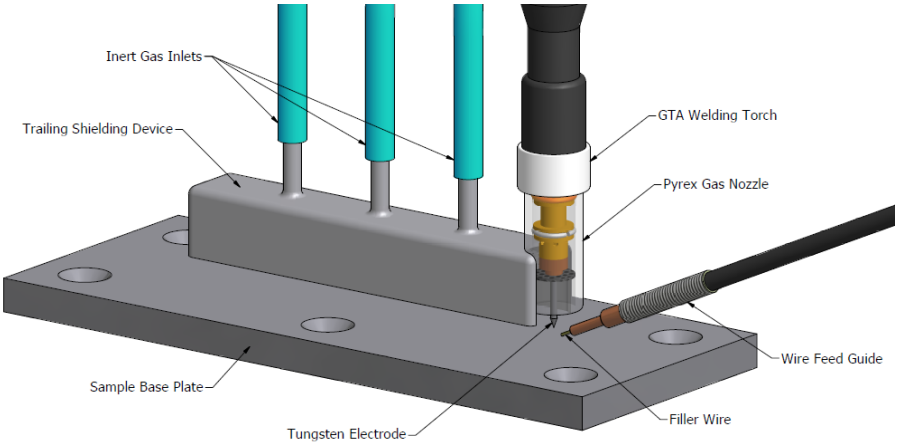

Figure 4.2 General arrangement of welding torch, wire feed and inert trailing shielding used to produce additively manufactured samples.

Inert gas shielding of the weld zone was achieved with welding grade pure argon using pre and post flow options through both the welding torch nozzle and custom fabricated trailing shield. Additional gas shielding of the deposited material was achieved using stainless steel plates measuring 300 mm x 100 mm x 6 mm with a slot 10 mm wide and 260 mm long cut centrally through the plate. As the build process progressed these 'shielding plates' were stacked over the base plate with the build-up protruding through the slot. The aim of this was to maintain a shielding envelope similar to that of a conventional bead-on-plate arrangement at all stages throughout the build process. Shielding gas flow rates and other common process parameters are detailed in Table 4.3. While the build-up in Figure 4.3 shows signs of colouration and hence atmospheric contamination, this colouration only appeared in the solid state away from the weld zone where deposition of subsequent weld beads reheated material outside the shielding envelope. As such, this contamination was considered to have very limited depth of penetration, with any surface layers of contaminated material removed during machining processes used to manufacture tensile and Charpy samples. This is thought to be a safe assumption based on the findings of Bendersky and Rosen [192] and Smarsly *et al.* [193] which detail the limited depth of hardening due to atmospheric contamination during heat treatments of Ti-6Al-4V which may be considered analogous to the solid state contamination of additively manufactured materials. The post-weld atmospheric contamination of Ti-6Al-4V deposits during arc-wire based additive manufacturing and its subsequent effects on mechanical properties is addressed in greater detail in Chapter 6.

Table 4.3 Summary of GTA welding parameters used to produce samples for mechanical testing.

Polarity	DCEN
Electrode	2% Ceriated, 2.4 mm Ø
Arc Current	140 A
Arc Length	3.5 mm
Travel Speed	240 mm/min
Arc Energy	488 J/mm
Wire Feed Speed	2565 mm/min
Specific Deposition Energy	13.2 kJ/g
Shielding gas	Welding Grade Argon
Flow rate – torch nozzle	8 L/min
Flow rate – trailing shield front	8 L/min
Flow rate – trailing shield rear	5 L/min
Pre-flow duration	3 seconds
Up slope duration	2 seconds
Down slope duration	1 second
Post flow duration	30 seconds

Figure 4.3 Additively manufactured deposit used for mechanical testing.

Samples for tensile and Charpy impact testing were prepared from the additively manufactured material in the normal (vertical) and longitudinal (horizontal) orientations, as illustrated in Figure 4.4, using a combination of milling and wire EDM cutting operations. Tensile samples were sub-size rectangular type as set out in Figure 1 of ASTM E8M for tensile testing of metallic materials [194] with a 25 mm gauge length, 6 mm nominal width and 5 mm thickness. Charpy impact samples were also prepared in two orientations as sub-size, measuring 5 mm x 5 mm x 55 mm with the 1 mm deep notch centrally located in accordance with Figure A3.1 of ASTM E23 for

notched bar impact testing of metallic materials [195]. Equal numbers of samples were prepared with the notch machined parallel and perpendicular to the plane of the build-up. Detailed drawings of sample geometry and dimensions are provided in Appendix B.

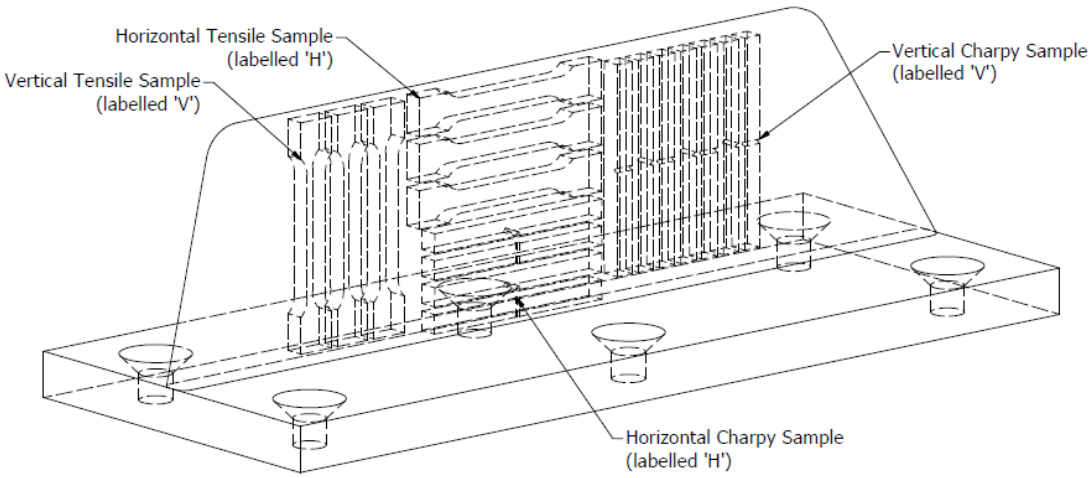

Figure 4.4 Orientation of samples prepared from additively manufactured build-up.

Samples for tensile and Charpy impact testing were also prepared from commercially sourced wrought plate sections in the longitudinal and transverse directions as indicated in Figure 4.5. A further set of additively manufactured samples were prepared to evaluate the joint strength at the interface of the base plate and build-up. The initial pre-form was produced by depositing an additively manufactured build-up of Ti-6Al-4V edgewise onto a separate 12 mm thick base plate. Welding process parameters were set to match those used in preparing previous mechanical testing samples, with 25 weld beads giving a build height of approximately 32 mm. Tensile samples were then prepared from this ‘composite’ preform such that the interface between wrought and additively manufactured materials was centred in the gauge length as shown in Figure 4.6. For tensile testing a minimum of three tensile samples were prepared for each orientation, with six used in the case of the joint-type samples. For Charpy impact testing, a minimum of four samples were prepared for each orientation. Further, sub-sets of Charpy samples were prepared with the V-notches prepared in both orientations perpendicular to the length of the sample to assess variations in crack propagation direction as well as sample orientation. Confidence intervals were determined using the method of the Student’s t distribution as described in Section 3.2.

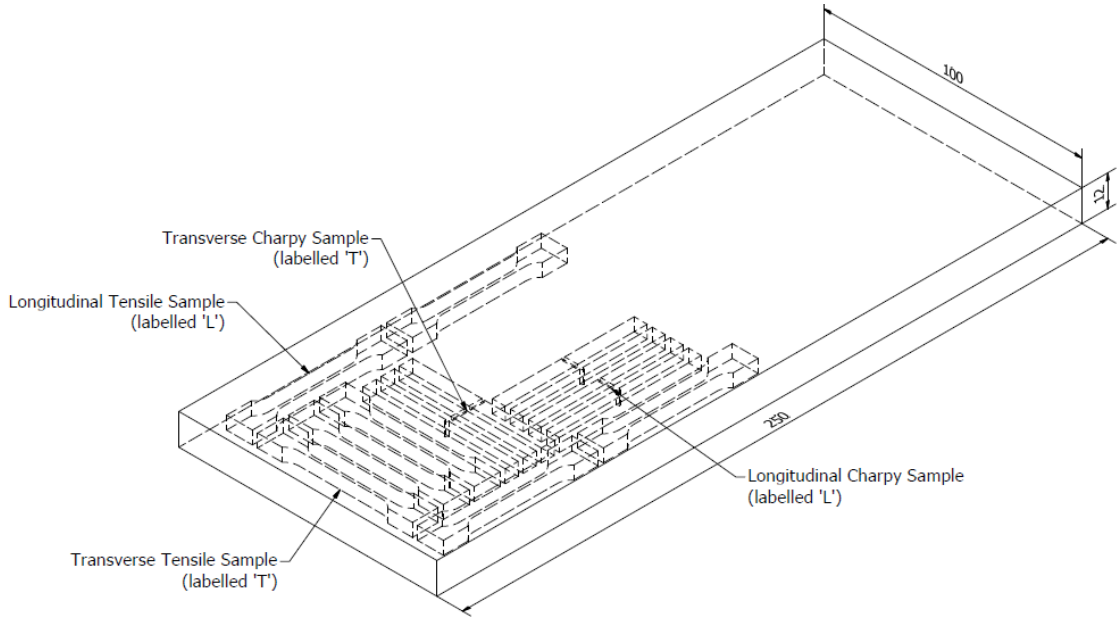

Figure 4.5 Orientation of samples prepared from commercially sourced wrought.

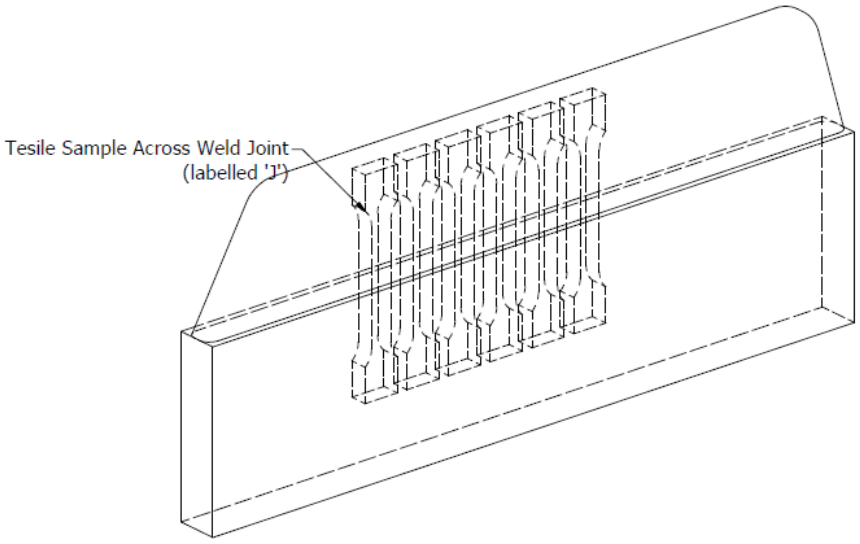

Figure 4.6 Preparation of tensile samples to test joint strength between base plate and additively manufactured materials.

Tensile testing was conducted on samples in the as-deposited condition (additively manufactured samples) or as-received condition (wrought samples) in accordance with ASTM E8M using a MTS Sintech 60/D universal testing machine fitted with 100 kN load cell and mechanical wedge grip jaws as shown in Figure 4.7. Tests were conducted under strain rate control in two stages, firstly from zero to 2 % total elongation at $\dot{\varepsilon}_1 = 0.015\ /min$ and then from 2 % total elongation to final fracture at $\dot{\varepsilon}_2 = 0.06\ /min$. An Epsilon axial extensometer with 25 mm gauge length was used to measure elongation. Sample dimensions were used in conjunction with force and

elongation measurements to produce engineering stress and strain curves from which mechanical properties were determined using MATLAB scripts.

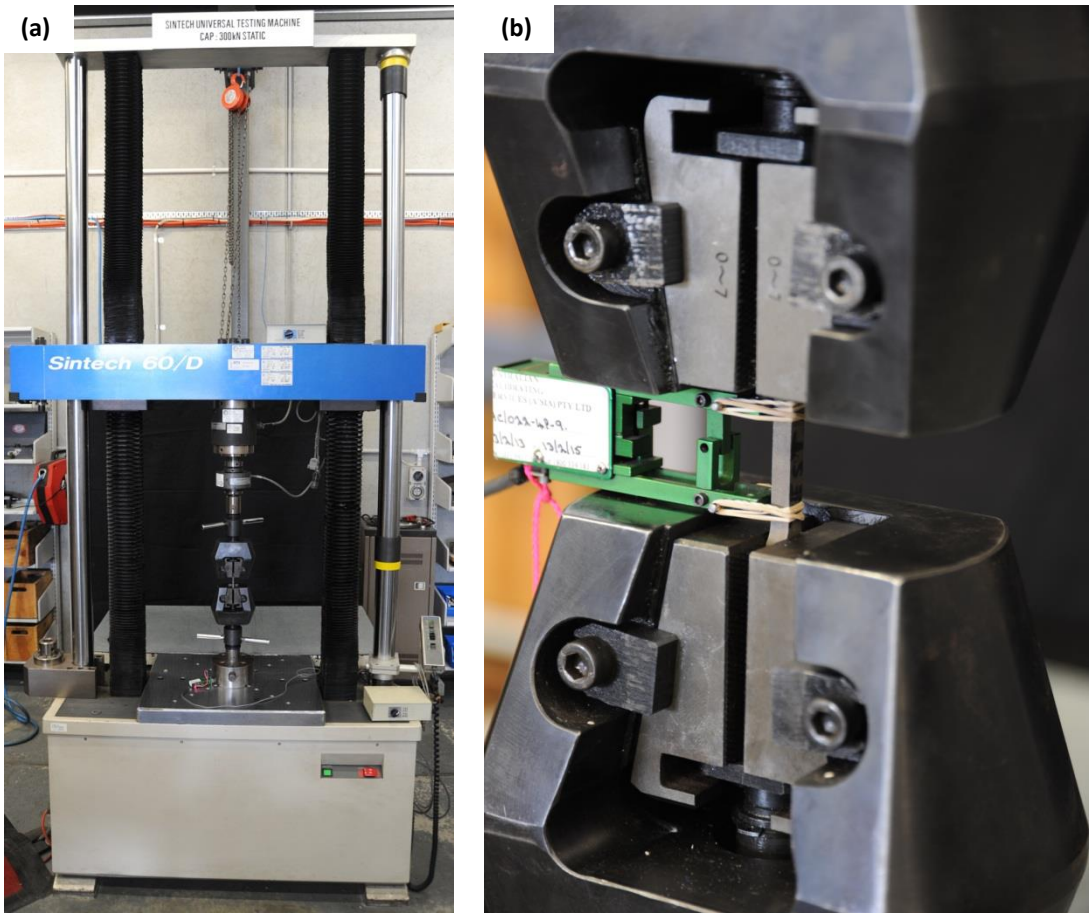

Figure 4.7 (a) MTS Sintech 60/D universal testing machine (b) mechanical wedge grip jaws with axial extensometer attached to rectangular tensile sample.

Charpy impact testing was conducted on samples in the as-deposited condition (additively manufactured samples) or as-received condition (wrought samples) in accordance with ASTM E23 using an Avery 300 J pendulum impact tester. Samples were tested at -40 °C with impact energy values read manually from the dial indicator. This temperature was selected based on the results of Herold *et al.* [196], which showed that predictions of the fracture toughness of Ti-6Al-4V from results of instrumented Charpy impact testing was most accurate at -40 °C. It should be noted that such determinations of fracture toughness values was not performed in the present study since no instrumented impact tester was available at the time and the validity of such extrapolations has not been fully proven for sub-size notched samples. The limited quantity of additively manufactured samples also prevented more extensive testing at additional temperatures. Following impact testing, fracture surfaces were examined by

scanning electron microscopy using a JEOL JCM-600 NeoScope benchtop SEM in secondary electron imaging (SEI) mode.

Offcuts of both additively manufactured and wrought plate materials from preparation of tensile and Charpy impact samples were used for inspection of microstructure and microhardness testing. Samples of at least 5 mm x 5 mm were prepared for each plane (XY, XZ and YZ) by hot compression mounting in phenolic powder. Mounted samples were plane ground using silicon carbide (SiC) and chemically-mechanically polished using modified colloidal silica solution (1 part H_2O_2, 2 parts NH_3 and 25 parts 0.25 μm OP-S) as per Struers application notes for titanium [27]. Samples were etched using Kroll's reagent (2 vol% HF, 6 vol% HNO_3 with balance H_2O) for optical microscopy, which was conducted using a Leica DMRM compound microscope. Vickers microhardness of each sample was determined using automated testing on a Struers Durascan 70 equipped with Ecos Workflow software. Using a load of 0.5 kg and a dwell time of ten seconds, a total of 81 indents were performed on each sample, placed in a 9-by-9 grid arrangement at 0.5 mm intervals.

4.2.2 Milling Trials

Machinability of additively manufactured deposits of Ti-6Al-4V produced by the GTAW-wire method was assessed through milling trials with cutting force used as the main means of evaluation. A total of five build-up structures were produced in a similar manner to that used in producing deposits for mechanical testing, with the key process variables for each listed in Table 4.4. To provide comparison to machining of wrought Ti-6Al-4V, a sample of similar geometry to the additively manufactured build-ups was fabricated from two sections of commercially sourced wrought Ti-6Al-4V plate measuring 200 mm x 50 mm x 12 mm. These were welded together in a T-fillet configuration as shown in Figure 4.8 using diameter 1.0 mm Ti-6Al-4V wire. A 'double-V' preparation was used on the vertical plate to achieve full penetration through the weld joint, however later sectioning revealed incomplete penetration in the joint. Prior to the machining trials, the vertical wall section of this T-fillet was milled along its entire length, reducing its thickness to 7 mm to better match the geometry of additive build-ups and hence produce comparable stiffness conditions.

Table 4.4 Key GTAW process parameters for preparation of additively manufactured samples for machinability trials.

Sample ID	Arc Energy (J/mm)	Specific Deposition Energy (kJ/g)	Passes	Total Build Height (mm)
Wall_02	482	21.0	35	29.0
Wall_03	525	16.2	27	28.8
Wall_04	504	12.1	21	29.0
Wall_05	497	12.1	24	29.9
Wall_07	493	13.2	48	60.0

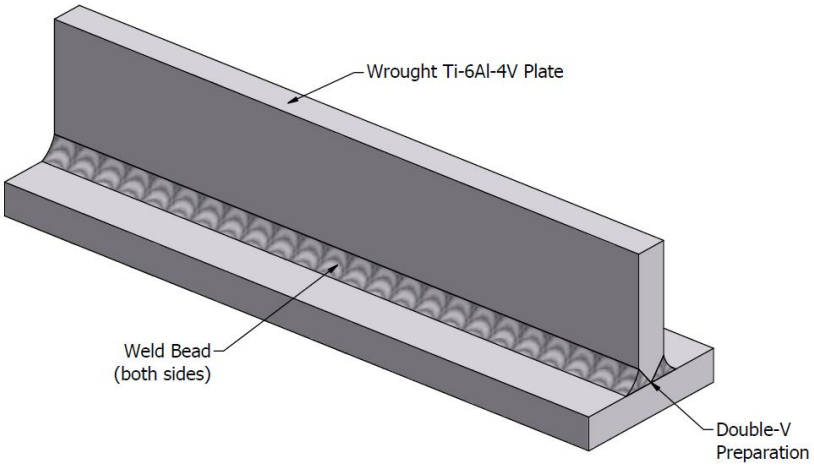

Figure 4.8 Schematic illustration of fabricated T-fillet structure produced from wrought plate for machinability trials.

Machining trials were conducted in collaboration with SECO Tools Australia using a DMG MORI DMU 70 5-axis CNC milling machine. Samples were securely fastened to a Kistler 9257A three-component force dynamometer which was mounted to the table of the milling machine as shown in Figure 4.9. The dynamometer was connected through three charge amplifiers to a computer where NI LabVIEW was used to measure cutting forces in three directions. End milling operations were performed on each sample using a 16 mm diameter SECO B39 JABRO HPM carbide end mill (designation JHP770160E2R250.0Z4A-SIRA) designed for machining of titanium alloys. This milling configuration, shown in Figure 4.10, was selected to simulate the manufacture of deep pocketed, thin-walled features typical in structural aerospace components made from titanium alloys. Such thin-walled features are ideally suited to production through GTAW-wire based additive manufacture where large savings in material and machining can be achieved. The coolant was a water-oil emulsion applied to the cutting zone using directed nozzles and through the spindle of the cutting tool at high pressure (60 bar).

Other parameters relating to the machining process are given in Table 4.5. For each sample an initial 'skimming' pass was performed to generate a smooth consistent surface, followed by two passes at the full radial depth of cut of 1.0 mm. In the case of the fabricated T-fillet sample these full depth cuts were performed one each on opposite sides of the wall. For additively manufactured samples, the two full depth cuts were taken on the same side to minimise the need for skimming processes which would have further reduced the wall thickness. Cutting forces in all three directions were recorded for each full depth cut and compared to assess the relative machinability of samples. The same end mill was used for all trials with the fabricated T-fillet machined first, followed by the additively manufactured samples.

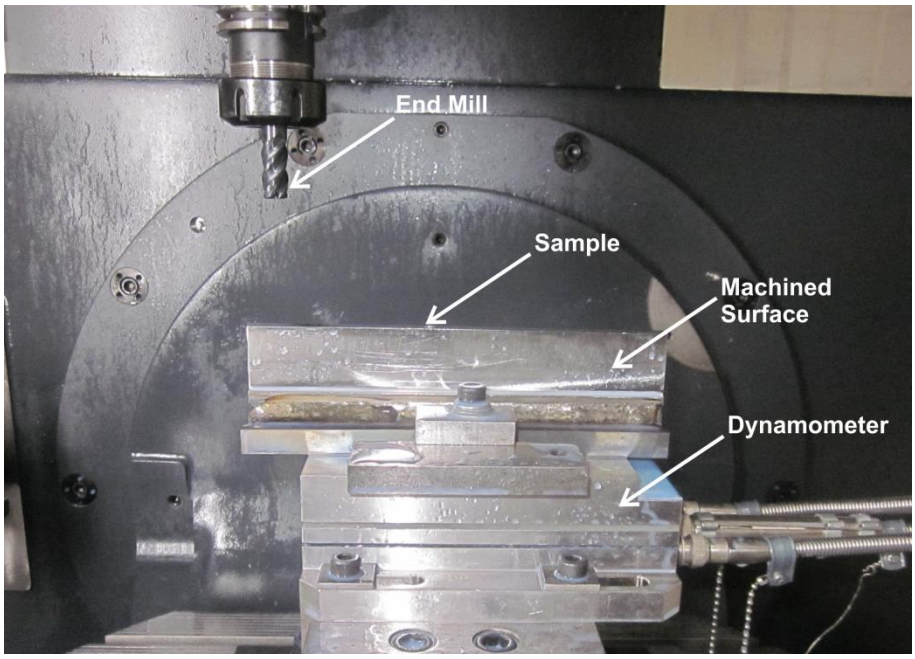

Figure 4.9 General arrangement of equipment used for milling trials with fabricated T-fillet sample mounted.

Table 4.5 Process parameters for end milling operations used to assess machinability.

Milling Configuration	Climb (Down) Milling
Cutter Diameter, D	16 mm
No. of Teeth, z	4
Feed Per Tooth, f_z	0.15 mm/tooth
Feed Per Revolution	0.60 mm/rev
Surface Cutting Speed, V_c	80 m/min
Axial Depth-of-Cut, a_p	30 mm
Radial Depth-of-Cut, a_e	1.0 mm
Cutting Length	≈200 mm

Following machining trials, surface finish was measured using a Hommelwerke T1000 profilometer and Turbo Datawin-NT 1.48 software. For each sample the measurement range was 80 μm and the assessment length set to 4.80 mm, running parallel to the feed direction and hence perpendicular to the chatter marks as shown in Figure 4.11. These surface profile measurements were converted to average surface roughness (Ra) values by the Turbo Datawin software according to ISO 11562 for measurement of surface profiles.

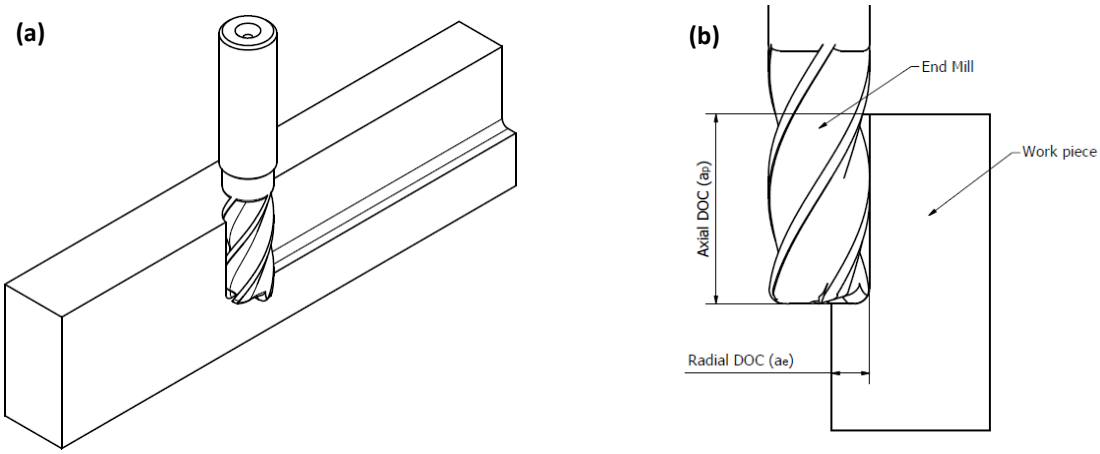

Figure 4.10 Illustration of (a) end milling using an end mill and (b) depth of cuts (DOC) during end milling operations.

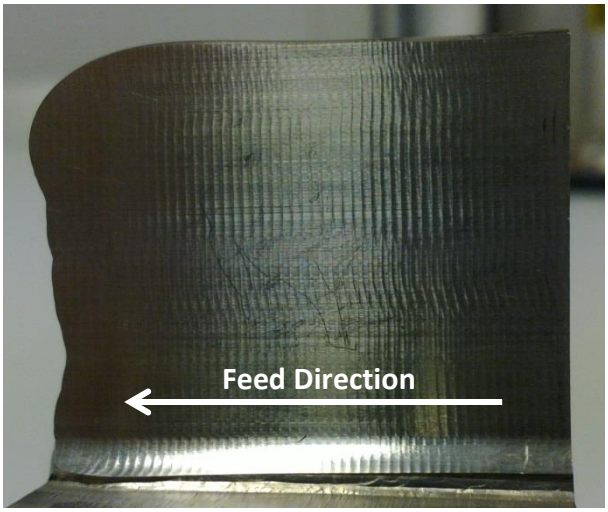

Figure 4.11 Finish machined surface of short section removed from additively manufactured 'Wall_02' with chatter marks evident perpendicular to the milling feed direction.

4.2.3 Drill Life Testing

Drill life testing was conducted as a second means of assessing machinability by evaluating cutting forces and tool wear. A large pad like deposit of Ti-6Al-4V was

produced using the same welding equipment as described previously. A total of 100 weld beads were deposited in 11 layers using the parameters set out in Table 4.6, yielding a deposit approximately 250 mm in length, 40 mm in width and 20 mm in height as shown in Figure 4.12. Despite the rigid clamping arrangement used during the welding process, the significant thermal cycling and material deposition caused a considerable amount of distortion in the base plate. As a result, the sample was prepared for drill testing by machining the bottom and top faces of the base plate and the top of the deposit to produce smooth flat surfaces for clamping and drilling. An equivalent sample of wrought Ti-6Al-4V measuring 250 mm x 36 mm x 24 mm was cut from a large billet section 55 mm in thickness and machined flat on the top and bottom faces in preparation for drill testing.

Table 4.6 Summary of GTA welding parameters used to produce sample for drill life testing.

Arc Current	140 A
Arc Length	4.0 mm
Travel Speed	150 mm/min
Arc Energy	634 J/mm
Wire Feed Speed	1470 mm/min
Specific Deposition Energy	18.9 kJ/g

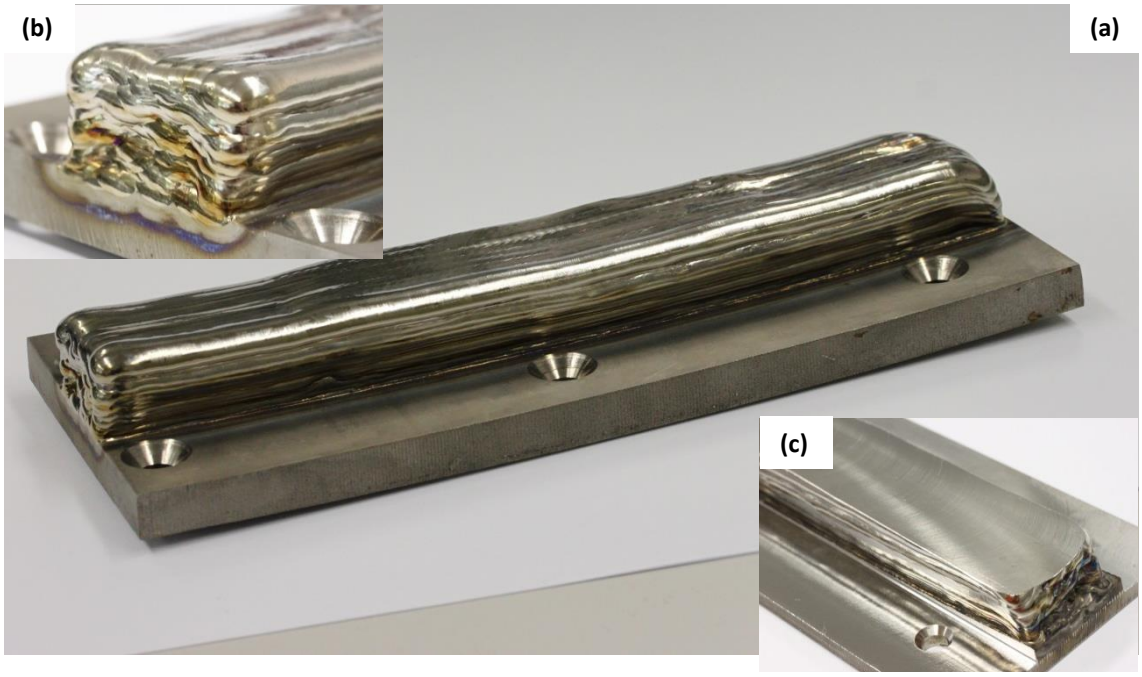

Figure 4.12 Additively manufactured pad sample for drill life testing (a) and (b) as-deposited, (c) machined flat in preparation for drill testing.

Drilling trials were conducted using a Haas TM-2P 3-axis CNC vertical milling machine, with samples securely fastened to a Kistler three-component force dynamometer which was mounted to the table of the milling machine. Again, the dynamometer was connected through three charge amplifiers to a computer where NI LabVIEW was used to measure cutting forces in three directions. Drilling operations were performed using 5.0 mm diameter (*D*) Sutton Tools R40 UNI stub drills (item number D155 0500) with a separate drill used on each sample. Coolant (water-oil emulsion) was applied at standard pressure to the drill using directed nozzles. A total of 112 holes were drilled to a depth of 12.5 mm (2.5*D*) in each sample with holes arranged in a grid pattern of 4-by-28 holes at 8 mm centre spacing. While it is common practice in drill testing for holes to be randomly located within a material test piece to account for sample variability, the relatively uniform nature of the current samples as well as restrictions due to their size meant that the grid arrangement described above was adopted. Sequencing of holes was used such that every seventh hole was drilled to avoid localised heating of the material influencing drill performance in adjacent holes. Other parameters relating to the machining process are given in Table 4.7. Cutting forces in all three directions were recorded for every fourteenth hole and compared to assess tool life and the relative machinability of samples.

Following drilling operations, each drill was inspected for wear using a Leica M205A stereo microscope with z-stacking used to obtain images with high depth-of-field. Sections of each sample were removed by wire EDM cutting and prepared for metallographic inspection and hardness testing using the methods described previously. Optical microscopy was conducted using a Leica DMRM compound microscope and Vickers microhardness testing of each sample was performed using a Struers Durascan 70 equipped with Ecos Workflow software. 20 microhardness measurements were performed on each sample using a load of 0.5 kg and a dwell time of ten seconds. Indents were randomly located across each sample surface; however care was taken to ensure indents were sufficiently spaced from one another, mechanically deformed surfaces and sample edges. Representative samples of swarf were also collected during drilling operations and characterised by optical and stereo-microscopy.

Table 4.7 Process parameters for drilling operations used to assess machinability.

Drill Diameter, D	5.0 mm
No. of Flutes	2
Flute Length, L_2	26.0 mm
Feed Per Revolution, f	0.09 mm/rev
Feed Rate, V_f	51.5 mm/min
Surface Cutting Speed, V_c	9.0 m/min
Drill Rotation	571 rev/min
Hole Depth	12.5 mm
Hole Count	112

4.3 Results and Discussion

4.3.1 Tensile Testing

Tensile testing of both wrought plate and additively manufactured Ti-6Al-4V samples showed typical tensile stress-strain behaviour with linear elastic deformation up to strains of approximately 0.01 mm/mm followed by yielding with combined elastic and plastic deformation continuing to total strains in excess of 0.14 mm/mm. This behaviour is shown in Figure 4.13 which presents the engineering stress-strain curves for a sample prepared from wrought plate material with loading in the transverse direction. It must be noted that the 'step' feature in the curve after the onset of plastic deformation occurs at a total strain of 0.02 (equal to 2 %) and so corresponds to the change in strain rate from $\dot{\varepsilon}_1 = 0.015\ /min$ to $\dot{\varepsilon}_2 = 0.06\ /min$. While a step change in flow stress would be expected due to strain rate effects, it is considered that the observed step size is disproportionately large for the increase in strain rate and so is most likely due to the change in the sample loading method from strain rate control based on extensometer measurements, to control on the position of the mechanically driven crosshead. This change in control methods was necessitated due to the inability for the extensometer to remain attached to the sample up to the point of fracture.

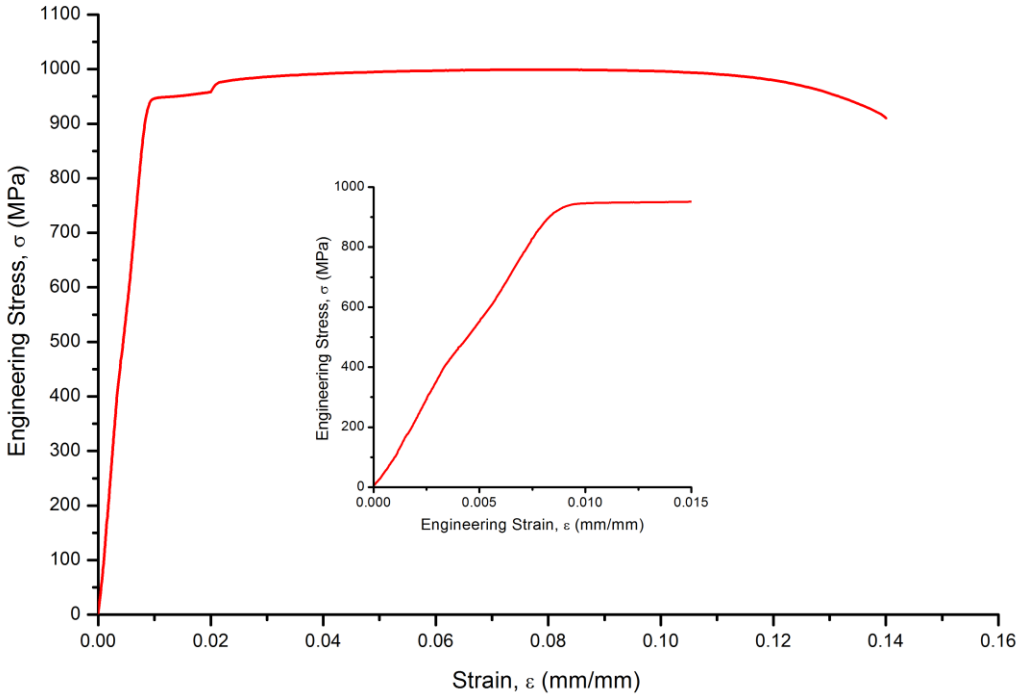

Figure 4.13 Engineering stress-strain curve for transverse tensile sample from wrought plate.

Considering firstly values of tensile elastic (Young's) modulus determined through tensile testing it was seen that samples prepared from wrought plate sections exhibited a high degree of anisotropy with the average value in the longitudinal direction some 20 GPa higher than that of the transverse direction. This anisotropy is attributed to the deformed and highly oriented microstructure developed during the plate rolling processes. In contrast, sample orientation is seen to have very little effect on elastic modulus in samples prepared from purely additively manufactured material with values of 114.3 GPa and 116.9 GPa for the longitudinal and normal directions respectively. The average value of elastic modulus measured in 'joint' samples was 112.4 GPa. These samples can be thought of as composite materials comprising of both transverse wrought plate and normal additively manufactured sections and so it seems reasonable that their elastic moduli should be between that of the wrought material in the transverse direction and the additively manufactured samples in the normal direction. These results are summarised in Figure 4.14.

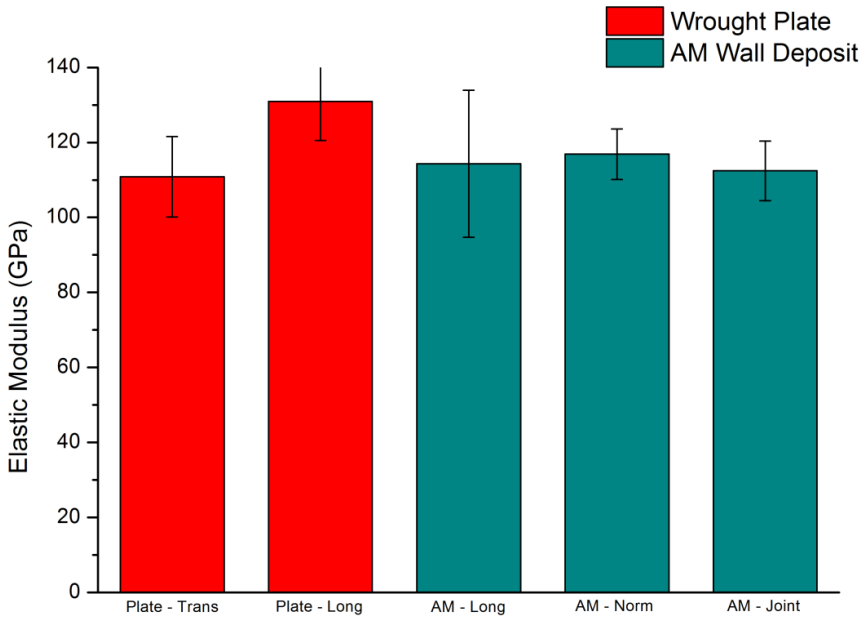

Figure 4.14 Elastic modulus of tensile samples. Error bars represent the 95 % confidence interval.

Due to the lack of a clearly defined yield point, yield strength (σ_y) was determined from engineering stress-strain data as a 0.2 % proof (offset) stress. Additionally, this definition of yield strength is consistent with minimum values published in ASTM standards for titanium plate, billet and castings [197-199] and so allows direct evaluation of the test materials against relevant industry standards. Ultimate tensile strength (σ_{ts}) values were defined as the maximum engineering stress supported by each sample. Results for both yield strength and ultimate tensile strength are summarised in Figure 4.15 with the minimum strength values for bars and billets according to ASTM B348 indicated. It should be noted that these minimum values for Ti-6Al-4V (ASTM grade 5) of 828 MPa for yield strength and 895 MPa for ultimate tensile strength are identical to those specified in ASTM B265 for plate, sheet and strip sections.

These results show that the yield strength of wrought plate sections easily exceeds the minimum requirements for ASTM certification with average values of 948 MPa in the transverse direction and 1023 MPa in the longitudinal direction. Of the samples produced by additive manufacturing, only the joint-type met the minimum requirements with samples from longitudinal and normal orientations displaying average yield strengths of 803 MPa and 806 MPa respectively. While these values fail to meet the minimum yield strength requirements for ASTM standards relating to wrought Ti-6Al-4V, they fall within the range of yield strengths specified by Boyer [21] as being from 760 MPa to 895 MPa. Based on the work of Wang *et al*. [16] and Brandl *et al*.

[13] it is anticipated the minimum yield strength requirements could be achieved through the use of different deposition process parameters or post weld heat or mechanical treatments. Additionally, should yield strength values remain below the minimum requirements specified by ASTM standards, additively manufactured Ti-6Al-4V could still be used in structural applications with the marginal decrease in yield strength compensated for in the design of components. In such cases the minimal increase in component weight would have to be compared to the potentially substantial financial savings during production.

In terms of ultimate tensile strength, both wrought plate and additively manufactured samples are seen to exceed the minimum requirements of relevant ASTM standards. Again, samples from wrought plate with longitudinal orientation show the greatest strength at 1078 MPa, more than 75 MPa greater than the transverse direction. While anisotropy was not evident in values of yield strength for additively manufactured samples, there does appear to be orientation dependence in ultimate tensile strength where samples with normal orientation, on average, showed strengths 80 MPa greater than those with longitudinal orientation. Samples from wrought plate however show anisotropy in both yield and ultimate tensile strengths with values in the longitudinal orientation approximately 75 MPa higher in both cases.

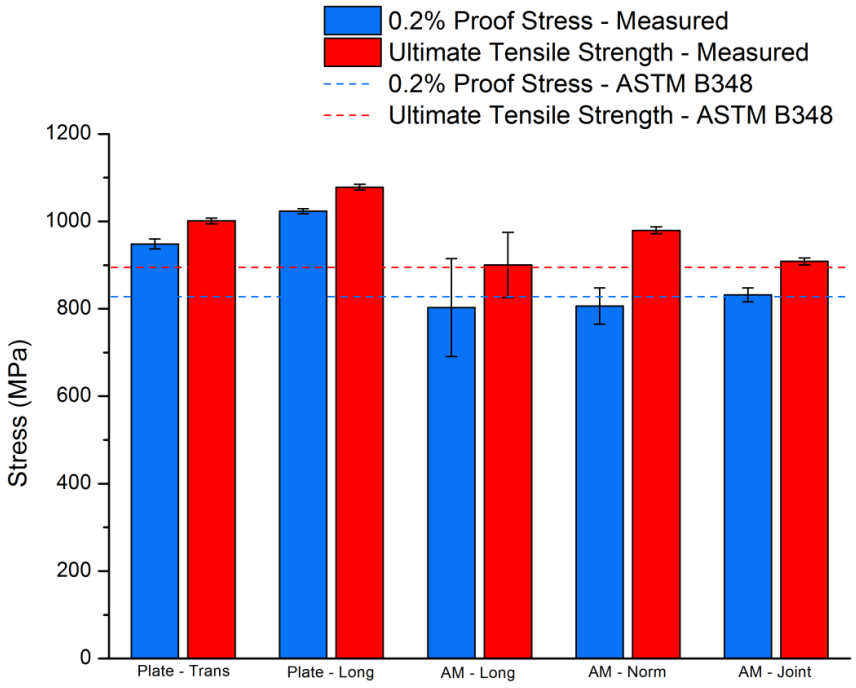

Figure 4.15 Yield and ultimate tensile strength of tensile samples with minimum ASTM requirements indicated. Error bars represent the 95 % confidence interval.

In contrast to both elastic modulus and strength, the ductility of wrought plate samples appears to be isotropic with average values of 13.5 % and 13.1 % for the transverse and longitudinal directions respectively. The marginally higher elongation in samples with transverse orientation is consistent with their reduced strength values compared to those samples with longitudinal orientation. While showing lower ductility than their wrought plate equivalents, samples of additively manufactured Ti-6Al-4V still exceeded the minimum ASTM requirements of 10 % elongation. Only the joint-type samples failed to achieve the minimum requirements for ductility with an average plastic elongation of 6.4 %. However, this low value is attributed to the composite nature of these samples where the yield strength of the wrought plate component is more than 140 MPa greater than that of the additive manufactured material. As such, during tensile testing, yielding will take place first in the additively manufactured portion of the sample with plastic strain then localised to only half of the measured 25 mm gauge length. In this way the measured ductility for these joint samples is considerably lower than the true ductility of either the wrought plate or additively manufactured portions and so should not be considered a representative value. This is supported by the observation that each of the six joint-type samples tested failed in the additively manufactured portion of the sample which, from other results, is known to have lower ultimate tensile strength than the wrought plate material. This also showed that the joint interface between the wrought plate substrate and additively manufactured build-up is not the main point of weakness in components produced by this method. Ductility results are given in Figure 4.16, again with minimum values for bars and billets according to ASTM B348 indicated.

Inspection of fracture surfaces from tensile testing samples revealed a typical ductile fracture with necking observed in all samples and fracture surfaces inclined relative to direction of applied load. Samples also showed evidence of micro-void formation and significant plastic deformation prior to fracture. Plate rolling direction was clearly visible in fractures of wrought plate samples which tended to adopt a ‘V-shaped’ wedge like profile. Fracture surfaces of additively manufactured samples didn’t show alignment of this type with many planes of fracture showing and no clear orientation relationships between each other. A number of samples of additively manufactured material, primarily those of the joint configuration, showed signs of porosity in the fracture surface which is thought to have to promoted failure of the sample in these locations. The presence of such defects is also thought to have contributed to the

comparatively large scatter seen in strength and ductility values for additively manufactured samples. The internal surface of these pores, clearly identified in Figure 4.17, was bright silver in appearance with no signs of discolouration, suggesting the entrapped gas was most likely argon from the shielding gas rather than oxygen or nitrogen. Initial attempts have been made to characterise such porosity in samples of additively manufactured Ti-6Al-4V using X-ray tomography with little input from the author. As such the results as such results from these measurements will not be presented or discussed in this thesis, but rather they will be published in a co-authored paper in the near future. Additional characterisation of internal defects through neutron tomography using the DINGO instrument located at the OPAL research facility operated by the Australian Nuclear Science and Technology Organisation (ANSTO), however delays in commissioning and licencing of the instrument prevented this work from being conducted in the required timeframe of the thesis project.

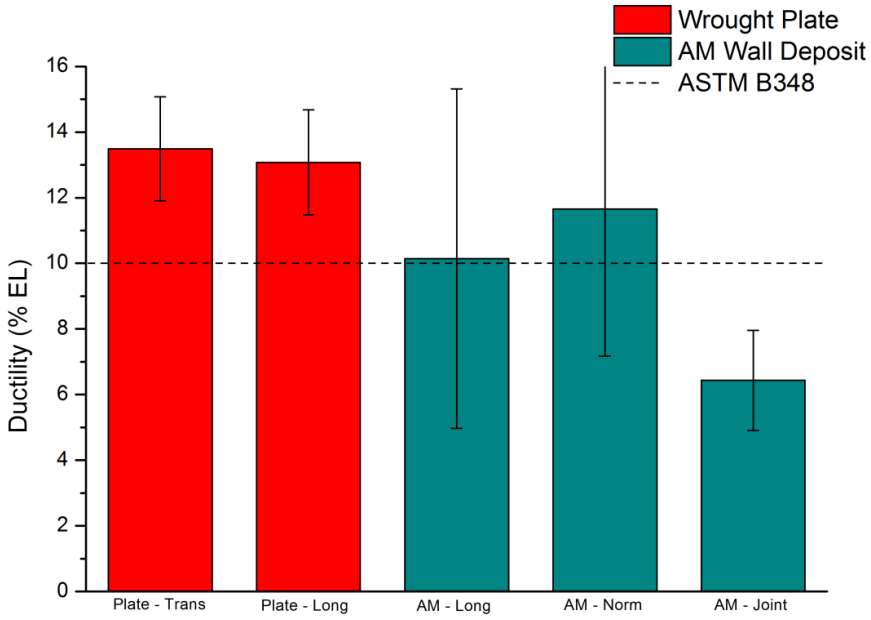

Figure 4.16 Ductility of tensile samples with minimum ASTM requirements indicated. Error bars represent the 95 % confidence interval.

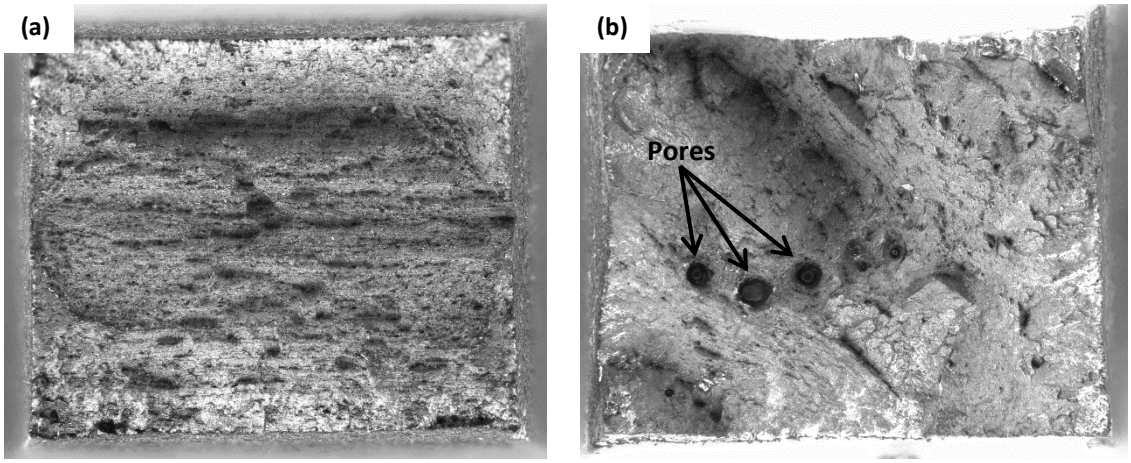

Figure 4.17 Macro image fracture surfaces from tensile test samples of (a) wrought plate and (b) additively manufactured materials. Fracture surfaces shown are approximately 6 mm wide and 5 mm high.

Mechanical properties of wrought plate, billet and GTAW-wire additively manufactured from Ti-6Al-4V were also characterised by microhardness measurements, with these results summarised in Figure 4.18. Considering all of the samples tested, it can be seen that none exceed the maximum hardness value of 365 BHN (approximately 384 HV using ASTM E140 [200]) specified in ASTM B367 for castings of titanium and titanium alloys [199]. It is evident that across all directions measured, plate materials exhibit the highest hardness, followed by billet materials with additively manufactured samples showing the lowest hardness. This is considered to originate from the significant levels of plastic deformation involved in forming of the plate section with final rolling completed below the recrystallisation temperature, giving some degree of work hardening. It is also seen that for each of the three materials tested, the XY plane (perpendicular to the longitudinal direction) exhibits the highest hardness with the XZ and YZ planes being of approximately equal hardness. Of the three materials tested, the samples of Ti-6Al-4V produced by arc-wire based additive manufacture show the greatest homogeneity in hardness with uncertainties of less than ±2 HV and less than 1 % variation between orientations. The marginally lower hardness observed in additively manufactured materials when compared to wrought plate materials suggests that there was little if any atmospheric contamination of the weld metal during deposition.

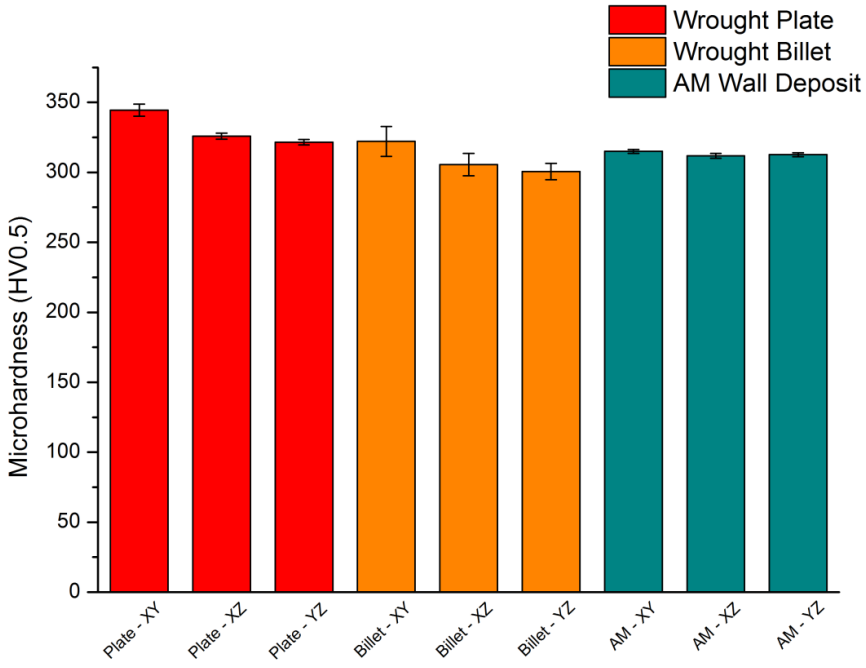

Figure 4.18 Microhardness values for plate, billet and additively manufactured Ti-6Al-4V. Error bars represent the 95 % confidence interval.

4.3.2 Charpy Testing

Charpy impact testing was used as a simple means of evaluating the fracture performance of Ti-6Al-4V produced by GTAW-wire additive manufacturing. A large degree of uncertainty exists in the results presented in Figure 4.19 due to the low resolution of absorbed energy values read from the dial indicator compared to the high impact energy of the striker. This is evident in the error bars of Figure 4.19 which allude to high relative errors of up to 33 %. Considering the results for additively manufactured samples tested in the longitudinal direction, the limited number of samples tested all showed the same absorbed energy which is why no error bars are present, however the accuracy of these measurements must be questioned when considering the ability to resolve such low energy readings on a full scale of 300 J. Nevertheless, a consistent trend is observed indicating that for all sample orientations tested, additively manufactured samples absorbed more energy in the fracture process than wrought plate samples.

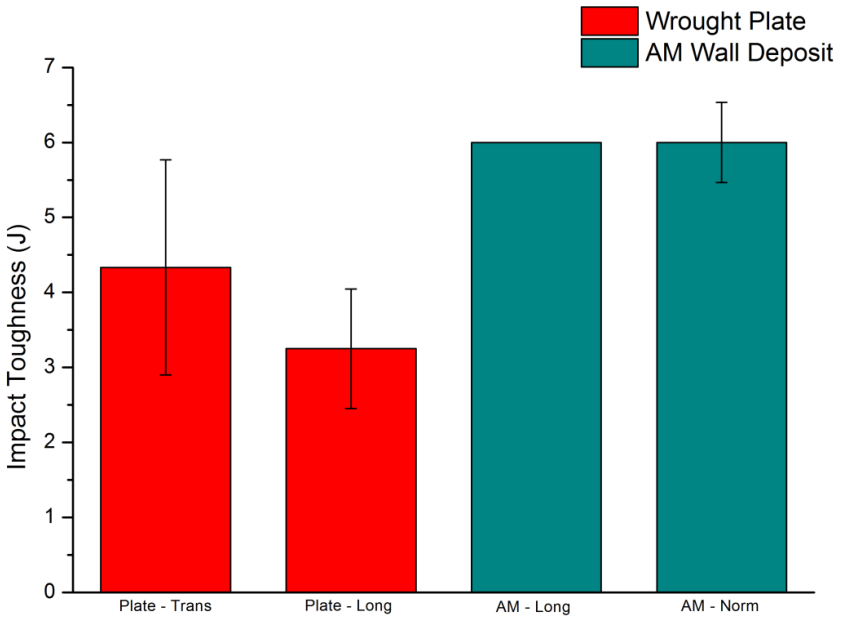

Figure 4.19 Impact energy absorbed during Charpy impact testing**.** Error bars represent the 95 % confidence interval.

More accurate results may be obtained by conducting tests on larger sample populations on an instrumented impact testing machine with higher resolution in absorbed energy. Alternatively, thicker additively manufactured deposits could be produced to allow the preparation and testing of full size 10 mm x 10 mm Charpy impact samples which would absorb greater levels of energy during fracture, and so reduce uncertainties associated with resolution of absorbed energy.

Examination of all samples after testing showed evidence of small shear lips at each side of the fracture surface with no obvious signs of lateral contraction. In general, shear lips were smaller and less pronounced in samples of wrought plate product, which also showed a relatively planar central fracture surface in which the rolling direction of the plate was obvious. In contrast, the central fracture surface in samples of addtively manufactured material were less planar being more irregular and fibrous in appearance. These initial observations were supported with scanning electron microscopy, where fracture surfaces of wrought plate samples showed evidence of ductile fracture with rough fibrous dimpled profiles typical of micro-void formation and growth as shown in Figure 4.20. The fracture surfaces of Figure 4.21 show no significant variation across the central region of the fracture surface, which appeared to have relatively consistent surface relief.

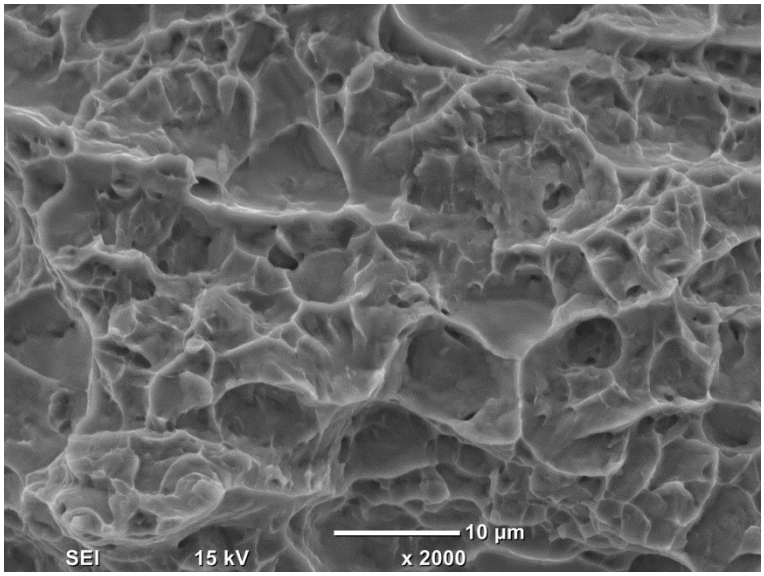

Figure 4.20 Fibrous fracture surface of Charpy impact sample from wrought plate.

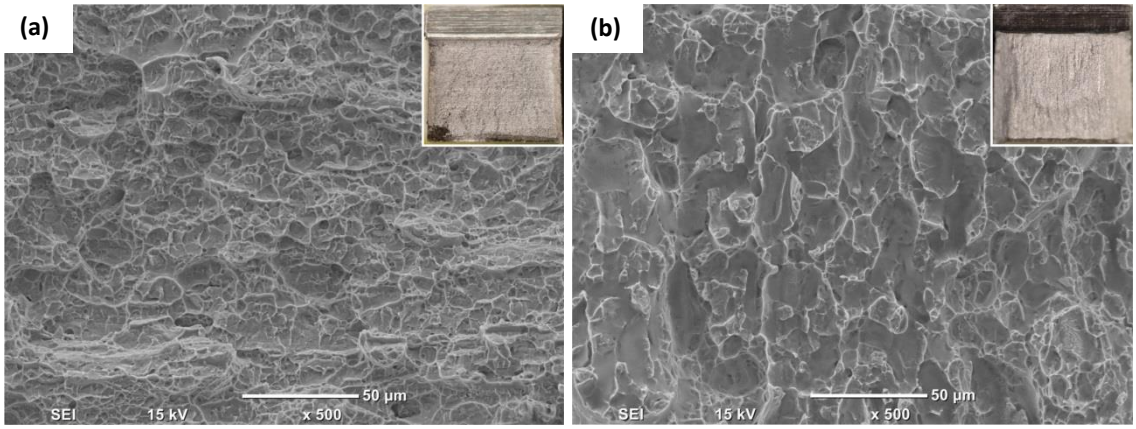

Figure 4.21 Scanning electron micrographs of fracture surfaces in Charpy impact samples from wrought plate in the (a) longitudinal and (b) transverse directions. In each case crack propagation was from top to bottom in the image, corresponding to the (a) normal and (b) transverse directions. Inset images show macro photographs of the entire fracture surface.

Fracture surfaces of additively manufactured samples showed the same evidence of ductile fracture with rough fibrous surfaces from micro-void growth and coalescence. However, the bulk fracture surface appears to be more irregular with fracture planes inclined relative to the macroscopic plane of fracture as shown in Figure 4.22. Further, there was evidence of secondary cracking as shown in Figure 4.23. This increased surface roughness and the presence of secondary cracking would absorb more energy during the fracture process and so is considered to be the source of the increased impact toughness measured in additively manufactured samples.

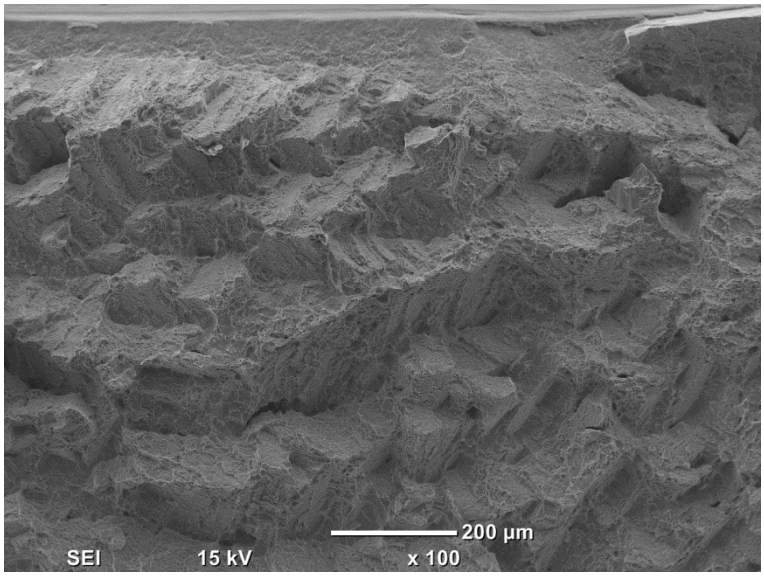

Figure 4.22 Angular fracture surface at the root of the notch feature in Charpy impact sample of additively manufactured Ti-6Al-4V with signs of secondary cracking. Crack propagation was from top to bottom in the image corresponding to the normal direction.

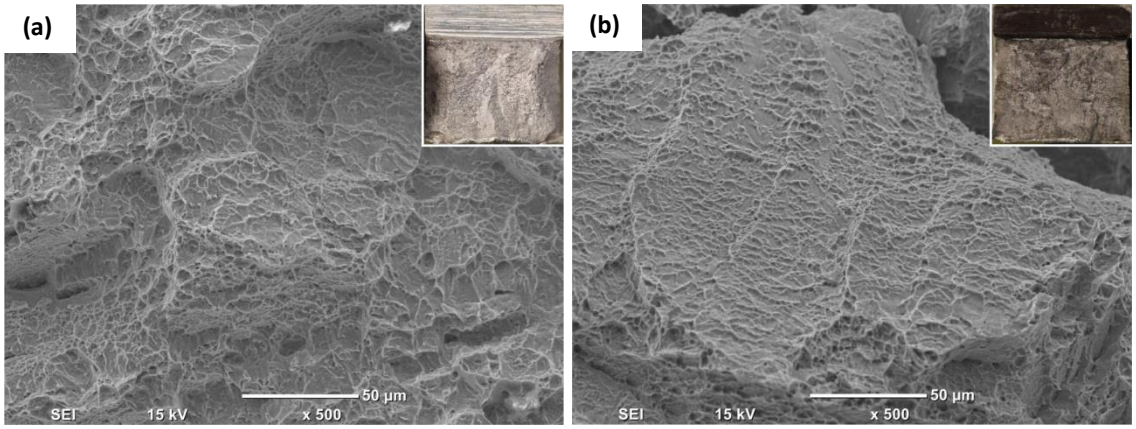

Figure 4.23 Scanning electron micrographs of fracture surfaces in Charpy impact samples from additively manufactured material in the (a) longitudinal and (b) normal directions. In each case crack propagation was from top to bottom in the image, corresponding to the (a) transverse and (b) longitudinal directions. Inset images show macro photographs of the entire fracture surface.

While Charpy impact toughness measurements are an effective means of characterising the fracture behaviour of additively manufactured Ti-6Al-4V, it is considered that a more suitable method would be the characterisation of fracture toughness using either three-point bending or compact tension testing methods.

4.3.3 Machinability

The machinability of additively manufactured Ti-6Al-4V material produced by GTAW-wire based deposition was assessed relative to conventionally processed wrought

material by consideration of machining forces during an end-milling operation. These forces were considered in terms of those acting upon the cutting tool using a conventional Cartesian coordinate system as defined in Figure 4.24. Using the measured forces in the radial (X) and feed (Z) directions, a single resultant force acting on the cutting tool in the plane of the base plate was determined with its angle of action taken relative to the feed direction. Results of machining trials are summarised in Table 4.8 which presents average force values for each full depth cut on both wrought and additively manufactured samples. Additively manufactured 'Wall_02' was used as an initial trial to validate the machining approach and CNC G-code and so force measurements for this sample are not presented. Similarly, results for additively manufactured 'Wall_07' are not presented since this build-up was of greater height than the remaining samples and was machined in a different manner.

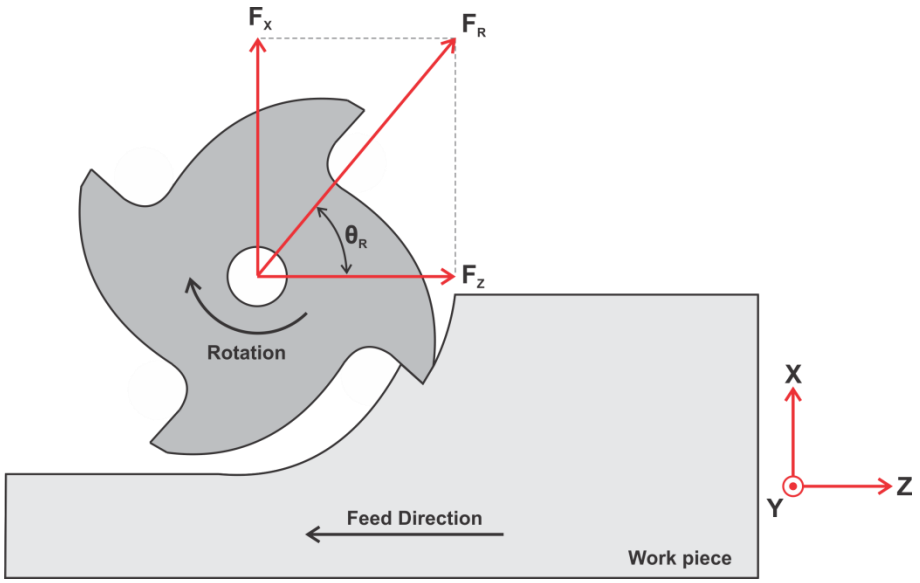

Figure 4.24 Machining forces acting on cutting tool during climb milling.

Table 4.8 Summary of average machining forces during end milling trials of wrought and additively manufactured Ti-6Al-4V.

Sample	Machining Pass	Measured Forces			Resultant	
		F_X (N)	F_Y (N)	F_Z (N)	F_R (N)	θ_R (deg)
Wrought T-fillet	Cut A	966	-406	642	1160	56.3
	Cut B	-893	-420	-645	1101	54.1
Additive Wall_03	Cut A	815	-354	546	982	56.1
	Cut B	926	-358	588	1098	57.6
Additive Wall_04	Cut A	837	-336	522	988	58.0
	Cut B	958	-338	567	1114	59.4
Additive Wall_05	Cut A	912	-337	545	1063	59.1
	Cut B	1050	-341	583	1202	60.9

In all machining trials it was observed that axial force (in the Y-direction) was negative irrespective of which side of the wall cutting was taking place, implying that the force on the cutting tool was downward toward the work-piece. This is as would be expected given the helix angle of the end mill which gives cutting in an upward manner as the tool rotates. In contrast the sign of forces in the radial and feed directions are seen to change as machining changes from one side of the wall feature to the other. Again this is logical since the direction of tool rotation remains constant so force, as measured below the sample, changes direction. This was only observed for the wrought T-fillet sample where machining was conducted on both sides of the wall. In additively manufactured samples, forces in the radial and feed directions were positive for all trials.

Plots of measured forces against time are presented in Figure 4.25 for the first of the two full depth cuts performed on each sample. In each case the same general profile is observed with the magnitude of forces increasing to a maximum value at the time when the tool becomes fully engaged with the work-piece before dropping and oscillating about a steady state value for the remainder of the machining process. Forces measured during machining of additively manufactured samples also tend to show a slight increase in magnitude immediately before the end of each machining pass, particularly in the radial and feed directions. It is thought the initial peak in cutting forces is due to the tool path used, where the initial tool entry was through a circular arc originating at right angles to the wall and the tool exit path was parallel to the wall as illustrated in Figure 4.26. To achieve sequential full depth cuts this tool path was offset by the

required amount only in the radial (X) direction. It follows then that the maximum tool engagement is during the final section of the entry arc on the trailing side of the cutting tool. At this point the radial depth of cut is equal to the full distance from the periphery of the tool to the outermost surface of the wall, producing the initial peak in cutting forces observed. The increase in machining force at the end of additively manufactured samples cannot be explained in terms of cutting tool path since this was common to all samples. Instead it is thought to stem from a variation in stiffness due to the increased wall thickness present at the start of the weld bead as described in Chapter 3. This is the result of non-steady state operating conditions where weld travel speed was accelerating and so is below its nominal constant value, yielding a more broad molten pool and hence thicker wall than that produced once steady state conditions have been achieved.

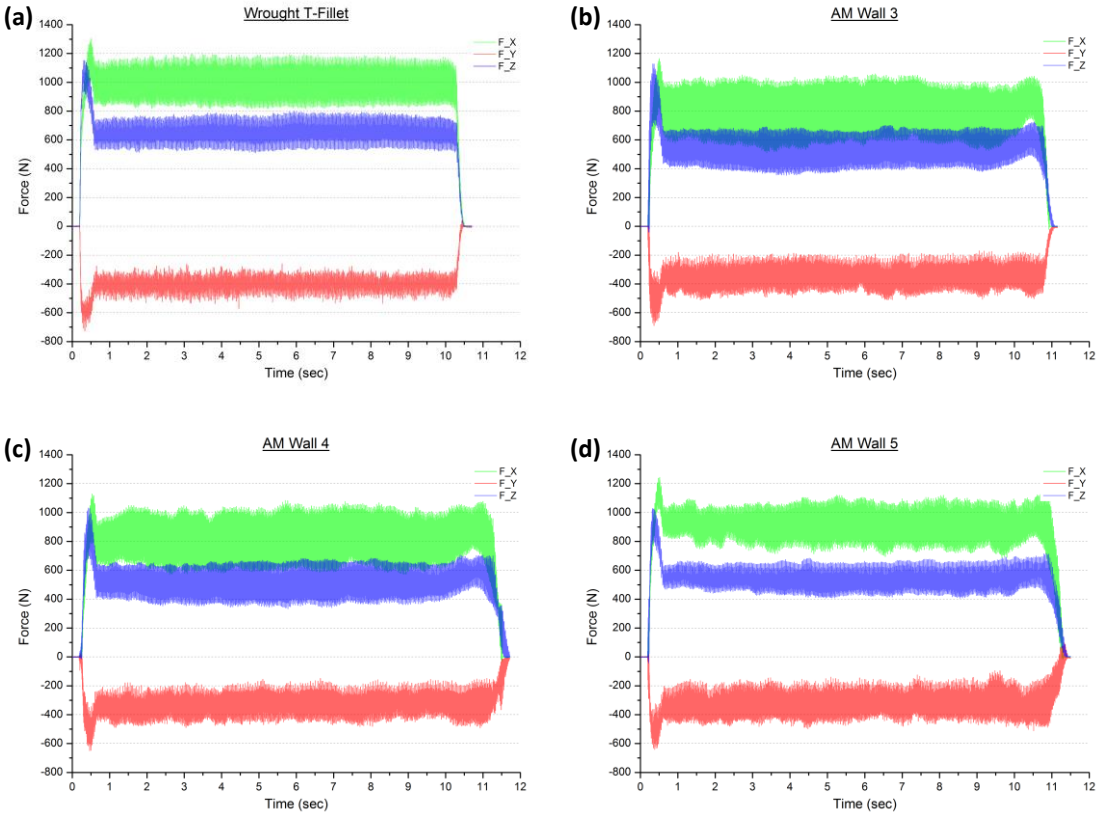

Figure 4.25 Cutting forces in the radial (X), axial (Y) and feed (Z) directions presented as a function of time for (a) wrought T-fillet and (b) - (d) additively manufactured samples.

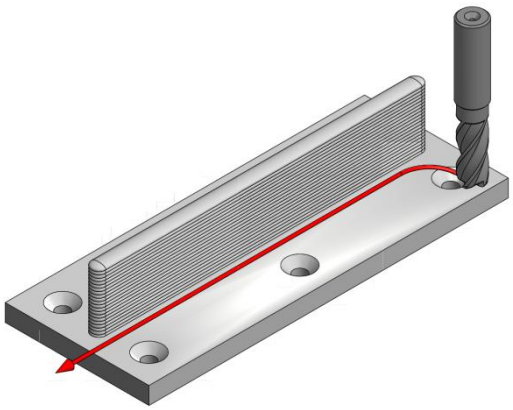

Figure 4.26 Schematic illustration of tool path used for milling trials.

The oscillations or fluctuations in cutting force noted above are more clearly illustrated in Figure 4.27 where cutting force is plotted as a function of tool rotation. From this it is clear that the primary source for the oscillation in cutting force is the interrupted cutting characteristic of the milling process where engagement of individual cutting edges varies with tool rotation. Close observation of these oscillations reveals a periodic ramp like increase of cutting forces repeated every four peaks. Since the end mill used featured four cutting edges, each peak in cutting force corresponds to the maximum engagement of one single cutting edge. It is clear then that the periodic increase in cutting force is an indication of eccentricity in the cutting tool, resulting in non-uniform engagement of the four cutting edges.

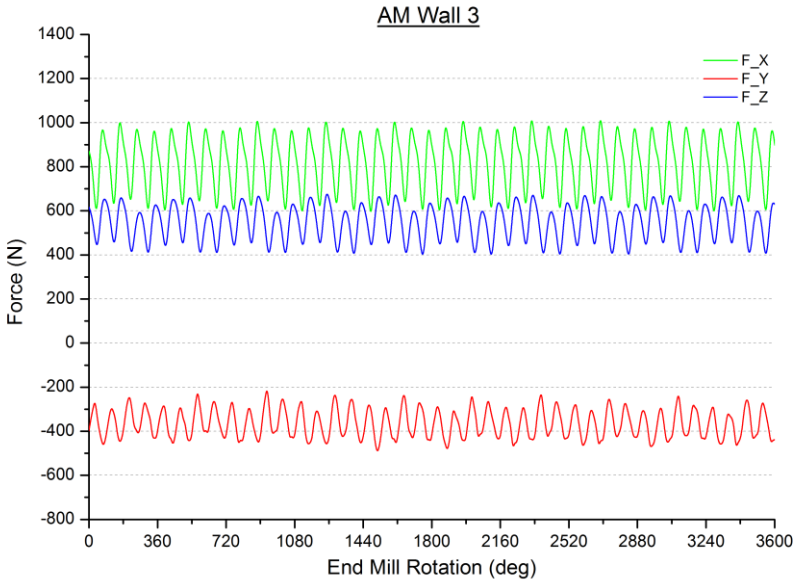

Figure 4.27 Cutting forces in the radial (X), axial (Y) and feed (Z) directions as a function of tool rotation for milling of additively manufactured 'Wall_03'.

From the plots in Figure 4.25 it can be seen that the range of these oscillations tends to be greater in samples of additively manufactured Ti-6Al-4V suggesting a greater variation in cutting edge engagement during the machining process. The most likely origin of this variation is wall deflection during machining. While efforts were made to match the geometry of the T-fillet to that of the additively manufactured samples, the overall height of the wall section in the fabricated sample was approximately 10mm higher. Since machining trials of all samples were conducted using the same axial depth of cut, the base section of the T-fillet sample remained approximately 12mm in thickness while the equivalent region in additively manufactured samples was reduced to below 6 mm. It follows then that the overall stiffness of the T-fillet sample was greater than that of the additively manufactured samples, giving greater resistance to deflection under the influence of cutting forces and hence less variation in cutting edge engagement. This is verified by the surface profile measurements presented in Figure 4.28 where the final surface of the additively manufactured sample shows a comparatively larger variation in surface profile. The corresponding average roughness (Ra) values were 0.7 μm and 0.9 μm for the wrought T-fillet and additively manufactured samples respectively. The differences in base plate geometry between samples also required different clamping arrangements during machining which may have further contributed to variations in stiffness. Such variations could be eliminated in future studies by using samples with more closely matched geometry and using 'jacking bolts' or some other equivalent to support the wall feature and hence reduce deflection.

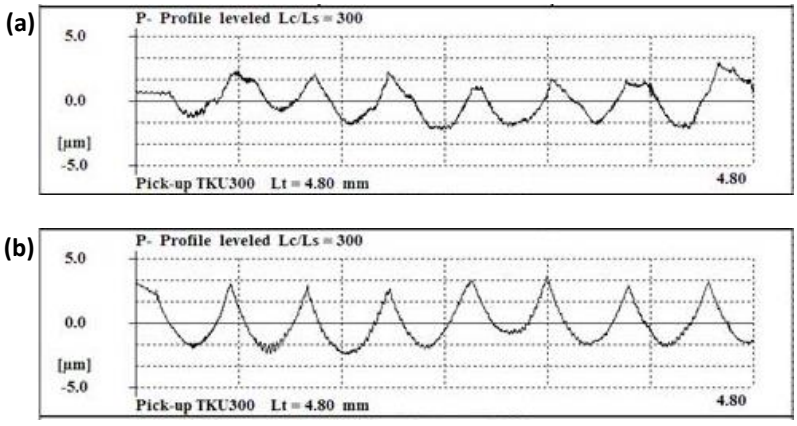

Figure 4.28 Surface profile measurements (unfiltered and levelled) of the machined surface in (a) wrought T-fillet and (b) additively manufactured samples.

Comparing forces from the two full depth cuts performed on each sample, no appreciable change in cutting force is observed for the wrought T-fillet sample. In

contrast, additively manufactured samples show an average increase of 14 % in the radial direction and 8 % in the feed direction with negligible change in the axial direction. Tool wear is not considered to contribute to these increases in cutting force since the effects were only noted in the radial and feed directions and didn't increase continually from one sample to the next despite the same cutting tool being used for all samples. It is also unlikely that the increase in cutting force is due to different radial depths of cut with initial skimming passes used to ensure planar cutting surfaces were produced prior to completing full depth cuts. One possible explanation is work hardening of the material adjacent to the cutting zone during cut A, requiring increased cutting force during cut B which was performed on the same side of the additively manufactured build-up. This argument is supported by the lack of change in machining forces in the wrought T-fillet sample where both full depth cuts were performed on opposite sides of the wall section. However, it is considered that the use of climb milling would have reduced the likelihood of such extensive work hardening. The most likely cause for the observed increase in force is thought to be changes in sample geometry due to material removal. Due to the differences in wall geometry between the wrought T-fillet and additively manufactured samples, the proportion of material removed in each machining pass is far greater in additively manufactured samples, producing a more noticeable change in the sample's response to machining. This is shown in Figure 4.29 which compares the radial force for sequential full depth cuts in both wrought and additively manufactured samples.

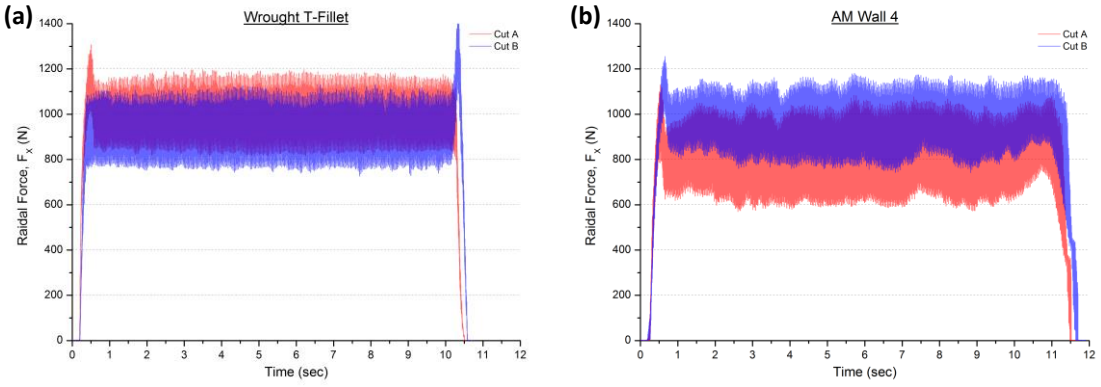

Figure 4.29 Comparison of radial cutting force between sequential full depth cuts for (a) wrought T-fillet and (b) GTAW-wire additively manufactured samples.

Another observation from analysis of cutting force data is that fluctuations in force values are more uniform in the wrought T-fillet sample, with additively manufactured

samples showing variation along the length of the machining pass. Moreover, equivalent variations are evident in both the first and second cuts as clearly seen in Figure 4.29b. This suggests that the machining behaviour of the additively manufactured samples is not uniform along the length of the sample. The two most likely causes for such inhomogeneity are thought to be variations in mechanical properties or non-uniform wall profile in the as-deposited condition giving variable wall thickness, and hence stiffness, since only one side of the build-up was machined to a smooth profile.

From the data presented in Table 4.8 it can be seen that the radial force acting on the cutting tool is approximately 13 % lower for additively manufactured samples during the first machining pass. However, due to the increase in cutting forces previously described, the radial force is on average 10 % greater in the additively manufactured samples during the second machining pass. A similar observation can be made in terms of cutting force in the feed direction where additively manufactured samples show 19 % lower forces during the first machining pass and only 11 % lower during the second machining pass. Combining the feed and radial components into a single resultant force acting in the plane of the base plate, it is seen that in general additively manufactured samples required less cutting force than the wrought T-fillet sample during the machining operations. This is best illustrated in Figure 4.30 which clearly shows a reduced magnitude of resultant force in additively manufactured Ti-6Al-4V with the angle of action approximately equal. It is also apparent that the axial force is considerably lower for machining samples of additively manufactured Ti-6Al-4V with a difference of between 17 % and 21 %.

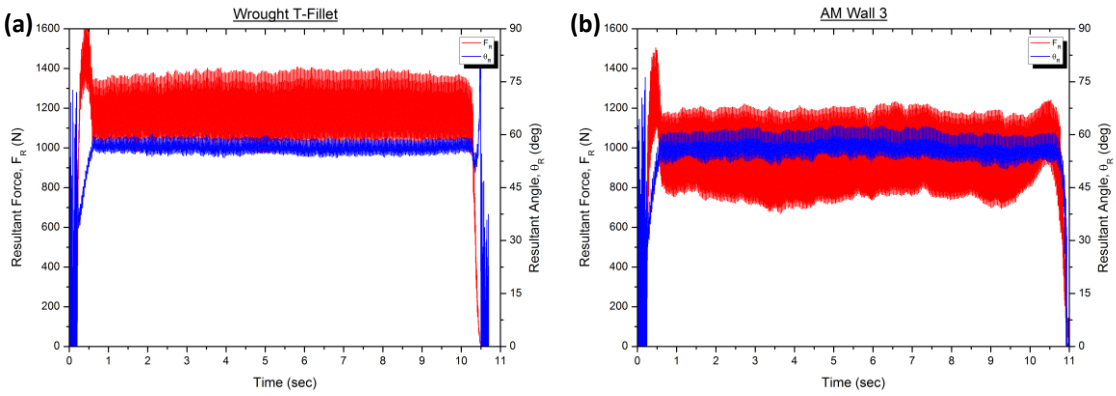

Figure 4.30 Resultant cutting force magnitude and angle of action in the plane of the base plate for (a) wrought T-fillet and (b) GTAW-wire additively manufactured samples.

The overall reduction in cutting force when machining Ti-6Al-4V produced by GTAW-wire based additive manufacture compared to conventionally processed material is readily explained by consideration of the mechanical properties of each. As detailed in section 4.3.1 of this chapter, both the yield and ultimate tensile strength of the additively manufactured material is below that of the wrought product, as is the hardness. With the relationship between mechanical properties and cutting forces during machining of metals being clearly understood, the result of reduced cutting force in additively manufactured Ti-6Al-4V is not unexpected.

4.3.4 Drill Life Testing

Initial qualitative assessment of drill performance showed little difference between samples of wrought and additively manufactured Ti-6Al-4V with no perceivable change in process acoustics, such as a loud screech often used to indicate tool life [201], or premature tool failures. In general, force measurements during drilling were as would be expected; with force in the normal (Y) direction rising to some steady state value while force in the transverse (X) and longitudinal (Z) directions oscillated about zero as shown in Figures 4.31. The periodic natures of these oscillations, which correspond to rotation of the cutting edges on the drill, are shown more clearly in Figure 4.32.

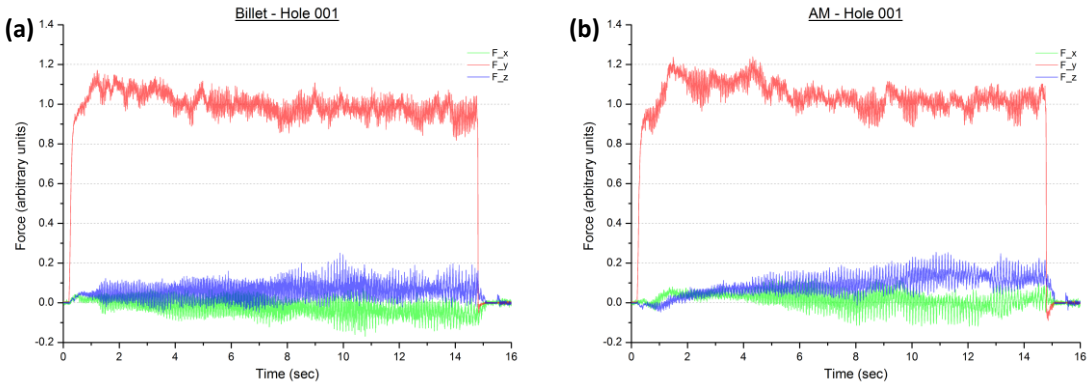

Figure 4.31 Measured force values during drilling operations in samples of (a) wrought billet and (b) additively manufactured Ti-6Al-4V.

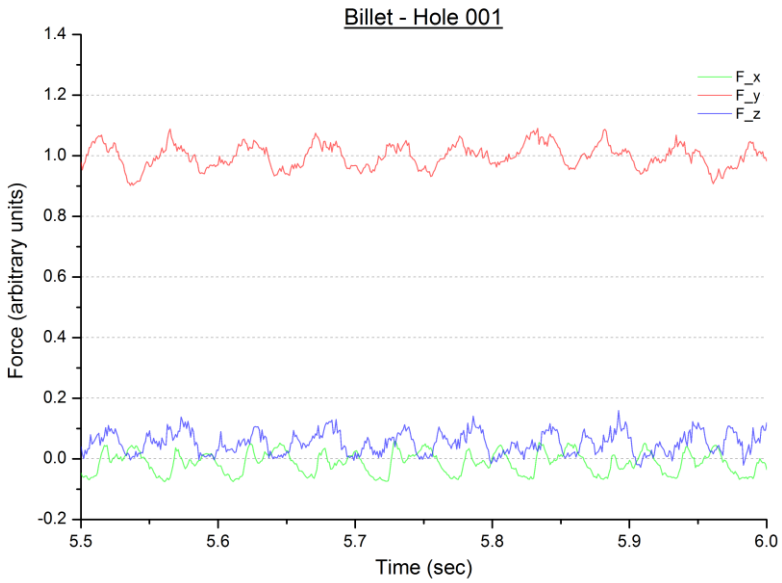

Figure 4.32 Oscillations in measured force values during drilling of wrought billet.

Considering the profile of the normal force during the drilling operation there appear to be five distinct zones as defined in Figure 4.33. Zone I sees a sharp increase in force with little 'noise' in measured force data and corresponds to the initial contact between the drill tip and the work-piece. This is followed by zone II where force continues to increase but at a lesser rate and with more noise in the measurements. This stage corresponds to the progressive engagement of the drill cutting edges, which produce the oscillations in measured force. Zone III sees a short period of approximately constant force which begins once the cutting edges of the drill are fully engaged and so the hole is at full diameter. Normal force is then seen to drop slightly to a lower steady state value for the remainder of the drilling operation, termed zone IV. Finally, zone V sees a rapid drop in force as the drilling operation has achieved full depth and the drill is retracted from the hole. During this retraction, the normal force becomes slightly negative as the swarf laden drill tip is pulled from the top of the hole.

In general, zone III was more distinct in force data from the additively manufactured sample, with the transition between zones III and IV indistinguishable for some holes in the wrought billet sample. For a homogenous metal it is thought that zone III should not exist and force should reach and maintain a steady state value from the time when full engagement of the cutting edges is achieved. For the case of the additively manufactured sample, the higher force in zone III is thought to originate from inhomogeneity in mechanical properties of the deposit, with the top layer having been

subjected to far fewer thermal cycles during deposition than the material in the preceding layers and so exhibiting different strength or hardness. More comprehensive analysis of variation in hardness and microstructure across a full cross-section in the XY plane of this sample would be needed to verify this hypothesis.

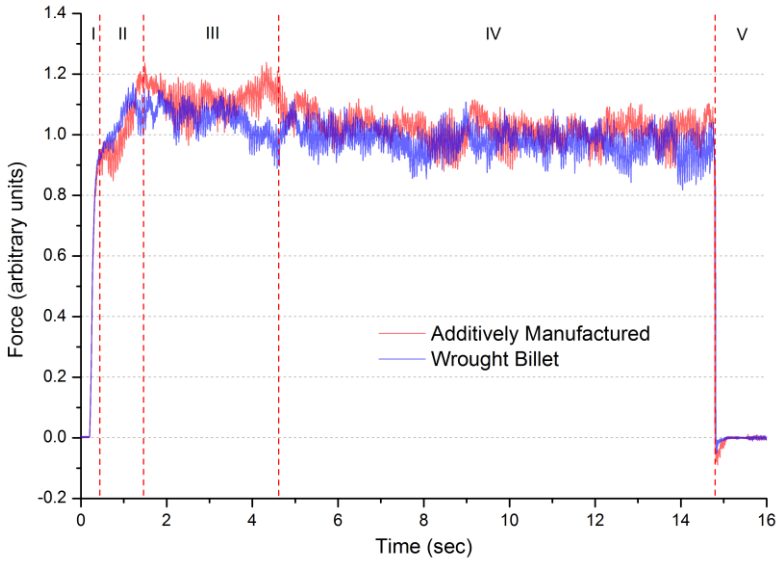

Figure 4.33 Defined zones with respect to force in the normal direction during drilling.

Considering the variation in force as a function of the number of holes drilled, shown in Figure 4.34, it is evident that forces in both the transverse and longitudinal directions are scattered about zero. In contrast, it is apparent that at all times, the drilling of additively manufactured Ti-6Al-4V required between 10 % and 15 % additional force in the normal direction to maintain the constant feed rate of 0.09 mm/rev. It is considered that the primary reason for this increased force is the higher hardness of the additively manufactured material, clearly shown in Figure 4.35. From this it can be seen that the Ti-6Al-4V produced by GTAW-wire based additive manufacture has on average 8 % higher hardness than the wrought billet equivalent. As hardness can be related to mechanical strength, the difference in normal force during drilling may also correlate to differing yield and ultimate tensile strengths between the two materials, however tensile testing of samples prepared from the billet material would need to be performed to verify this. It is also worth noting that the hardness values for this additively manufactured pad are greater than those of the additively manufactured wall features used in mechanical testing trials, while the hardness of the billet sample is less than that of the wrought plate material. Firstly for the additively manufactured samples, the

origin of these differences is most likely the different process parameters used as well as the differing arrangements of sequential layers and the increased residual stress in the pad welded structure resulting from increased thermal cycling and deposition of a greater volume of material in the pad structure. In the case of the wrought products, it is clear that the plate section would have been subjected to far greater amounts of thermomechanical deformation and so would be expected to show increased hardness compared to the billet material due to work hardening.

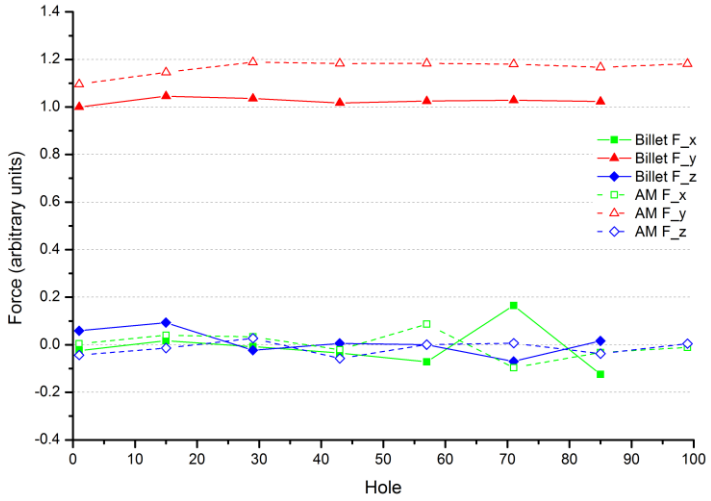

Figure 4.34 Average force during drilling operations as a function of number of holes drilled for both wrought billet and additively manufactured samples.

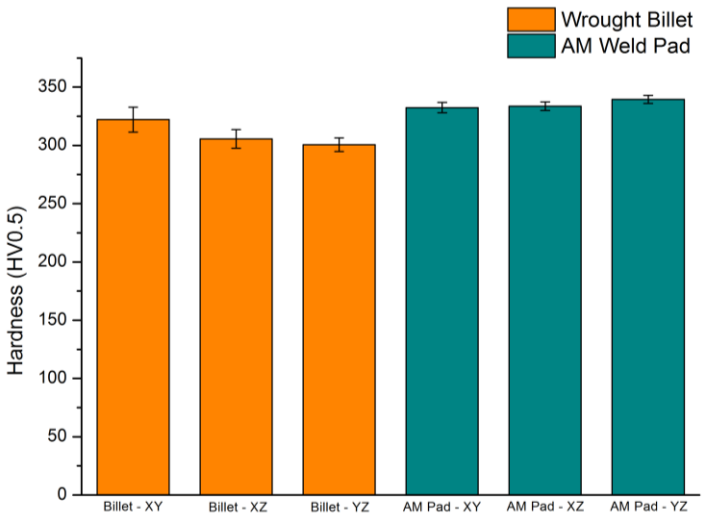

Figure 4.35 Average microhardness of both wrought billet and additively manufactured samples as measured in three planes. Error bars represent the 95 % confidence interval.

Optical microscopy of sectioned surfaces prepared from both wrought billet and additively manufactured samples near to the hole edges showed microstructures

equivalent to the bulk sample with a narrow region of deformed material directly adjacent to the drilled surface. This deformation layer was most evident in the XZ plane, perpendicular to the axis of the hole as shown in Figure 4.36. From this it can be seen that the deformation layer is more extensive in samples of additively manufactured material, being approximately twice the thickness of that seen in the wrought billet sample. This suggests that the additively manufactured material has comparatively low strength and higher ductility, a result which is contrary to observations of drilling force and hardness. Additionally, it appears there is a small degree of stabilisation of the α-Ti phase in the billet sample directly adjacent to the cut edge, commonly referred to as 'alpha case'. Such stabilisation is not evident in the additively manufactured sample, however this may be because the grain structure at the hole edge is difficult to resolve due to the severe localised plastic deformation.

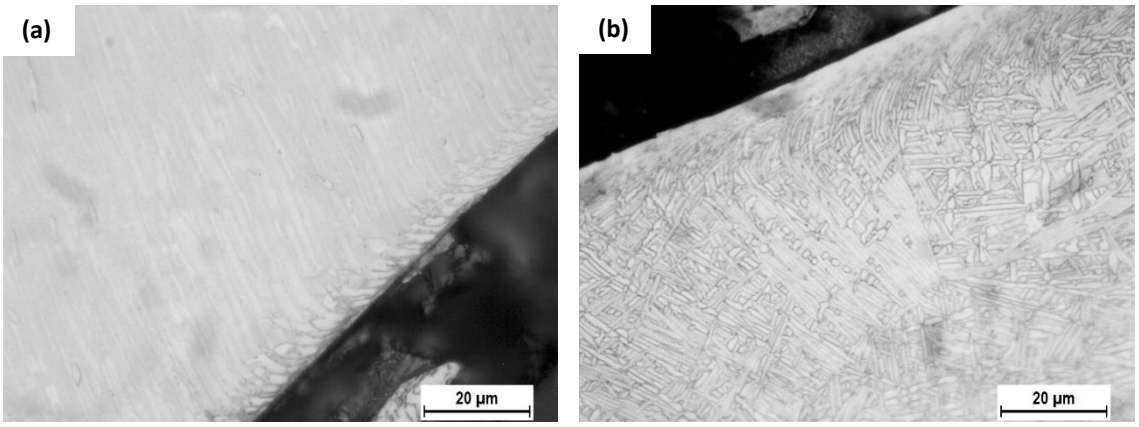

Figure 4.36 Optical micrographs showing deformation layers adjacent to the drill hole edge in (a) wrought billet and (b) additively manufactured samples.

Qualitative examination of swarf from drilling operations by stereomicroscopy shows a typical 'curled ribbon' morphology from both materials, with shorter, more broken segments also produced from accumulation and compaction in the drill flutes where swarf ejection was compromised. Closer inspection revealed rougher surface finish in swarf from drilling of the wrought billet, with a more pronounced 'saw-tooth' type profile of burrs evident at the periphery, as seen in the higher magnification images presented in Figure 4.37. These figures also appear to show fracturing in some ribbon sections. While this may be due to lower ductility and higher strength, such breaks in the swarf could just as easily occur during ejection should there be an obstruction or restriction of some form in the flutes. Optical microscopy of swarf showed distinct deformation shear bands within a continuous chip in both wrought billet and additively

manufactured samples, as illustrated in Figure 4.38. Lamellar chip formation of this type is typical for materials with high ductility and high strength, particularly where cutting speeds are also high [202]. While the spacing of these shear bands is approximately equal in both materials, the extent of shear banding is far greater in the billet material where they are seen to have increased penetration as well as void formation. This would suggest chip formation was almost segmented in nature and so allude to a difference in mechanical properties of each material since all influential cutting parameters such as rake angle and cutting speed were constant for all trials.

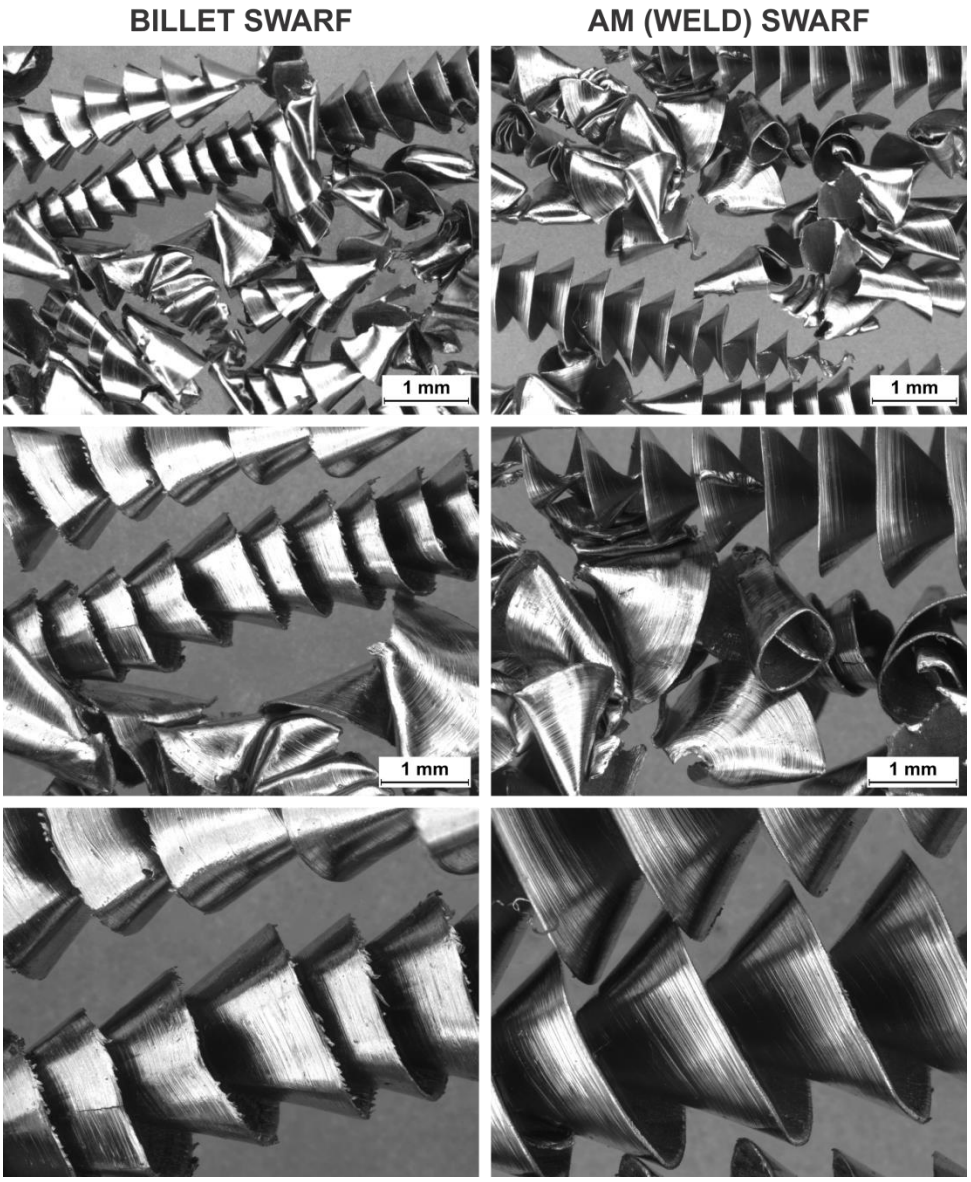

Figure 4.37 Macro images of swarf collected from drilling of left: wrought billet and right: additively manufactured Ti-6Al-4V. Magnification increases from top to bottom.

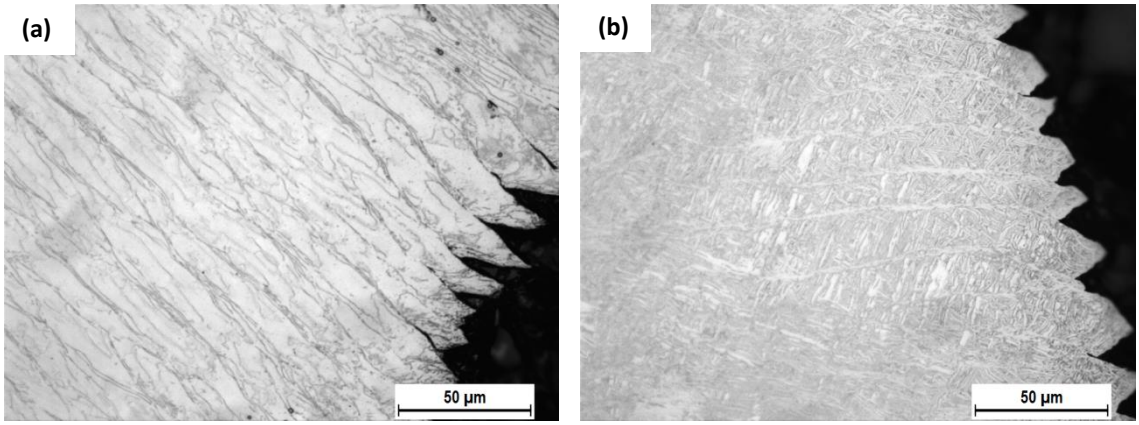

Figure 4.38 Optical micrographs showing lamellar chip formation in swarf from drilling of (a) wrought billet and (b) additively manufactured Ti-6Al-4V.

Drilling performance was also assessed through observations of tool wear through stereo-microscopy as shown in Figure 4.39. The geometry of the used drills was compared to that of an unused equivalent to assess wear. While neither drill showed significant loss of profile in the cutting edges, both did appear to show wear on the chisel point and a loss of the TiAlN coating in areas of the cone immediately behind the cutting edges. This loss of coating increased toward the periphery of the drill where cutting speeds were higher. From these images it is apparent that there was a greater amount of wear on the margin of the drill used in the wrought billet material, with signs of tool chipping and build-up of work-piece material. While such wear was not observed on the drill used in the additively manufactured material, there is still evidence of built-up titanium on the margin towards the drill point. The observation of increased wear on that drill used for wrought billet Ti-6Al-4V would again suggest that this material has higher hardness which is contrary to the observations of cutting force and hardness.

While examining the drills used to assess general machinability, it was noticed that all drills supplied were not identical despite being the same item number from the supplier. From the macro images presented in Figure 4.39 it is clear that the flute geometry on the drill used for wrought billet Ti-6Al-4V differs from that of the drill used in additively manufactured material and the reference drill. While the essential cutting geometry such as included point angle, helix angle, lip clearance angle and body clearance are the same across all drills, the difference in flute profiles will significantly modify the removal of swarf from the drill hole which in turn will effect tool wear and swarf formation. The altered flute profiles will also change the stiffness of the drill body which may

contribute to the differences in cutting forces observed. As such, it is considered that all observations and results with respect to drilling trials cannot be reasonably assessed or explained due to the variations in drills supplied. These trials would need to be repeated using drills of identical profile and would be best complemented by mechanical testing of samples from billet material to have definitive values for yield strength, ultimate tensile strength and ductility to compare to those of the additively manufactured materials.

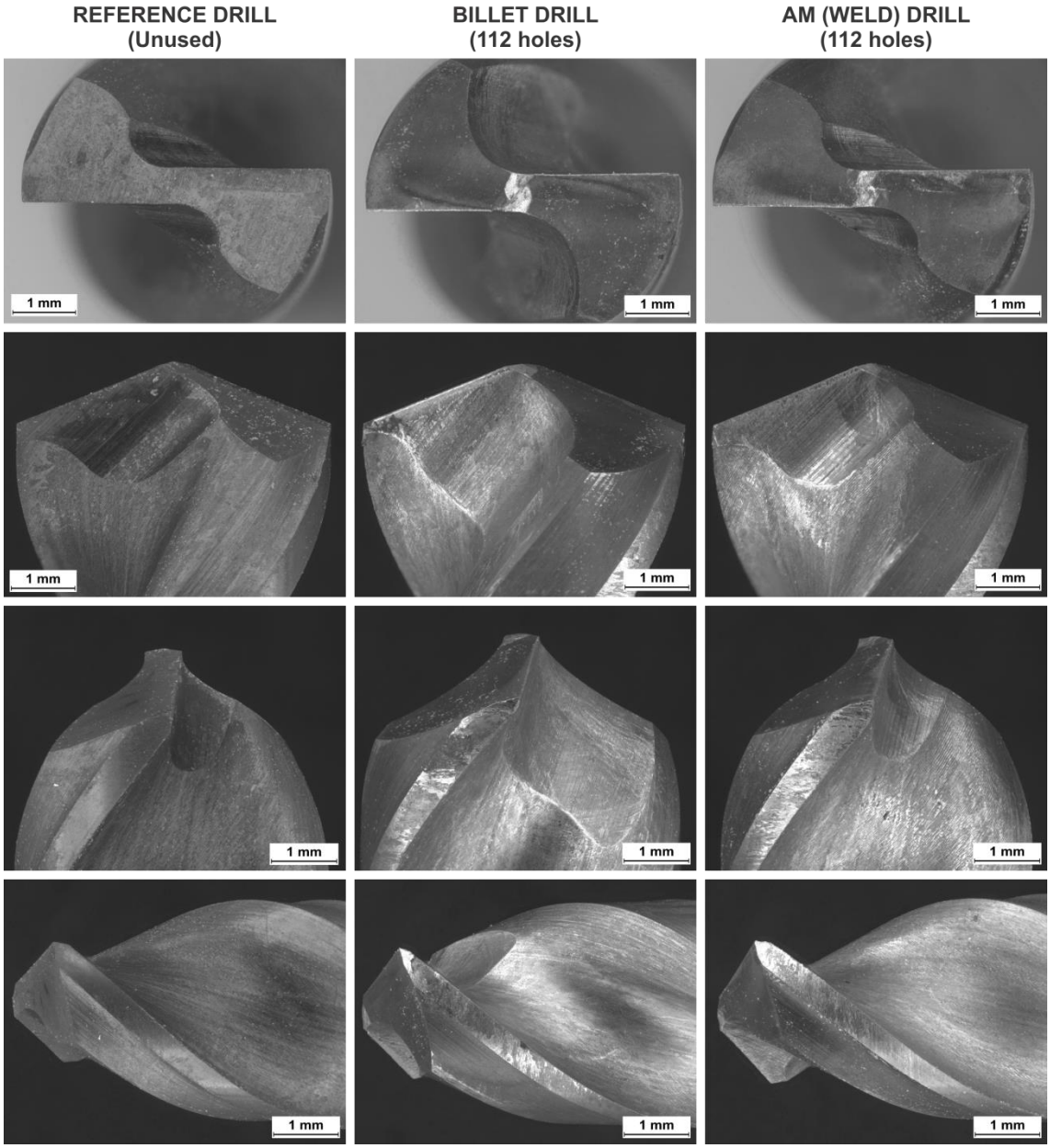

Figure 4.39 Macro images of drills after machining trials used to assess tool wear.

4.4 Conclusions

Mechanical testing of Ti-6Al-4V produced by GTAW-wire based additive manufacturing produced results that are in close agreement with published data from literature for other additive layer manufacturing processes. In comparison to commercially sourced wrought plate product, the additively manufactured material was seen to exhibit greater homogeneity in mechanical properties, particularly the modulus of elasticity. Measured yield strengths in samples produced by additive manufacturing were less than those for the wrought product and failed to meet the minimum requirements set out in relevant industry standards by approximately 3 %. While the ultimate tensile strength of the additively manufactured material was below that of the wrought product, it was seen to exceed the minimum requirements set out in the same industry standards. It is thought both yield and ultimate tensile strength could be increased by further optimisation of the deposition process as well as through the use of post-weld heat and mechanical treatments. Alternatively, designs of components to be made by this method could be modified to compensate for this reduced strength. Ductility of the additively manufactured material exceeded the minimum requirement of 10 % in both directions measured and hardness values were well below the maximum allowable limits for Ti-6Al-4V. Charpy impact testing of sub-size samples was conducted, revealing that samples produced from additively manufactured material had superior impact toughness. Examination of fracture surfaces suggested a ductile fracture mechanism with evidence of secondary cracking also observed.

Investigations relating to machinability of the materials showed that Ti-6Al-4V structures produced by additive manufacturing required lower cutting force in all three principal directions compared to an equivalent structure fabricated from wrought plate sections. An increase in the required cutting force was observed for both the radial and feed between successive machining passes in additively manufactured samples. No such increase was observed for any direction in the wrought T-fillet sample or in the axial direction for additively manufactured samples. Variation in cutting force was observed to be greater in samples produced by additive manufacture and was attributed to comparatively lower sample stiffness. This was verified through measurements of surface roughness where ‘chatter’ was found to be less in the wrought T-fillet sample.

Measurements of machinability performed by drilling trials were inconclusive. While cutting force and hardness of additively manufactured material were higher than the wrought billet equivalent, observations of deformed microstructure, swarf and tool wear suggested the wrought billet material was more difficult to drill. These inconsistent observations are thought to stem from the differing geometry of drills used to perform the trials and as such it is felt that such measurements need to be performed again.

Overall, the assessment of mechanical properties and machinability of Ti-6Al-4V produced by GTAW-wire based additive manufacture is favourable with behaviour similar to commercially sourced wrought material. Future studies should lead to an improvement in mechanical properties through process optimisation and also further characterise material properties through assessment of fracture and fatigue behaviour.

CHAPTER 5 – RESIDUAL STRESS

5.1 Introduction

Residual stresses are those stresses which remain within a solid body, or component, after all externally applied factors such as mechanical loadings and thermal gradients are removed. These stresses are commonly generated during virtually all manufacturing processes, as well as in service, and can be both detrimental and beneficial in terms of the mechanical and physical behaviour of the component. Understanding the origins of residual stress during a manufacturing process, such as the GTAW-wire based additive manufacture of Ti-6Al-4V, and how these stresses may be influenced by processing parameters, is critical in assessing the viability of the process for the manufacture of any given component.

The aim of the present body of work was to characterise residual stresses on the macro scale within representative components of Ti-6Al-4V produced through the GTAW-wire based additive manufacturing technique. Of particular interest were the effects of welding parameters, such as specific deposition energy and pulse arc current, on the residual stresses in the steady state build region of these components. Additional work was aimed at assessing the effectiveness of post-weld heat treatments (PWHT) on relieving residual stresses in these representative components. Results for additively manufactured samples were also compared to measurements taken from equivalent components produced by conventional subtractive manufacturing and welded fabrication processes.

5.1.1 Residual Stresses Definitions

In essence, residual stresses are the result of non-uniform plastic deformations across the component, which require the surrounding material to deform elastically for dimensional continuity to be preserved [203]. Deformation of this kind is a key feature in many manufacturing processes such as rolling, forging, bending and extrusion where force is used to form material into a desired profile. Non-uniform deformation may also occur in service through applied external loadings. Residual stresses may also arise through surface modifications both during manufacture and in service, with common causes including grinding, peening and carburising as well as corrosion or oxidation. One of the major sources of residual stresses is changes in material phase or density due

to large localised thermal gradients such as those found in welding, casting and heat treatment processes.

It is well understood that residual stresses have a profound effect on the performance of engineering components in service. In general, tensile residual stresses are considered undesirable since they act to promote fracture by contributing to crack initiation and accelerating crack growth. Additionally, tensile residual stresses typically reduce fatigue performance, degrade materials through stress corrosion and can be related to several cracking phenomena in welds such as solidification hot cracking and hydrogen assisted cold cracking. While compressive residual stresses may be beneficial in retarding crack initiation and crack growth, particularly in fatigue applications, it has been shown that high levels of compressive residual stress can reduce the buckling strength of engineering structures [204, 205]. In addition to the effects on mechanical behaviour, residual stresses often lead to physical distortion of components causing them to exceed dimensional tolerances or be subjected to abnormal loadings during installation and service.

Residual stresses are commonly categorised according to the range or length scale over which they act, as shown in Figure 5.1. While this figure only shows stress variation in a single direction, it must be understood that residual stresses may be present in all three dimensions within a solid body, often generating complex tri-axial stress states. Type I stresses, σ^{I}, are those which act over the length scale of many grains and are in effect the average stress at a particular location [206]. Due to the length range over which they are considered, these Type I stresses are also commonly referred to as ‘macro stresses’. Type II stresses, σ^{II}, are intergranular stresses that extend over the length of a single grain. These stresses vary from one grain to the next as a function of the different crystallographic orientations which, due to anisotropy, have different slip and elastic response behaviour [206]. These variations also arise in multi-phase materials where the crystal structure and mechanical behaviour of the various phases, and hence grains, differ within a single polycrystalline solid. Type III stresses, σ^{III}, are intragranular, acting over the scale of several atomic spacing within a single grain and are related to stress fields around atomic defects, dislocations and grain boundaries [203, 206]. Both intergranular and intragranular stresses may be referred to as ‘micro stresses’. When considering residual stresses in engineering structures and components, it is most often

the Type I macro stresses that are of the greatest importance since they have the greatest influence on the fracture, fatigue and stress corrosion behaviour [203].

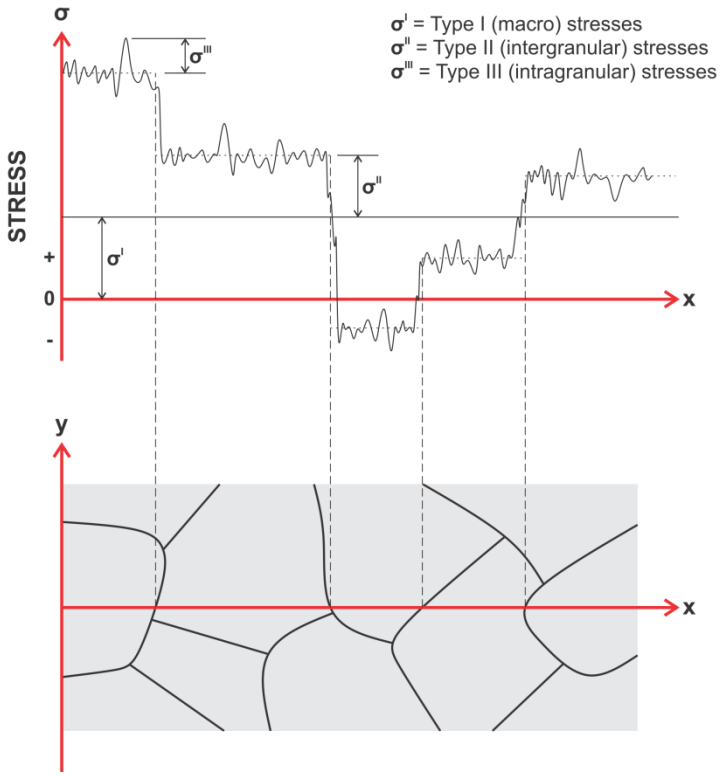

Figure 5.1 Schematic illustration of residual stresses in a polycrystalline solid categorised according to the length scale over which they act. Adapted from Holden [206].

5.1.2 Residual Stresses and Fusion Welding

Fusion welding, due to the nature of the process, inevitably produces residual stresses within both the weld metal and surrounding parent material, which can then have a significant effect on the performance of the weldment. The origin of residual stresses that form during fusion welding processes is the differential thermal contraction of material in the weld zone on cooling. The process of residual stress formation during simple bead-on-plate or butt welding is commonly described using a three-bar analogy, as shown in Figure 5.2. In this, three identical metallic bars are held together by two rigid blocks, all of which are initially at ambient temperature. Heating the central bar would ordinarily give an increase in length due to thermal expansion; however the constraints imposed by the adjacent unheated bars restrict this expansion and place the central bar into compression with the adjacent bars being stressed in a tensile manner. Increasing the temperature of the central bar increases the thermally induced compressive stresses, but also reduces the compressive yield strength of the material,

causing the central bar to plastically deform. Once the heat source is removed the central bar cools, but is restricted in its thermal contraction by the adjacent bars causing the previous compressive stresses to be overcome by tensile stresses. While it is possible for the central bar to yield and deform plastically to relieve some of these tensile stresses, the yield strength of the metal increases on cooling and so once thermal equilibrium is achieved a high level of tensile residual stress will exist in the central bar. To satisfy the conditions for static equilibrium, the adjacent bars will both be in compression with stresses one-half the magnitude of the tensile stress in the central bar [115].

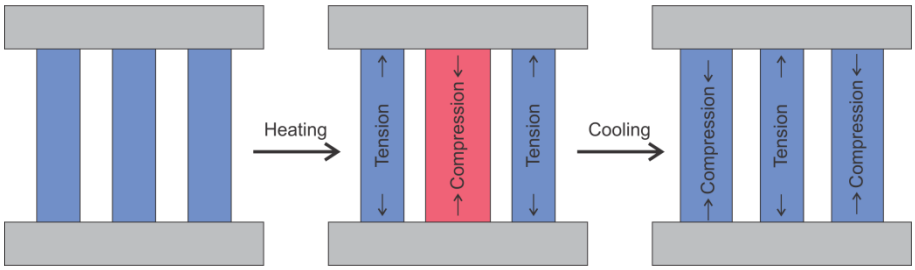

Figure 5.2 Three-bar analogy to illustrate residual stress formation during simple bead-on-plate and butt welding. Adapted from Kou [115]

In this analogy the central bar represents the heated region of the weld bead while the side bars and rigid joining blocks represent the surrounding parent material and the constraint it provides. This is a somewhat simplified scenario since during fusion welding some portion of the weld area is molten and as such can't support any stress, be it tensile or compressive. The phase change of this molten material from liquid to solid on cooling introduces further volume changes, and hence stresses, on top of those from thermal contraction and solid state phase transformations. The addition of filler material during the welding process will also influence the development of residual stresses since it represents an additional volume of material which will transform and shrink on cooling. Figure 5.3 shows the distribution of transverse and longitudinal residual stresses in the plane of the work-piece resulting from a single pass butt weld. The magnitude and distribution of residual stresses that result from fusion welding have been extensively studied and are understood to be influenced by numerous material and process factors including yield strength, coefficient of thermal expansion, thermal conductivity, thermally induced phase transformations, heat input and constraint of the weldment [207].

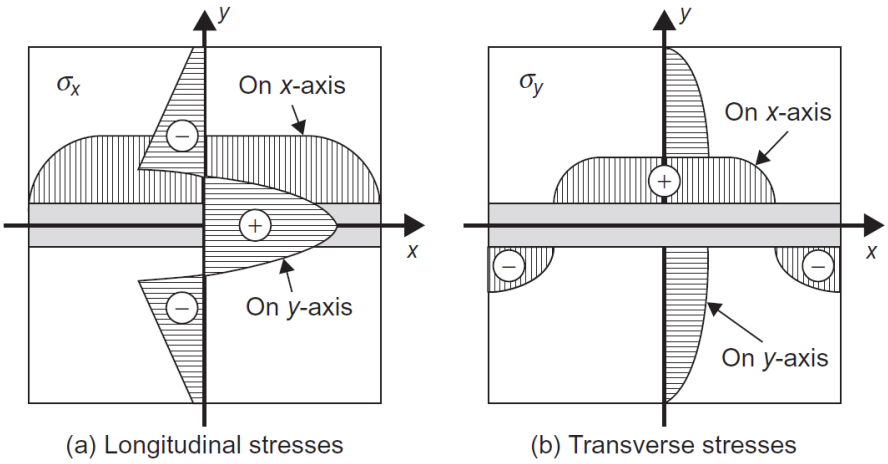

Figure 5.3 Typical distribution of residual stresses within the weldment resulting from a simple butt weld. From Ueda *et al*. [208]

Since residual stresses are those which exist in the absence of externally applied loadings, the residual stresses within a solid body, or component, must be in equilibrium across the whole component. If this is not the case, the imbalance in internal stresses will cause distortion of the component to redistribute these stresses such that static equilibrium is achieved. It must be noted that the presence of such distortion does not imply that residual stresses within the component are eliminated, only that they have been equilibrated. Distortion of this kind is commonly observed in welded structures with Figure 5.4 showing linear shrinkage and angular distortion in butt and fillet welded profiles. Residual stresses can also produce distortion when the constraints within a solid body are changed, for example by cutting or material removal processes, requiring the stresses to be redistributed in order to maintain static equilibrium.

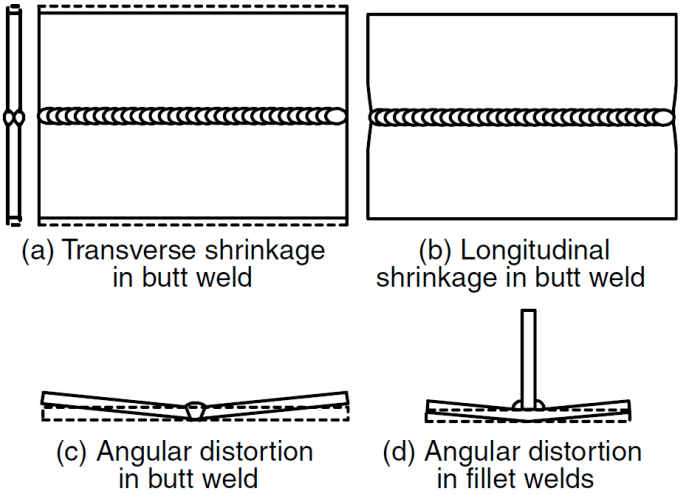

Figure 5.4 Distortion of welded structures. From Kou [115].

As previously discussed, residual stresses are typically detrimental to the performance of engineering structures and components, compromising mechanical and physical behaviour. Though the formation of residual stresses cannot be avoided during fusion welding processes, measures can be taken to minimise their effect. Firstly, in terms of distortion, the weldment can be altered to counter the effects through pre-setting angular offsets prior to welding, altering weld sequences or using additional constraints to limit mobility of the weldment. While these methods can negate the distortion that results from residual stress, they do not eliminate the stresses themselves. One common approach to reducing residual stresses in a welded body is the use of post-weld heat treatment (PWHT) where the area to be relieved is slowly heated to a suitable temperature and held for some predetermined period of time to allow relaxation of strains prior to being slowly cooled to ambient conditions [208, 209]. In addition to reducing residual stresses, PWHT can result in changes to microstructure, and hence properties such as ductility, toughness and stress corrosion behaviour [207]. These processes are typically avoided where ever possible as they represent an additional processing step which increases cost and can be difficult to implement, particularly on large structures. Other methods used to relieve or counter residual stresses in weldments include mechanical overloading [210, 211], vibratory excitation [212-215], shot peening [216-218] or laser peening [219-221] of the welded structure.

5.1.3 Measuring Residual Stresses

Through continued investigation and understanding, a number of methods have been developed to measure residual stresses within engineering structures. Since these stresses exist within the solid body without any external loadings they cannot be directly quantified, with measurements usually related to observations of strain over various length scales. As residual stresses are elastic in nature, stress values can be derived from measured strains, and hence deformations, with knowledge of the materials elastic properties. The resolution of these strain measurements is governed by the technique used, with measurements not possible at a single point location but rather obtained as an average across an area or ‘gauge volume’. Techniques for residual stress measurement may be classified as either destructive or non-destructive according to their impact on the work-piece being evaluated. Figure 5.5 presents a graphical comparison of a number of residual stress measurement techniques on the basis of spatial resolution and depth of

penetration. This figure clearly illustrates that a compromise exists in the measurement of residual stresses, with increasing depth of penetration typically accompanied by a loss of spatial resolution. In some cases such a loss can be tolerated, however it must be considered when trying to characterise residual stress gradients in one or more directions, which represent regions of high uncertainty in terms of the effects on mechanical behaviour [203]. A full discussion of these techniques including their procedures, advantages and disadvantages is well beyond the scope of this component of the research project and so only a brief overview of the basic operating principles is presented.

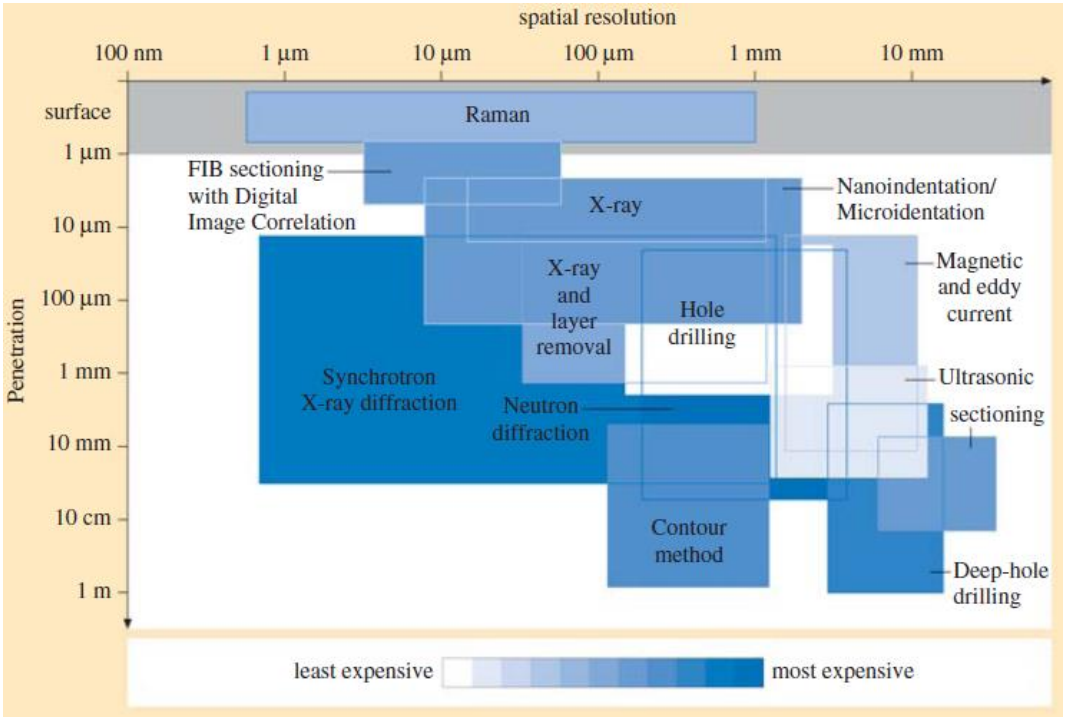

Figure 5.5 Comparison of spatial resolution and depth of penetration for various residual stress measurement techniques. From Schajer [203].

The general operating principle of the destructive evaluation methods relies on the self-equilibrating elastic nature of residual stresses where a component which contains residual stresses will deform in such a way as to maintain static equilibrium should there be a disturbance to the stress state in the body. Essentially, the removal of a section of material from a stressed body causes a redistribution and relaxation of stresses within the part, which is accompanied by elastic deformations or strains. Since these relaxation strains are elastic, the stresses released can be determined using linear relationships with the observed deformation. The first step in evaluating residual stress by any of the destructive methods is characterisation of the sample geometry in the

stressed condition to act as a reference measurement. Stressed material is then removed by cutting, sectioning, machining or drilling, giving relaxation of the stresses in the sample and producing elastic deformations. This deformed profile is then accurately measured, with analytical or finite element based methods used to calculate the stresses required to 'pull' the distorted sample profile back to its original shape. It is this need for material removal that renders the component of interest useless for its intended application, hence the term 'destructive'.

Examples of destructive evaluation methods include splitting, sectioning, layer removal, hole drilling, the ring core (trepan) method and the contour method. The hole drilling method starts with the application of a strain gauge rosette to the surface of the sample around the location of interest. A hole is then drilled centrally between the strain gauges to give relief of stresses in the surrounding material, with deformations quantified through strain gauge measurements or full-field optical techniques [203]. The ring core method operates in a similar manner with material removed in a ring around the outside of a centrally located strain gauge rosette. The contour method is performed by sectioning the sample though the plane of interest usually by wire EDM cutting with the distorted profile of the cut surface accurately measured using a coordinate measuring machine or laser profilometer. Using this distorted profile, the original residual stresses can be determined across the full area of the sectioned plane using finite element methods. Clearly, these methods may be used in combination with, for instance, strain gauges used on a sample which is also being evaluated by sectioning or the contour method. The deep-hole drilling method may be considered a combination of the hole drilling and ring core methods with the distortion of a centrally located deep-hole used to measure relaxation of stresses during the ring core process rather than strain gauges, thus allowing the evaluation of stresses far deeper within the sample.

Unlike the destructive methods, non-destructive methods allow the determination of residual stresses within a component or sample without adversely affecting its ability to perform its intended role. This is a key advantage of the non-destructive methods, with evaluated components able to be used in, or returned to service following testing without any compromise in function. A number of the non-destructive methods also have high spatial resolution, allowing the characterisation of high stress gradients in components [203]. The majority of these methods involve the use of diffraction techniques to measure the lattice spacing of a desired crystallographic plane or set of

planes. When considered on the atomic scale, elastic strains relate directly to the extension or compression of inter-atomic bonds and so are simply distortions of the lattice spacing away from its equilibrium position. It follows then that residual strains, and hence stresses, can be determined through measurement of the strained inter-planar lattice spacing, d_{hkl}, with knowledge of the unstressed inter-planar spacing, d_0. In this nomenclature the subscript *hkl* corresponds to the Miller indices for the crystallographic plane(s) of interest. The inter-planar spacing, d_{hkl}, is determined through diffraction according to Bragg's Law, shown in Equation 5.1, where n is an integer, λ is the wavelength of the electromagnetic radiation, d_{hkl} is the distance between the diffracting lattice planes (inter-planar spacing) and θ is the Bragg scattering angle. These parameters are illustrated in Figure 5.6.

$$n\lambda = 2d_{hkl} \sin\theta$$

Equation 5.1 Bragg's Law for diffraction.

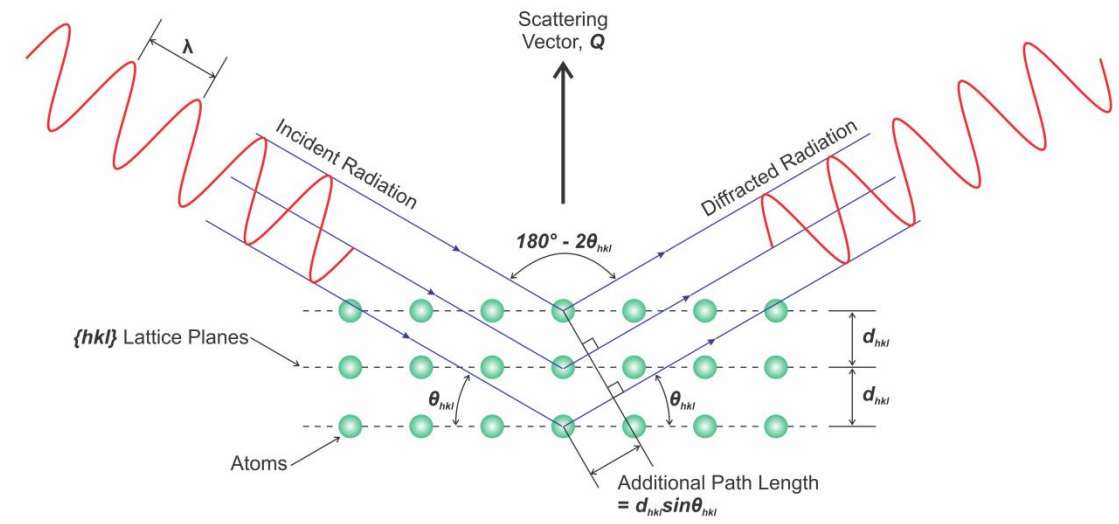

Figure 5.6 Constructive interference through diffraction of electromagnetic radiation by planes within a crystal structure.

Bragg's Law describes the conditions required for constructive interference of the radiation waveforms by diffraction. Constructive interference is seen as peaks in the intensity profile of the diffracted radiation, which may be plotted as a function of scattering angle, 2θ, for a given wavelength λ or as a function of λ for a given 2θ. With knowledge of the radiation wavelength and the scattering angle for the peak(s) observed, the inter-planar spacing can be readily determined for the planes of interest. It must be noted that each peak in the intensity profile corresponds to a specific set of

crystallographic planes and that the inter-planar spacing is measured normal to the diffracting planes, and so at an angle which bisects the incident and diffracted beams. Typically, measurement of at least six stress tensors is required to fully define the stress state in a solid body; however, knowledge of the principal directions allows the number of measurement directions to be reduced to three. In order to calculate the principal elastic strains, and hence principal stresses from the measured values of inter-planar spacing, the unstrained spacing d_0 must be known. One approach to measuring these values is by performing diffraction in a small representative portion of the material of interest which has been sectioned into a cube or comb profile [207] within which it can be assumed all residual stresses have been relaxed. Alternatively, diffraction measurements can be conducted in a location within the bulk sample where boundary conditions of known stress state can be applied to back calculate or 'de-convolute' the values of d_0 [222]. An example of this would be measurements of d_{hkl} taken near and normal to a free surface where the residual stresses in this direction normal to the free surface can be assumed to be zero. Irrespective of how the measurement of d_0 values is performed, it must be conducted in a sample of material with the same chemistry and processing history as the bulk sample being evaluated. Once both the strained and unstrained inter-planar lattice spacings are known, the elastic strains can be determined for that given direction and, once ascertained for all three directions in the Cartesian coordinate system, used to calculate residual stresses through Hooke's law for elastic deformation.

Diffraction based techniques commonly used for residual stress analysis include laboratory X-ray diffraction (XRD), synchrotron X-ray diffraction and neutron diffraction (ND). Laboratory XRD techniques are used extensively in engineering and materials science applications with high spatial resolutions possible through control of the incident and detected beam sizes, which define the gauge volume. The limited penetration of the low energy (5 to 18 keV) X-rays used means measurements are typically restricted to analysis of surface regions in the order of 25 μm thick [203]. While this shallow examination depth presents a number of limitations, it means that the gauge volume being examined is in a state of plane stress only with the stress normal to the free surface being zero. As such there is no need for an explicit measurement of the unstrained lattice plane spacing. The high electron energies found in synchrotron sources are capable of producing X-rays with energies far greater than conventional

laboratory sources, typically in excess of 50 keV [203]. With such high energies, the depth of penetration of these ‘hard’ X-rays is far superior to that of conventional laboratory XRD with no compromise in spatial resolution. Neutron diffraction makes use of ‘thermal’ (non-relativistic) neutrons which have wavelengths similar to the inter-planar lattice spacing of many engineering materials and so are well suited to stress examinations in these materials [207]. The ND technique operates with the same general principle as the X-ray diffraction techniques, with the primary difference being that neutrons are diffracted by interactions with the nuclei of the atoms within the sample while X-rays interact with electrons. As such, the depth of penetration for ND measurements is far greater in materials with both high and low atomic (Z) number, with gauge volumes, and hence spatial resolutions, typically no smaller than 0.5 mm x 0.5 mm x 0.5 mm. One significant limitation of both the synchrotron and ND techniques is that they are inextricably linked to large infrastructure and so are laboratory based, meaning components must be brought to the specific facility for evaluation. The high capital cost of the required infrastructure means such facilities are not widely available and operate with limited access. However, once these are established, the actual cost associated with performing an individual measurement is lower than either the contour or deep-hole drilling methods.

Other non-destructive methods for evaluating residual stress include magnetic, ultrasonic, thermoelastic, photoelastic and indentation techniques, each with their own characteristics, advantages and limitations. These, along with the other measurement techniques identified are described and evaluated in greater detail by Withers and Bhadeshia [223] and Schajer [203] amongst others. Of those techniques considered, the neutron diffraction method was selected to conduct measurements of residual stress in representative samples of Ti-6Al-4V produced by GTAW-wire based additive manufacturing. In addition to the relative ease of access to ND measurement facilities through the Australian Nuclear Science and Technology Organisation (ANSTO) and the Australian Institute of Nuclear Science and Engineering (AINSE), the neutron diffraction technique offered suitable spatial resolution combined with the ability to examine samples at substantial depths where complex tri-axial stress states critical to mechanical performance are expected to be present. Also, being non-destructive, the ND technique allowed for subsequent examination and further characterisation to be conducted on the same samples.

5.1.4 Neutron Diffraction

Neutrons used to analyse residual stress by diffraction may be produced either by fission in a nuclear reactor, or by bombarding the nucleus of a target with pulses of high energy protons in a spallation source. The high energy neutrons released from either of these sources are then 'moderated' to suitable energies in the 'thermal' range, corresponding to wavelengths of 0.7 Å to 3.0 Å, through collisions with a hydrogenous material [203, 224], before being directed to the diffraction instrument through neutron guide tubes. There are typically two experimental methods possible for the use of ND in residual stress measurement, conventional $\theta/2\theta$ scanning and time-of-flight (TOF) techniques, with the method used depending on the neutron source [223].

Spallation sources produce a pulsed beam of neutrons with a wide range of energies and hence wavelengths, all of which are directed onto the sample at a fixed Bragg angle (usually 2θ=90°). Through measurement of the TOF of neutrons, which is a function of energy and hence wavelength, it is possible to determine the inter-planar spacing for multiple crystallographic planes simultaneously. Strains can be determined from minute changes in the TOF, with resolution improved by increasing TOF and hence the flight path length [223]. The simultaneous measurement of several diffraction peaks, or the entire diffraction pattern, is particularly useful for stress measurements in multi-phase materials or where the determination of intergranular strains is of importance.

Reactor sources, such as the OPAL research reactor utilised at ANSTO, produce an uninterrupted stream of neutrons which, upon reaching the diffraction instrument, are passed through a monochromator to yield a continuous beam of neutrons with a specific wavelength. Diffraction is conducted using the conventional $\theta/2\theta$ method with the detector located at a pre-defined angular position, corresponding to the Bragg scattering angle of the specific set of *hkl* planes of interest for the single wavelength selected by the monochromator. During measurements of this type, the gauge volume is defined by size of the incident and diffracted beams, which is in turn controlled by various arrangements of slits and collimators as shown in Figure 5.7. It must be noted that in this figure grain size is somewhat exaggerated for clarity. Ordinarily there are a large number of grains contained in the gauge volume, only a fraction of which are favourably oriented to satisfy the criteria for constructive interference. Plotting detected intensity as a function of 2θ and fitting with a Gaussian distribution yields a peak whose

location (in the θ domain) is directly related to the inter-planar spacing of the *hkl* planes. Minor 'shifts' in the peak position, as shown in Figure 5.8, relate to variations in the inter-planar spacing due to tensile or compressive stresses, and so can be used to determine elastic lattice strain, ε, using Equation 5.2. The uncertainty in the calculated strain value, $\Delta\varepsilon$, can then be determined using the peak shift as shown in Equation 5.3.

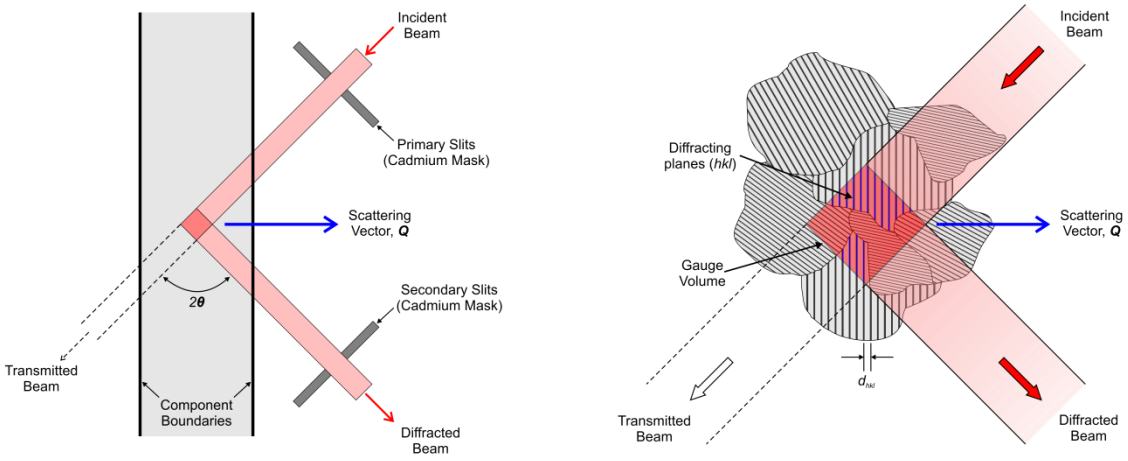

Figure 5.7 Definition of the gauge volume during ND due to slits on the incident and diffracted beams. Adapted from Schajer [203] and Ziara-Paradowska [207].

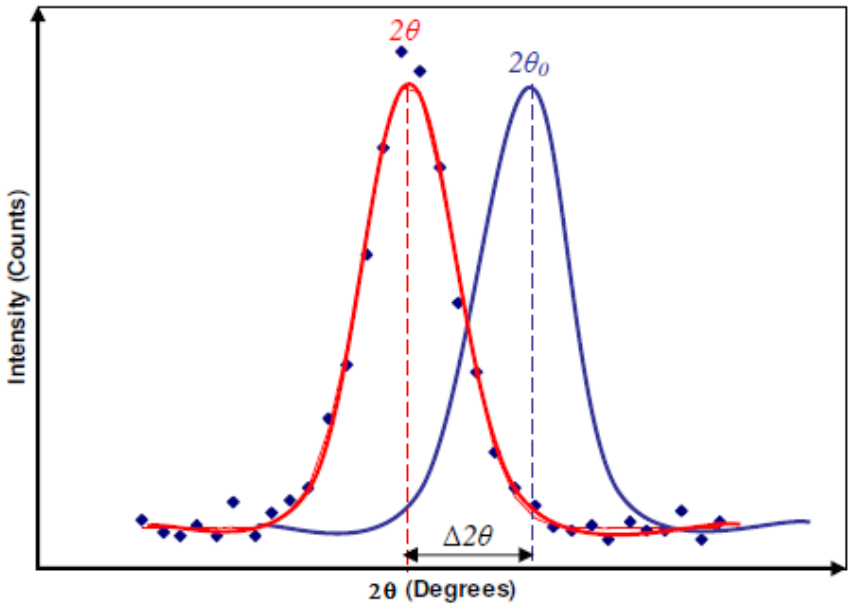

Figure 5.8 Illustration of diffraction peaks observed during ND for residual stress measurements, with a shift in peak position of $\Delta 2\theta$ away from the unstrained value of $\Delta 2\theta_0$. From Ziara-Paradowska [207].

$$\varepsilon_{hkl} = \frac{\sin\theta_0}{\sin\theta} - 1$$

Equation 5.2 Calculation of elastic strain from observations of intensity peak position.

$$\Delta\varepsilon = \left(\frac{\sin\frac{\theta}{2}}{\sin\left(\frac{\theta_0 - \Delta\theta}{2}\right)} - 1 \right) - \varepsilon$$

Equation 5.3 Calculation of uncertainty in elastic strain values based on peak shift $\Delta\theta$.

These strain calculations are more commonly performed in terms of the inter-planar lattice spacing, rather than scattering angle, as shown in Equation 5.4.

$$\varepsilon_{\mathrm{h}kl} = \frac{d_{\mathrm{h}kl} - d_0}{d_0}$$

Equation 5.4 Calculation of elastic strain from measured values of the strained and unstrained inter-planar spacing.

The uncertainty in strain can then be determined from the standard deviation (SD) associated with the Gaussian fit of the peak profile using Equation 5.5.

$$\Delta\varepsilon = \frac{d_{\mathrm{h}kl}}{d_0}\sqrt{\left(\frac{SD_{d_{\mathrm{h}kl}}}{d_{\mathrm{h}kl}}\right)^2 + \left(\frac{SD_{d_0}}{d_0}\right)^2}$$

Equation 5.5 Calculation of uncertainty in elastic strain values based on standard deviations in Gaussian fitting of intensity data.

In order to fully describe a strain tensor at a given location, a minimum of six measurements of strain need to be obtained in independent directions. However, where the orientation of the principal strains are known, only the three principal strains are required [203]. In the case of the linear bead-on-plate welding arrangement used for production of additively manufactured samples, the principal directions are as defined in Figure 5.9 with the transverse (X) being perpendicular to the weld, the normal (Y) being normal to the plate (i.e. in the build direction) and the longitudinal (Z) being parallel to the welding direction. Hence, by performing strain measurements in these three orthogonal directions, the stress at the measurement location can be fully defined.

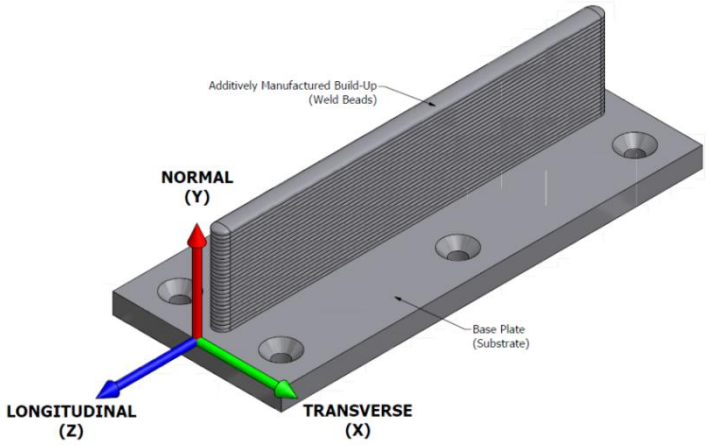

Figure 5.9 Coordinate system used in reference to additive manufactured structures.

With strain values determined in the three principal directions, values of principal stress can be calculated for all three directions from Hooke's law for linear elasticity in a continuous body, as presented in Equation 5.6, where *E* and *v* are the elastic modulus and Poisson's ratio of the material, respectively.

$$\sigma_{xx} = \frac{E}{(1+\nu)(1-2\nu)}\left[(1-\nu)\varepsilon_{xx} + \nu\left(\varepsilon_{yy} + \varepsilon_{zz}\right)\right]$$

$$\sigma_{yy} = \frac{E}{(1+\nu)(1-2\nu)}\left[(1-\nu)\varepsilon_{yy} + \nu(\varepsilon_{xx} + \varepsilon_{zz})\right]$$

$$\sigma_{zz} = \frac{E}{(1+\nu)(1-2\nu)}\left[(1-\nu)\varepsilon_{zz} + \nu\left(\varepsilon_{xx} + \varepsilon_{yy}\right)\right]$$

Equation 5.6 Calculation of principal stresses from elastic strains.

The uncertainty in calculated values of principal stress can then be determined through propagation of errors based on the uncertainties in strain values, as shown in Equation 5.7.

$$\Delta\sigma_{xx} = \frac{E}{(1+\nu)}\sqrt{\left[\left(\frac{\nu}{(1-2\nu)}\right)(\Delta\varepsilon_{xx})^2 + \left(\frac{\nu}{(1-2\nu)}\right)^2\left(\Delta{\varepsilon_{xx}}^2 + \Delta{\varepsilon_{yy}}^2 + \Delta{\varepsilon_{zz}}^2\right)\right]}$$

$$\Delta\sigma_{yy} = \frac{E}{(1+\nu)}\sqrt{\left[\left(\frac{\nu}{(1-2\nu)}\right)\left(\Delta\varepsilon_{yy}\right)^2 + \left(\frac{\nu}{(1-2\nu)}\right)^2\left(\Delta{\varepsilon_{xx}}^2 + \Delta{\varepsilon_{yy}}^2 + \Delta{\varepsilon_{zz}}^2\right)\right]}$$

$$\Delta\sigma_{zz} = \frac{E}{(1+\nu)}\sqrt{\left[\left(\frac{\nu}{(1-2\nu)}\right)(\Delta\varepsilon_{zz})^2 + \left(\frac{\nu}{(1-2\nu)}\right)^2\left(\Delta{\varepsilon_{xx}}^2 + \Delta{\varepsilon_{yy}}^2 + \Delta{\varepsilon_{zz}}^2\right)\right]}$$

Equation 5.7 Calculation of uncertainty in principal stress values based on uncertainties in strains.

5.1.5 Residual Stresses and Additive Manufacture

Since the GTAW-wire based additive manufacture of components from Ti-6Al-4V is essentially a process of repeated fusion welding, it is clear that any structure produced in this way would be expected to show significant residual stresses. While considerable work has been done in understanding residual stresses associated with fusion welding processes, much of this may not be applicable to the additive manufacturing process due to the unique conditions of repeated material deposition and thermal cycling. Clearly, a thorough understanding of how these residual stresses arise during GTAW-wire based additive manufacture of Ti-6Al-4V, and how they may be influenced by processing parameters is critical in assessing the viability of the process for the manufacture of any given component, particularly those being targeted in structural applications.

A considerable amount of literature exists relating to the measurement of residual stresses in welds of titanium, particularly linear friction and friction stir processes, using a variety of measurement techniques [225-227]. However, being a relatively new process, there has been very little work published in relation to residual stresses resulting from the arc-wire based additive manufacturing, particularly in titanium alloys. The work of Ding [137] and Colegrove [228] shows the measurement of residual stresses in additively manufactured steel structures produced using gas metal arc (GMA) welding processes, while Brice *et al*. [229] analyse the residual stresses within an aluminium structure produced by electron beam welding. These studies show that residual stresses are concentrated toward the root of the additively manufactured build-up, near the interface with the substrate. Further, the longitudinal stress components (parallel to the welding direction) are seen to be dominant, with stress levels exceeding 50 % of the materials' yield strength. Beuth and Klingbeil [172] have predicted the maximum residual stress values in thin walled structures produced by powder based laser additive layer manufacturing, with calculations based on thermal gradients obtained through process modelling, though no validation through experimental measurements is presented. Residual stresses in cylindrical Ti-6Al-4V components produced from powder feedstock by selective laser melting (SLM) have been assessed by Knowles [230] using the hole drilling method, however the application of these results to the GTAW-wire AM method is somewhat limited due to differences in sample geometry, constraints and process characteristics. Measurement of lattice parameters for additively manufactured Ti-6Al-4V have been made across a range of temperatures by

Swarnakar *et al.* [11] using X-ray diffraction, however the study was aimed at assessing phase stability rather than residual strains.

The purpose of the present study was to make use of neutron diffraction techniques for the measurement of residual strains, and hence stresses, within additively manufactured samples of Ti-6Al-4V produced by arc-wire deposition. Using this, the influence of welding parameters such as specific deposition energy and pulse arc current, on the residual stresses in these components would be assessed, as would the effectiveness of PWHT in relieving residual stresses in such representative components. As a means of comparison, results for additively manufactured samples were also evaluated against measurements taken from equivalent components produced by conventional subtractive manufacturing and welded fabrication processes. It is hoped that the results of this study would generate a basic understanding of residual stresses in additively manufactured titanium components and act as a foundation for future studies and more comprehensive assessment of the manufacturing process.

5.2 Methods and Methodology

Residual stresses in representative samples of Ti-6Al-4V produced by GTAW-wire based additive manufacture were evaluated using neutron diffraction techniques, with microhardness also used as a means of characterisation. Samples took the form of a thin vertical wall-like feature protruding at right angles to the upper surface of the considerably thicker base plate. This geometry was utilised as it was considered to be representative of a thin-walled, deep pocket feature common in structural aerospace components manufactured from titanium alloys, such as the landing gear beam shown in Figure 5.10. Components with features of this type can be understood to have extremely high buy-to-fly ratios and so are ideal candidates for production through additive manufacture.

Figure 5.10 Computer generated model of a landing gear beam commonly produced from titanium alloys by subtractive manufacturing processes. From Sandvik Coromant [231].

Additively manufactured build-ups were produced by sequential deposition of weld beads onto a commercially sourced Ti-6Al-4V base plate measuring 250 mm x 100 mm x 12 mm. This base plate was fastened to a 25 mm thick mild steel adaptor plate which in turn was mounted to the modified lathe linear actuator system. Since residual stress formation during fusion welding processes is heavily dependent on the constraint of the work-piece, care was taken to ensure that the restraint used was consistent in the production of all samples. Welding of samples with continuous direct current was performed using a Kemppi MasterTIG MLS 2000 inverter power supply, while samples produced using pulsed current were welded using a custom experimental power source with fast current switching [232, 233]. In both cases a water cooled Conley & Kleppen (CK) machine mount welding torch was used. Independent wire feed of diameter 1.0 mm Ti-6Al-4V wire was provided through a CK WF3 dedicated wire feed unit. The combined torch and wire feed arrangement was mounted above the linear actuator with height adjustment possible through a manually operated rack-and-pinion.

Inert gas shielding of the weld zone was achieved with welding grade pure argon using pre and post flow options through both the welding torch nozzle and custom fabricated trailing shield. Additional gas shielding of the deposited material was achieved using stainless steel plates measuring 300 mm x 100 mm x 6 mm with a slot 10 mm wide and 260 mm long cut centrally through the plate. As the build process progressed, these ‘shielding plates’ were stacked over the base plate with the build-up protruding through the slot. The aim of this was to maintain a shielding envelope similar that of a conventional bead-on-plate arrangement at all stages throughout the build process.

Shielding gas flow rates and other process parameters common to all additively manufactured samples are given in Table 5.1.

Table 5.1 Summary of GTA welding parameters used to produce samples for mechanical testing.

Polarity	DCEN/Pulsed
Electrode	2% Ceriated, 2.4 mm Ø
Arc Length	3.5 mm
Travel Speed	150 mm/min
Shielding gas	Welding Grade Argon
Flow rate – torch nozzle	8 L/min
Flow rate – trailing shield front	10 L/min
Flow rate – trailing shield rear	7 L/min
Pre-flow duration	3 seconds
Up slope duration	2 seconds
Down slope duration	1 second
Post flow duration	30 seconds

A total of five additively manufactured samples were produced for residual stress measurements using various combinations of process parameters and post-weld conditioning, as detailed in Table 5.2. It should be noted that for each additively manufactured sample, arc current for the first weld pass was set approximately 25 % higher than the steady operating value listed. Arc current was gradually reduced during each of the following five passes until the steady operating value was reached. This reduction in arc current was done to counter chill from the base plate which was seen to cause narrowing of the weld bead during the initial stages of the build.

Additively manufactured walls 9 and 10 were produced with equivalent arc energies, and hence heat inputs, but with differing wire feed rates to give different deposition rates. These parameters were selected to yield nominal specific deposition energies of 10 kJ/g and 20 kJ/g respectively which, from observations made during process characterisation trials, were considered to represent practical bounds for the process operating envelope.

Table 5.2 Key GTAW process parameters for preparation of samples for residual stress measurements.

Sample ID	Peak Current, I_p (A)	Background Current, I_b (A)	Pulse Frequency (Hz)	Pulse Period, T (ms)	Peak Width, t_p (ms)
Wall_09	110	-	-	-	-
Wall_10	110	-	-	-	-
Wall_11	140	-	-	-	-
Wall_16	140	80	1.0	1000	500
Wall_17	140	80	5.0	200	100
Wall_18	110	-	-	-	-

Sample ID	Wire Feed Speed (mm/min)	Arc Energy (J/mm)	Specific Deposition Energy (kJ/g)	Passes	Total Build Height (mm)
Wall_09	2000	487	10.5	26	≈37
Wall_10	1000	495	21.5	48	≈38
Wall_11	1000	-	-	-	-
Wall_16	1000	557	23.5	64	≈38
Wall_17	1000	550	23.0	63	≈38
Wall_18	1000	542	23.4	48	≈38

Due to the formation of residual stresses in fusion welding of Ti-6Al-4V, weldments intended for fatigue-critical applications, such as structural aerospace components, are commonly subjected to post weld heat treatments [21]. In order to assess the effectiveness of such heat treatments in relieving residual stresses found in additively manufactured Ti-6Al-4V structures, a sample (Wall 18) manufactured with process parameters approximately equivalent to those used to produce Wall 10 was subjected to a stress relieving heat treatment. The PWHT was performed under standard atmosphere in a laboratory muffle furnace pre-heated to 600 °C. The sample was held at this temperature in the as-deposited condition for four hours before being slow cooled at 50 °C per hour to 450 °C then air cooled to ambient conditions, as illustrated in Figure 5.11. This regime was selected based on the recommendations of Boyer *et al*. [21], who state that stress relief annealing of Ti-6Al-4V weldments is commonly performed at 595 °C for between two and four hours. From the stress-relief nomograph shown in Figure 5.12 it is suggested that this PWHT would relieve approximately 72 % of residual stress. Conducting the heat treatment above the Ti_3Al solvus temperature of 500 °C negated any increase in strength due to precipitation of Ti_3Al in the α-Ti grains, and would be expected to give a marginal loss of strength with an accompanying increase in ductility.

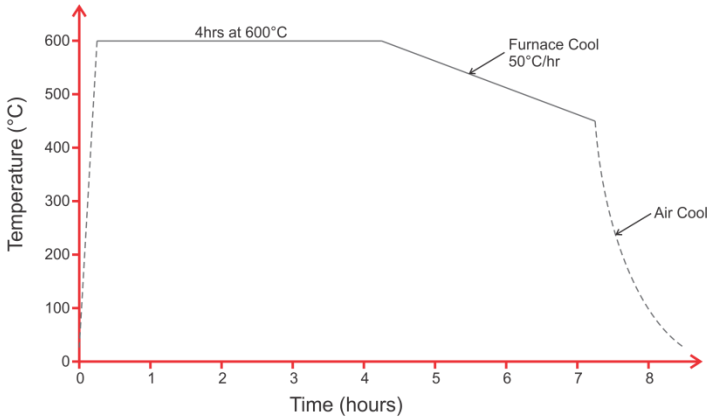

Figure 5.11 Schematic of PWHT used for stress relieving of additively manufactured wall 18.

It is acknowledged that conducting the PWHT under standard atmosphere rather than in an inert atmosphere or vacuum would cause atmospheric contamination of the sample, particularly by oxygen and nitrogen. Since the contaminant species occupy interstitial lattice positions in the solid solution, they cause distortion of the crystal lattice and so may impair the ability to measure residual stresses by neutron diffraction. Smarsly [193] states that the random walk distance for the diffusion of oxygen in Ti-6Al-4V held for four hours at 950 °C is approximately 200 μm. This is corroborated by the work of Bendersky [192] who shows that the depth of hardening in Ti-6Al-4V resulting from exposure to atmosphere for four hours at 900 °C would be approximately 350 μm. Given that these temperatures are far higher than the 600 °C used in the present study, and that diffusion is a thermally activated process which follows the Arrhenius equation, it is thought the depth of contamination penetration would be far less than these values. Boyer *et al*. [21] suggest that exposure of Ti-6Al-4V to atmosphere at temperatures up to 650 °C for up to twelve hours requires a minimum of 15 μm material be removed from each exposed surface in order to remove contaminated material. As such, it is considered that any atmospheric contamination resulting from the PWHT would be isolated to the near surface regions and so would not influence measurements of residual stress conducted in the bulk material. Further, by conducting the PWHT in the as-deposited condition, any contaminated material is expected to have been removed by subsequent machining processes used to produce the final geometry of the samples.

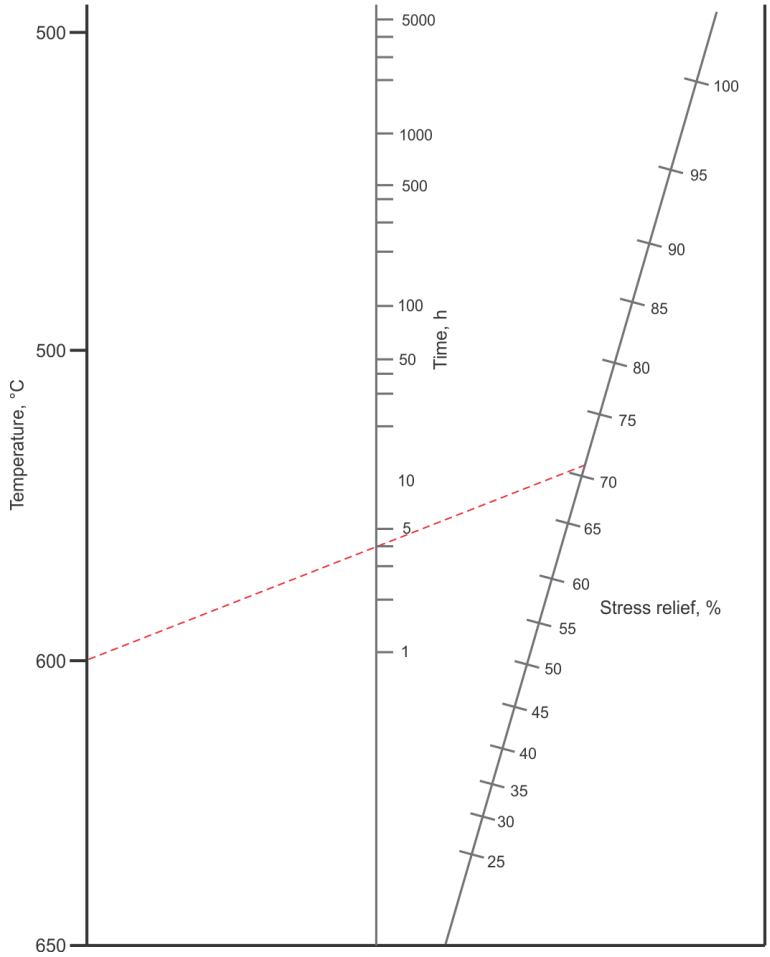

Figure 5.12 Combined effects of temperature and time in stress relieving heat treatments of Ti-6Al-4V. Adapted from Boyer *et al.* [21].

Pulsed current has been widely investigated [117-119, 157, 159, 234, 235] as a possible method to subdue grain growth during fusion welding of titanium alloys by generating instability in the molten pool and so interrupting epitaxial grain growth. Balasubramanian *et al.* [234] also state that the use of pulsed current during GTAW processes reduces residual stress and distortion in the final weldment. More specifically to the case of arc-wire based additive manufacturing of Ti-6Al-4V, the influence of pulsed current waveforms on microstructure and the formation of large columnar grains during the build-up process has been examined by Wang *et al.* [114] and Mitzner [120]. In order to investigate the influence of pulsed current on residual stresses formed during the GTAW-wire based additive manufacturing process, walls 16 and 17 were produced using square wave pulsed arc current at frequencies of 1 Hz and 5 Hz respectively. To provide a reasonable basis for comparison, peak and background values of the pulsed arc current were selected to maintain arc and specific deposition energies approximately equal to those of Wall 10 while also yielding a build-up with equal wall thickness. The

pulse frequency of 5 Hz was selected based on the results of the previously mentioned studies which indicated that for Ti-6Al-4V, the greatest reduction in grain size and increase in mechanical properties occurs at frequencies between 3 Hz and 6 Hz. The low frequency of 1 Hz was selected to act as a reference which would be expected to show a lesser effect on microstructure, mechanical properties and potentially residual stress.

To fully evaluate the residual stress observations made in additively manufactured structures, two reference samples were produced using conventional manufacturing methods currently used to produce components from Ti-6Al-4V. The first reference sample was produced from commercially sourced wrought Ti-6Al-4V billet material 55 mm in thickness using purely subtractive manufacturing processes, as would be common practice in the production of most structural aerospace components which contain thin-walled, deep pocket features. The second reference sample was produced by welded fabrication through joining of smaller pre-forms. Two sections of wrought Ti-6Al-4V plate measuring 250 mm x 100 mm x 12 mm and 250 mm x 40 mm x 8 mm were welded together in a T-fillet configuration to yield a sample of similar geometry to the additively manufactured build-ups. A 'double-V' preparation was used on the vertical plate to achieve full penetration through the weld joint, with diameter 1.0 mm Ti-6Al-4V filler wire used to create the joint. While this type of manufacture is used extensively in the production of structural components for general engineering for a variety of materials, it is relatively under-utilised in the production of structural aerospace components from titanium alloys. Still, it presents significant opportunities for improved material utilisation and overall cost reduction, and so can be considered as a competitive alternative to arc-wire based additive manufacture of components from Ti-6Al-4V. Following production, wire EDM cutting was used to extract a slice of the vertical wall section 4mm in thickness from the end region of all samples, as shown in Figure 5.13, to act as the unstressed d_0 reference samples.

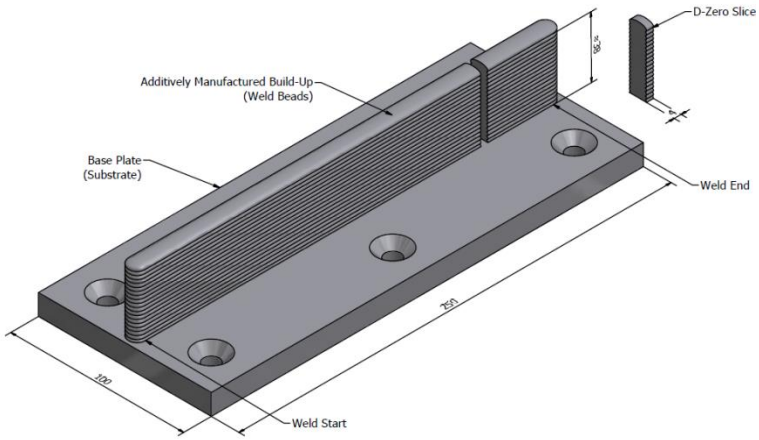

Figure 5.13 Preparation of d_0 samples from additively manufactured samples.

All samples were then finish machined to a common final geometry which featured a wall 5 mm in thickness, 36 mm in height and 178 mm in length protruding from the base plate, whose thickness was reduced to 10 mm as shown in Figure 5.14. Finish machining was performed using a Haas TM-2P 3-axis CNC vertical milling machine. Firstly the base plate section of each sample was milled back and front using a 50 mm diameter TaeguTec 90° 6-insert *ChaseMill* to achieve the 10 mm thickness and to remove distortion in the base plate from the welding process which would make mounting for subsequent machining processes difficult. The wall feature was then machined using a 20 mm diameter Sutton Tools *Harmony* 4-flute solid carbide end-mill with a 2.0 mm corner radius (item number E559 2020). Machining was conducted in accordance with the end-mill manufacturer's recommendations, with roughing passes conducted as required before a single finishing pass was used to yield the final profile. Coolant was a water-oil emulsion applied to the cutting zone using directed nozzles. Other parameters relating to the machining process are summarised in Table 5.3. Figure 5.15 shows all samples in the as-machined condition prior to measurement of residual stresses by neutron diffraction.

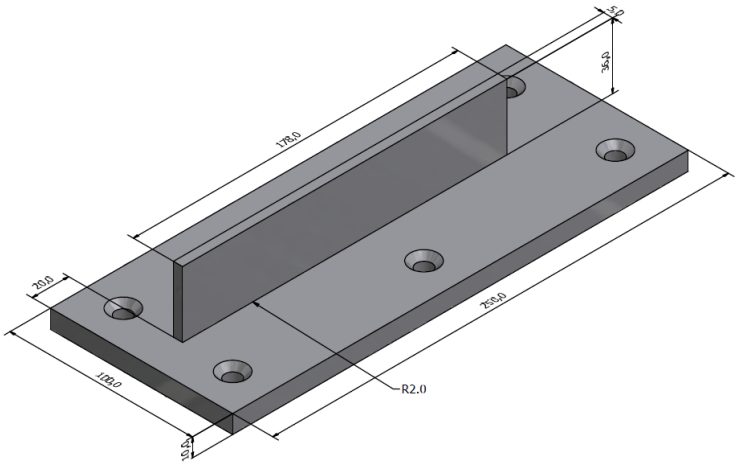

Figure 5.14 Final geometry of the thin-walled structure prepared from all samples including fabricated and billet samples.

Table 5.3 Process parameters for end milling operations used to machine samples for residual stress evaluation.

Milling Configuration	Climb (Down) Milling
Cutter Diameter, D	20 mm
No. of Teeth, z	4
Feed Per Tooth, f_z	0.071 mm/tooth
Feed Rate, V_f	250 mm/min
Spindle Speed, N	875 rev/min
Surface Cutting Speed, V_c	55 m/min
Axial Depth-of-Cut, a_p	36 mm
Radial Depth-of-Cut, a_e	2.0 mm roughing 1.0 mm finishing

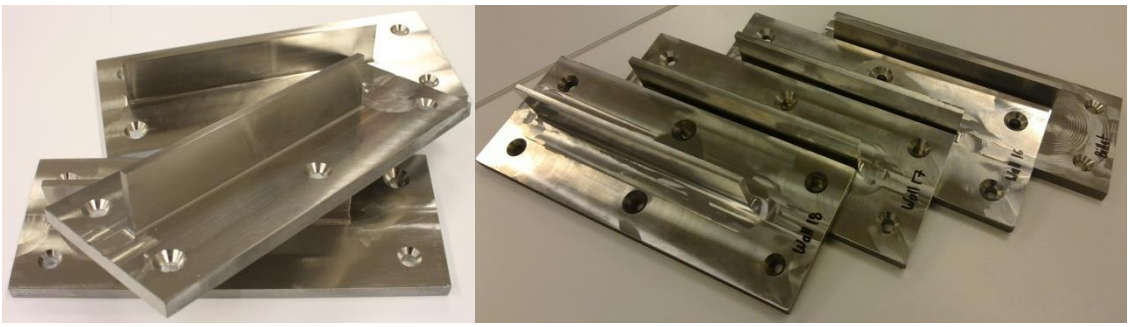

Figure 5.15 As-machined condition of samples prepared for residual stress measurements.

Residual strain measurements were performed non-destructively using the KOWARI strain-scanning diffractometer [236] located at the OPAL research facility operated by ANSTO. The general arrangement of this instrument is shown in Figure 5.16.

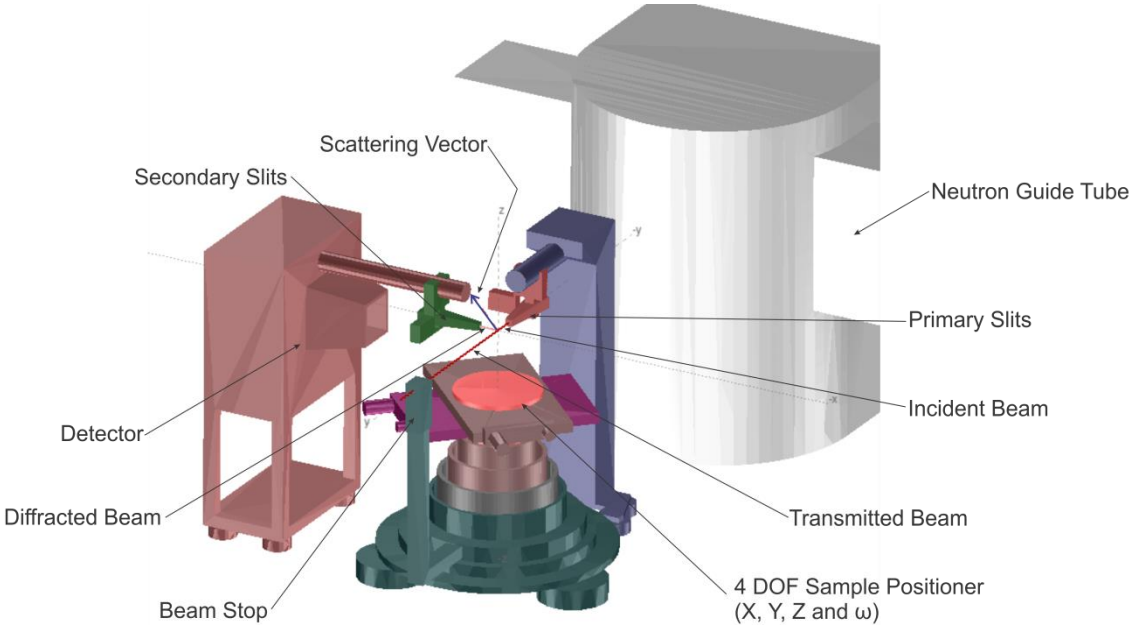

Figure 5.16 General arrangement of the KOWARI strain-scanning diffractometer.

Prior to conducting actual diffraction experiments, each sample was fitted with a total of six steel spheres 10 mm in diameter which served as datum or 'fiducial' points to help with positioning of the sample in the instrument space during experiments. A three-dimensional virtual model of each sample was generated using a coordinate measuring machine (CMM) fitted with a laser profile scanner, followed by definition of the fiducial points using a CMM touch probe. Using the virtual laboratory provided in SScanSS software [237], these data files were combined to produce an experimental model of each sample, as shown in Figure 5.17. In this model measurement points were then defined at locations of interest within the sample geometry. For the sample geometry used this was along the weld centreline, below the weld toe through the thickness of the base plate, and below the surface or the base plate at increasing offset from the weld centreline, as shown in Figure 5.18. A total of 37 measurement points were used in additively manufactured samples, with all points lying on a single XY plane located 80 mm from the start edge of the base plate where steady state welding (and hence stress) conditions exist. The location of this plane is indicated with the dashed line running perpendicular to the wall feature in Figure 5.17. These points were positioned at 1 mm intervals near the base of the wall feature and at 2 mm intervals in the base plate. The spacing between points was increased with increasing offset from the root of the wall where variations in residual stress were predicted to be less severe. Fewer measurement points were used in the fabricated T-fillet and billet samples since

the processing history and greater homogeneity of microstructure was expected to give less variation in residual stress. Once mounted to the positioner table in the instrument area, samples were accurately located using a touch probe mounted to a CMM to pinpoint the previously defined fiducial points. Doing so ensured precise positioning of the gauge volume to within 50 μm of the desired measurement location. Simulations of the measurement process were then run in SScanSS, which also produced control parameters that allowed automation of the actual experiment [238].

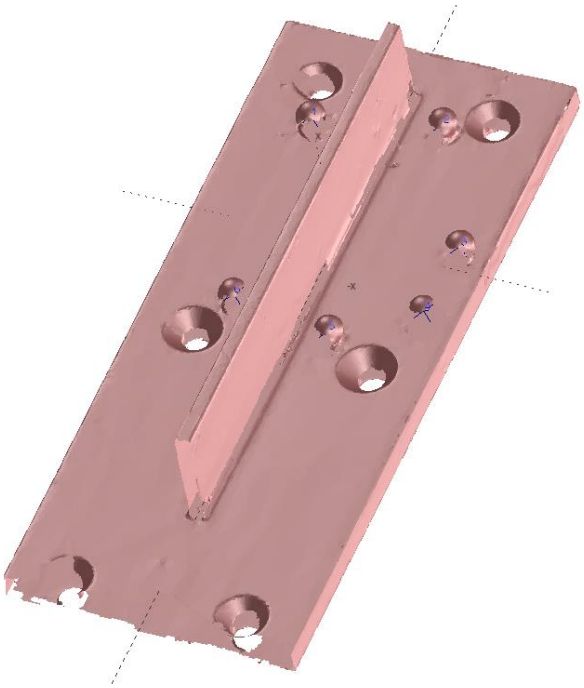

Figure 5.17 Computer generated model of the sample in the SScanSS software with the centre point of fiducial spheres indicated by blue crosses.

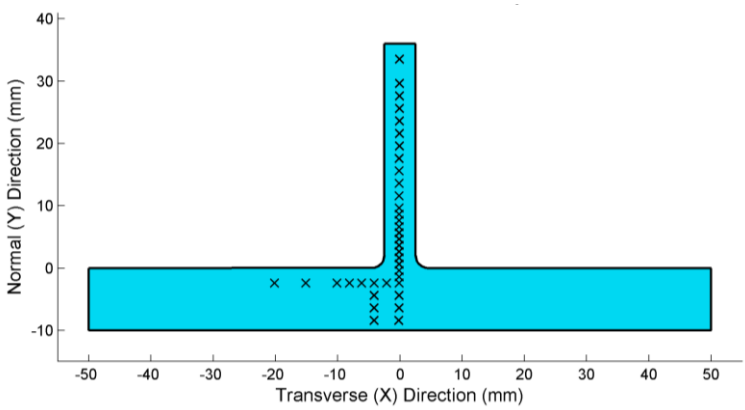

Figure 5.18 Location of measurement points within the vertical wall and base plate of additively manufactured samples.

Neutron diffraction was conducted using a constant wavelength of 1.70 Å, selected from the white neutron beam through a Si (400)-type double focusing monochromator. The 300 mm x 300 mm (420 channel) area detector was positioned at an angle of $2\theta = 90.4°$, corresponding to Bragg reflections for the α-Ti (103) plane. This plane was selected as it produces a convenient square gauge volume and also has mechanical properties similar to the bulk values for Ti-6Al-4V. Measurements were made for each of the three principal directions by aligning the direction of interest with the scattering vector as shown in Figure 5.19. It should be noted that measurements in the longitudinal direction required two separate sample orientation to optimise the path length when measuring strains in the base plate. The gauge volume was defined using slits of cadmium to 'crop' the incident and diffracted beams. Measurements in the longitudinal direction were made using an experimental gauge volume of 2 mm x 2mm x 2mm since variations in stress are significant transverse to the welding direction. As there is little variation in stresses along the length of the weld in the steady state region, the experimental gauge volume for measurements in the normal and transverse directions was expanded in the longitudinal direction to 2 mm x 2 mm x 20 mm.

Various counting times were used for each measurement point and orientation depending on the gauge volume and path length for the particular configuration. In all cases the time was sufficient to ensure a clearly defined diffraction peak (peak to background ratio in excess of 4:1) was obtained. Counting times for measurements in the longitudinal direction were between 30 minutes and 60 minutes due to the relatively small gauge volume and large path lengths particularly in the base plate. In contrast, the comparatively large gauge volume and short path lengths allowed the use of 5 minute counting times in the normal and transverse directions.

Thin slices of each sample prepared to determine d_0 values were measured in the same manner, with an experimental gauge volume of 2 mm x 2mm x 2mm used at six measurement points for the longitudinal and normal directions, and an experimental gauge volume of 2 mm x 2 mm x 20 mm used across the height of the sample for the transverse direction. The positioning of these samples for measurement in the normal and longitudinal directions is shown in Figure 5.20. Count times for these thin slice samples were similar to those used in the bulk additively manufactured structures.

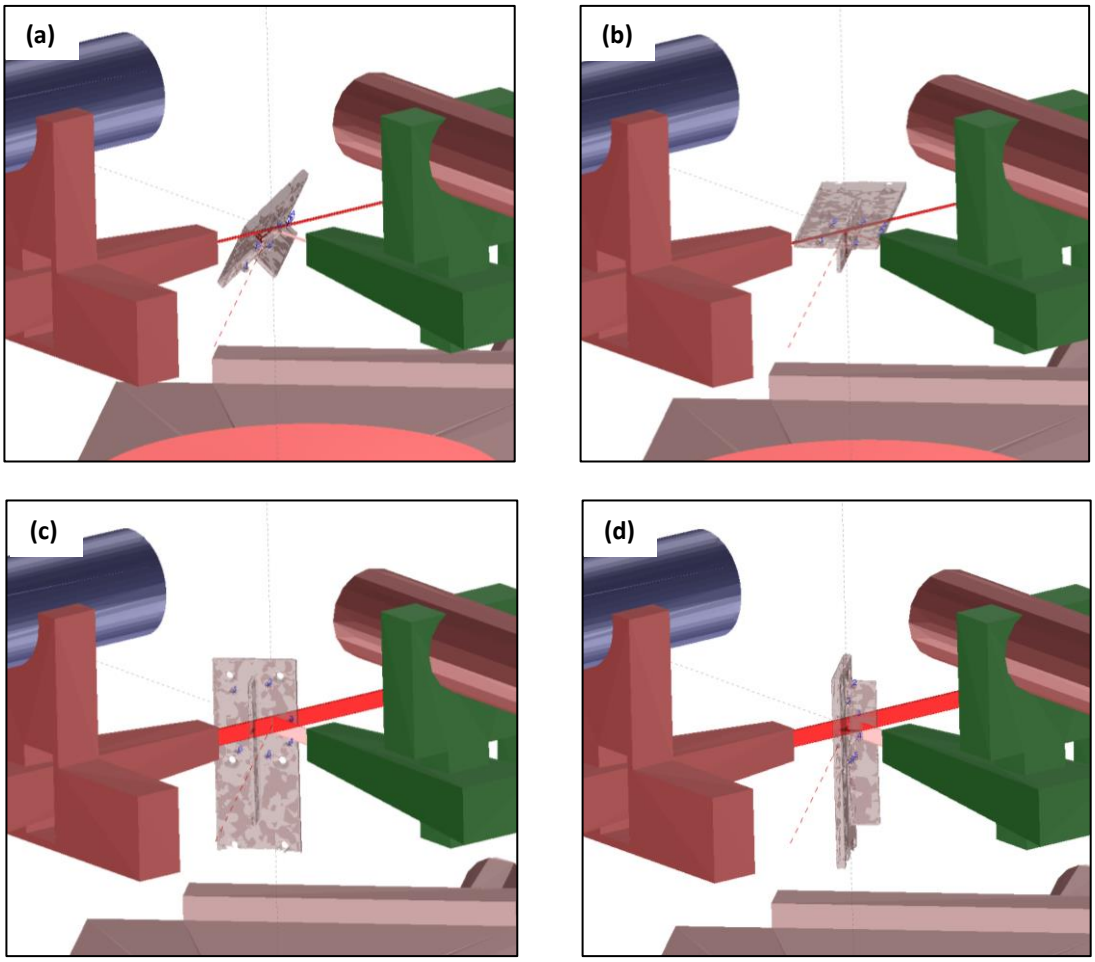

Figure 5.19 Sample positioning for strain measurements in the (a) longitudinal direction in the base plate, (b) longitudinal direction in the wall, (c) normal direction throughout and (d) transverse direction throughout. Incident and diffracted beams are shown in solid and transparent red respectively with the dashed line representing the scattering vector.

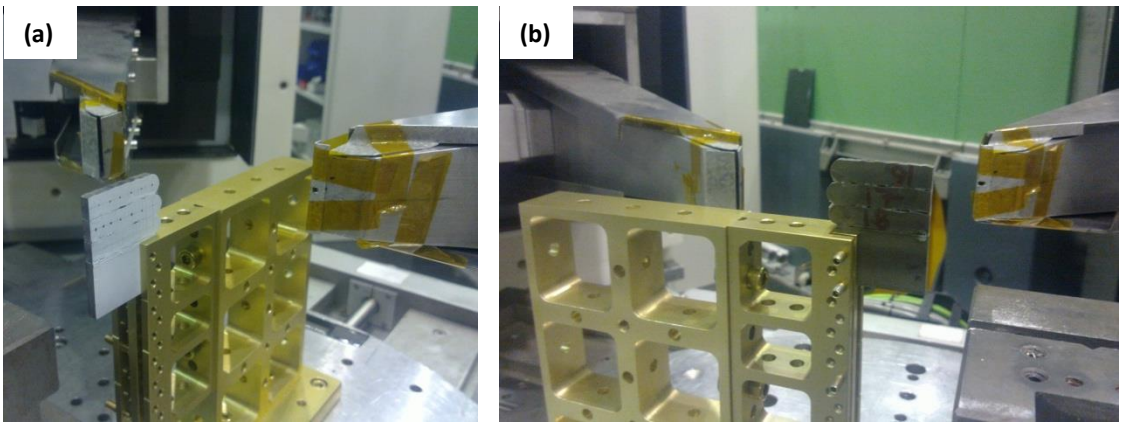

Figure 5.20 Positioning of samples (several glued together) for measurement of the unstrained inter-planar spacing in the (a) normal and (b) longitudinal directions. In each case the primary slits are to the right of the picture with the secondary slits and detector to the left, behind the sample.

The position of diffraction peaks in terms of scattering angle was determined by first plotting the experimental counts against angular position and then fitting these profiles with a Gaussian peak shape on a flat background. This fitting was performed using the QKowari software as shown in Figure 5.21 with the results for inter-planar spacing automatically calculated and exported to spreadsheets for further analysis. This data, in conjunction with measured values of d_0, was used to determine strains in the three principal directions using Equation 5.4. Principal stresses were calculated using Hooke's law for linear elasticity in a continuous body, as presented in Equation 5.6. The values of the elastic modulus and Poisson's ratio for the α-Ti (103) direction were calculated to be $E_{\alpha\text{-}Ti(103)}$ = 120.6 GPa and $\nu_{\alpha\text{-}Ti(103)}$ = 0.31 respectively using the diffraction elastic constants (DEC) and DECcalc software [239]. Once the principal stresses were determined, both hydrostatic, σ_H, and von-Mises equivalent, σ', stresses were calculated using Equations 5.8 and 5.9.

$$\sigma_H = \frac{1}{3}(\sigma_{xx} + \sigma_{yy} + \sigma_{zz})$$

Equation 5.8 Calculation of hydrostatic stress from principal stresses.

$$\sigma' = \sqrt{{\sigma_1}^2 + {\sigma_2}^2 + {\sigma_3}^2 - \sigma_1\sigma_2 - \sigma_2\sigma_3 - \sigma_1\sigma_3}$$

Equation 5.9 Calculation of von-Mises equivalent stress from principal stresses.

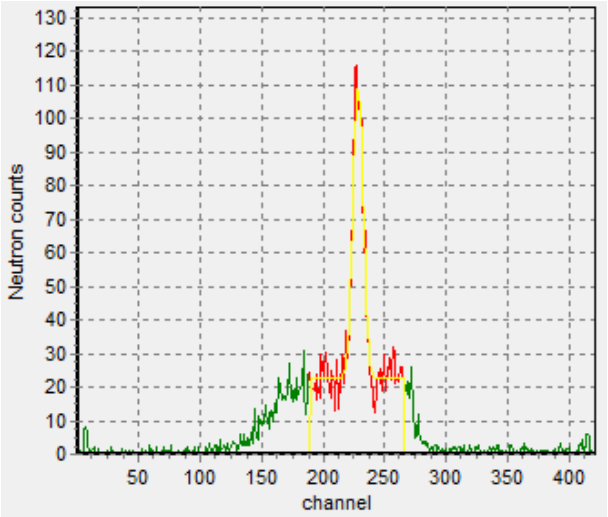

Figure 5.21 Determination of peak position using QKowari software. The red data series indicates the 'window' of experimental data to which the Gaussian fit (yellow) is applied.

Following neutron residual stress measurements, Walls 9, 10 and 11 were sectioned along the measurement plane (some 80 mm from the end of the base plate) in order to evaluate residual stresses destructively using the contour method. This work was performed by the Institute of Materials Engineering (IME) at ANSTO with little input from the author and as such results from these measurements will not be presented or discussed in this thesis, but rather they will be published in a co-authored paper in the near future. Such sectioning and measurement of residual stress was not performed on the remaining samples so that they would remain intact and so be able to be measured using TOF techniques in the future.

For those samples which were sectioned, a slice approximately 10 mm in thickness was removed using wire EDM cutting to allow examination of microstructure and measurement of mechanical hardness. These were prepared for metallographic examination through plane grinding and chemical mechanical polishing as recommended by Struers in application notes for preparation of titanium [27]. Samples were etched using Kroll's reagent (2 vol% HF, 6 vol% HNO_3 with balance H_2O) for optical microscopy, conducted using a Leica DMRM compound microscope, and macro-imaging with a Leica M205A stereo microscope and Canon EOS 60D digital SLR fitted with a 60 mm macro lens. Vickers microhardness of each sample was determined through automated testing on a Struers Durascan 70 equipped with Ecos Workflow software. Measurements were performed using a load of 0.5 kg and a dwell time of ten seconds. Approximately 1160 indents were made at 0.5 mm intervals in an array covering an area of 2 mm x 35 mm in the wall, and 9 mm x 20 mm in the base plate. All points were located to one side of the weld centreline with symmetry assumed about this line.

5.3 Results and Discussion

5.3.1 Qualitative Observations

Initial qualitative observations of the additively manufactured samples in the as-deposited condition revealed noticeable levels of angular distortion of the base plate section in both the longitudinal and transverse directions for all samples, as shown in Figure 5.22. Such distortion, due to the thermal contraction of the weld metal, is commonly observed in these bead-on-plate type welds and clearly indicates the

development of residual stresses during the welding process. Similar observations of distortion have been made by Martina *et al.* [171] in the additive manufacture of Ti-6Al-4V using plasma arc welding (PAW) with controlled wire addition. While not quantitatively characterised, the observed distortion was estimated to produce a deviation of approximately 1.0 mm along the length of the sample and 0.5 mm across the width of the base plate. It is suggested that future studies related to the additive manufacture of Ti-6Al-4V aim to relate such observations of distortion to measured values of residual stress by accurately characterising the distorted sample profiles using either a CMM or laser profile scanner.

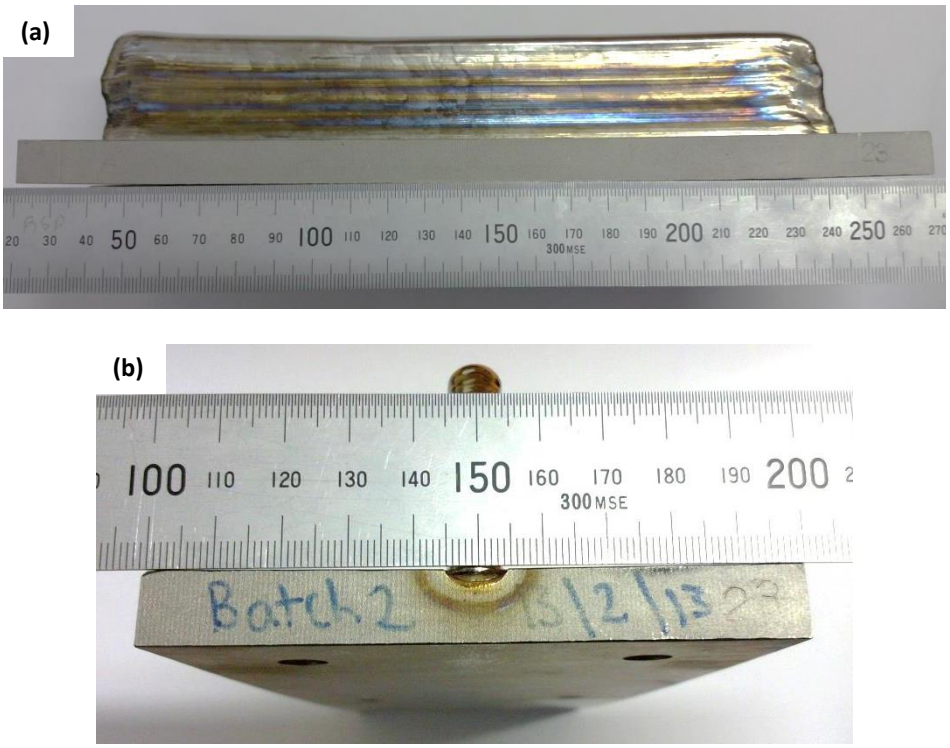

Figure 5.22 Angular distortion of the base plate in the (a) longitudinal and (b) transverse directions.

Observations of the sidewalls of additively manufactured samples in the as-deposited condition clearly revealed the prior β-Ti grain structure with large grains visible due to the significant growth which takes place during the repeated welding processes. With reference to the use of pulsed welding currents and their effectiveness in grain refinement, no clear dependence was observed, with large columnar prior β-Ti grains evident in samples produced with and without pulsed current as shown in Figure 5.23. From these figures it may be argued that those samples deposited using pulsed current show a more columnar morphology in the prior β-Ti grains, indicating promotion of the epitaxial grain growth. Full quantitative characterisation of microstructural features

including prior β-Ti grain size, α-Ti colony size and α-Ti lath width was not possible since preparation of suitable samples for metallographic analysis is destructive in nature and would render the additively manufactured sample as a whole useless for future studies of residual stress by TOF neutron diffraction techniques.

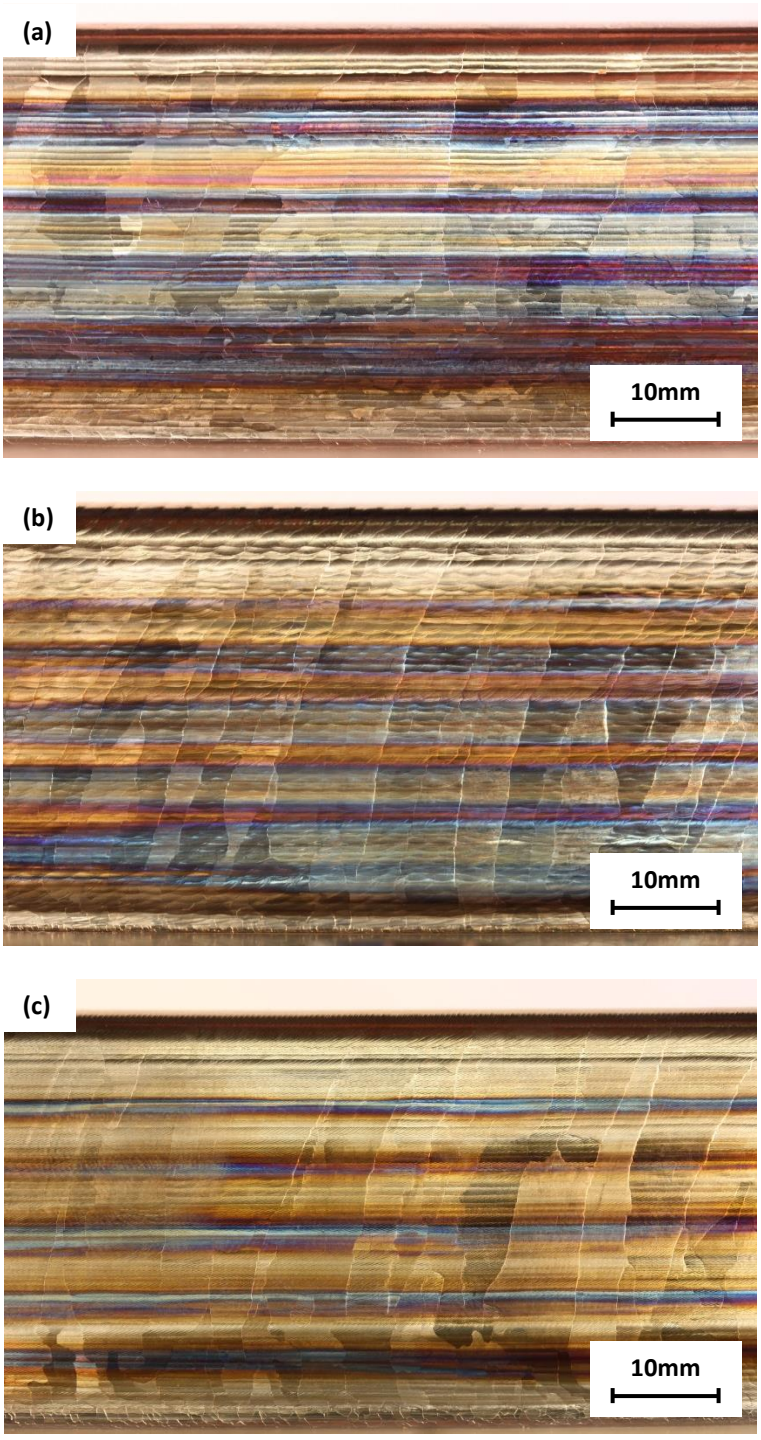

Figure 5.23 Macro photographs of the prior β-Ti grain structure in as-deposited additively manufactured Ti-6Al-4V produced using (a) constant arc current, (b) pulsed current at 1 Hz and (c) pulsed current at 5 Hz. In all cases the welding direction is from right to left.

5.3.2 Residual Stress

Considering then the measurement of the unstrained inter-planar spacing, d_0, values of this reference parameter were obtained in each of the principal directions for all samples using the thin slices described in Section 5.2. This gave values for d_0 in wrought and additively manufactured Ti-6Al-4V which could be used to determine elastic strains and hence residual stresses. Those values measured in the wrought material were seen to be in close agreement for all three principal directions, particularly at distances far removed from the HAZ, as shown in Figure 5.24a. As such these values were taken as being representative of a truly strain free lattice spacing for the α-Ti (103) planes, allowing the average d_0 value to be used in the subsequent determination of elastic strains at all measurement points within the wrought material. In contrast, the measurements of d_0 taken from additively manufactured material show great variability and so limited reliability, as illustrated in Figure 5.24b. This is attributed to the poor statistics associated with low neutron counts resulting from the highly oriented grain structure, which will be further addressed in the following sections of this discussion. In these locations where d_0 could not be accurately measured, values of the unstrained inter-planar spacing were found using the boundary condition of balanced biaxial plane stress at measurement locations close to the free surface [222, 240] where stress normal to the free surface is taken to be zero. In the vertical wall section of additively manufactured samples this implies the transverse stress is zero, while at subsurface locations within the base plate the normal stress is taken to be zero. This approach of 'deconvoluting' d_0 from an applied boundary condition of stress was verified using measurements performed in the wrought material, with the measured and deconvoluted values showing close agreement.

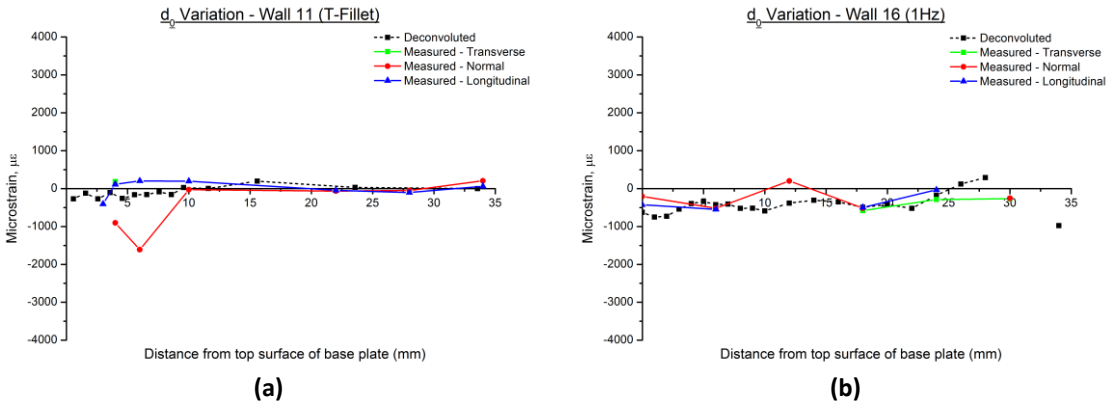

Figure 5.24 Comparison of measured and deconvoluted values for d_0 in terms of microstrain for (a) wrought plate and (b) additively manufactured Ti-6Al-4V.

Addressing firstly the residual stress measurements performed in the billet reference sample produced entirely through material removal (subtractive) processes, the plots of measured principal stress presented in Figure 5.25 show that this material is effectively free of any significant macroscopic residual stresses. Observed minor variations in residual stress may be related to those stresses induced during the casting and rolling processes used in initial forming of the billet. It is expected that much of these would have been relieved by heat treatments during processing as well as material removal used to form the final sample profile. As the majority of structural components produced from Ti-6Al-4V are produced in this manner, these results are taken to represent the 'benchmark' against which the additively manufactured samples must be assessed.

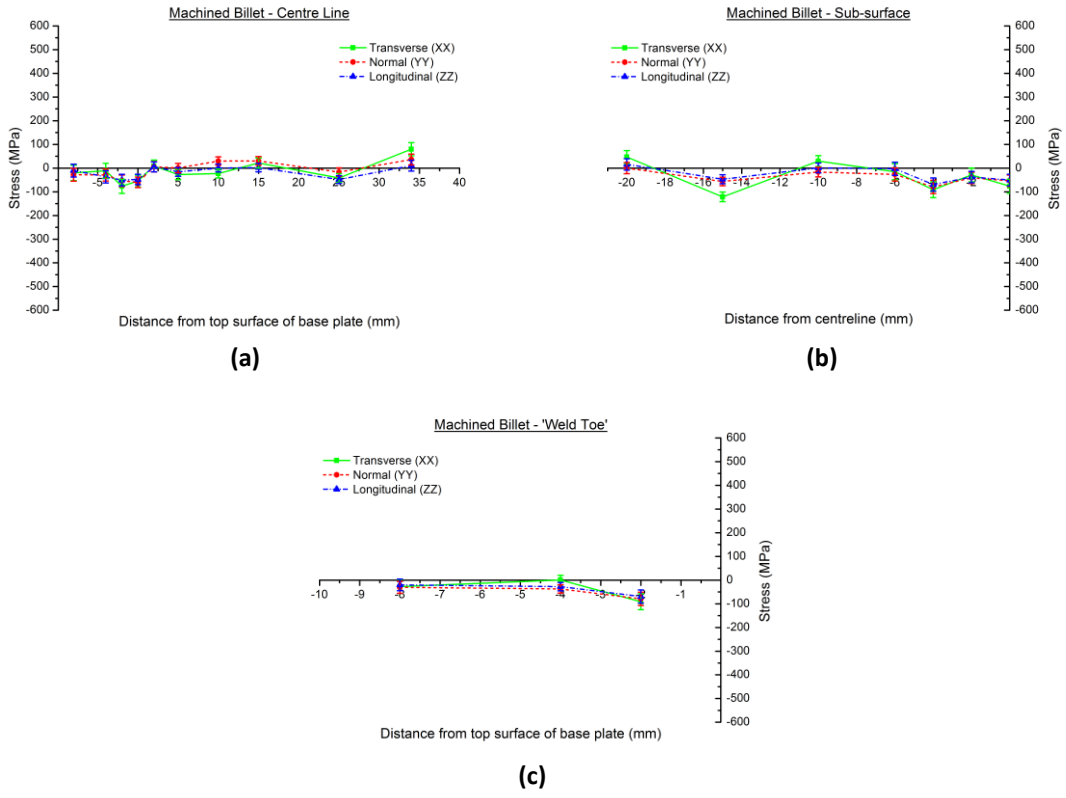

Figure 5.25 Measured residual stresses in transverse (XX), normal (YY) and longitudinal (ZZ) directions for the sample produced by subtractive manufacture from wrought Ti-6Al-4V billet (a) along the centreline of the thin wall feature, (b) below the top surface of the base plate and (c) in the base plate below what would be the weld toe.

Measured values of residual stress in the T-fillet sample produced by welded fabrication show significant stress levels, far greater than anything observed in the billet sample. In particular, stresses in the longitudinal direction were seen to be dominant in all regions of interest, as shown in Figure 5.26, with a peak tensile stress of approximately

400 MPa found in both fusion and heat affected zones of the vertical wall as well as the HAZ of the base plate. Tensile stresses in the order of 300 MPa were measured in the base plate beneath the toe of the weld line. The maximum compressive stresses were approximately 250 MPa in magnitude and located in the upper most regions of the vertical wall. The transition from tension to compression within the vertical wall feature is considered to be analogous to the elastic bending of a beam. In this case, the removal of clamping restraints used during the welding process changes the equilibrium of forces acting on the component, allowing it to distort angularly under the influence of imbalanced residual stresses. This results in the upper region of the wall being placed into compression and the lower regions into tension. Residual stresses in all three principal directions are seen to extend some 12 mm away from the weld centreline in the subsurface layer (2 mm below the free surface) of the base plate. This relatively broad distribution is attributed to the multi-pass welding procedure required to ensure full joint penetration and complete filling of the double-V preparation used to form the joint. These multiple welding passes generate a significantly broader HAZ than a single pass fillet weld and so give rise to the broadly distributed stress. This is also thought to be the origin of the high longitudinal stresses observed in the vertical wall, up to 10 mm away from the root of the joint.

The general profile of these residual stress distributions is consistent with literature [241-245], however the maximum measured stress values in the base plate are approximately 30 % lower than those reported by Song *et al.* [246] for a simple single pass T-fillet weld made in Ti-6Al-4V. The primary reason for this is thought to be the multi-pass welding used in the current study, with repeated thermal cycling of previously welded material giving an annealing type effect and so relieving residual stresses formed in prior welding passes. The apparent decrease in residual stresses measured in the base plate at the centreline of the vertical wall feature may be due to lack of fusion at the root of the joint, thus leaving what would be in effect free surfaces that are unable to support such stresses. However, no such defects were observed when the sample was sectioned to conduct residual stress measurements by the contour method and so this too is thought to originate from the annealing effects produced by multi-pass welding. Given the observed residual stress distribution, and with the maximum longitudinal stress in the fabricated T-fillet being approximately 50 % of the material's yield strength, it is considered that the mechanical behaviour of components

produced by welded fabrication would be significantly compromised unless further processing was used to relieve these stresses.

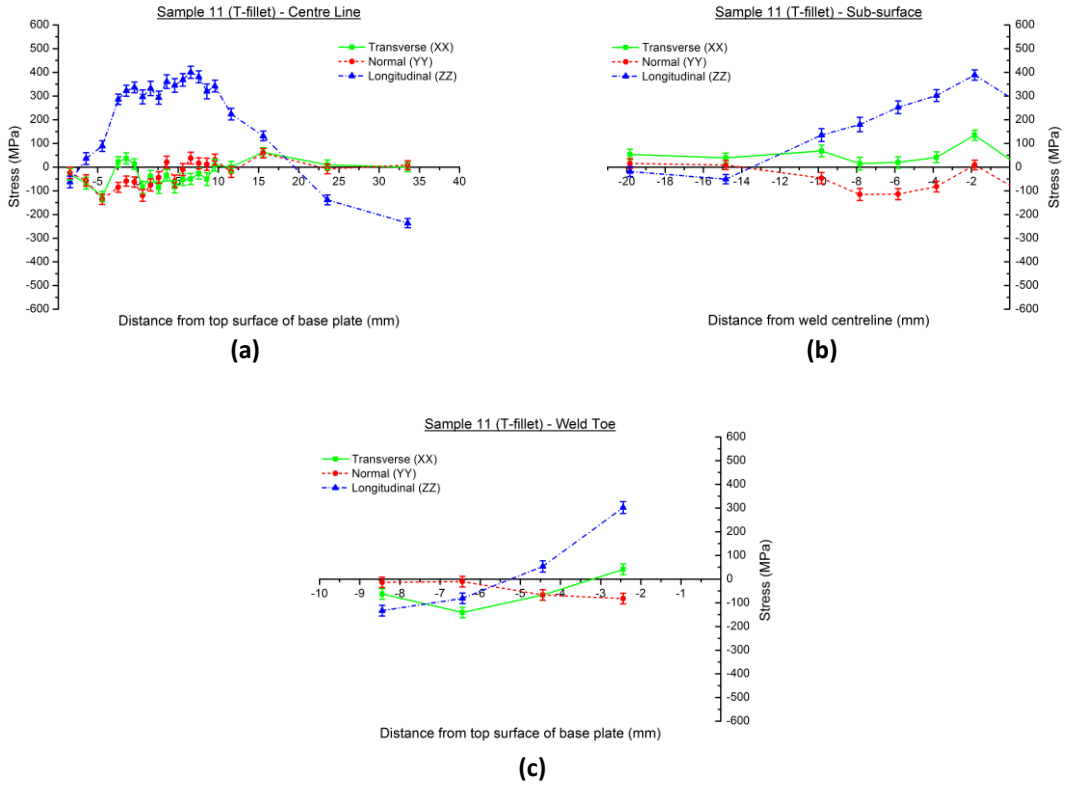

Figure 5.26 Measured residual stresses in transverse (XX), normal (YY) and longitudinal (ZZ) directions for the T-fillet sample produced by welded fabrication from wrought Ti-6Al-4V plate (a) along the centreline of the thin wall feature, (b) below the top surface of the base plate and (c) in the base plate below what would be the weld toe.

Considering then the measured residual stresses in samples of Ti-6Al-4V produced by GTAW-wire based additive manufacturing, general profiles were seen to be similar in form to those observed in the fabricated T-fillet sample, as shown in Figure 5.27. Again, the longitudinal stress is dominant in all regions of interest and shows a distinct transition from tensile to compressive stress along the centreline of the vertical wall. This transition can be readily explained by considering the general characteristics of the process. While the initial deposition of the first weld metal layer onto the base plate is essentially a single bead-on-plate process, the subsequent deposition of layers can be understood to influence the residual stress in two ways. Firstly, repeated thermal cycling may be considered analogous to a localised annealing process that relieves stresses generated from preceding welds. However the high temperatures experienced (approaching the melting point of the material) also give rise to further stresses from volume changes associated with thermal contraction and phase changes. Secondly, as

the build-up progresses the deposited wall acts as an integrated rib stiffening structure, and so further constrains the base plate in the longitudinal direction. When the additive manufacturing process is completed, the removal of mounting constraints (hold down bolts in this case) allows the structure to deform under the influence of residual stresses, resembling elastic bending of a beam. This part of the manufacturing process contributes to the observed transition from tensile to compressive longitudinal stress over the height of the wall.

Additionally, it is clear that the greatest variation in all three principal stresses is in the region adjacent to the interface between the wall and base plate. These results are in agreement with the those of Ding *et al.* [137] and Colegrove *et al.* [228], which show similar distributions of stress within additively manufactured wall structures. Additional plots showing residual stress distributions for the remaining additvely manufactured samples are presented in Appendix C.

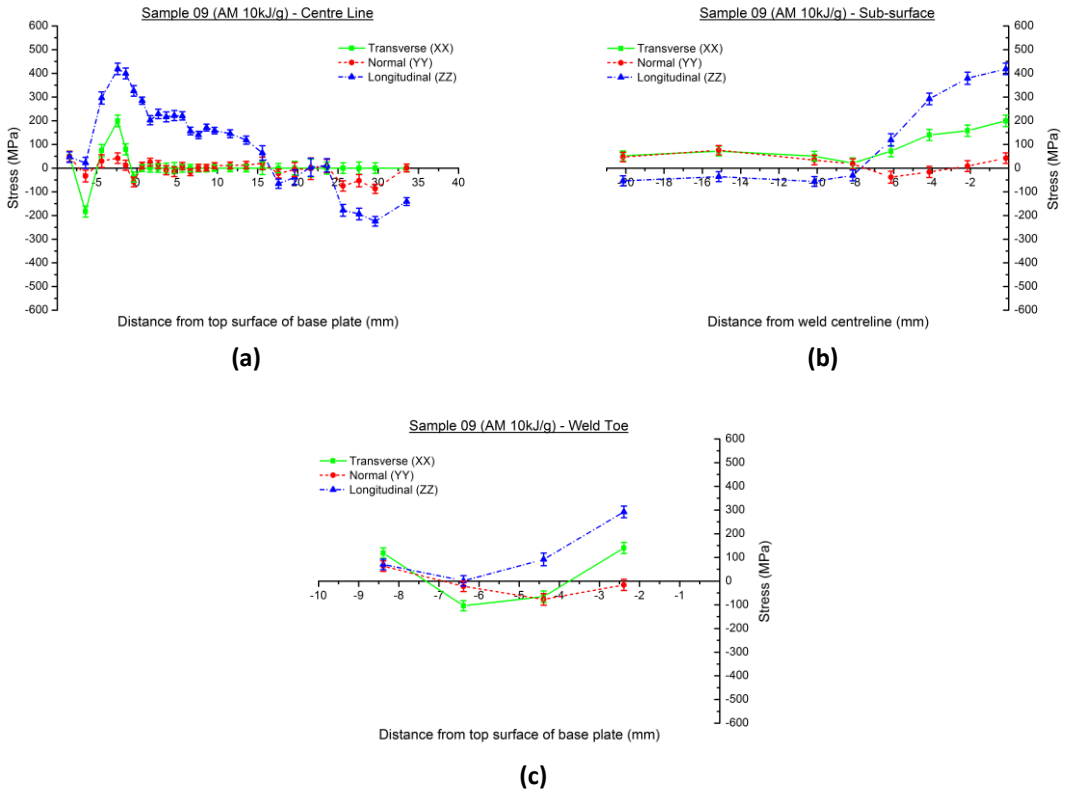

Figure 5.27 Measured residual stresses in transverse (XX), normal (YY) and longitudinal (ZZ) directions for the additively manufactured sample produced with low specific deposition energy (a) along the centreline of the thin wall feature, (b) below the top surface of the base plate and (c) in the base plate below what would be the weld toe.

From the preceding discussions it is clear that in all samples produced using fusion welding the residual stresses far exceed those in the sample produced by subtractive methods. It is also apparent that of the three principal directions, stresses are most significant in the longitudinal direction. This is unsurprising considering the severe thermal gradients in this direction, which combine with it having the greatest length and most significant constraint. Also, the majority of measurement points were located within 2.5 mm of a free surface, meaning much of the comparatively large 2 mm x 2 mm x 20mm gauge volume used for measurements in the normal and transverse directions was in regions where the balanced biaxial stress state exists and so stresses perpendicular to the free surface (i.e. in the transverse and normal directions) are negligible. As such, much of the remaining discussion relating to the influence of various additive manufacturing processing parameters will be confined to considerations of the longitudinal stress only.

Like the fabricated T-fillet sample, the residual stresses measured in additively manufactured samples show a maximum tensile residual stress of between 400 MPa and 500 MPa at locations on the weld centreline, near to the top surface of the base plate. As in the fabricated T-fillet sample, this maximum stress is approximately 50 % of the minimum yield strength specified for Ti-6Al-4V in ASTM B348 [197], far greater than any apparent stresses in the billet sample. Meanwhile, the region of maximum stress is seen to be narrower in samples produced by additive manufacture, with peak stresses more localised in areas near to the base of the wall feature, corresponding to the fusion and heat affected zones of the initial welding passes. This is evident in Figure 5.28 where the maximum longitudinal stress appears to be in the base plate rather than the vertical wall, as was the case in the fabricated T-fillet. One consequence of this more localised peak stress in the base plate material is the generation of a comparatively steep stress gradient through the thickness of the base plate, while simultaneously reducing the corresponding stress gradient over the height of the vertical wall. Figure 5.29 also shows that this region of peak stress is more concentrated in the direction perpendicular to the vertical wall, again producing comparatively steep stress gradients. This is readily explained considering that the HAZ which results from the GTAW-wire based additive manufacturing process, which is in effect a single bead-on-plate type weld, is far narrower than that of the multi-pass weld used in the fabrication of the T-fillet.

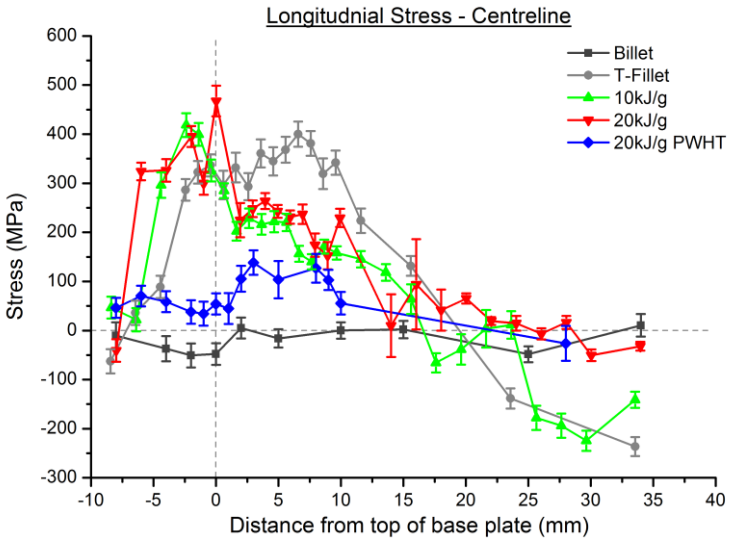

Figure 5.28 Comparison of longitudinal residual stresses along the weld centreline of additively manufactured samples produced with different specific deposition energies and PWHT.

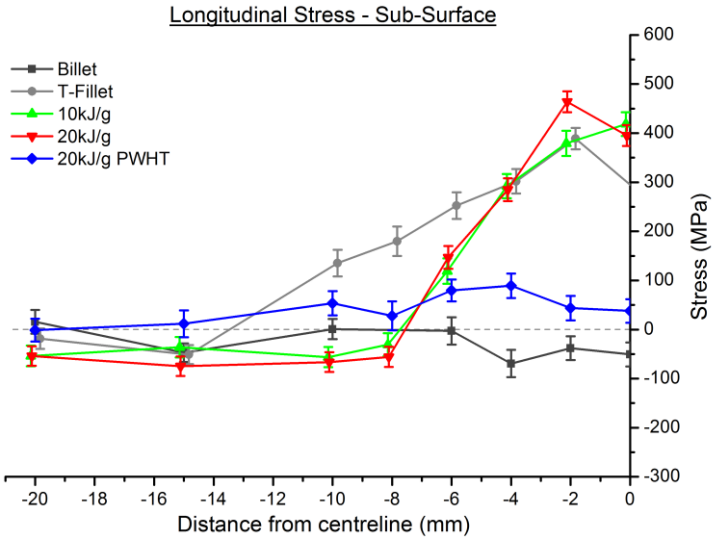

Figure 5.29 Comparison of longitudinal residual stresses in the base plate of additively manufactured samples produced with different specific deposition energies and PWHT.

While the use of differing specific deposition energies appears to have no significant influence on longitudinal residual stress across the majority of the additively manufactured components, some deviation is evident toward the top of the vertical wall. Here the sample produced with lower specific deposition energy (and hence higher deposition rate) shows a transition into compression similar to that observed in the fabricated T-fillet sample, while the longitudinal stress in the sample with higher specific deposition energy tends to reduce to a neutral value. In this case, the reduced

deposition rate yields less height build-up per pass and so produces more overlap of each HAZ with the previously deposited material. This would be expected to give a more thorough annealing effect and so reduce the need for the redistribution of stresses when the welding constraints are removed; reducing the elastic bending beam type response thought to causes the transition into compression.

As with the measurement of the unstrained inter-planar lattice spacing, the measured values of stress at some locations within the additively manufactured vertical wall show poor reliability. This is particularly evident in for that sample produced using nominal specific deposition energy of 20 kJ/g, where there are clear deviations from an otherwise consistent trend and comparatively large uncertainties in measured stress. Again, this is attributed to the highly oriented microstructure within large individual prior β-Ti grains which develops on solidification and cooling during each welding process.

Results presented in Figures 5.28 and 5.29 also show the ability of post-weld heat treatment to reduce residual stresses in Ti-6Al-4V structures produced by GTAW-wire based additive manufacturing. For the PWHT investigated it was found that longitudinal stress within the base plate was reduced significantly to an approximately constant tensile stress of less than 100 MPa, a reduction of some 75 %. While not fully eliminated or reduced to the levels apparent in the billet sample, longitudinal stresses along the centreline of the vertical wall were also significantly reduced, with a peak stress of less than 140 MPa. These reductions in residual stress are in agreement with those predicted for the PWHT using the stress relief nomograph presented in Figure 5.12. This suggests that stress relief techniques established for conventionally processed Ti-6Al-4V are equally suited to use in additively manufactured materials. It is also interesting to see that this relaxation of longitudinal stresses was accompanied by a redistribution of stresses such that the region of peak stress shifted from within the base plate to the bottom region of the vertical wall. This is presumably to maintain static equilibrium within the sample where uniform tension now exists in the base plate.

Residual stress distributions in samples of additively manufactured Ti-6Al-4V produced with pulsed arc current show similar general profiles to those observed in other additively manufactured samples produced with equivalent arc and specific deposition energies using constant arc current. This is illustrated in Figures 5.30 and 5.31. In

general, the distribution of longitudinal stress along the centreline of the vertical wall in those samples produced using pulsed arc current agree closely with that of the equivalent sample produced using constant arc current. The only exception appears to be an uncharacteristic reduction in longitudinal stress near to the top surface of the base plate in the sample produced using a current pulse frequency of 5 Hz. Significantly, all samples produced with nominal specific deposition energy of 20 kJ/g show a gradual reduction in tensile longitudinal stress with increasing distance from the base plate. Values appear to be approximately neutral at the top of the vertical wall, in contrast to the fabricated T-fillet and 10 kJ/g additively manufactured samples which exhibited a transition to compressive stresses. Again, the field of peak stress along this wall centreline is narrowed and located deeper below the top surface of the base plate when compared to the fabricated T-fillet sample. This is in line with observations made in additively manufactured samples produced using continuous arc current.

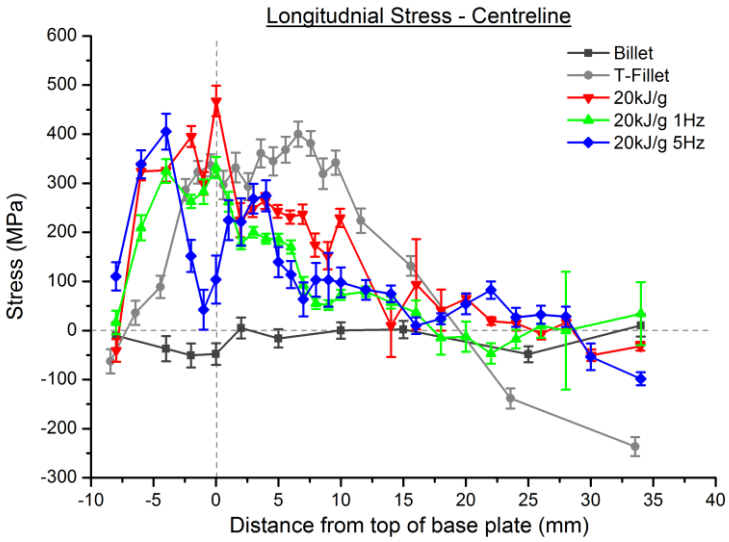

Figure 5.30 Comparison of longitudinal residual stresses along the weld centreline of additively manufactured samples produced using pulsed arc current.

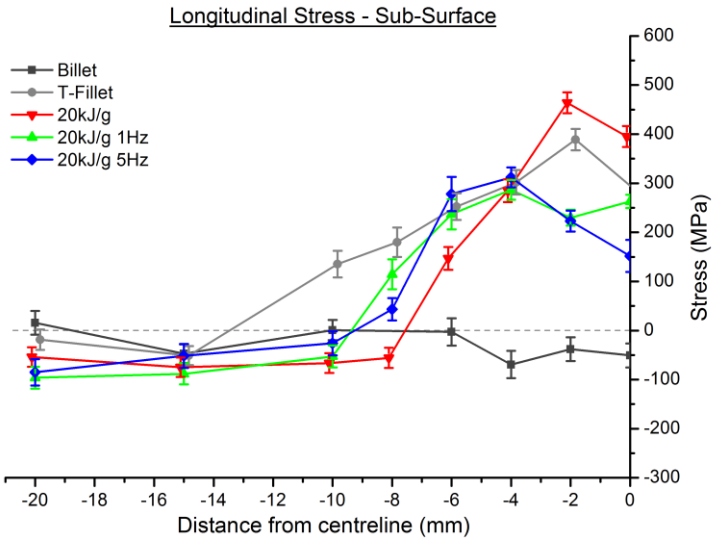

Figure 5.31 Comparison of longitudinal residual stresses in the base plate of additively manufactured samples produced using pulsed arc current.

Considering the distribution of longitudinal residual stresses in the subsurface of the base plate perpendicular to the vertical wall, there appears to be a broadening of the stress distribution due to the use of pulsed arc currents. This is accompanied by a reduction in peak stresses from 464 MPa ± 21 MPa to 312 MPa ± 20 MPa, as shown in Figure 5.31. The origin of these changes is thought to result from the effect of the pulsed welding current on the size of the fusion and heat affected zones. In order to achieve and equivalent arc energy (and hence heat input), the peak current used in pulsed welding must be substantially higher that the corresponding constant current value. As such, the size of the molten pool is comparatively larger when this peak current is operating, meaning the thermal effects which give rise to residual stresses are more widely distributed about the weld centreline. Further, the larger fusion and heat affected zones means there is an increased volume of material able to support the loadings produced by volume changes on cooling. The result is a reduction in the magnitude of peak stresses, which are more broadly distributed, compared to those resulting from an equivalent heat input produced using constant arc current.

It should be noted that this apparent broadening of residual stresses in the subsurface of the base plate could also be due to positioning errors in measurement locations used during neutron diffraction. Such errors are not related to inaccuracies with the positioning of the gauge volume at the locations within the sample prescribed through the SScanSS model, but rather from a lack of symmetry in the final sample profile due

to manufacturing processes. The CNC code used to machine the final sample profiles was such that the 5 mm thick vertical wall was positioned centrally across the width of the base plate. However, if the initial weld deposit was not centrally located on this base plate, then machining would have not been uniform with more of the deposited material would be removed from one side compared to the other. As a result the centreline of the wall and the centreline of the weld beads would not be coincident and measured stress distributions would appear to be translated away from their true location. While efforts were made to minimise such errors, the actual origin of the apparent broadening would only be revealed by conducting residual stress measurements on both sides of the wall feature, rather than only one side and assuming symmetry. While possible using neutron diffraction, the required experimental time for each sample would be impractically long and so the use of some other means such as the contour method is thought to be most appropriate.

In order to assess the potential impact of residual stresses on the mechanical behaviour of Ti-6Al-4V produced by GTAW-wire based additive manufacturing, it is necessary to consider both the hydrostatic and von-Mises equivalent stresses, which take into account principal stresses in all three directions. Hydrostatic stress is of particular importance since it is seen to influence fracture behaviour. Under externally applied loadings, the nucleation of micro-voids (and hence internal cracks) takes place at locations where hydrostatic tension is greatest. Hydrostatic tension also acts to distort the crystal lattice of the solid material, increasing the size of interstitial lattice positions. Such lattice distortions can facilitate the accumulation of impurities such as hydrogen in any regions with high hydrostatic tension which in turn can dramatically alter the mechanical properties and physical behaviour of the material. Meanwhile, the presence of hydrostatic compression can be understood to aid in the suppression of crack formation and hence prevent failure by fracture.

Considering firstly the fabricated T-fillet structure, it was found that tensile hydrostatic residual stresses exist broadly across the welded joint region with maximum magnitude of approximately 175 MPa found in the HAZ within the base plate, as shown in Figure 5.32. In contrast, the region of tensile hydrostatic stress in samples produced by additive manufacture is far more localised to the base plate directly below the vertical wall. In addition to being more concentrated, the maximum stress levels are also greater than in the fabricated T-fillet sample, reaching values of 220 MPa in samples produced

using constant arc current. As was observed in the dominant longitudinal stresses, the region of peak hydrostatic stress is further removed from the weld centreline and lower in magnitude in samples produced using pulsed arc current. Again, the effectiveness of PWHT on relieving residual stresses is clear when considering hydrostatic stress, with the heat treated sample showing average and maximum tensile hydrostatic stresses of 31 MPa and 66 MPa respectively. Additional plots showing distribution of hydrostatic residual stress for the remaining additvely manufactured samples are presented in Appendix C.

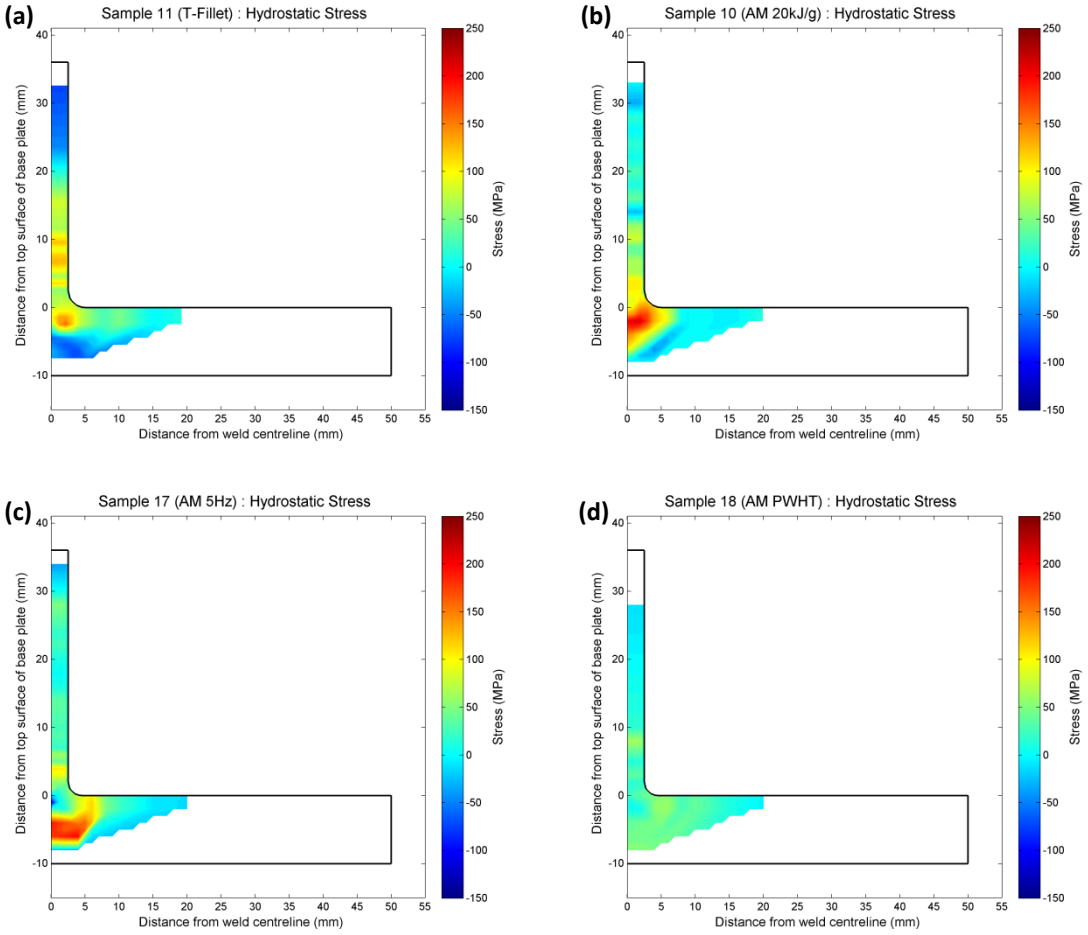

Figure 5.32 Distribution of hydrostatic stresses in additively manufactured and fabricated thin walled structures.

From these observations it is considered that the region adjacent to the intersection of the base plate and additively manufactured deposit would be most susceptible to failure by fracture. These areas would be prone to crack formation during service in a structural application due to the combined effects of relatively high levels of hydrostatic tensile stresses and stress concentration of externally applied loadings by the abrupt corner

geometry. Should the measured levels of hydrostatic residual stress be deemed too high for an intended application, additional processing such as PWHT would need to be employed.

Von-Mises equivalent stress is commonly used to characterise the cumulative effect of a complex stress state on the mechanical behaviour of a material or component as a single parameter. While von-Mises equivalent stress is predominantly used to assess yielding and plastic deformation behaviour, it also has application in assessing the fatigue performance under complex combined loadings. As was observed with hydrostatic stresses, the fabricated T-fillet structure showed the broadest distribution of elevated von-Mises equivalent stress, extending approximately 10 mm up the vertical wall, 10 mm away from the weld centreline and 4 mm deep in the base plate, as shown in Figure 5.33. Within this region, the maximum von-Mises equivalent stress was 415 MPa. Conversely, the region of greatest equivalent stress in samples produced by additive manufacture was more localised in terms of extension into the vertical wall and distance from the welding centreline, but extended further into the base plate, consistent with observations of the dominant longitudinal stresses. In most cases the peak equivalent stress was found in the base plate, corresponding to the fusion and head affected zones of the initial weld bead and was less than 350 MPa. The sole exception to this was the sample produced with nominal specific deposition energy of 20 kJ/g, where the peak equivalent stress was calculated to be 581 MPa, however this corresponds to the erroneous value of longitudinal stress which resulted from uncertainty associated with localised grain orientation. As was observed in both the longitudinal and hydrostaic stresses, the region of peak von-Mises equivalent stress is further removed from the weld centreline and lower in magnitude for those samples produced using pulsed arc current. Again, the effectiveness of PWHT on relieving residual stresses is clear when considering effective stress, with the heat treated sample showing average and maximum values of 51 MPa and 151 MPa respectively. Additional plots showing distribution of von-Mises equivalent stress for the remaining additvely manufactured samples are presented in Appendix C.

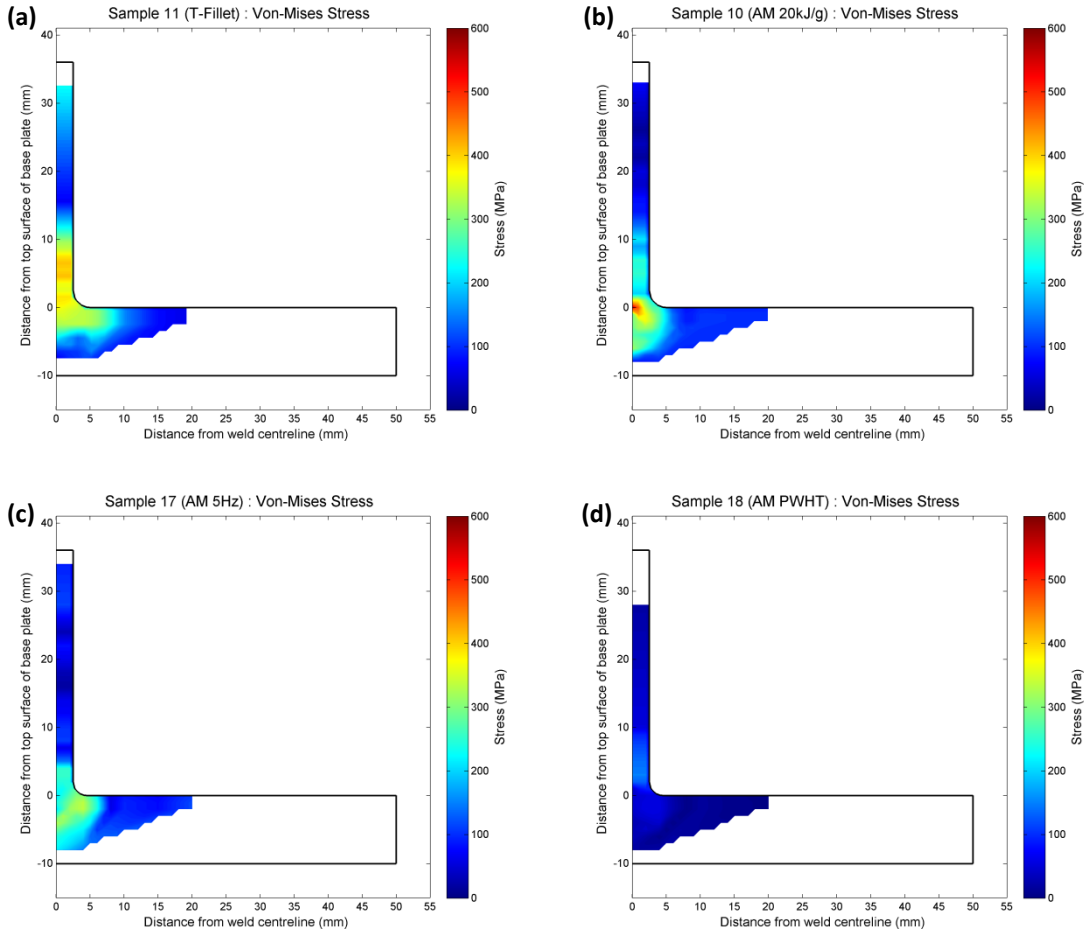

Figure 5.33 Distribution of von-Mises equivalent stresses in additively manufactured and fabricated thin walled structures.

As with measured values of hydrostatic stress, observations of von-Mises equivalent stress show that the region of material directly adjacent to the intersection of the base plate and additively manufactured deposit would be most susceptible to failure by yielding or fatigue. In service in a structural application this would be due to the combined effects of relatively high levels of equivalent stress and stress concentration of externally applied loadings resulting from the abrupt corner geometry. In particular, the proximitity of elevated equivalent stresses to the free surface may be concerning in fatigue critical applications, with fatigue failures commonly initiated at such surfaces where defects and damage are present. The mechanical behaviour of such structures, be they manufactured additively or through welded fabrication, could be enhanced through additional processing such as PWHT.

Finally, it is acknowledged that the removal of a significant portion of the deposited weld metal through finish-machining will have altered the as-deposited residual stress

within both the additively manufactured and fabricated T-fillet components. Measurements were intentionally made in this final machined condition as this most closely represents the final form that a component produced by arc-wire based additive manufacturing would be expected to take. As such, the stresses present in this condition are considered more relevant than those in the as-deposited profile. It is possible that minor additional stresses were generated in the component during the machining process. However, these are considered to be confined to small regions directly adjacent to the machined surface, which cannot be assessed through neutron diffraction due to the gauge volume being much larger than the volume of affected material adjacent to the machined surface.

Future studies could be performed before and after machining to assess the impacts of residual stresses. Further, the work of the present study was concentrated on characterising residual stresses within the central region of the weld, where steady state conditions exist. Additional work is required to characterise variations in residual stresses along the length of the additively manufactured structure, particularly at the start and end regions where both welding conditions and mechanical constraints differ. Such studies would be best conducted using time-of-flight (TOF) neutron diffraction techniques which allow the simultaneous measurement of multiple diffraction peaks from various lattice planes, and so would counter one of the main shortcomings of the present research where only the α-Ti phase was considered, neglecting both the macro stresses in the β-Ti phase and intergranular micro stresses.

5.3.3 Microstructure

Observations of the macro-structure of additively manufactured samples showed typical bead-on-plate type fusion and heat affected zones within the base plate, while banding was apparent in the vertical wall section corresponding to the deposition of successive layers of material. As seen in Figure 5.34, the spacing of these bands is far larger for that sample produced with a nominal specific deposition energy of 10 kJ/g since this sample has higher deposition rate, and hence build-up per pass. These macro photographs also show the large prior β-Ti grain size which can exceed several millimetres in equivalent diameter, and in the base plate, indents from Vickers microhardness testing.

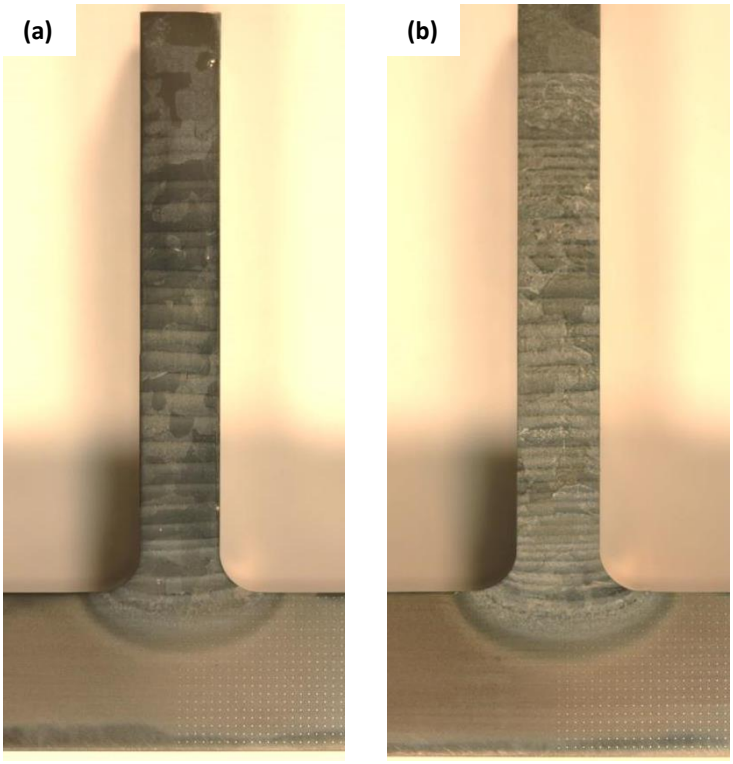

Figure 5.34 Macro photographs of additively manufactured samples produced with nominal specific deposition energies of (a) 10 kJ/g and (b) 20 kJ/g.

Analysis of as-deposited weld microstructures by optical microscopy revealed solidification type structures typical of Ti-6Al-4V weldments, with large equiaxed prior β-Ti grains in excess of 1 mm in the FZ and ranging from 100 μm to 500 μm in the HAZ. No significant coarsening of the β-Ti grains was observed with increasing build-up height. As described in Chapter 3, these large grains are understood to form through epitaxial grain growth on solidification, with those grains showing preferred orientation with respect to the thermal gradient becoming dominant. Upon cooling, the Widmanstätten laths of α-Ti nucleate heterogeneously and grow into the large prior β-Ti grains to produce the so-called 'basket weave' morphology. In this, the orientation of the α-Ti laths is directly related to that of the prior β-Ti grains according to the Burgers orientation relationship. As such, the final microstructure consists of colonies of aligned α-Ti laths surrounded by retained β-Ti as seen in Figure 5.35.

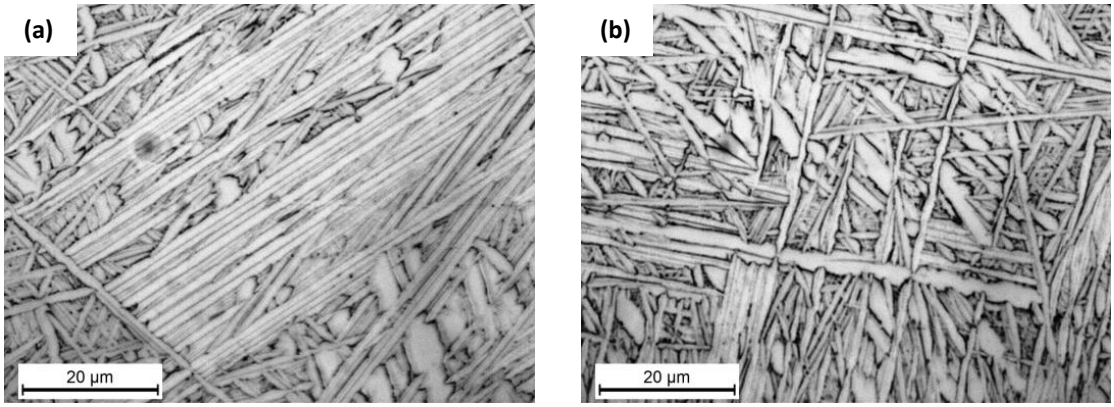

Figure 5.35 Optical micrographs of the as-deposited microstructure in (a) the top region and (b) the bottom region of the thin-walled structure

Optical micrographs reveal a more refined structure in the bottom region of the wall with less alignment of adjacent laths and reduced lath aspect ratios. This is attributed to the increased thermal cycling experienced by this bottom region from subsequent weld layers. The strong alignment of α-Ti laths within each colony gives rise to localised regions of strong orientation. Since neutron diffraction experiments were conducted solely on the α-Ti (103) planes, any region of localised orientation presents difficulties in measurement of inter-planar lattice spacing, since there is reduced likelihood of the <103> type being oriented favourably with respect to the scattering vector. This localised orientation is believed to be a major contributing factor in difficulties experienced in neutron diffraction strain measurements at discrete locations within regions of additively manufactured material. These difficulties, created by relatively low scattering counts resulting in poor resolution of the diffraction peak, have also been observed by Nishida *et al.* [247] in the measurement of residual stresses in Ti-6Al-4V castings by neutron diffraction. Such difficulties could be overcome by using significantly longer measurement times and measurement of numerous crystallographic orientations, or preferably by employing TOF diffraction techniques, allowing the simultaneous measurement of more than one crystallographic reflection.

5.3.4 Microhardness

Mechanical properties of additively manufactured structures produced using constant arc current were quantitatively assessed through microhardness testing, conducted in an array across the sectioned plane of these samples used for the contour method. These results, presented in Figure 5.36, show a steady value of approximately 325 HV in the majority of the additively manufactured material in both samples. While this extended

across the entire additively manufactured region of the sample produced with nominal specific deposition energy of 20 kJ/g, the microhardness appears to decrease in that produced with 10 kJ/g from approximately 20 mm from the top surface of the base plate onward. The most pronounced drop occurs in the final (top) 5 mm of the wall, to a value of approximately 305 HV. Although this decrease in microhardness appears to correspond to the previously described transition of longitudinal stress from tension to compression, there is no sound evidence that the two observations are linked. This variation in microhardness does however correspond to the observed change in microstructure and HAZ of the final welding pass and so is also linked to the greater number of thermal cycles experienced by this bottom region, giving a more refined, normalised microstructure with somewhat higher hardness.

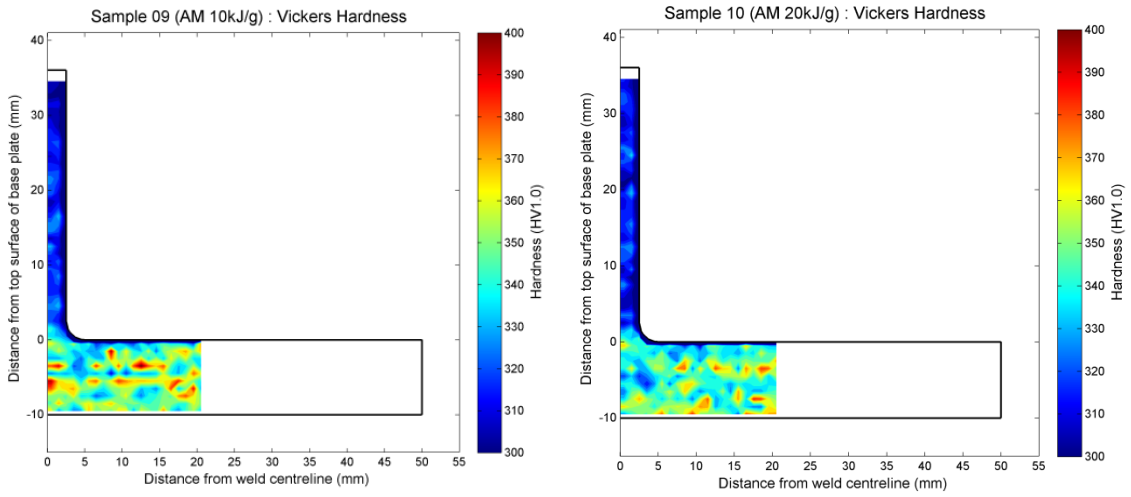

Figure 5.36 Variation in microhardness across the additively manufactured profiles and base plates of samples used for residual stress measurement.

The microhardness of the wrought base plate material is significantly higher than that of the additively material, with an average value of approximately 350 HV compared to the average of less than 320 HV in the additively manufactured material. This difference in hardness may be related to differences in chemical composition between the wrought plate and drawn wire used to produce samples. Additionally, it is clear that the microhardness is far more uniform in the additively manufactured material, than in the roll-formed base plate. The ‘bands’ of high hardness observed in the base plate, are attributable to the heterogeneous rolled microstructure that is present in those regions as a result of the TMP used to form the plate.

5.4 Conclusions

Residual stress in samples of Ti-6Al-4V produced by GTAW-wire based additive manufacturing were characterised using neutron diffraction techniques. Of particular interest was the influence of key process parameters, namely specific deposition energy and pulsed arc current. The effectiveness of conventional PWHT in the relief of these thermally induced residual stresses was also examined, with all results compared to measurements taken in reference samples produced by subtractive manufacturing and welded fabrication. Residual stresses were analysed in the three principal directions at numerous points located in the three key regions of each sample; along the weld centreline, below the weld toe through the thickness of the base plate and below the surface or the base plate at increasing offset from the weld centreline. Microstructure of additively manufactured samples was examined and mechanical properties assessed through microhardness testing.

Measurement of lattice strains in some locations proved difficult due to strong localised grain orientation related formation of α-Ti colonies within the prior β-Ti grain boundaries. In particular, the measurement of unstrained lattice spacing, d_0, produced unreliable values in additively manufactured material, requiring the use of d_0 values calculated using suitable boundary conditions with respect to stress normal to a free surface.

As would be expected, no significant macro stresses were found in the reference sample produced by machining from wrought billet material. In contrast, distinct residual stress distributions were observed in all additively manufactured samples, with general stress profiles in agreement with both the fabricated T-fillet sample and literature. In all samples the longitudinal stress was found to be dominant. Compared to the fabricated T-fillet, additively manufactured samples showed similar levels of peak stress approaching 50 % of the specified yield strength for Ti-6Al-4V. These regions of peak stress were far more concentrated in additively manufactured samples and were predominantly localised in the HAZ of the base plate. Samples produced using pulsed arc current showed a slight broadening of the longitudinal stress distribution within the base plate, with lower peak stress levels compared to equivalent samples produced

using constant arc current. Analysis of hydrostatic and von-Mises equivalent stresses showed similar trends to those observed in the dominant longitudinal residual stresses.

The use of conventional post-weld heat treatment proved effective in significantly reducing residual stresses within samples of Ti-6Al-4V produced by GTAW-wire based additive manufacturing, suggesting that stress relief techniques established for conventionally processed Ti-6Al-4V are equally suited to additively manufactured materials.

Optical microscopy revealed a basket weave microstructure of Widmanstätten α-Ti laths in a matrix of retained β-Ti, as would be expected for fusion welded Ti-6Al-4V. Microhardness was seen to reduce towards the top region of the additively manufactured wall in samples where high deposition rates were used, corresponding to deposited material that had not been subjected to reheating by subsequent welding layers. A distinct difference in microhardness was observed between the additively manufactured material and the wrought base plate, with the additively manufactured region showing greater homogeneity.

It is intended that the results of this study would generate a basic understanding of residual stresses in additively manufactured titanium components and how they may be influenced by processing parameters. Further, it is hoped that these results act as a foundation for future studies and more comprehensive assessment of the GTAW-wire based additive manufacturing process and point to methods of controlling any adverse effects of residual stress.

CHAPTER 6 – ATMOSPHERIC CONTAMINATION

6.1 Introduction

One of the attractive properties of titanium and its alloys is the excellent corrosion resistance which results from the dense, stable oxide that forms on the surface due to titanium's high chemical affinity for oxygen [27]. As temperature is increased, the reactivity of titanium with oxygen also increases. Above approximately 500 °C the corrosion resistance is lost as the stable oxide layer decomposes, readily allowing the diffusion of oxygen and other interstitial species into the bulk material [180]. Such contamination is seen to produce embrittlement of the material with increased strength and hardness and reductions in ductility and toughness [180, 248]. Understandably, this high temperature oxidation behaviour contributes to the common perception that welding of titanium alloys is problematic, particularly when not performed in a strictly controlled environment. Being a fusion welding process, it is clear that these aspects of atmospheric contamination must be considered when evaluating the GTAW-wire based additive manufacture process for the production of components from Ti-6Al-4V.

Table 6.1 illustrates the effect of interstitial impurities on the mechanical behaviour of commercially pure titanium (ASTM grades 1-4) as well as the Ti-6Al-4V alloy, with data for standard and extra low interstitial (ASTM grades 5 and 23 respectively) variants presented. The effect of oxygen on the strength of the Ti-6Al-4V alloy is illustrated more clearly in Figure 6.1. Many of the changes in mechanical behaviour can be related to the way in which oxygen, and to a lesser extent other interstitial species such as nitrogen, hydrogen and carbon, distort the crystal lattice structure. In the α-Ti phase, the presence of interstitial oxygen distorts the hexagonal close-packed crystal lattice structure, altering the aspect ratio of lattice parameters and so reducing the number of active slip planes for dislocation movement from three to one [104, 249]. While increased oxygen content is seen to reduce the ductility of the β-Ti phase, there is no evidence to suggest subsequent embrittlement [250], with oxygen acting to supress the formation of the ω-Ti phase [21]. Discussions relating to the influence of oxygen on the properties of Ti-6Al-4V are predominantly concerned with its interactions in the α-Ti phase since this is the dominant phase in Ti-6Al-4V and because oxygen is a potent stabiliser of the α-Ti phase.

Table 6.1 Maximum allowable impurity contents for ASTM grades of commercially pure titanium and Ti-6Al-4V with mechanical properties included to illustrate the effect of oxygen and nitrogen on mechanical behaviour. Compiled from ASTM B348 [197], Aerospace Specification Metals, Inc. [109-112, 251, 252] and CES Edupack [25].

ASTM Grade	Composition, maximum allowable (wt%)								
	C*	H*	N*	O*	Fe*	Residuals#	Al	V	Ti
1	0.08	0.015	0.03	0.18	0.20	0.4	-	-	balance
2	0.08	0.015	0.03	0.25	0.30	0.4	-	-	balance
3	0.08	0.015	0.05	0.35	0.30	0.4	-	-	balance
4	0.08	0.015	0.05	0.40	0.50	0.4	-	-	balance
5	0.08	0.015	0.05	0.20	0.40	0.4	5.5-6.75	3.5-4.5	balance
23	0.08	0.0125	0.03	0.13	0.25	0.4	5.5-6.5	3.5-4.5	balance

*Maximum allowable compositions
#Maximum allowable total of all residuals

ASTM Grade	Yield Strength (MPa)	σ_{ts} (MPa)	Ductility (%EL)	Hardness, Vickers (HV)	Charpy Impact Toughness (J)	Fracture Toughness ($MPa.m^{1/2}$)	Fatigue Strength (MPa)
1	170	240	24	122	140	58	200
2	275	345	20	145	65	58	271
3	380	450	18	225	27	53	331
4	483	550	15	280	-	48	386
5	828	895	10	349	17	75	510
23	759	828	10	341	24	100	300

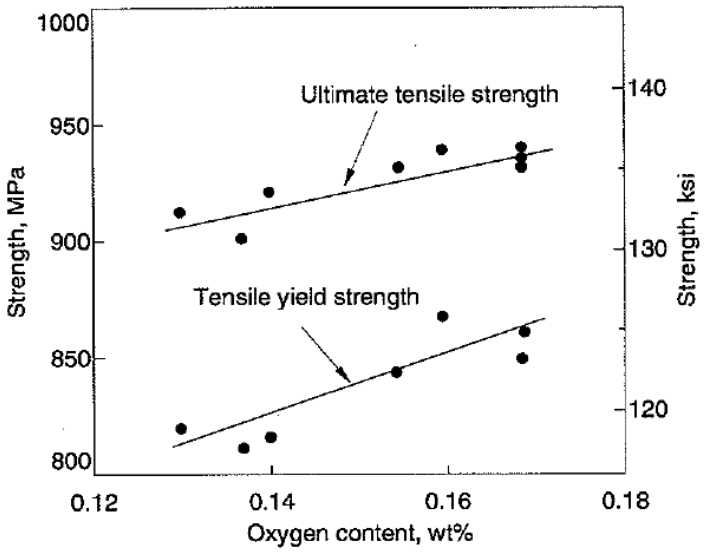

Figure 6.1 Relationship between oxygen content and yield and ultimate tensile strengths in Ti-6Al-4V. From Boyer *et al.* [21]

In Ti-6Al-4V, an alternating layered structure of Al_2O_3 and TiO_2 exists on the exterior of the metal, with the Al_2O_3 being at the free surface and TiO_2 being directly adjacent to the bulk titanium [253]. It is this oxide layer which provides corrosion resistance, however cracking is possible between these layers, compromising the mechanical properties and oxidation resistance of the material. Above 400 °C to 500 °C this oxide film becomes unstable and dissolves with the oxygen going into solid solution [21, 180]. The formation of the Ti[O] solid solution from decomposition of TiO_2 is accompanied by a reduction in volume of approximately nine percent [193]. Oxidation continues with sustained exposure at elevated temperatures and can be characterised through mass gain as shown in Figure 6.2. The reaction rate of oxidation for Ti-6Al-4V as a function of temperature is illustrated in Figure 6.3, being firstly logarithmic in the temperature range from 300 °C to 500 °C, then parabolic from 500 °C to 750 °C and finally linear above 750 °C. Grain size is seen to have a significant influence of oxidation behaviour, with increased oxygen pick-up in fine grained Ti-6Al-4V structures such as those used in superplastic forming processes [254], indicating the significance of grain boundary diffusion mechanisms. While the diffusion of aluminium and vanadium is relatively slow below approximately 550 °C, interstitial oxygen becomes mobile above 350 °C [250] and is understood to diffuse away from grain boundaries up to an order of magnitude faster than the substitutional alloying elements [193]. Temperature is seen to have greater influence on the rate of oxygen diffusion than time, with little additional increase in surface hardening for extended exposure times [255]. This temperature dependence is also more pronounced for intragranular diffusion compared to the grain boundary diffusional processes in Ti-6Al-4V [254].

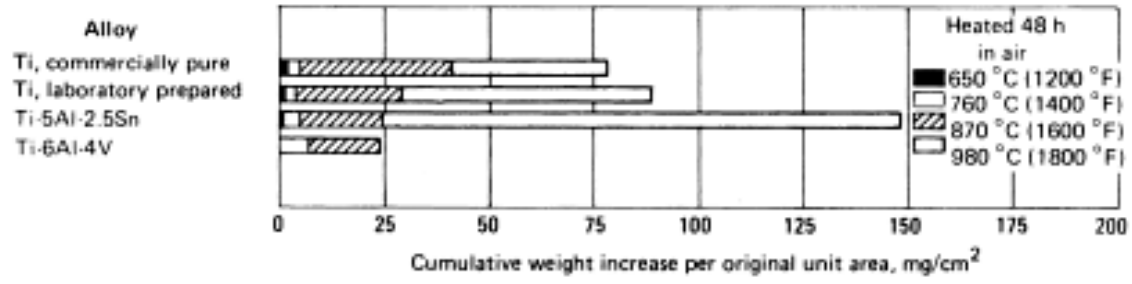

Figure 6.2 Mass gain of a number of titanium alloys held for 48 hours in air at various temperatures to assess oxidation. From Figure 5.4, Donachie [121]

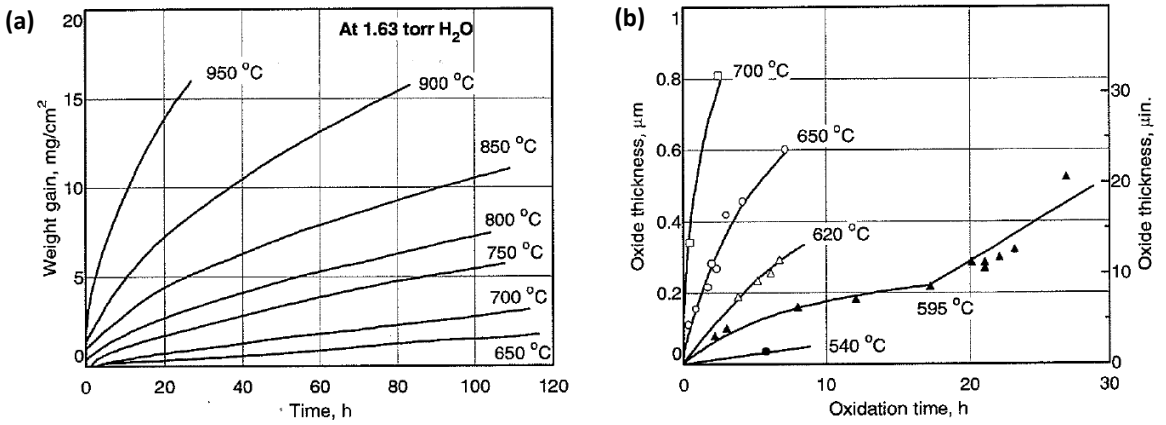

Figure 6.3 Oxidation of Ti-6Al-4V as a function of temperature in terms of (a) weight gain and (b) oxide thickness. From Boyer *et al*. [21].

The atmospheric contamination of Ti-6Al-4V during thermomechanical processing, particularly by oxygen, and its subsequent effects on mechanical performance has been extensively documented. The two main effects of oxygen contamination in Ti-6Al-4V are reduced volume fraction of the β-Ti phase and formation of an interstitial solid solution [255, 256]. With reference to the first effect, atmospheric contamination of titanium alloys by oxygen is often characterised by the formation of the so-called 'alpha case' at the exposed surface where the α-Ti phase is heavily stabilised by high oxygen content. This alpha case is harder and less ductile than the bulk Ti-6Al-4V, meaning the contaminated section of material acts as a composite with unpredictable mechanical properties due to stress concentration effects [192, 255]. While this alpha case is readily removed after thermomechanical processing by chemical milling, doing so is potentially hazardous to workers and may lead to hydrogen contamination and embrittlement of the material [248]. In high concentrations hydrogen is also effective at pinning grain boundaries in Ti-6Al-4V, which is particularly useful in producing ultra-fine grain structures for superplastic forming applications [257, 258]. It must be emphasised that the thickness of the alpha case corresponds only to the depth to which the oxygen concentration is sufficient to supress the formation of the β-Ti phase. As the actual depth of penetration of contaminant oxygen extends beyond this, chemical removal of surface layers may not remove all affected material. The stabilising effect of oxygen means increased oxygen contents can also lead to precipitation of secondary α-Ti within retained β-Ti during heat treatments [250].

Considering then the effects of oxygen in forming a solid solution, by occupying interstitial lattice positions, the hexagonal close-packed crystal lattice structure of α-Ti

becomes distorted. As a result, pyramidal and basal slip become favoured over prismatic slip and a more heterogeneous dislocation structure occurs [259, 260]. This altered dislocation slip behaviour produces the reduced ductility and increased strength associated with increasing oxygen content, with hardness also seen to link directly to the square root of oxygen content [250]. Figure 6.4 shows the depth of hardening in Ti-6Al-4V due to prolonged exposure to elevated temperatures. While both oxygen and aluminium stabilise the α-Ti phase, increased levels of oxygen reduce the solubility of aluminium in titanium which in turn promotes formation of the α_2 (Ti_3Al) phase, particularly above 500 °C where oxygen mobility is increased and ordering is not favoured [260]. These precipitates promote coarse planar glide on the $\{10\bar{1}0\}$ prismatic planes and may be produced through heat treatment processes to counter the heterogeneous slip resulting from lattice distortions [261].

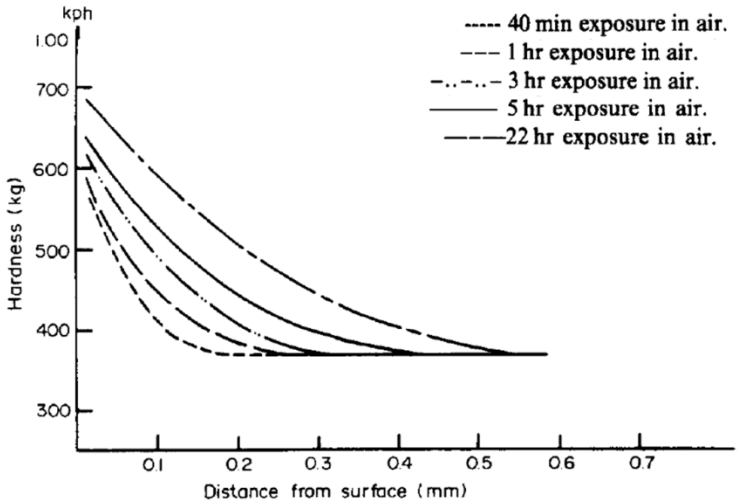

Figure 6.4 Depth of hardening (Knoop pyramid hardness) in Ti-6Al-4V due to prolonged exposure to air at 900°C. From Figure 1, Bendersky and Rosen [192].

Being a thermal process, fusion welding of titanium and its alloys can lead to atmospheric contamination of the fusion and heat affected zones, and so loss of mechanical properties in the welded joint. The gas tungsten arc welding process is used extensively for welding of titanium and titanium alloys due to its low capital costs and ability to produce high quality welds [159, 262]. While showing lower contamination potential than other arc-based fusion welding processes, the GTAW process is still susceptible to a small degree of atmospheric contamination regardless of the material being welded, as shown in Figure 6.5. In the GTA welding of titanium the most likely sources of contamination are oxygen and nitrogen from entrainment of air into the inert

shielding envelope by turbulence, impure shielding gases and hydrogen from moisture and surface contamination [263]. In addition to the general effects of atmospheric contamination discussed previously, contamination by hydrogen can lead to precipitation of titanium hydrides and hydrogen assisted cold cracking (HACC) which originates in regions of high triaxial stress such as those formed by residual stresses [107, 108]. According to Mathers [263], the maximum allowable limits for oxygen, nitrogen and hydrogen in titanium welds are 0.30 wt%, 0.15 wt% and 150 ppm respectively. It follows then that the reduction or elimination of such contamination is key in the execution of high quality welds as required for typical titanium applications.

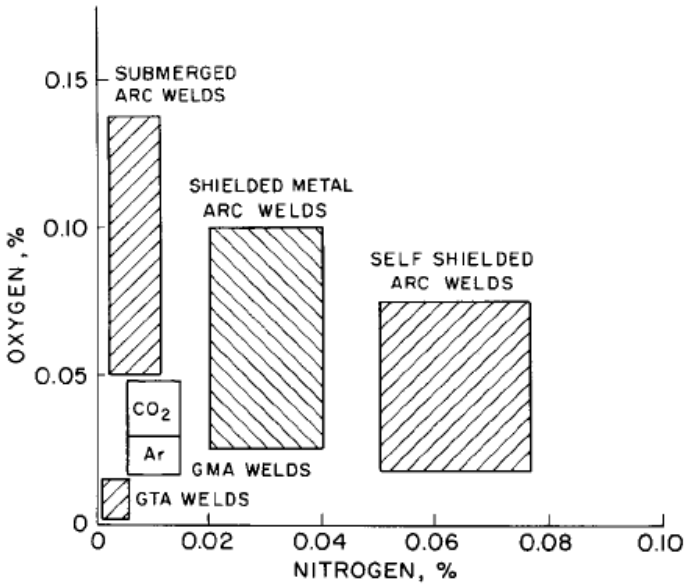

Figure 6.5 Expected levels of oxygen and nitrogen contamination for several conventional welding processes. From Figure 3.1, Kou [115].

While much research has been conducted into the atmospheric contamination of weldments in titanium and titanium alloys, the approaches to achieving and validating quality welds are somewhat primitive. To ensure satisfactory welds are achieved, titanium welding guidelines, published predominantly by titanium and welding equipment manufacturers, state that the weld and all adjacent regions must be shielded from the atmosphere whenever their temperature exceeds 800 °F (427 °C) [8, 10, 87, 88, 264]. This temperature corresponds to the published values for the point where the protective surface oxide layer breaks down and diffusion of contaminants into the bulk is unimpeded. Typically such protection from atmosphere is achieved through extensive shielding of the entire weld zone with inert gases using non-conventional nozzles and trailing shield devices or by completing welding processes in a controlled atmosphere

such as a purged glove box or vacuum chamber. Atmospheric contamination of titanium and its alloys causes discolouration of the surface and the presence, and degree, of such surface discoloration is commonly considered a measure of weld quality [10, 87, 180, 262, 264]. Despite the highly subjective nature of this surface-based assessment, and the acknowledgement that atmospheric contamination is possible without any colouration [104], this approach to assessing weld quality is still recommended by a number of technical guidelines [8, 106]. It is worth noting that Harwig *et al.* [181] propose another method of weld quality assessment where mechanical hardness of the weld region is measured by an ultrasonic contact impedance method. This hardness value may then be related to an oxygen equivalence (OE) which reflects the material composition [179, 180], and so may be used to give an indication of the contamination in the weld relative to the base parent material.

Compared to thermomechanical processes such as heat treatments and superplastic forming where atmospheric contamination is usually considered, the thermal cycle associated with fusion welding processes has the potential for exposure to far higher temperatures but for much shorter periods of time. In the case of GTAW-wire based additive manufacturing, this thermal cycle is repeated many times, presenting ample opportunity for atmospheric contamination of the deposit and adjacent material. In this process there are considered to be two main sources of contamination:

i) contamination of the immediate weld area in both liquid and solid states during deposition, and
ii) contamination of material outside the inert shielding envelope which are reheated during deposition of subsequent layers

In the first case, contamination of the liquid state may result from poor shielding, entrainment of atmospheric gases or poor cleaning of the weld area and filler wire. Contamination of the weld area in the solid state may also be caused by poor shielding and entrainment of atmospheric gases, but is more likely to be due to its premature removal from the inert gas shielding envelope. Irrespective of whether the contamination occurs in the solid or liquid phase, there is a high likelihood of contaminants penetrating into the bulk material through mixing in the molten pool during either the present weld or subsequent welding passes. As such, contamination of this first type is of great concern during the additive manufacturing process and must be

prevented to ensure the quality of the build-up is not compromised. In contrast, for the second case, contamination is only understood to take place in the solid state where material outside the inert gas shielding envelope is reheated during deposition of subsequent layers. Since there is no re-melting following the contamination, the penetration of any such contaminants can only occur by diffusion processes and so is expected to be limited to the regions immediately adjacent to the exposed surface. While still undesirable, it is thought that contamination of this second type may be tolerated during the build-up process since the depth of penetration is shallow and the contaminated surface layers will be removed by finish machining processes used to produce the final component profile.

While these forms of contamination could be negated during GTAW-wire based additive manufacturing of Ti-6Al-4V by conducting the process in a purged glove box or vacuum chamber, the use of these controlled environments presents a number of restrictions. Welding in a contained vessel restricts the size of the build envelope. Large build chambers could be developed to accommodate the large scale of target aerospace components however; the capital costs associated with these would be expected to become significant. It has also been reported that welding of Ti-6Al-4V in vacuum conditions gives a loss of aluminium from the molten pool due to its high vapour pressure and so yields a final weldment with composition outside the accepted limits specified by relevant standards [141]. This can be countered by using specially developed filler wire with increased aluminium content, however the need for a non-standard feed material adds further costs to the process. It is for these reasons that use of the GTAW-wire based additive manufacture in an uncontrolled environment is being pursued.

The primary aim of this component of the research was to investigate and characterise aspects of atmospheric contamination specific to the arc-wire based additive manufacture of Ti-6Al-4V with particular reference the effect on the mechanical properties of the final component. It was intended that this work would apply existing knowledge of thermally activated atmospheric contamination of Ti-6Al-4V to the unique thermal processing that occurs during additive manufacturing. This was done initially through a series of bead-on-plate welding trials to establish the origins of contamination in multi-pass welding, with observations related to colouration and mechanical hardness. Additional trials were conducted to investigate the colouration of

Ti-6Al-4V during thermal cycles analogous to those present in GTAW-wire based additive manufacturing. While these experiments were somewhat primitive from a scientific point of view, they were designed to provide industrially significant insights into the atmospheric contamination processes and act as a proof of concept in addition to forming the foundation for future studies.

6.2 Methods and Methodology

6.2.1 Bead-on-Plate Trials

Aspects of atmospheric contamination associated with the GTAW-wire based additive manufacture of Ti-6Al-4V were initially assessed through a series of bead-on-plate welding trials. Welds were performed as linear beads along the length of strip sections of commercially sourced Ti-6Al-4V plate measuring approximately 250 mm x 32 mm x 12 mm. For all trials this strip section was fastened to a 25 mm thick mild steel adaptor plate which in turn was mounted to the modified lathe linear actuator system. Welding was conducted using a water cooled Conley & Kleppen (CK) machine mount torch coupled to a Kemppi MasterTIG MLS 2000 inverter power supply. Where used, independent wire feed of 1.0 mm diameter Ti-6Al-4V wire was provided through a CK WF3 dedicated wire feed unit. The combined torch and wire feed arrangement was held stationary above the linear actuator. Process parameters of arc current, arc length and travel speed are detailed in Table 6.2. These values were selected based on the results of process characterisation studies with the aim of producing weld beads approximately 10 mm in width using arc energy similar to that used in additive manufacture processes.

Table 6.2 Summary of GTA welding parameters used for bead-on-plate trials.

Polarity	DCEN
Electrode	2% Ceriated, 2.4 mm Ø
Arc Length	3.5 mm
Arc Current	125 A
Weld Travel Speed	150 mm/min
Shielding gas	Welding Grade Argon
Pre-flow duration	3 seconds
Up slope duration	2 seconds
Down slope duration	1 second
Post flow duration	30 seconds

Trials were performed with either single or multiple welding passes using differing configurations of inert gas shielding as detailed in Table 6.3. In all trials, inert gas shielding of the weld pool was achieved with welding grade pure argon using pre and post flow options through the welding torch nozzle. Additional shielding of the weld zone during cooling was implemented for a number of trials using a custom fabricated trailing shield, shown in Figure 6.6, with welding grade pure argon fed into the front and rear ports at differing flow rates as given in Table 6.3, again with pre and post flow options. These variations in trailing shielding were intended to assess the extent of atmospheric contamination of the fusion zone in the solid state upon cooling. The use of multiple welding passes was designed to allow the assessment of atmospheric contamination from the inert shielding gas itself as well as the effects of repeated fusion and mixing in distributing the contaminants throughout the fusion zone. While the majority of trials were conducted autogenously, a single trial was performed with filler metal addition to observe any effects associated with this. Temperature profiles for each trial were monitored through NI LabVIEW software using K-type thermocouples attached to the underside of each sample and oxide colours observed.

Table 6.3 Summary of variables used to assess atmospheric contamination during bead-on-plate trials.

BOP Trial	Wire Feed Speed (mm/min)	Shielding Gas (L/min)		Weld Passes
		Ø19 mm Nozzle	Trailing Shield	
Trial A	nil	8	nil	1
Trial B	nil	8	*Front* 10, *Rear* 7	1
Trial C	150	8	*Front* 10, *Rear* 7	1
Trial D	Nil	8	nil	50
Trial E	nil	8	*Front* 10, *Rear* 7	50

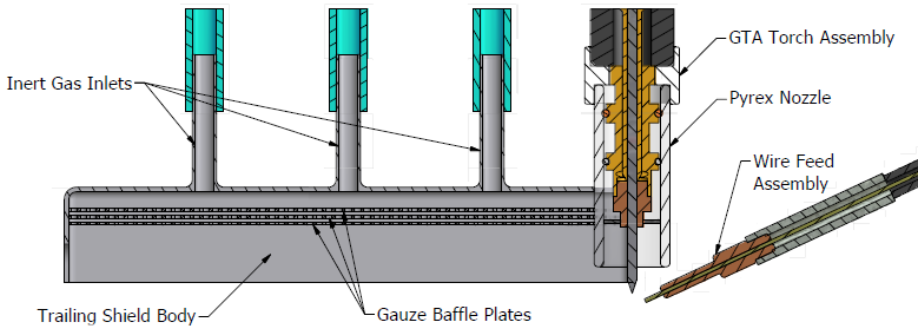

Figure 6.6 Section view of the welding torch arrangement showing trailing shield structure and wire feed assembly.

Following welding, a thin cross section was prepared from each sample by cutting perpendicular to the welding direction at its mid-length before being hot compression mounted in phenolic powder. Mounted samples were plane ground using silicon carbide (SiC) and chemically-mechanically polished using modified a colloidal silica solution (1 part H_2O_2, 2 parts NH_3 and 25 parts 0.25 μm OP-S) as per Struers application notes for titanium [27]. Samples were etched using Kroll's reagent (2 vol% HF, 6 vol% HNO_3 with balance H_2O) for optical microscopy using a Leica DMRM compound microscope and macro imaging with a Leica M205A stereo microscope.

The effects of atmospheric contamination on mechanical properties were assessed through Vickers hardness testing on the sectioned and polished samples. Initial measurements were conducted using a load of 0.5 kg and a dwell time of ten seconds with indents placed 0.5 mm apart on a square grid to give a rectangular array measuring 15 mm x 4.5 mm located across the full width of the weld bead, corresponding to Map 1 in Figure 6.7. These area maps served as a preliminary investigation to check for symmetry about the weld centreline and observe general trends to direct further measurements. A second series of measurements were performed using load of 0.2 kg and a dwell time of ten seconds with indents placed 0.2 mm apart on a square grid to give a rectangular array of 5 by 51 indents, covering a strip 1 mm x 10 mm aligned with the centreline of the weld bead. This is identified as Map 2 in Figure 6.7. Where reinforcement existed in the weld bead, these maps were extended into the reinforcement to fully assess the fusion zone. The average of the five microhardness values in each row were obtained and used to observe trends along the centreline through the parent metal, HAZ and FZ. A final set of hardness maps were conducted using a load of 1.0 kg and a dwell time of ten seconds with indents placed 0.5 mm apart on a square grid to give a rectangular array measuring 12 mm x 8 mm located across half of the weld bead and extending well into the parent material, as shown by Map 3 in Figure 6.7. These were intended to serve as a more detailed map of hardness variation across the weld bead and parent material with symmetry assumed about the weld centreline. These maps were positioned within the boundaries of the parent metal and so did not extend to areas of reinforcement. All microhardness testing was performed in an automated manner using a Struers Durascan 70 equipped with Ecos Workflow software. It must be noted that between each series of microhardness measurements, samples

were again plane ground and polished to remove regions of deformation that would influence results of subsequent testing.

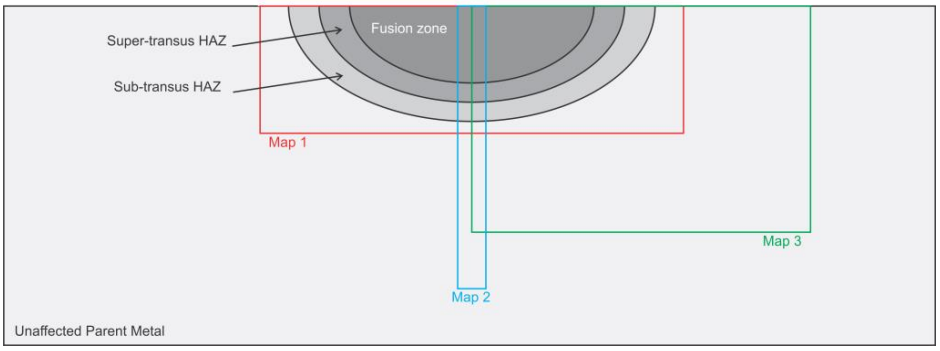

Figure 6.7 Schematic illustration of location of microhardness measurements with respect to weld beads.

6.2.2 Colour Assessments

Atmospheric contamination of Ti-6Al-4V during and following fusion welding was qualitatively assessed through observations of surface colour on samples subjected to heating cycles in-line with those found during the GTAW-wire based additive manufacturing process. Firstly, representative thermal profiles were obtained by measuring those of an actual additive manufacture deposit. A section of commercially sourced Ti-6Al-4V plate measuring 250 mm x 50 mm x 12 mm was held on edge in a steel clamping arrangement to simulate the steady state region of a wall-like build-up, with the entire fixture attached to the modified lathe linear actuator, above which the torch and wire feed were held stationary. Welding was conducted using a water cooled Conley & Kleppen (CK) machine mount torch coupled to a Kemppi MasterTIG MLS 2000 inverter power supply with wire feed provided through a CK WF3 dedicated wire feed unit. A total of 27 weld beads were deposited to give a final build height of approximately 29 mm. While trailing shielding was used to minimise atmospheric contamination, the use of side shielding plates like those used in the production of samples for mechanical testing was not possible due to the location of thermocouples. Evidently, this resulted in compromised inert gas shielding however, it was considered there would be no significant effect on the measured thermal profiles which were the primary focus of the experiment. Shielding gas flow rates and other common process parameters are detailed in Table 6.4. As shown in Figure 6.8, the final build-up shows significant signs of atmospheric contamination with formation on a flaky surface oxide on the exposed sides of the additively manufactured build-up

Table 6.4 Summary of GTA welding parameters used to measure thermal profiles.

Polarity	DCEN
Electrode	2% Ceriated, 2.4 mm Ø
Arc Current	110 A
Arc Length	3.5 mm
Travel Speed	150 mm/min
Arc Energy	510 J/mm
Wire Feed Speed	1500 mm/min
Specific Deposition Energy	14.4 kJ/g
Shielding gas	Welding Grade Argon
Flow rate – torch nozzle	8 L/min
Flow rate – trailing shield front	10 L/min
Flow rate – trailing shield rear	7 L/min
Pre-flow duration	3 seconds
Up slope duration	2 seconds
Down slope duration	1 second
Post flow duration	30 seconds

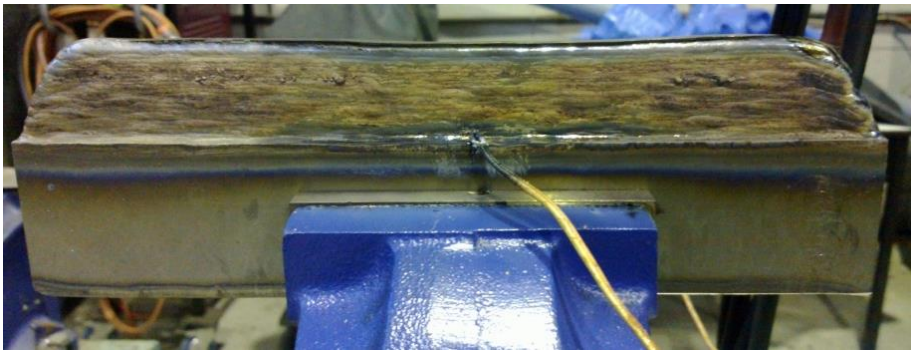

Figure 6.8 Additively manufactured deposit used for measuring thermal profiles with K-type thermocouples attached.

Temperature profiles were measured through NI LabVIEW software using two K-type thermocouples which were attached one each side to the build-up after the completion of 8 welding passes. The attachment of these thermocouples was delayed for a number of reasons. Firstly, had these nickel based thermocouples been attached earlier they would have most likely detached during the welding process due to high peak temperatures allowing the formation of the Ti-Ni eutectic which becomes liquid at approximately 950 °C. Secondly, thermal profiles measured prior to these initial welding passes before would have not been representative due to the work-piece being not fully heated and so influencing cooling rates measured. Finally, and most

importantly, the attachment of the thermocouples corresponded to the first indication of colouration on the surface of the deposit and so was taken to represent the point at which atmospheric contamination of the heated material began. As such, thermal profiles of the preceding passes were considered to be of little interest since they only occur within the inert gas shielding envelope where atmospheric contamination of solid material is thought to be negligible.

To assess colouration associated with thermally induced atmospheric contamination, samples of Ti-6Al-4V measuring 10 mm x 10 mm x 90 mm were prepared from commercially sourced plate 12 mm in thickness. Each side of these samples were prepared with a different surface finish to assess how surface finish influences colour. Surface finishes used were as received, EDM wire cut, milled (Ra ≈ 1.6 μm) and polished. Holes were drilled and tapped in each end to allow samples to be mounted between stainless steel contact electrodes as shown in Figure 6.9. This entire assembly was housed in a sealed Perspex chamber which also contained an electric fan, used to control cooling rates, and monitoring equipment for temperature and humidity. Once sealed, the atmosphere in this chamber could be controlled by purging with welding grade pure argon. Exhaust gases from the chamber were passed through a Cambridge Sensotec Rapidox 1100 gas analyser to monitor oxygen content inside the chamber during heating cycles. Heating of samples was by electrical resistance with alternating current provided though a variable autotransformer, which was adjusted to give the desired temperature for each sample. Temperature profiles were measured through NI LabVIEW software using a single K-type thermocouple attached centrally on the face with as received surface finish. All trials were videoed to observe the time dependence of colour formation on the polished face using a Canon EOS 60D digital SLR fitted with a 60 mm macro lens.

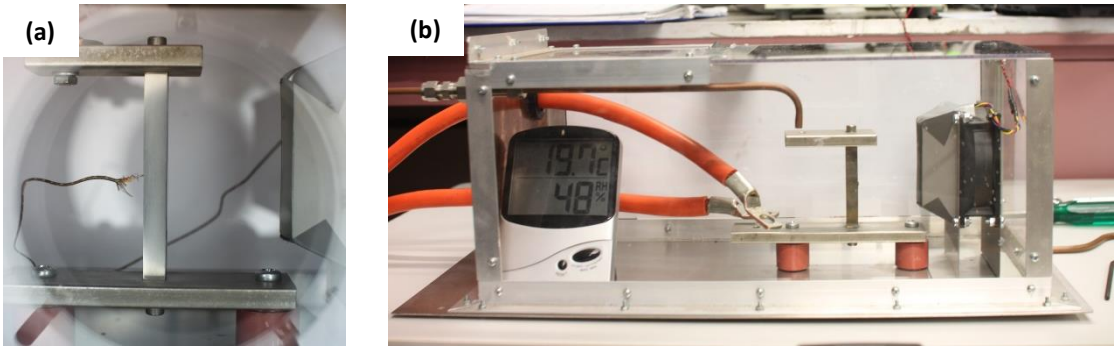

Figure 6.9 (a) Sample mounting arrangement and (b) controlled atmosphere chamber used for colour assessment trials.

Initial trials involved rapidly heating the sample in air and holding at a constant temperature for two minutes followed by controlled cooling. Holding temperatures ranged from 200 °C to 600 °C and were achieved by manually varying the voltage, and hence current, from the autotransformer using feedback from temperature measurements in NI LabVIEW. Similar holding experiments were conducted for temperatures of 700 °C and 900 °C in a welding grade pure argon atmosphere. Lower holding temperatures were not assessed in the argon atmosphere as the extent of colouration was expected to be negligible and so of little use. To further reduce oxygen content below that of the argon supply, a heated coil of commercially pure titanium wire was also placed inside the Perspex chamber to preferentially react with residual oxygen and so 'scrub' the argon to higher levels of purity. Extended holding trials were also performed on samples for 25 minutes at 300 °C and 15 minutes at 500 °C. Thermal profiles for those trials conducted in air are shown in Figure 6.10.

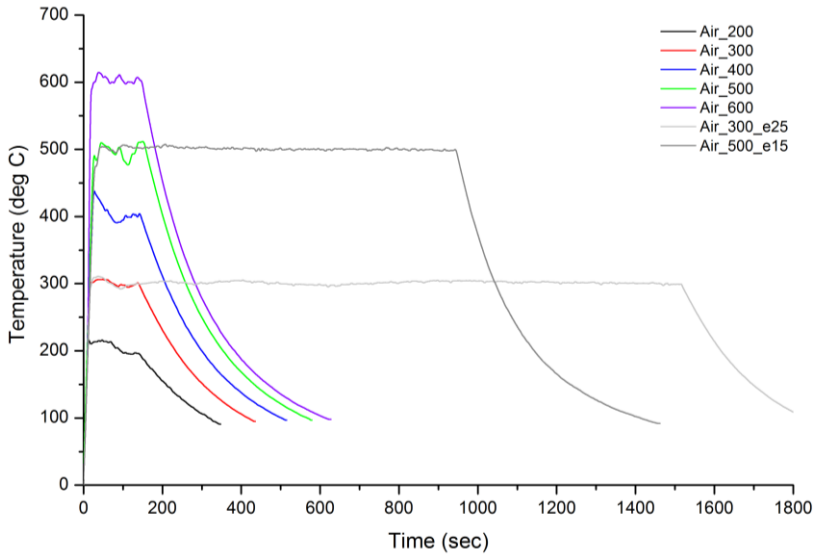

Figure 6.10 Thermal profiles used to assess colour formation with atmospheric contamination in air.

Further trials were conducted in both air and argon atmospheres with 20 repeated thermal cycles based on thermal profiles shown in Figure 6.11 which were measured during the additive manufacturing trial described above. In terms of the timing between successive heating cycles, the two alternatives were thought to be either a constant time interval or a constant interpass temperature. In the additive manufacture of a given component it is more likely that a constant time interval would apply between successive heating cycles, however the duration of this time period clearly depends on the build geometry and weld bead sequencing. It is for this reason that the present trials made use of a constant interpass temperature of 200 °C between heating cycles. This condition may be present during additive manufacturing where pre-heat is used or heat inputs are sufficiently high to maintain temperature throughout the part. A total of three samples were subjected to this 'multi-pass' thermal cycling for each of the two atmospheres considered. One of these samples was used for colour assessment while the remaining two were used for Charpy impact testing. Those samples used for Charpy impact testing were V-notched prior to heating to ensure any atmospheric contamination that took place during heating would be present in the origin location of fracture. Following the heating regimes, the Charpy samples were trimmed to length to give a full size ASTM sample of 10 mm x 10 mm x 55 mm. Charpy impact testing was conducted in accordance with ASTM E23 using a 750 J capacity Instron MPX series instrumented pendulum impact tester. Samples were tested at -20 °C with impact energy values calculated by the linked Fracta software.

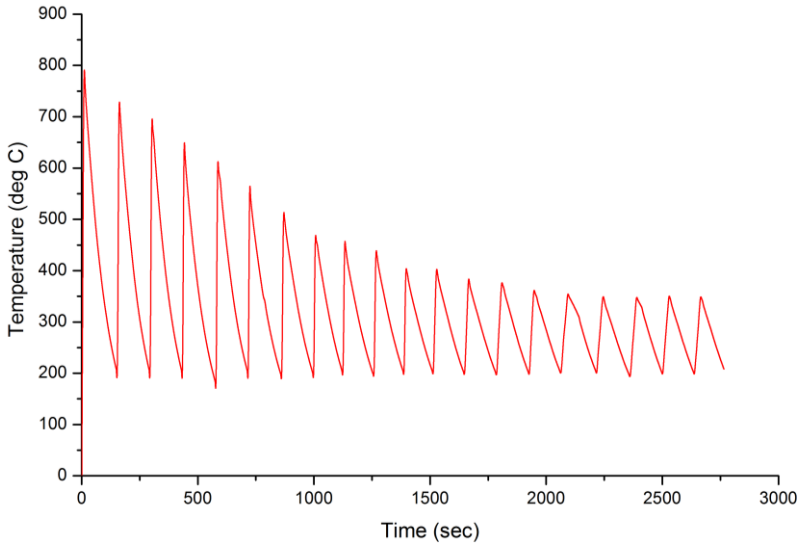

Figure 6.11 Thermal profiles from additive manufacturing trial used to simulate heating cycles during 'multi-pass' trials for colour assessment.

6.3 Results and Discussion

6.3.1 Bead-on-Plate Trials

Considering firstly general observations of weld bead appearance, it was seen that those bead-on-plate trials which involved multiple welding passes had significant levels of weld reinforcement, despite being conducted autogenously. This is attributed to the combined effects of welding travel and arc force exerted on the molten pool. During the welding process, arc force acts to depress the surface of the molten pool, which has a 'teardrop' shape when viewed from above with the elongation being on the trailing side. Due to the shape of this molten pool and the displacement of melt due to arc force, there is a net flow of the liquid metal to the trailing side of the molten pool. These effects are commonly observed in single pass autogenous fusion weld with a slight crater at the stopping point. When many weld beads are performed successively, these effects are repeated in each pass, producing the reinforcement observed with significant cratering at the stopping point. While such an observation may seem trivial, it is of significance in the present trials as it alters the volume of material which can potentially be contaminated by atmosphere. Since all beads were performed with equal arc energies, it can be assumed that each weld bead had a constant weld pool volume; however as the number of welding passes increases, the depth of fusion becomes shallower relative to the first weld bead due to the accumulated reinforcement. As such, the depth of mixing of what could be expected to be previously contaminated layers is shallower with each welding pass, albeit by a small amount.

Turning then to observations of weld bead colour, it was clear that those welds executed using additional inert gas shielding, provided through the trailing shielding device, were consistently silver in appearance. In contrast, those welds performed using only the conventional gas shielding nozzle were deep straw and blue in colour, indicating atmospheric contamination of the weld bead and adjacent parent metal. This is clearly shown in Figure 6.12, which also shows the coarse prior β-Ti grain structure in the fusion zone. While this was true for the vast majority of the weld length, a region of silver weld bead was observed at the end of all beads as illustrated in Figure 6.13. Further trials showed that this region of silver bead was obtained while welding over previously coloured, and hence contaminated, weld beads when the welding process was stopped mid-run as shown in Figure 6.14. As an aside, these figures also show the

crater feature at the end point of weld beads which results from arc force and weld pool elongation as described previously. In all cases, this region of silver bead corresponds to the point where welding stops and the torch remains stationary over the solidifying molten pool with 30 seconds of post-flow inert gas shielding provided through the torch nozzle to protect from atmosphere during cooling.

Two conclusions may be drawn from these observations of colour relating to the atmospheric contamination of Ti-6Al-4V during additive manufacture by GTAW. Firstly, the lack of colour below the gas nozzle of the welding torch indicates that the majority of atmospheric contamination is occurring post-weld where the solidified weld metal is removed from the inert gas shielding envelope while above the critical temperature for formation of the protective oxide layer. Since the atmospheric contamination is occurring in solid material over a short period of time, the depth to which these contaminant species are able to penetrate by diffusion processes is thought to be very shallow. As such, contaminated material of this type may be readily removed during finish machining processes on additively manufactured components. Secondly, since welding over a previously coloured weld bead with suitable inert gas shielding can produce a new bead which is silver in appearance, the use of colour alone is a poor indicator of bulk contamination. This is because the contamination which produced the colour in the previous weld bead has presumably been mixed through the fusion zone of the following bead. As a result the bulk weldment should now be contaminated to a greater depth with somewhat reduced concentrations, which colour alone does not reveal. Further images of weld bead colour for bead-on-plate trials of Ti-6Al-4V are presented in Appendix D.

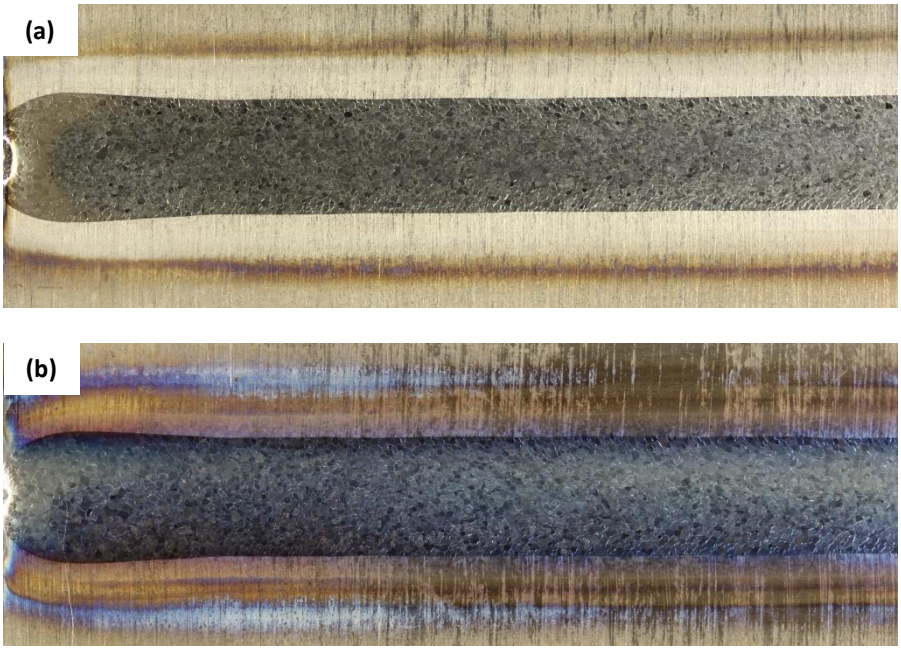

Figure 6.12 Surface colouration of single pass autogenous bead-on-plate welds performed (a) with and (b) without the use of additional inert gas trailing shielding. Welding direction is from left to right.

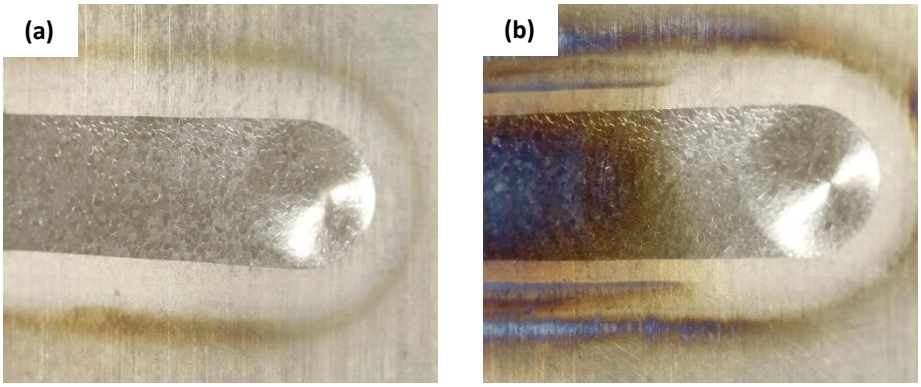

Figure 6.13 Silver weld bead appearance at the end of single pass autogenous bead-on-plate welds performed (a) with and (b) without the use of additional inert gas trailing shielding.

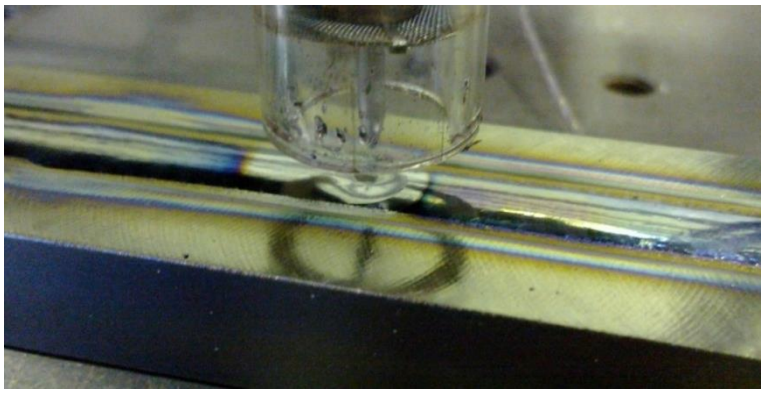

Figure 6.14 Silver appearance of weld bead on top of a previously coloured bead below the shielding nozzle of the welding torch during multi-pass bead-on-plate trials conducted without use of additional inert gas trailing shielding

Results from microhardness testing conducted across the full cross section of weld beads revealed relatively uniform microhardness throughout the fusion zone, with more variation in the small region of parent metal surveyed. This is attributed to the uniform fine Widmanstätten α-Ti microstructure of the FZ which differs from the comparatively coarse and highly oriented rolled α-Ti grain structure present in the parent material, where hardness measurements are more dependent on indentation location. Another key observation is the symmetry of microhardness profiles about the weld centreline, as shown in Figure 6.15. While conducting these initial measurements, it became apparent there was a compromise between the area of coverage that could be reasonably assessed and the spatial resolution of measurement locations. It was felt that these full cross section hardness maps didn't encompass enough of the parent material and lacked resolution in key areas such as the heat affected zone and reinforcement. As such, these initial results served more as a guide to conduct more targeted measurements firstly with high resolution along the weld centreline and secondly more broadly across half of the weld region using symmetry about the centreline.

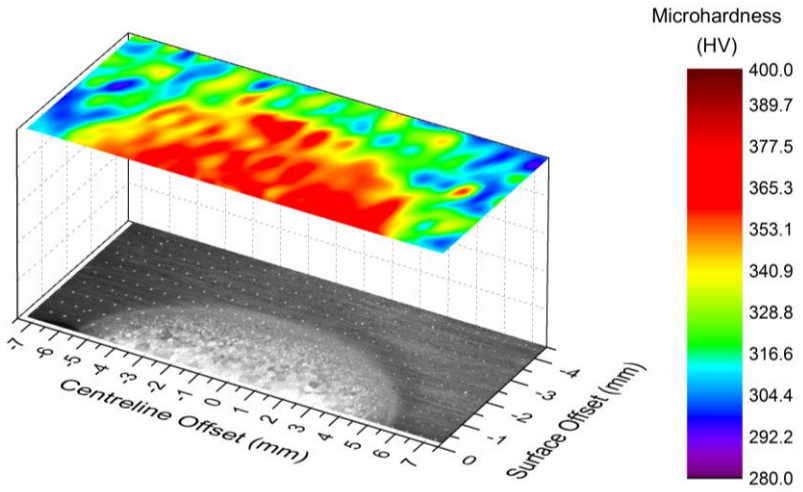

Figure 6.15 Two dimensional contour plots showing microhardness profiles (upper surface) and corresponding microstructure (lower surface) for bead-on-plate Trial C.

Results of microhardness measurements performed along the centreline of bead-on-plate welds through the thickness of samples reinforce observations from initial map measurements. From the data presented in Figure 6.16 it is clear that mechanical hardness is far more uniform through the FZ and HAZ than in the adjacent parent metal. Each of the successive peaks and troughs seen in the parent metal are thought to be related to 'banding' of some form in microstructure of the rolled plate section. This data

also shows a slight increase of approximately 5 % in average hardness through the FZ and HAZ compared to the parent material.

Comparing single pass welds conducted with and without the use of additional inert gas trailing shielding, there is no discernible difference in microhardness for the region measured. This indicates that the atmospheric contamination which produced surface colouration did not penetrate in any significant concentration to a depth of more than 100 μm, the offset of the shallowest hardness measurements in the series from the exposed surface. Considering then the results from bead-on-plate Trial C performed with the addition of filler wire, again there is no appreciable change in microhardness within the FZ. This implies there was no additional increase in atmospheric contamination due to the deposition of weld metal.

Looking then at results from multi-pass bead-on-plate trials, the microhardness in the bottom region of the FZ is in-line with the values measured for single pass welds suggesting no increase in concentration of atmospheric contaminants to these depths due to the repeated welding passes. In contrast, hardness is seen to increase in the top region for the FZ and through the reinforcement, particularly in Trial D conducted without the use of additional inert gas trailing shielding. The depth at which hardness is seen to increase is thought to correspond to the *actual* depth of the FZ during the final welding passes which, as described previously, migrates to higher levels with increasing numbers of welding passes due to arc force producing reinforcement. The marked increase in hardness seen in Trial D clearly indicates a significant accumulation of oxygen and other interstitial contaminants during multi-pass autogenous welds due to remelting and mixing of previously coloured, and hence contaminated material, culminating in the FZ of the final beads. In comparison, the increase in hardness seen in the upper region of Trial E is far less severe, indicating a lesser level of contamination. Given this weld was well protected from post-weld atmospheric contamination using the additional inert gas trailing shielding, it is thought the source of such contamination is either entrainment of atmospheric gases through turbulence in the shielding envelope or pick-up of residual oxygen and other interstitial contaminants present in the welding grade pure argon used for shielding. Regardless of the source of this contamination, it is clearly reduced through the more broad application of inert gas shielding.

The hardening effects observed in the FZ of multi-pass bead-on-plate trials are thought to be a 'worst case scenario' for GTAW-wire based additive manufacturing of Ti-6Al-4V, where the overlap in fusion zones of consecutive deposition layers is far less than that in bead-on-plate trials performed autogenously. This reduced overlap clearly minimises remelting and mixing of potentially contaminated layers, and hence significantly reduces the localised accumulation of contaminant species in later weld beads which manifested itself in the form of increased hardness. These results would be well complemented by quantitative analysis of chemical composition along the weld centrelines, allowing direct correlation to observations of mechanical hardness. This would be best done as line scans using either electron probe micro-analysis (EPMA) or secondary ion mass spectrometry (SIMS) with the atomic species of interest being primarily oxygen, but also nitrogen, carbon and hydrogen.

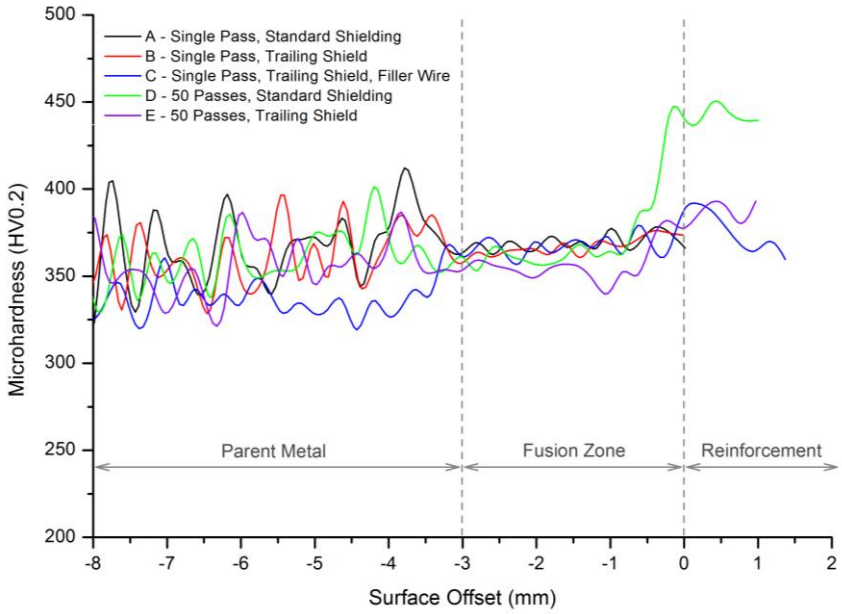

Figure 6.16 Microhardness along weld centrelines in bead-on-plate trials. Values are the average of five measurements taken at each depth with error bars corresponding to the 95 % confidence interval omitted for clarity.

Broad analysis of microhardness across the weld zone and surrounding parent material performed through half maps assuming symmetry about the weld centreline produced similar trends to those of previous measurements. These results, shown in Figure 6.17, clearly illustrate a high level of homogeneity throughout the FZ, which also has increased hardness with respect to the surrounding parent material. This is most evident in Trial C (where wire addition was used) not because the FZ is any higher in hardness

than other trials, but because the surrounding parent material shows lower hardness. This is because the strip section used for Trial C was prepared from plate such that its longitudinal orientation was at right angles to that of strip sections used in the remaining four trials. As shown in Chapter 4, the hardness of the commercially sourced Ti-6Al-4V plate differs with different orientations with respect to the plate rolling direction. The area maps in Figure 6.17 also illustrate banding in hardness values through the parent material, presumably related to the rolled microstructure in those regions.

It could also be suggested that these plots show a 'rim' of increased hardness surrounding the FZ, corresponding to the HAZ of the first welding pass. While this was supported by qualitative observations during hardness testing and is not unexpected considering the different microstructure found in the HAZ, such an increase was not evident in measurements performed along the weld centreline. This layer of hardening is also not discernible in Trial C but this is thought to be because it is minor compared to the relatively large difference hardness between the FZ and parent metal.

From the microhardness profiles and microstructure images presented in Figure 6.17 it can be seen that the depth of the penetration of the weld bead, and hence the region of altered hardness, is shallower in Trial C compared to those trials welded autogenously. This can be readily explained since all trials were performed using the same arc energy but the addition of filler wire consumes energy in melting and so reduces the amount of energy available to melt the parent material, reducing the size of the molten pool formed.

Finally, the increase in microhardness observed in the upper FZ and reinforcement of multi-pass bead-on-plate trials during measurements performed along weld centrelines is also evident in these area maps. This is particularly true for Trial D which was conducted without the use of additional inert gas trailing shielding. Here, a band of particularly high mechanical hardness can be seen at the level corresponding to what would have been the original free surface of the parent metal. Since this region of increased hardness extends the full width of the fusion zone it is considered that the atmospheric contamination from mixing is distributed through the entire FZ of the final weld bead. While inclusion of the reinforcement in area maps would confirm this, such an extension of the map was considered unnecessary when the measurements from weld centrelines were also considered.

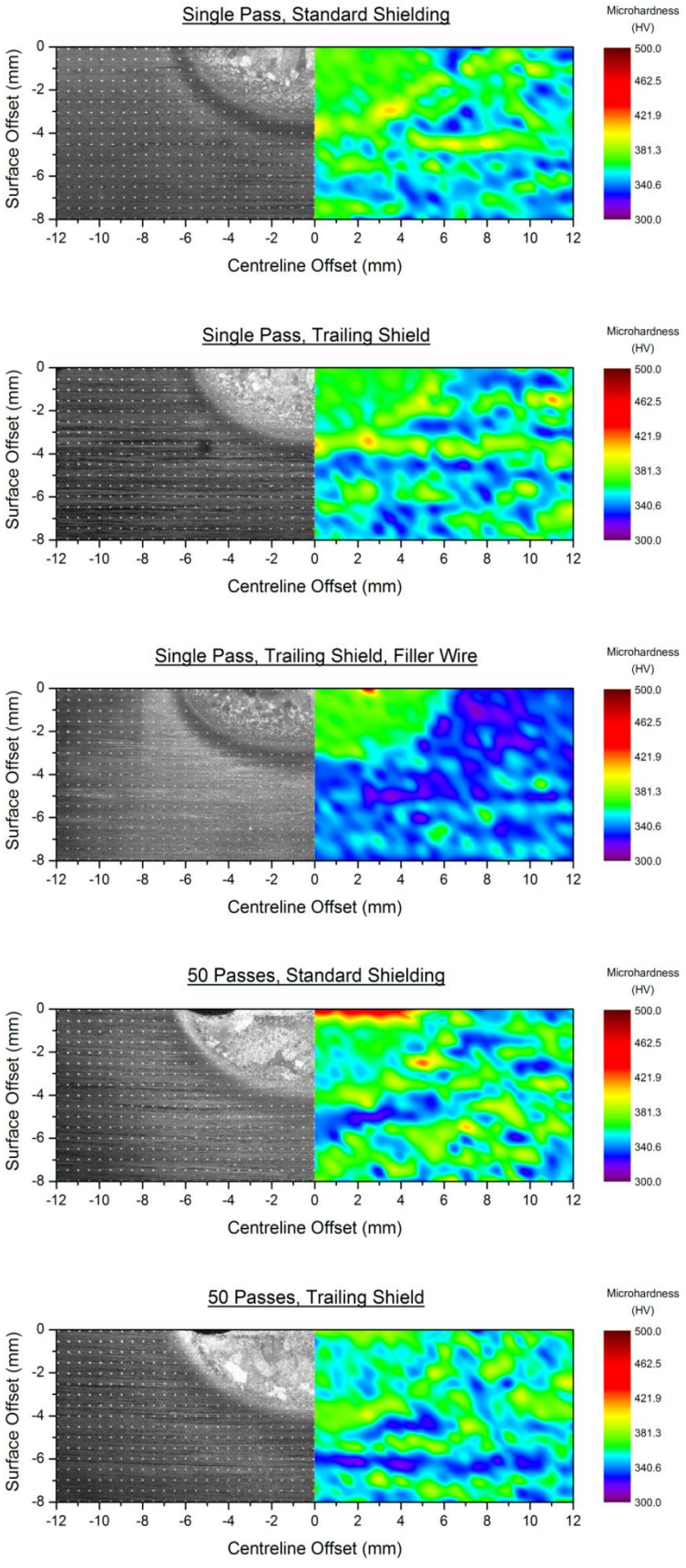

Figure 6.17 Illustration of the relationship between microstructure and microhardness for bead-on-plate welding trials. Note: the colour scale used in these figures differs from that used in Figure 6.15.

6.3.2 Colour Assessments

Thermal profiles for material outside the inert gas shielding envelope, and hence susceptible to atmospheric contamination, measured during the GTAW-wire based additive manufacturing process showed the typical form for welding processes with a sharp rise to peak temperature followed by an exponential decay type cooling profile. As the number of deposited layers increased, so too did the offset between the weld zone and the location of temperature measurement. With this increase in offset came a corresponding reduction in heating and cooling rates as well as a drop in peak temperature, which was reached after progressively longer times relative to the start of each weld bead, as illustrated in Figure 6.18. While these observations are common and well understood for fusion welding processes, one abnormality of note was the small initial peak seen from pass 20 onward. This is the result of radiant heating of the exposed thermocouple attached to the side of the build-up by the arc as it passes overhead with the true peak temperature in the material occurring some time later once the thermal energy of the welding processes has been conducted through the work-piece.

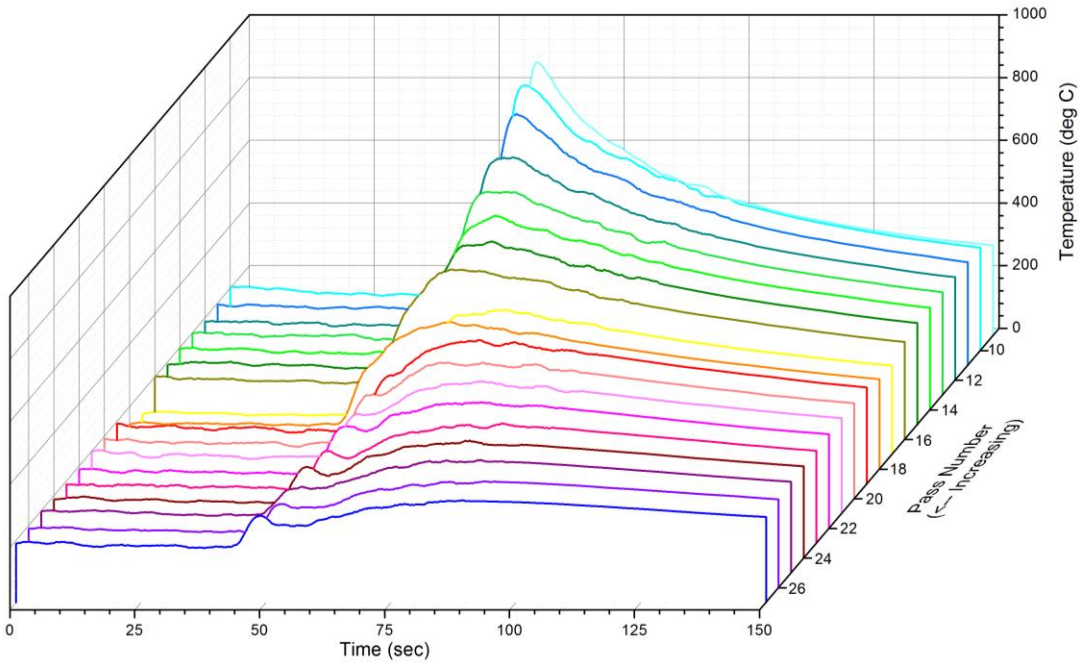

Figure 6.18 Thermal profiles in Ti-6Al-4V due to successive welding passes in the GTAW-wire based additive manufacturing process.

When using these thermal profiles for electrical resistance heating of samples to assess colour formation there were two key parameters of interest, namely the peak

temperature and average cooling rate. These are shown for the GTAW-wire based additive manufacturing process in Figure 6.19 as a function of offset between the thermocouple and FZ with each data point corresponding to an individual welding pass. Both of these parameters are seen to decrease in an exponential manner with increased distance from the weld zone. The one major discontinuity in the values of peak temperature was due to a longer than normal time delay between welding passes where the tungsten electrode needed to be re-ground. In this case, the average of the two adjacent values was used as the peak temperature during trials to assess colour formation.

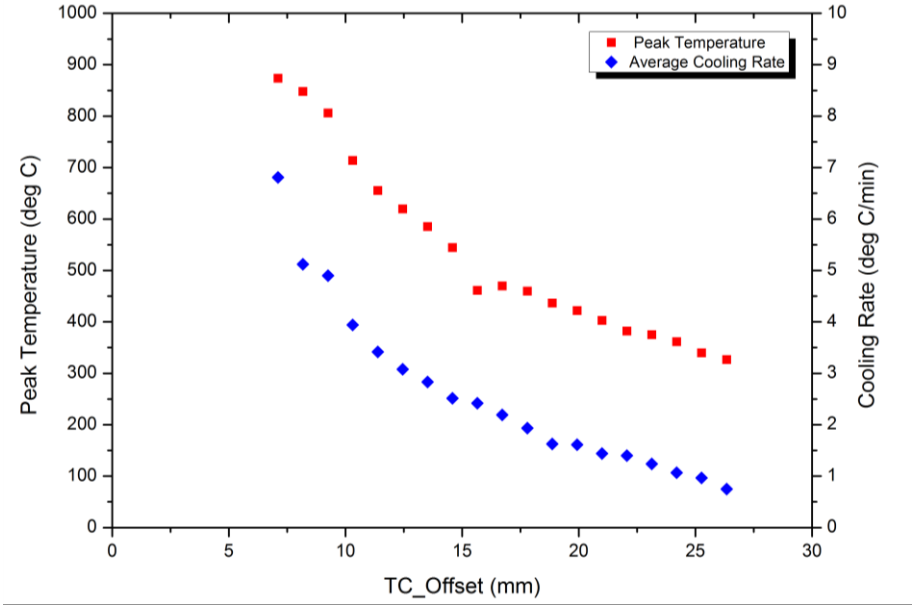

Figure 6.19 Peak temperature and average cooling rate as a function of distance from the weld zone during the GTAW-wire based additive manufacture of Ti-6Al-4V.

In terms of general observations from experimental trials, purging of the glove box with welding grade argon showed that steady state oxygen levels of 10 ppm or less could be achieved. During an initial test run conducted in this argon rich atmosphere it was seen that heating of the sample was accompanied by generation of smoke from each end of the sample due to burn off of residual volatiles from the cutting compound used to produce the tapped holes. This burn-off of volatiles consumed oxygen from within the chamber, reducing the oxygen level to approximately 0.01 ppm. Using the heating coil featuring commercially pure titanium wire, oxygen content in the order of 1 ppm could be easily achieved and maintained for trials conducted in argon. As a result of these observations, all samples were cleaned thoroughly using acetone and held at 200 °C for

5 minutes prior to testing to burn off any volatiles. This brief, low temperature heating cycle was considered to have no significant effect on the subsequent atmospheric contamination of samples.

Considering then the evolution of colour due to surface contamination as observed on the polished face of samples, it was seen the standard progression for titanium alloys was followed. This is clearly illustrated in Figure 6.20 for the sample heated and held at 600 °C in open (air) atmosphere where a straw colour formed first, followed by purple and dark blue with continued exposure producing a light blue, almost grey colour. These figures also show that the regions of strongest colour are away from the centre where temperature was measured, toward the ends where the mounting holes reduce the sample cross sectional area and hence facilitate heating to higher temperatures. Edges of the samples were also seen to show increased colour suggesting they were heated to higher temperatures than the central regions of each face.

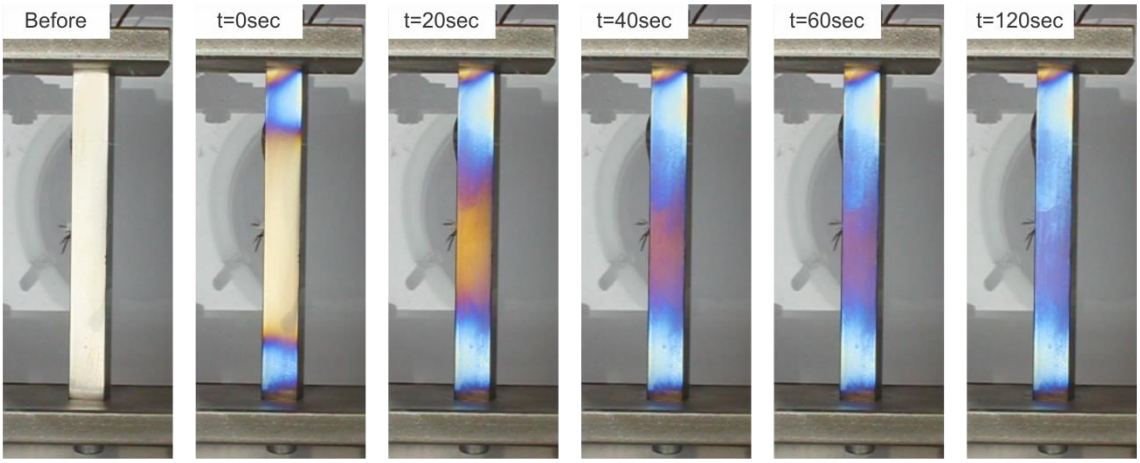

Figure 6.20 Formation of colour from atmospheric contamination of Ti-6Al-4V held in air at 600 °C for 120 seconds. Note: t=0 sec corresponds to the time at which the peak temperature was first achieved.

This same progression of colour formation was seen in samples subjected to multiple heating cycles as shown in Figure 6.21 for the sample heated in argon where the first heating cycle yielded a straw colour which transitioned to blue by the fourth cycle but then failed to show any subsequent colour change. In contrast, the colour of the sample subjected to repeated heating in air transformed from silver, to straw, to blue, to a pearly grey in the first heating cycle and showed little change thereafter, as shown in Figure 6.22.

From the images presented in Figure 6.23 it can be seen that while this same colour progression occurs for exposure to increasing temperatures, the surface finish of the

material has a significant influence on the colour formed at any given temperature. For samples heated in air, the first formation of straw colour in the central region where temperature was measured was seen at 400 °C on the polished surface but not until 500 °C on the machined surface. At this temperature the wire cut surface was already showing signs of purple and blue. Extended exposure time at 500 °C gave formation of light blue on the wire cut surface and strong blue on the as received and polished surfaces but only straw on that face with machined finish. After repeated thermal cycling to simulate that of the GTAW-wire based additive manufacturing process, all sides of the sample held in air were dull grey in appearance. While surface colour was observed to form on samples heated in the argon rich atmosphere, the inert shielding it provides clearly delayed the onset of colour formation with the colours exhibited by the sample held at 500 °C in air not seen until approximately 700 °C in argon.

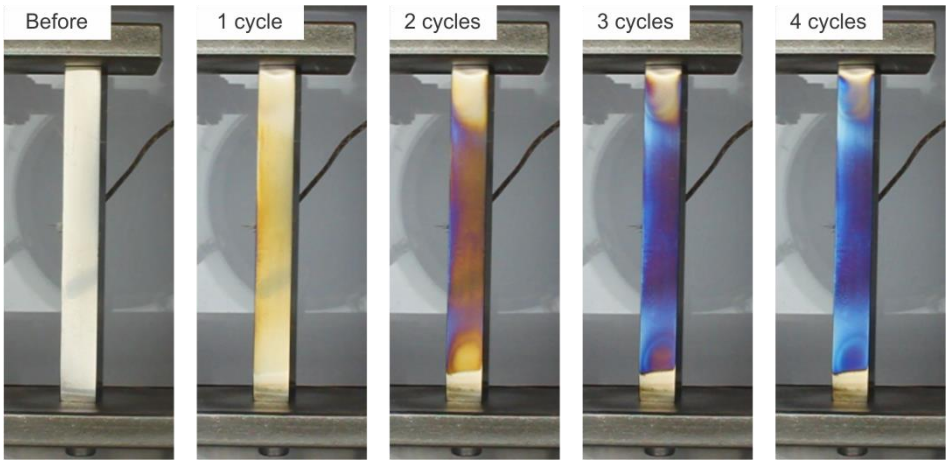

Figure 6.21 Formation of colour from atmospheric contamination of Ti-6Al-4V subjected to repeated thermal cycling in an argon atmosphere.

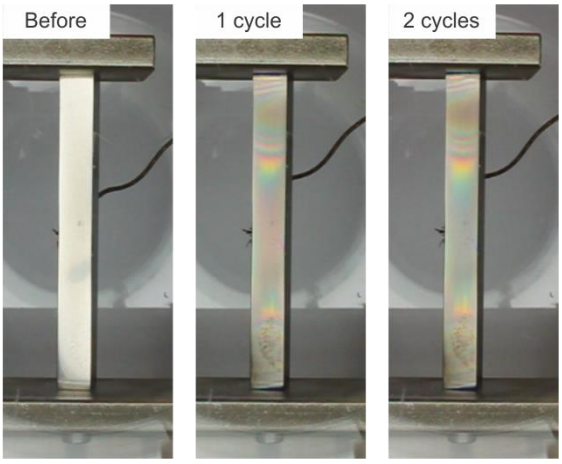

Figure 6.22 Formation of colour from atmospheric contamination of Ti-6Al-4V subjected to repeated thermal cycling in air.

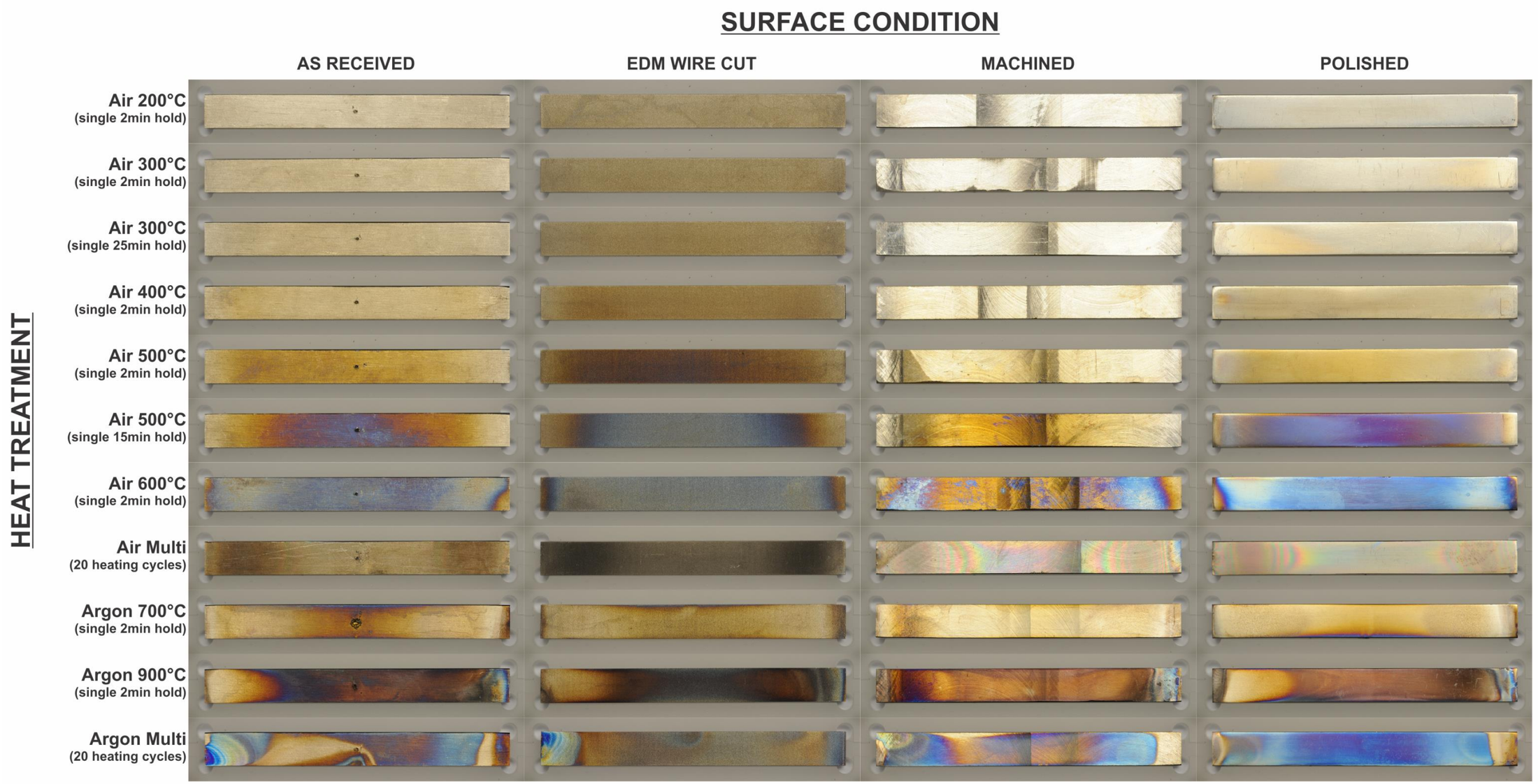

Figure 6.23 Surface colour due to atmospheric contamination of samples of Ti-6Al-4V subjected to various thermal treatments in either argon or open (air) atmosphere.

In terms of the origin of these differences in colour with surface finish, it is understood that each surface finish may have different emissivity, and hence be heated to different temperatures. However, the observed variations in colour are considered to be too large for the minor temperature deviations that would be expected. Instead it is thought that the variations stem from either the manner in which the atmospheric contamination takes place on each surface and so the actual extent of contamination, or the way in which light is scattered by the surface oxide layers and hence how the colour is perceived. In order to establish the true origins of the colour variation, these samples would need to be sectioned through their midpoint and suitably examined. Due to the relatively mild nature of the thermal cycles used, it is expected the depth of any contamination would be extremely shallow and unresolvable through optical microscopy of microhardness testing. Instead quantitative analysis of chemical composition would be required again by either EPMA or SIMS, with the atomic species of interest being oxygen, nitrogen, carbon and hydrogen. If possible, the depth of contamination could be assessed using an ultra-micro indentation system (UMIS) with results correlated to composition analysis. Assessment of the actual oxide layer may also be possible through transmission electron microscopy or other advanced high resolution techniques.

Regardless of the underlying mechanisms that produce colour during atmospheric contamination of titanium and its alloys, the present results show that the use of colour alone as a means of assessment is highly subjective and so fundamentally flawed. A better alternative may be found through modelling of the contamination and diffusion processes as a function of the heat treatment regime and atmospheric conditions. Clearly such models would need to be validated through experimental studies before being implemented into industrial processes such as the GTAW-wire based additive manufacture of Ti-6Al-4V.

Finally, considering the impact toughness of samples of Ti-6Al-4V subjected to repeated thermal cycling in air and argon atmospheres, there was no appreciable difference in absorbed energy with values ranging from 15 to 17 joules as shown in Figure 6.24. These values are in agreement with the 17 joules specified in Table 6.1 for Ti-6Al-4V and are not unexpected considering the work of Bendersky and Rosen which showed the critical exposure temperature for altering fracture properties in Ti-6Al-4V is greater than 800 °C [265], with peak temperatures in the current trials not exceeding

770 °C. It is worth noting that while these values of impact toughness are far greater than those obtained in mechanical testing described in Chapter 4, the samples in the present study were not sub-size and so had four times the cross sectional area to those in Chapter 4. Observation of fracture surfaces also showed no significant variation due to the heating in either air or argon. The lack of variation between samples implies that for the heating cycles used, atmospheric contamination is restricted to the surface of the sample only and has no apparent effect on the mechanical behaviour of the bulk material.

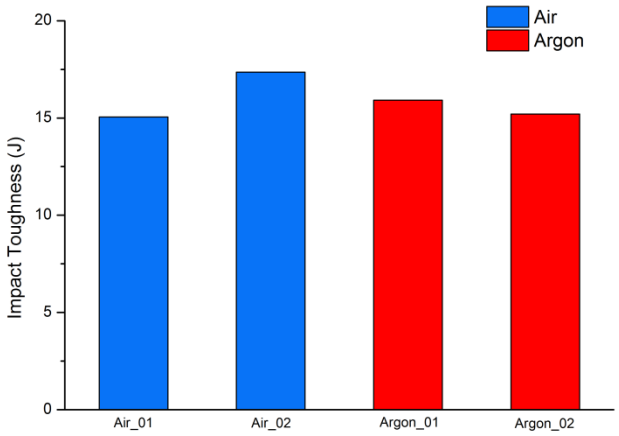

Figure 6.24 Results of Charpy impact testing conducted on Ti-6Al-4V subjected to repeated thermal cycling analogous to that of the GTAW-wire based additive manufacturing process in air and argon.

6.4 Conclusions

Aspects of atmospheric contamination specific to the arc-wire based additive manufacture of Ti-6Al-4V were assessed with particular reference to the effect on the mechanical properties of the final component. This was done initially through a series of bead-on-plate welding trials to establish the origins of contamination in multi-pass welding, with observations related to colouration and mechanical hardness. Additional trials were conducted to investigate the colouration of Ti-6Al-4V during thermal cycles analogous to those present in GTAW-wire based additive manufacturing.

Results of bead-on-plate trials revealed that the most likely source of atmospheric contamination during the GTAW-wire based additive manufacture of Ti-6Al-4V is post-weld where the solidified material is prematurely exposed a reactive atmosphere while still heated to temperatures where the protective oxide layer is stable.

Microhardness testing showed that the effect of this contamination is surface based and extremely shallow with respect to the weld bead size, and so does not penetrate the bulk material. Multi-pass bead-on-plate trials showed that repeated welding of previously contaminated material can allow the contaminant species to penetrate the bulk material through mixing in the fusion zone and in sufficiently high concentrations, alter the mechanical hardness of the weld metal. It was seen that the use of extended inert gas shielding of the weld pool and cooling material could reduce such contamination and so help better maintain the mechanical properties of the Ti-6Al-4V.

Trials used to assess the influence of surface finish on atmospheric contamination highlighted shortcomings in the use of colour as a means of assessment. While colours related to surface oxidation were observed to form in the standard progression for titanium and its alloys, the actual colour formed on a sample at any given temperature varied with each surface finish. In general, surfaces prepared by EDM wire cutting showed the greatest colouration while those faces prepared by machining showed the least. Again, the use of inert gas shielding was seen to reduce the apparent extent of contamination during thermal cycling. Charpy impact testing of samples subjected to thermal cycles analogous to those present in GTAW-wire based additive manufacturing showed no apparent variation with the atmosphere under which heating was conducted.

While further trials are needed, the outcomes of the present study suggest that post-weld atmospheric contamination of Ti-6Al-4V during the GTAW-wire based additive manufacturing process is minor and surface based. Post-weld atmospheric contamination does not affect the bulk mechanical properties, and hence any layers of contaminated material would be readily removed during the finish machining processes used to generate the final component profile. Despite the rudimentary nature of the results from these preliminary studies, they are considered to provide industrially relevant information regarding aspects of atmospheric contamination associated with the production of components from titanium and its using arc-wire based additive manufacturing.

CHAPTER 7 - CONCLUSIONS AND RECOMMENDATIONS

7.1 Conclusions

The crux of the present research project was the investigation of aspects of weldability associated with the additive manufacture of freeform structures from the Ti-6Al-4V titanium alloy using arc-wire deposition techniques based on the GTAW process. This was done both qualitatively and quantitatively with consideration of mechanical and physical properties and how they are related to the additive manufacturing process. It was intended that these results would contribute to a more thorough understanding of the GTAW-wire based additive manufacture method and its viability for the manufacture of large scale titanium aerospace components.

Initial studies were aimed at characterising the influence of key process parameters on the geometry and microstructure of additively manufactured Ti-6Al-4V produced by the GTAW-wire based method. Empirical curvilinear models were generated using multiple regression techniques to relate characterised features to the process parameters considered. These results clearly showed that the geometry of additively manufactured structures could be well predicted from knowledge of the arc current, weld travel speed and wire feed speed, with arc length and interpass temperature exerting little influence. Key microstructural features including volume fraction of α-Ti phase, α-Ti lath width and length, α-Ti colony size and prior β-Ti grain size appeared to show some dependence on the process parameters considered but are more likely related to cooling rate through the β-transus which was not characterised in the present work. The relationships between process variables and the resulting mechanical properties were evaluated through microhardness testing, with results showing a strong dependence on arc length. Additionally, qualitative observations of deposits suggest an effective process operating envelope exists in terms of specific deposition energy, which is based on arc energy and deposition rate. Overall it is considered that the mathematical models developed, particularly those relating to geometry of deposits, show considerable promise for both process optimisation and control in process automation.

Mechanical properties of the additively manufactured Ti-6Al-4V were evaluated through tensile testing, Charpy impact testing and hardness testing. While the results of tensile testing showed that the ultimate tensile strength and ductility of additively

manufactured samples was below that of equivalent conventionally processed plate material, measured values still satisfied the requirements for Ti-6Al-4V set out in relevant ASTM standards. The measured yield strength of additively manufactured samples was marginally less than the minimum specified limits, but may be improved to exceed these requirements with further process optimisation or using additional post weld processing. Tensile samples prepared transverse to the interface between the additively manufactured material and wrought base plate consistently fractured in the additively manufactured material indicating the interface is not the primary weakness in these 'composite' structures. Additively manufactured material also showed lower mechanical hardness than both wrought plate or billet materials, but satisfied ASTM standards for cast Ti-6Al-4V. Further, the impact toughness of additively manufactured material was seen to exceed that of equivalent wrought plate samples. This initial evaluation of mechanical properties shows significant promise, with further improvements expected through process optimisation and the use of post-weld heat treatments.

Machinability of the additively manufactured Ti-6Al-4V materials was investigated through milling and drill life trials. Cutting force during milling trials was lower in additively manufactured materials compared to conventionally manufactured wrought materials due to their lower strength and hardness. In contrast, the force during drilling operations conducted on additively manufactured Ti-6Al-4V was seen to be higher, despite drills used in this material showing less tool wear. Further investigation of drills used revealed variations in flute geometry which alter chip ejection from the drill hole and so influence drill performance. In general it is considered that Ti-6Al-4V produced by GTAW-wire based additive manufacturing responds to general material removal processes in a similar manner to conventionally manufactured wrought materials.

Residual stresses within representative thin-walled samples of Ti-6Al-4V produced by GTAW-wire based additive manufacturing were characterised through neutron diffraction with results compared to processing parameters. Residual stresses in additively manufactured structures were found to be considerably higher than in an equivalent sample produced from wrought billet by material removal processes, but similar in magnitude to those in a T-fillet sample manufactured by welded fabrication. Stress in the longitudinal direction was found to be dominant in all samples produced by welding, with peak stresses more localised to the HAZ in those which were additively

manufactured. The use of pulsed welding current broadened the region over which tensile residual stresses were found in the base plate, but also gave a reduction in the magnitude of peak stress. These relatively high residual stresses have the potential to compromise the mechanical performance of additively manufactured structures. While the use of PWHT showed the ability to significantly relieve such stresses, full relaxation of all residual stresses to produce a completely stress free structure, which would better withstand failure by fracture or fatigue, is not possible. When compared to that of an equivalent fabricated T-fillet structure, the residual stress profiles within additively manufactured samples are considered to be more favourable with peak stresses less broadly distributed in the structure. Hardness testing of these samples showed a lower level of microhardness in the additively manufactured material, which was also more homogeneous than the wrought base plate.

Aspects of atmospheric contamination associated with the GTAW-wire based additive manufacturing process were investigated through bead-on-plate welding trials and atmospheric exposure. These results indicate that the vast majority of atmospheric contamination of fusion welds in Ti-6Al-4V occurs post-weld in the solid state where insufficient inert gas shielding is provided to the welded material as it cools. The current means of contamination assessment by observation of surface colour was shown to be highly subjective in nature and not representative of any bulk contamination which may have occurred during the welding process. While high levels of interstitial impurities such as oxygen were shown to increase mechanical hardness, such effects are restricted to a thin layer of material adjacent to the exposed surface. As such, the occurrence of this type of post-weld atmospheric contamination during the additive manufacturing process would be negated by removal of these affected layers during subsequent finish machining processes used to produce the final component profile. Hence, it is considered that such contamination would have no discernible impact on the mechanical properties of a final component produced by the GTAW-wire based additive manufacturing method.

By encompassing a wide range of weldability aspects including mechanical properties, residual stresses and atmospheric contamination as well as process control, it is anticipated that the present study will contribute to the development of arc-wire based additive manufacture as an industrially viable means of producing structural titanium components. Additionally, it is hoped that this body of work will develop technical

know-how which assists Australian manufactures to compete globally in the supply of structural titanium components, particularly for the defence and aerospace sectors.

7.2 Recommendations for Future Work

The primary aim of the current research project was to conduct an investigation into the aspects of weldability associated with the additive manufacture of freeform structures from the Ti-6Al-4V titanium alloy using arc-wire deposition techniques based on the gas tungsten arc welding (GTAW) process. While the work conducted in this thesis is valuable in characterising and validating the GTAW based additive manufacture of components from titanium alloys, it has also highlighted a number of shortcomings in the current understanding which present opportunities for future work.

7.2.1 Process Optimisation

From the experimental work presented in Chapter 3 it is clear that the process models developed could be improved in a number of ways. Firstly, the measure of sidewall roughness needs to be revised with further work to try and better characterise the factors influencing machining layer thickness, or alternatively the definition of a more suitable metric. The characterisation of phase volume fractions could be improved using bulk diffraction techniques such as synchrotron x-ray or neutron diffraction. These are thought to be more suitable than standard laboratory x-ray diffraction since their increased penetration allows analysis of a bulk volume rather than surface layers. While it is thought the dependence of hardness on arc length is related to atmospheric contamination by interstitial species, this hypothesis needs to be verified through computational fluid dynamic modelling to observe how the inert gas shielding envelope is altered by arc length, as well as quantitative compositional analysis to measure contamination levels. Specific deposition energy was identified as a key processing parameter which also allows evaluation of process efficiency. As such it is suggested further work should be conducted to quantitatively assess the influence of specific deposition energy on additively manufactured deposits in terms of microstructure and mechanical properties.

While the empirically derived mathematical models produced show promise and appear to accurately predict geometrical and microstructural features in additively

manufactured structures of Ti-6Al-4V, it is clear that such models are of little use until they have been evaluated with and validated by experimental data independent from that used to create them. It follows then that additional experimental work needs to be conducted to produce and characterise a number of samples using parameter sets different to those from the present study. It is suggested that such validation trials be conducted using larger sample geometries, which better simulate the thermal characteristics of structural components targeted for manufacture with the GTA-wire based additive manufacturing method. Ideally, any such samples would be large enough to allow preparation of tensile and fatigue samples to give full evaluation of mechanical properties; however the size requirements for any such samples would incur high costs in terms of raw materials and sample preparation time.

The models generated could also be coupled with finite element and phase field models developed by other researchers to improve accuracy. As previously stated, process models generated may be adapted into a closed loop feedback type control system used in automation of the process. One example would be monitoring of arc voltage as a means of measuring arc length with wire addition controlled accordingly to maintain consistent build height should the height profile deviate from the desired value. The control system could also incorporate dynamic control of arc energy, travel speed and deposition rate to eliminate the bulge and narrowing features seen at the start of weld beads. Process control could be further enhanced by inclusion of visual sensors for monitoring of bead geometry [266] and acoustic sensors to monitor process stability [267, 268]. Clearly the development of such a system for robotic manipulators or computer numerically controlled equipment would require extensive work and validation.

7.2.2 Mechanical Properties

While the results presented in Chapter 4 show that Ti-6Al-4V produced by GTAW-wire based additive manufacturing behaves in a similar manner to commercially sourced wrought product mechanically, it is clear that a great deal of work remains to be done in this area. Firstly, drill tests conducted to assess machinability need to be repeated since variations in drill geometry were found after these tests in the present study were conducted. Machinability trials should be re-evaluated and repeated with newly

prepared samples which are more consistent and so eliminate uncertainty introduced through variable geometry.

It is felt that the mechanical properties of the additively manufactured material would be better compared to those of samples prepared from wrought billet material rather than plate sections. This is because any component for which the GTAW-wire based additive manufacturing process is being considered would ordinarily be manufactured using subtractive processes from billet sections and so this is the product form against which properties should be evaluated.

Further work may be done to better assess the influence of deposition process parameters on mechanical properties through preparation of a larger group of samples with, for example, differing values of heat input and specific deposition energy. This work could be extended by including an assessment of post-weld heat treatments, particularly those used to relieve residual stress or the common solution treated and aging process. In conjunction with the results presented in Chapter 3, such data would help significantly in process optimisation.

It is also clear that for such a process to be viable for the production of structural components from Ti-6Al-4V, the evaluation of mechanical properties needs be extended to include key characteristics for titanium alloys such as fracture toughness, fatigue and creep behaviour. Full characterisation of these properties is particularly important for potential aerospace applications where titanium alloys are selected for their excellent fracture and fatigue properties.

7.2.3 Residual Stress

Considering the measurements of residual stress described in Chapter 5, it is thought that the current results could be supplemented by a number of fields of future work.

Firstly, due to the limitations of the $\theta/2\theta$ neutron diffraction technique used being able to only measure diffraction from one single crystallographic plane at a time, and the observed difficulties in obtaining reliable diffraction data due to strong grain orientation, it is recommended that the samples from the present study be measured using an independent technique such as the contour method or time-of-flight neutron diffraction. While it is possible to measure multiple diffraction peaks using the KOWARI strain scanner at ANSTO, the required changes in experimental configuration are time consuming and were not considered to be the most efficient use of the beam-

time allocated. Instead it was considered that the time would be better spent analysing the same diffraction peak in multiple samples produced with different processing parameters. Collaborative work with the Institute of Materials Engineering (IME) at ANSTO has been established to destructively evaluate residual stresses using the contour method. The use of TOF techniques would be most beneficial, giving simultaneous measurement of multiple diffraction peaks from various lattice planes and so allow the characterisation of macro stresses in both the α-Ti and β-Ti phases as well as the determination of intergranular micro stresses. Proposals for such experiments were submitted to both the Rutherford Appleton Laboratory (ISIS) in the United Kingdom and the Japan Proton Accelerator Research Complex (JPARC), however due to the highly competitive selection process these applications were unsuccessful and hence, the envisaged experiments could not be conducted as part of the present study.

While such studies have been previously undertaken, it is suggested that the microstructural changes due to the use of pulsed arc current be investigated for samples used in the current study. Such work was not conducted since preparation of suitable samples for metallographic analysis is destructive in nature and would have rendered these additively manufactured samples as a whole useless for planned studies of residual stress by TOF neutron diffraction techniques.

The results of the present work represent a preliminary investigation of the residual stress of Ti-6Al-4V components formed using GTAW-wire based additive manufacture. As such there is still a substantial amount of further investigation required to fully validate the use of the process for manufacture of engineering components. Firstly, the distribution of residual stresses needs to be characterised along the length of the additively manufactured structure, particularly at the start and end regions where both welding conditions and mechanical constraints differ. This could then be extended to investigate the effects of different mechanical constraints, alternative build sequences, the use of preheat in the base plate and interpass heat treatments. Also of interest would be the influence of finish machining which could be assessed by conducting measurements on the same sample both before and after machining. An understanding of how machining causes stresses to redistribute through an additively manufactured component, and leads to distortion of such a component, is vital in the design of welding and machining sequences for complex thin-walled, deep pocketed profiles for which this process is best suited.

It is suggested that any similar measurements made in future studies would be well complemented by measurements of distortion in the as deposited condition using a CMM or laser profilometer. These measured distortions could then be related to both the physical constraints used during the manufacturing process and measured residual stresses. Such measurements of distortion could also be performed before and after PWHT to assess the extent of stress relaxation and how the component geometry changes to compensate and redistribute remaining residual stresses.

7.2.4 Atmospheric Contamination

Despite the primitive nature of the experimental work conducted, the results presented in Chapter 6 revealed a number of significant aspects relating to the atmospheric contamination of components produced from Ti-6Al-4V using GTAW-wire based additive manufacturing. This work also highlighted a number of areas where further study could be conducted. Firstly, the results of both bead-on-plate trials and experiments related to surface colouration could be greatly enhanced by coupling with quantitative analysis of chemical composition. This would be best done as line scans oriented from the contaminated surface into the bulk material using either electron probe micro-analysis (EPMA) or secondary ion mass spectrometry (SIMS). In these tests, the atomic species of interest would be primarily oxygen, but also nitrogen, carbon and hydrogen. If possible, the depth of contamination could be assessed using an ultra-micro indentation system (UMIS) with results correlated to composition analysis. The extent of atmospheric contamination in samples of the bulk additively manufactured material could be quantitatively analysed using suitable methods such as inductively coupled plasma-mass spectrometry (ICP-MS) or the inert gas fusion (IGF) technique.

It is also suggested that the use of colour as a means of assessing atmospheric contamination is flawed with a better alternative possibly being found through modelling of the contamination and diffusion processes. It is thought such a model could incorporate the time based integral of the overall thermal profile from the repeated heating during the additive manufacturing process, This could then be related to diffusion theory to predict the expected depth of contamination, termed the ‘cumulative contamination potential’, based on the atmospheric conditions under which the heating was conducted. Clearly such models would need to be validated through

experimental studies before being implemented into industrial processes such as the GTAW-wire based additive manufacture of Ti-6Al-4V.

In terms of practical recommendations for the use of the GTAW-wire based additive manufacturing process in industry for the production of components from Ti-6Al-4V, should the minimal atmospheric contamination observed be considered too high, it is thought there are two alternatives to help maintain the required mechanical properties. Firstly, rather than welding in a fully enclosed environment which places restrictions on build size, the process could be conducted in an open topped vessel which is purged with welding grade argon. Due to it being of higher density than air, this argon would settle in the bottom of the vessel and give an atmosphere with reduced oxygen concentration. Welding would then be conducted using the inert gas shielding from the welding torch and trailing shield as it currently is in air. While this wouldn't be as 'clean' an environment as a fully sealed and purged container, it could reduce the oxygen content in the region surrounding the welding process sufficiently to negate the effects of entrainment of air into the shielding envelope and solid state contamination of the reheated material which is outside the primary shielding envelope.

Secondly, to counter the adverse effects of atmospheric contamination, additive manufacturing of Ti-6Al-4V could be performed using ASTM grade 23 welding wire which is commercially available. This grade is essentially Ti-6Al-4V with extra-low interstitial (ELI) alloying contents. As such, any contamination of the deposited material by interstitial species such as oxygen, nitrogen and hydrogen during the additive manufacturing process would simply bring the mechanical properties back into line with standard Ti-6Al-4V (ASTM grade 5). This approach is recommended for conventional welding of Ti-6Al-4V by TIMET [269] and so could be readily implemented if required.

7.2.5 General Recommendations

Overall, it is considered that the next progression of the GTAW-wire based additive manufacturing is automation of the process. This would be best achieved, and is currently being developed [14], using a 6-axis robotic manipulator with process control based on the process characterisation work as identified in Section 7.2.1. Further, work is required to develop automated connections between computer aided design (CAD)

software and final weld path programming, as has been demonstrated by Ding *et al.* [270].

In terms of industrial manufacturing of large scale structural components, the GTAW-wire based process is not expected to entirely replace current subtractive manufacturing processes. Rather, the two should complement each where possible to reduce material usage and hence final costs. An example of this is the pylon bracket shown in Figure 7.1 where the protruding sidewall features, which would ordinarily require a thick billet section for manufacture, could be additively deposited onto a thinner slab section which is still machined to remove material and generate the required internal base profiles. Additive manufacturing as a whole will also facilitate alternative design possibilities where component geometry had previously been limited by manufacturing methods and acceptable costs. This additive manufacturing method also presents itself as being competitive with casting processes used for some titanium alloys, particularly those whose mechanical properties are less dependent on thermomechanical processing than Ti-6Al-4V [130].

Figure 7.1 Aircraft pylon bracket considered as a prime candidate for combined additive and subtractive manufacturing. From Sandvik Coromant [271].

Finally, the GTAW-wire based additive manufacture process may find application with materials other than Ti-6Al-4V where the potential cost savings or design benefits are considered to be advantageous. In any such case, the same regime of process characterisation, mechanical property evaluation and residual stress measurement would need to be performed, in addition to any material-specific considerations such as atmospheric contamination.

RFERENCES

1. Wessel, J.K., *The Handbook of Advanced Materials*. 2004, Hoboken, New Jersey: John Wiley & Sons, Inc.
2. Collings, E.W., *The Physical Metallurgy of Titanium Alloys*. 1984, Metals Park, Ohio: American Society for Metals.
3. Hummel, R.C. *Review Article - Titanium*. 2000 [cited 2010 April 29]; Available from: http://www.csa.com/discoveryguides/titanium/overview.php.
4. MII. *Titanium*. 2010 February 22 [cited 2010 April 29]; Available from: http://www.mii.org/Minerals/phototitan.html.
5. Tuck, C. and R. Hague, *The pivotal role of rapid manufacturing in the production of cost effective customised products.* International Journal of Mass Customisation, 2006. **1**(2/3): p. 360-373.
6. Markillie, P. (2012) *Manufacturing: The Third Industrial Revolution*. The Economist.
7. Danielson, P., R. Wilson, and D. Alman, *Microstructure of Titanium Welds*. 2004, U.S. Department of Energy: Albany, OR.
8. WTIA, *TGN-MS-02 Welding of Titanium Alloys*. 2006, Welding Technology Institute of Australia: Silverwater. p. 1-4.
9. Norrish, J., et al., *Titanium Weldability Investigation-Proposed Extension of Previous Work*, in *Australian JSF Advanced Technology and Innovation Conference*. 2010: Melbourne.
10. Kobelco. *Titanium Properties*. 2003 [cited 2011 January 25]; Available from: http://www.kobelco.co.jp/english/titan/files/details.pdf.
11. Wohlers, T. and T. Gornet, *History of additive manufacturing*, in *Wohlers Report 2011 - State of the Industry*. 2011, Wohler Associates, Inc.
12. Baufeld, B., E. Brandl, and O. van der Biest, *Wire based additive layer manufacturing: Comparison of microstructure and mechanical properties of Ti–6Al–4V components fabricated by laser-beam deposition and shaped metal deposition.* Journal of Materials Processing Technology, 2011. **211**(6): p. 1146-1158.
13. Brandl, E., et al., *Additive manufactured Ti-6Al-4V using welding wire: comparison of laser and arc beam deposition and evaluation with respect to aerospace material specifications.* Physics Procedia, 2010. **5, Part B**(0): p. 595-606.
14. Escobar-Palafox, G., R. Gault, and K. Ridgway, *Robotic manufacturing by shaped metal deposition: State of the art.* Industrial Robot, 2011. **38**(6): p. 622-628.
15. Sequeira Almeida, P.M. and S. Williams. *Innovative process model of Ti-6Al-4V additive layer manufactuiring using cold metal transfer (CMT)*. in *SFF Symposium 2010*. 2010. Austin, Texas.

16. Wang, F., et al., *Microstructure and Mechanical Properties of Wire and Arc Additive Manufactured Ti-6Al-4V*. Metallurgical and Materials Transactions A, 2013. **44**(2): p. 968-977.

17. Charles, C., *Modelling microstructure evolution of weld deposited Ti-6Al-4V*, in *Division for Material Mechanics - Department of Applied Physics*. 2008, Lulea University of Technology: Lulea.

18. MacDonald, W., *LIGHT METALS: Process Innovation to Create New Metals Industry*. CSIRO SOLVE, 2006. **2006**(8).

19. Higgins, R.A., *Materials for the Engineering Technician*. 2nd ed. 1991, New York, New York: Edward Arnold.

20. Nave, C.R. *Abundances of the Elements in the Earth's Crust*. 2008 [cited 2011 April 25]; Available from: http://hyperphysics.phy-astr.gsu.edu/hbase/tables/elabund.html.

21. Boyer, R., E.W. Collings, and G. Welsch, *Materials Property Handbook: Titanium Alloys*. 1994, Materials Park, OH: ASM International.

22. Callister, W.D., *Materials Science and Engineering, an Introduction*. 7th ed. 2007, New York: John Wiley & Sons, Inc.

23. Lutjering, G. and J.C. Williams, *1. Introduction*, in *Titanium*, B. Derby, Editor. 2007, Springer. p. 1-14.

24. Seong, S., O. Younossi, and B.W. Goldsmith, *Titanium: Industrial Base, Price Trends, and Technology Initiatives*. 2009, Santa Monica, California: RAND Corporation. 155.

25. *CES EduPack 2012 Version 11.9.9*. 2012, Granta Design: Cambridge UK.

26. Fix, D.V., et al., *Susceptibility of welded and non-welded titanium alloys to environmentall assisted cracking in simulated concentrated ground waters*, in *Corrosion/2004*. 2004: New Orleans, LA.

27. Struers, B. Taylor, and E. Weidmann. *Application Notes - Metallographic Preparation of Titanium*. [PDF] 2009 [cited 2009 October 2]; Available from: http://www.struers.com/resources/elements/12/104827/Application_Note_Titanium_English.pdf.

28. Taneichi, K., et al., *Alloy Design and Property Evaluation of New Beta Type Titanium Alloy with Excellent Cold Workability and Biocompatibility*. ISIJ International, 2006. **46**(2): p. 292-301.

29. Wang, X., et al., *Porous TiNbZr alloy scaffolds for biomedical applications.* Acta Biomaterialia, 2009. **5**: p. 3616-3624.

30. Lockheed_Martin_Corporation. *F-35 Lightning II*. 2009 [cited 2009 October]; Available from: http://www.lockheedmartin.com/data/assets/aeronautics/products/f35/f35_6.jpg.

31. Bhadeshia, H.K.D.H. *Metallurgy of Titanium and its Alloys: Applications*. 2004 [cited 2009 October]; Available from: http://www.msm.cam.ac.uk/phasetrans/2004/titanium/titanium2.html.

32. TITAN. *U Tube Titanium Heat Exchanger*. 2011 [cited 2011 April 25]; Photo of U Tube Titanium Heat Exchanger]. Available from: http://www.titanmf.com/products/chemical/pic6b-heat-exchangers.htm.

33. Corin_USA. *Tri-fit Total Hip System*. 2006 [cited 2009 October]; Available from: http://www.corin.co.uk/USA/usawebsite/productsHips.html.

34. Lynskey. *Mountain Bike Gallery*. 2008 [cited 2009 November]; Available from: http://www.lynskeyperformance.com/a/pages/gallery/mountain-bikes.php.

35. Hogan, L., E. McGinn, and R. Kendall, *Research and Development in Titanium - Implications for a Titanium Metal Industry in Australia*. 2008, Australian Bureau of Agriculture and Resource Economics.

36. Hoyt, P., *Titanium Emerges as New Seawater Piping for Navy Vessels.* Welding Journal, 2006. **85**(6): p. 62-65.

37. Lutjering, G. and J.C. Williams, *4. Commercially Pure and Alpha Alloys*, in *Titanium*, B. Derby, Editor. 2007, Springer. p. 86-115.

38. MatWeb, *Online Materials Information Resource*. 2014, MatWeb, LLC.

39. Boyer, R.R. and R.D. Briggs, *The Use of Beta Titanium Alloys in the Aerospace Industry.* Journal of Materials Engineering and Performance, 2005. **14**(6): p. 681-685.

40. Dehghan-Manshadi, A. and R.J. Dippenaar, *Development of [alpha]-phase morphologies during low temperature isothermal heat treatment of a Ti-5Al-5Mo-5V-3Cr alloy.* Materials Science and Engineering A, 2011. **528**(3): p. 1833-1839.

41. Sakamoto, T., et al., *Precipitation of β′ Phase in a Low Cost Beta Titanium Alloy.* Materials Science Forum, 2010. **638-642**: p. 461-464.

42. Mantione, J.V. and T.D. Bayha. *ATI Allvac Development of Ti-5-5-5-3 for Aerospace Applications*. in *18th AeroMat Conference and Exposition*. 2007. Baltimore, Maryland.

43. Veeck, S., et al., *The castability of Ti-5553 alloy.* Advanced Materials and Processes, 2004. **162**(10): p. 47-49.

44. Hurless, B.E. and F.H. Froes, *Lowering the Cost of Titanium.* The AMPTIAC Quarterly, 2002. **6**(2): p. 3-9.

45. Yang, X. and C.R. Liu, *Machining titanium and its alloys.* Machining Science and Technology, 1999. **3**(Compendex): p. 107-139.

46. CarbideDepot. *Machinability Comparison Chart*. 2005 [cited 2011 May 26]; Available from: http://www.carbidedepot.com/formulas-machinability.htm.

47. EngineeringToolbox. *Metals Machinability*. 2011 [cited 2011 May 26]; Available from: http://www.engineeringtoolbox.com/machinability-metals-d_1450.html.

48. Barnes, J.E., et al. *LMCut Benefits - An OEM Perspective*. in *Australian JSF Advanced Technology and Innovation Conference*. 2010. Melbourne, Australia.

49. Rosenberger, B. *Direct Manufacturing Overview*. in *Australian JSF Advanced Technology and Innovation Conference*. 2010. Melbourne, Australia.

50. Geoscience_Australia. *Titanium - Mineral Fact Sheets - Australian Mines Atlas*. 2011 [cited 2011 June 3]; Available from: http://www.australianminesatlas.gov.au/education/fact_sheets/titanium.jsp.

51. Veldhuizen, J., *Austpac Resources N.L (APG) Brokerage Report*. 2000, BNP Equities Private (Australia) Limited. p. 1-8.

52. Gambogi, J., *2009 Mineral Yearbook - Titanium [Advance Release]*, in *Minerals Yearbook*, U.S.G. Survey, Editor. 2009, United States Geological Survey. p. 1-19.

53. Titanium_Era. *Titanium Facts*. n.d. [cited 2009 October]; Available from: http://www.titaniumera.com/index/pagepopup/doc/titanium_facts.

54. Lutjering, G. and J.C. Williams, *3. Technological Aspects*, in *Titanium*, B. Derby, Editor. 2007, Springer.

55. Lancashire, R.J. *Chemistry of Titanium*. 2001 November 14, 2007 [cited 2009 October]; Available from: http://www.chem.uwimona.edu.jm/courses/titanium.html.

56. TOHO_Titanium. *Titanium Metals - Titanium Sponge*. 2009 [cited 2009 October]; Available from: http://www.toho-titanium.co.jp/en/products/sponge_en.html.

57. Sumitomo_Corporation. *Titanium Department*. 2008 [cited 2011 July 8]; Available from: http://www.sumitomocorp.co.jp/titanium/.

58. Kraft, E., *Summary of Emerging Titanium Cost Reduction Technologies*. 2004, EHK Technologies-for ORNL: Vancouver, WA. p. 1-59.

59. Gerdemann, S.J., *Titanium Process Technologies.* Advanced Materials and Processes, 2001. **159**(7): p. 41-43.

60. Fuller, B., *Initiating Low Cost Titanium Parts*, in *Australasian Cold Spray 2011 Conference*. 2011: Melbourne, Australia.

61. Araci, K., M.K. Akhtar, and D. Mangabhai, *From Powder to Lower Cost Titanium Parts*, in *Ti-2011 The 12th World Conference on Titanium*. 2011: Beijing, China.

62. Cristal_Global. *International Titanium Powder Fact Sheet*. 2009 [cited 2011 July 12]; Available from: http://wwww.cristalarabia.com/AboutCristalGlobal_Resources/ITP_FactSheet_5-19_FINAL.pdf.

63. CSIRO. *Making titanium metal powder*. 2010 [cited 2011 July 12]; Available from: http://www.csiro.au/science/TiRO--ci_pageNo-1.html.

64. CSIRO. *Cutting the cost of making titanium metal*. 2006 [cited 2010 March 9]; Available from: http://www.csiro.au/science/TiRO.html#1.

65. Chen, G.Z., Fray, D.J., Farthing, T.W., *Direct electrochemical reduction of titanium dioxide to titanium in molten calcium chloride.* Nature, 2000. **407**: p. 361-364.

66. Metalysis. *Metalysis: Process*. 2009 [cited 2011 July 13]; Available from: http://www.metalysis.com/process.php.

67. Metalysis. *Metalysis: Benefits*. 2009 [cited 2011 July 13]; Available from: http://www.metalysis.com/benefits.php.

68. Fray, D.J., Chen, G.Z., *Reduction of titanium and other metal oxides using electrodeoxidation.* Materials Science and Technology, 2004. **20**(3): p. 295-300.

69. Metalysis. *Metalysis: Products & Applications*. 2009 [cited 2011 July 13]; Available from: http://www.metalysis.com/products.php.

70. Metalysis. *Production Facility*. n.d. [cited 2014 February 28]; Available from: www.metalysis.com/production-facility.

71. Withers, J.C., Cardarelli, F., Laughlin, J., Loutfy, R.O., *Recent Improvements for Electrowinning Titanium from Metal Composite Anodes*. 2008, Materials and Electrochemical Research Corporation.

72. Smock, D. *DARPA Seeks Titanium Alternatives*. 2007 [cited 2010 April 8]; Available from: http://www.designnews.com/article/2228-DARPA_Seeks_Titanium_Alternatives.php.

73. DuPont, *Titanium powder process.(EMERGING TECHNOLOGIES: industrial).* R & D, 2006. **48**(10): p. 47(1).

74. Austpac. *Technologies - ERMS SR*. n.d. [cited 2011 July 13]; Available from: http://www.austpacresources.com/erms.php.

75. Carpenter. *Technical Datasheet - Titanium Alloy Ti 6Al-4V*. 2000 [cited 2011 August 1]; Available from: http://cartech.ides.com/datatsheet.aspx?i=101&E=269.

76. Chretien, J., et al., *Titanium Alpha Case Prevention*. 2010, Worcester Polytechnic Institute.

77. Gurappa, I., *Prediction of titanium alloy component life by developing an oxidation model.* Journal of Materials Science Letters, 2003. **22**(10): p. 771-774.

78. Ohkubo, C., et al., *The machinability of cast titanium and Ti-6Al-4V.* Biomaterials, 2000. **21**(4): p. 421-428.

79. Ezugwu, E.O., et al., *The Effect of Argon-Enriched Environment in High-Speed Machining of Titanium Alloy.* Tribology Transactions, 2005. **48**(1): p. 18-18-23.

80. Mattox, D.M., *Handbook of physical vapor deposition (PVD) processing*. 1998, Westwood, New Jersey: Noyes Publications.

81. Child, H.C. and A.L. Dalton, *Machining of Titanium Alloys. Pt. 1-Metallurgical Factors Affecting Machinability.* Machinability, 1967: p. 139-142, 163-169.

82. Konig, W. and K.H. Schroder, *Face Milling and Drilling of Ti Alloys.* Influence of Metallurgy on Machinability. ASM, Metals Park, Ohio. 1975, 308-323, 1975.

83. Middleton, R. *Advanced Process Monitoring for Optimised Titanium Machining*. in *Australian JSF Advanced Technology and Innovation Conference*. 2010. Melbourne, Australia.

84. Ezugwu, E.O. and Z.M. Wang, *Titanium alloys and their machinability--a review.* Journal of Materials Processing Technology, 1997. **68**(3): p. 262-274.

85. Frayman, Y., S. Palanisamy, and S. Nahavandi. *Chatter suppression in Ti Machining*. in *Australian JSF Advanced Technology and Innovation Conference*. 2010. Melbourne, Australia.

86. Scherrer, M., et al. *Laser Assisted Machining of Titanium*. in *Australian JSF Advanced Technology and Innovation Conference*. 2010. Melbourne, Australia.

87. RMI, *Titanium Alloy Guide*. 2004, RTI International Metals Inc. p. 10-15.

88. TIMET, *Titanium design and fabrication handbook for industrial applications*. 2006, Titanium Metals Corporation. p. 14-33.

89. de Lacalle, L.N.L., et al., *Using high pressure coolant in the drilling and turning of low machinability alloys.* International journal of advanced manufacturing technology, 2000. **16**(2): p. 85-91.

90. Ezugwu, E.O., et al., *Surface integrity of finished turned Ti-6Al-4V alloy with PCD tools using conventional and high pressure coolant supplies.* International Journal of Machine Tools and Manufacture, 2007. **47**(6): p. 884-891.

91. Ezugwu, E.O., et al., *High Productivity Rough Turning of Ti-6Al-4V Alloy, with Flood and High-Pressure Cooling.* Tribology Transactions, 2009. **52**(3): p. 395-395-400.

92. Palanisamy, S., et al., *High pressure coolant application in milling titanium.* Materials Science Forum, 2009. **618-619**: p. 89-92.

93. Hong, S.Y., I. Markus, and W.-c. Jeong, *New cooling approach and tool life improvement in cryogenic machining of titanium alloy Ti-6Al-4V.* International Journal of Machine Tools and Manufacture, 2001. **41**(15): p. 2245-2260.

94. Machai, C. and D. Biermann, *Machining of [beta]-titanium-alloy Ti-10V-2Fe-3Al under cryogenic conditions: Cooling with carbon dioxide snow*. Journal of Materials Processing Technology, 2011. **211**(6): p. 1175-1183.

95. Barnes, J.E., et al., *High speed machining of titanium alloys.* Materials Science Forum, 2009. **618-619**: p. 159-163.

96. Weisert, E.D. and G.W. Stacher, *Concurrent Superplastic Forming/Diffusion Bonding of Titianium*, in *Superplastic Forming of Structural Alloys*, N.E. Paton and C.H. Hamilton, Editors. 1982, The Metallurgical Society of AIME. p. 273-289.

97. Low, R.J., et al., *Sintering of titanium powder compacts for containerless hot isostatic pressing.* Materials Science Forum, 2009. **618-619**(0255-5476, 0255-5476): p. 509-509-512.

98. Ezugwu, E.O., *Key improvements in the machining of difficult-to-cut aerospace superalloys.* International Journal of Machine Tools and Manufacture, 2005. **45**(12-13): p. 1353-1367.

99. Cantin, G.M.D., et al., *Innovative consolidation of titanium and titanium alloy powders by direct rolling.* Powder Metallurgy, 2011. **54**(3): p. 188-192.

100. Stone, N., et al., *Implementing the direct powder route for titanium mill product: Continuous production of cp sheet.* Materials Science Forum, 2009. **618-619**(0255-5476, 0255-5476): p. 139-139-142.

101. Dombrowski, H.S., *2,984,560 - Production of high-purity, ductile titanium powder*, U.S.P. Office, Editor. 1961: United States of America.

102. Dombrowski, H.S., *3,072,347 - Metal Processing*, U.S.P. Office, Editor. 1963: United States of America.

103. Dombrowski, H.S., *3,084,042 - Metal Production*, U.S.P. Office, Editor. 1963: United States of America.

104. Baeslack, W., J. Davis, and C. Cross, *Selection and weldability of conventional titanium alloys*, in *ASM International, ASM Handbook.* 1993. p. 507-523.

105. Moiseyev, V.N., *Titanium alloys; Russian aircraft and aerospace applications*. Advances in metallic alloys. Vol. 30. 2006: Taylor & Francis.

106. AWS, *AWS D1.9/D1.9M:2007 Structural Welding Code - Titanium*, in *Table 5.3 - Coloration Acceptance Criteria*. 2007, American Welding Society. p. 82.

107. Hua, F., et al., *Modeling the hydrogen-induced cracking of titanium alloys in nuclear waste repository environments.* JOM, 2005. **57**(1): p. 20-26.

108. Tal-Gutelmacher, E. and D. Eliezer, *Hydrogen cracking in titanium-based alloys.* Journal of Alloys and Compounds, 2005. **404–406**(0): p. 621-625.

109. ASM. *Titanium Grade 1*. 2011 [cited 2011 April 28]; Available from: http://asm.matweb.com/search/SpecificMaterial.asp?bassnum=MTU011.

110. ASM. *Titanium Grade 2*. 2011 [cited 2011 April 28]; Available from: http://asm.matweb.com/search/SpecificMaterial.asp?bassnum=MTU021.

111. ASM. *Titanium Grade 3*. 2011 [cited 2011 April 28]; Available from: http://asm.matweb.com/search/SpecificMaterial.asp?bassnum=MTU031.

112. ASM. *Titanium Grade 4*. 2011 [cited 2011 April 28]; Available from: http://asm.matweb.com/search/SpecificMaterial.asp?bassnum=MTU041.

113. TWI. *Weldability of materials. Titanium and titanium alloys.* 2009 [cited 2011 June 6]; Available from: http://www.twi-global.com/technical-knowledge/job-knowledge/weldability-of-materials-titanium-and-titanium-alloys-024/.

114. Wang, F., S. Williams, and M. Rush, *Morphology investigation on direct current pulsed gas tungsten arc welded additive layer manufactured Ti6Al4V alloy.* International Journal of Advanced Manufacturing Technology, 2011. **57**(5-8): p. 597-603.

115. Kou, S., *Welding Metallurgy*. 2nd ed. 2003, Hoboken, NJ: John Wiley & Sons Inc.

116. Hallum, D.L. and W.A. Baeslack, *Nature of Grain Refinement in Titanium Alloy Welds by Microcooler Inoculation.* Welding Research Supplement, 1990. **09**: p. 326-336.

117. Balasubramanian, M., V. Jayabalan, and V. Balasubramanian, *Effect of microstructure on impact toughness of pulsed current GTA welded α–β titanium alloy.* Materials Letters, 2008. **62**(6–7): p. 1102-1106.

118. Kishore Babu, N., et al., *Correlation of microstructure with mechanical properties of TIG weldments of Ti–6Al–4V made with and without current pulsing.* Materials Characterization, 2007. **58**(7): p. 581-587.

119. Sundaresan, S., G.D. Janaki Ram, and G. Madhusudhan Reddy, *Microstructural refinement of weld fusion zones in α–β titanium alloys using pulsed current welding.* Materials Science and Engineering: A, 1999. **262**(1–2): p. 88-100.

120. Mitzner, S.V., *Grain refinement and epitaxial interruption of freeform fabricated Ti-6Al-4V alloy*, in *Department of Metallurgical and Materials Engineering*. 2012, Colorado School of Mines: Golden, CO. p. 108.

121. Donachie, M.J.J., *Titanium - A Technical Guide*. 2nd ed. 1982, Metals Park, Ohio: American Society for Metals.

122. Inoue, H., S. Ohkita, and T. Nagatani, *Weld Cracking and Solidification Behavior of Titanium Alloys*, in *Nippon Steel Technical Report*. 2002.

123. Allen, J., *An Investigation into the Comparative Costs of Additive Manufacture vs. Machine from Solid for Aero Engine Parts*. 2006, Rolls Royce PLC: Derby, UK.

124. 3DSystems, *Direct Metal Production 3D Printers*. 2013: Rock Hill, SC.

125. Arcam. *EBM Process*. 2009 [cited 2011 July 29]; Available from: http://www.arcam.com/technology/ebm-process.aspx.

126. ReaLizer, *Selective Laser Melting - Visions become reality*. 2014, ReaLizer SLM.

127. Renishaw, *Brochure: The power of Additive Manufacturing*, R. plc, Editor. 2014: Stone, United Kingdom.

128. EOS. *Systems and Solutions for Metal Manufacturing*. n.d. [cited 2014 March 11]; Available from: http://www.eos.info/systems_solutions/metal.

129. Optomec. *LENS Technology*. 2006 [cited 2014 March 11]; Available from: http://www.optomec.com/Additive-Manufacturing-Technology/Laser-Additive-Manufacturing.

130. Kobryn, P.A., et al., *Additive Manufacturing of Aerospace Alloys for Aircraft Structures*. 2006, Wright-Patterson Air Force Base.

131. Alcisto, J., et al., *Tensile Properties and Microstructures of Laser-Formed Ti-6Al-4V*. Journal of Materials Engineering and Performance, 2011. **20**(2): p. 203-212.

132. DMG_MORI. *LASERTEC 65 AdditiveManufacturing*. 2014 [cited 2014 4 March]; Available from: http://pfronten.dmgmori.com/en/wp-lasertec-65-additive-manufacturing.htm.

133. MERCorp, *Plasma Transferred Arc Solid Free Form Fabrication*. 2005, Materials and Electrochemical Research Corporation.

134. Allen, B. *Electron Beam Freeform Fabrication*. NASA Technologies 2011 June 23, 2011 [cited 2014 March 11]; Available from: http://www.nasa.gov/topics/technology/features/ebf3.html.

135. Sciaky, *Additive Manufacturing*. 2013, Sciaky Inc.: Chicago, IL.

136. HRT. *LaserForge Technology*. Metallurgical-bond cold-coating & joining with advanced alloys n.d. [cited 2014 March 11]; Available from: http://www.hrtechnology.com/technology.html.

137. Ding, J., et al., *Thermo-mechanical analysis of Wire and Arc Additive Layer Manufacturing process on large multi-layer parts.* Computational Materials Science, 2011. **50**(12): p. 3315-3322.

138. Stavinoha, J.N., *Investigation of plasma arc welding as a method for the additive manufacturing of titanium-(6)aluminum-(4)vanadium alloy components*, in *General Engineering*. 2012, Montana Tech of The University of Montana: Butte. p. 197.

139. Hanlon, M. *Rapid prototyping to be used for human implant development* 2006 [cited 2011 July 28]; November 30, 2006]. Available from: http://www.gizmag.com/go/6657/.

140. Li, X., et al., *Fabrication and characterization of porous Ti6Al4V parts for biomedical applications using electron beam melting process.* Materials Letters, 2009. **63**: p. 403-405.

141. Brice, C.A., et al., *Chemistry control in electron beam deposited titanium alloys`*. Materials Science Forum, 2009. **618-619**: p. 155-158.

142. Robinson, L. and J. Scott, *Layers of Complexity: Making the Promises Possible for Additive Manufacturing of Metals.* JOM, 2014. **66**(11): p. 2194-2207.

143. Gockel, J. and J. Beuth, *Understanding Ti-6Al-4V Microstructure Control in Additive Manufacturing via Process Maps*, in *24th Annual International Solid Freeform Fabrication Symposium*. 2013, University of Texas Austin: Austin, TX. p. 666-674.

144. Janaki Ram, G.D., Y. Yang, and B.E. Stucker, *Effect of process parameters on bond formation during ultrasonic consolidation of aluminum alloy 3003.* Journal of Manufacturing Systems, 2006. **25**(3): p. 221-238.

145. Gao, Y. and C. Doumanidis, *Mechanical Analysis of Ultrasonic Bonding for Rapid Prototyping.* Journal of Manufacturing Science and Engineering, 2002. **124**(2): p. 426-434.

146. Janaki Ram, G.D., et al., *Interface Microstructures and Bond Formation in Ultrasonic Consolidation*, in *18th Annual International Solid Freeform Fabrication Symposium*. 2007: Austin, TX.

147. Pasang, T., et al., *Comparison of Ti-5Al-5V-5Mo-3Cr Welds Performed by Laser Beam, Electron Beam and Gas Tungsten Arc Welding.* Procedia Engineering, 2013. **63**(0): p. 397-404.

148. Benyounis, K.Y. and A.G. Olabi, *Optimization of different welding processes using statistical and numerical approaches – A reference guide.* Advances in Engineering Software, 2008. **39**(6): p. 483-496.

149. Dutta, P. and D.K. Pratihar, *Modeling of TIG welding process using conventional regression analysis and neural network-based approaches.* Journal of Materials Processing Technology, 2007. **184**(1–3): p. 56-68.

150. Lutjering, G. and J.C. Williams, *2. Fundamental Aspects*, in *Titanium*, B. Derby, Editor. 2007, Springer. p. 42-52.

151. Hoye, N., *Phase Transformation Investigations in Ti-6Al-4V Alloys*, in *Faculty of Engineering*. 2009, University of Wollongong: Wollongong. p. 116.

152. Lutjering, G., *Influence of processing on microstructure and mechanical properties of (a+b) titanium alloys.* Materials Science and Engineering A, 1998. **243**: p. 32-45.

153. Lutjering, G. and J.C. Williams, *5. Alpha+Beta Alloys*, in *Titanium*. 2007, Springer: Berlin. p. 203-258.

154. Sieniawski, J., et al., *Microstructure and Mechanical Properties of High Strength Two-Phase Titanium Alloys*, in *Titanium Alloys - Advances in Properties Control*, J. Sieniawski and W. Ziaja, Editors. 2013, InTech: Rijeka, Croatia.

155. Ahmed, T. and H.J. Rack, *Phase transformations during cooling in [alpha]+[beta] titanium alloys.* Materials Science and Engineering A, 1998. **243**(1-2): p. 206-211.

156. Sahay, S.K., et al., *Studies of Phase Transformations in Ti-Al-X Alloys.* High Temperature Materials and Processes, 2005. **24**(6): p. 345-358.

157. Balasubramanian, T.S., et al., *Influence of welding processes on microstructure, tensile and impact properties of Ti-6Al-4V alloy joints.* Transactions of Nonferrous Metals Society of China (English Edition), 2011. **21**(6): p. 1253-1262.

158. Balasubramanian, T.S., V. Balasubramanian, and M.A. Muthumanikkam, *Fatigue Performance of Gas Tungsten Arc, Electron Beam, and Laser Beam Welded Ti-6Al-4V Alloy Joints.* Journal of Materials Engineering and Performance, 2011: p. 1-11.

159. Short, A.B., *Gas tungsten arc welding of α + β titanium alloys: A review.* Materials Science and Technology, 2009. **25**(3): p. 309-324.

160. Yung, K.C., et al., *An investigation into welding parameters affecting the tensile properties of titanium welds.* Journal of Materials Processing Technology, 1997. **63**: p. 759-764.

161. Bontha, S., *The effect of process variables on microstructure in laser-deposited materials*. 2006, Wright State University: Ann Arbor. p. 179-179 p.

162. Kobryn, P.A. and S.L. Semiatin, *Microstructure and texture evolution during solidification processing of Ti–6Al–4V.* Journal of Materials Processing Technology, 2003. **135**(2–3): p. 330-339.

163. Kelly, S.M., *Thermal and microstructure modeling of metal deposition processes with application to titanium aluminum vanadium*. 2004, Virginia Polytechnic Institute and State University: Ann Arbor. p. 319-319 p.

164. Boyer, R.R. and D.U. Furrer, *The Potential Advantages of Microstructure Modeling of Titanium to the Aerospace Industry.* AIP Conference Proceedings, 2004. **712**(1): p. 1694-1699.

165. Moon, H.-S. and S.-J. Na, *Optimum design based on mathematical model and neural network to predict weld parameters for fillet joints.* Journal of Manufacturing Systems, 1997. **16**(1): p. 13-23.

166. Mishra, S. and T. DebRoy, *Tailoring gas tungsten arc weld geometry using a genetic algorithm and a neural network trained with convective heat flow*

calculations. Materials Science and Engineering: A, 2007. **454–455**(0): p. 477-486.

167. Esme, U., et al., *Mathematical Modeling for prediction and optimisation of TIG welding pool geometry.* Metallurgy, 2009. **48**(2): p. 109-112.

168. Tarng, Y.S., H.L. Tsai, and S.S. Yeh, *Modeling, optimization and classification of weld quality in tungsten inert gas welding.* International Journal of Machine Tools and Manufacture, 1999. **39**(9): p. 1427-1438.

169. Tarng, Y.S. and W.H. Yang, *Optimisation of the weld bead geometry in gas tungsten arc welding by the Taguchi method.* The International Journal of Advanced Manufacturing Technology, 1998. **14**(8): p. 549-554.

170. Nagesh, D.S. and G.L. Datta, *Genetic algorithm for optimization of welding variables for height to width ratio and application of ANN for prediction of bead geometry for TIG welding process.* Applied Soft Computing, 2010. **10**(3): p. 897-907.

171. Martina, F., et al., *Investigation of the benefits of plasma deposition for the additive layer manufacture of Ti–6Al–4V.* Journal of Materials Processing Technology, 2012. **212**(6): p. 1377-1386.

172. Beuth, J. and N. Klingbeil, *The role of process variables in laser-based direct metal solid freeform fabrication.* JOM, 2001. **53**(9): p. 36.

173. Higginson, R.L. and C.M. Sellars, *Worked Examples in Quantitative Metallography*. 2003, London: Maney Publishing.

174. ASTM, *ASTM E112 - 96 Standard Test Methods for Determining Average Grain Size*. 1996, ASTM International: West Conshohocken, PA.

175. Kobryn, P.A., E.H. Moore, and S.L. Semiatin, *The effect of laser power and traverse speed on microstructure, porosity, and build height in laser-deposited Ti-6Al-4V.* Scripta Materialia, 2000. **43**(4): p. 299-305.

176. Yang, Z., et al., *Evolution of Titanium Arc Weldment Macro and Microstructures Modeling and Real Time Mapping of Phases.* Welding Research Supplement, 2000.

177. Yang, Z., et al., *Three dimensional Monte Carlo simulation of grain growth during GTA welding of titanium.* Acta Materialia, 2000. **48**: p. 4813-4825.

178. Ma, N. and Y. Wang, *Beta Grain Growth Kinetics in Ti6Al4V*, in *NUMIFORM 2004*. 2004, American Institute of Physics: Columbus, Ohio.

179. Harwig, D.D., W. Ittiwattana, and H. Castner, *Advances in oxygen equivalent equations for predicting the properties of titanium welds.* Welding Journal, 2001. **80**(5): p. 126s-136s.

180. Harwig, D.D., et al., *Oxygen equivalent effects on the mechanical properties of titanium welds.* Welding Journal, 2000. **79**(11): p. 305s-316s.

181. Harwig, D.D., et al., *Portable Hardness Test Tehnology for Assessing Titanium Weld Quality*. 2002, Edison Welding Institute: Columbus, OH. p. 83-88.

182. McGlone, J.C. and D.B. Chadwick, *The submerged arc butt welding of mild steel Part 2: Prediction of weld bead geometry from the procedure parameters*. 1978, The Welding Institute.

183. Baufeld, B., O.V.d. Biest, and R. Gault, *Additive manufacturing of Ti–6Al–4V components by shaped metal deposition: Microstructure and mechanical properties.* Materials & Design, 2010. **31, Supplement 1**(0): p. S106-S111.

184. Baufeld, B. and O. van der Biest, *Mechanical properties of Ti-6Al-4V specimens produced by shaped metal deposition.* Science and Technology of Advanced Materials, 2009. **10**(1): p. 1-10.

185. Antonysamy, A.A., *Microstructure, Texture and Mechanical Property Evolution during Additive Manufacturing of Ti6Al4V Alloy for Aerospace Applications*, in *Faculty of Engineering and Physical Sciences*. 2012, The University of Manchester: Manchester. p. 315.

186. Baufeld, B., *Effect of deposition parameters on mechanical properties of shaped metal deposition parts.* Proceedings of the Institution of Mechanical Engineers. Part B, Journal of engineering manufacture, 2012. **226**(1): p. 126-136.

187. Brandl, E., C. Leyens, and F. Palm, *Mechanical Properties of Additive Manufactured Ti-6Al-4V Using Wire and Powder Based Processes.* IOP Conference Series: Materials Science and Engineering, 2011. **26**(1): p. 1-11.

188. Brandl, E., et al., *Mechanical properties of additive manufactured titanium (Ti–6Al–4V) blocks deposited by a solid-state laser and wire.* Materials & Design, 2011. **32**(10): p. 4665-4675.

189. Kobryn, P.A. and S.L. Semiatin, *Mchanical Properties of Laser-Deposited Ti-6Al-4V*, in *SFF Symposium*. 2001, The University of Texas at Austin: Austin, TX. p. 179-186.

190. Facchini, L., et al., *Ductility of a Ti-6Al-4V alloy produced by selective laser melting of prealloyed powders.* Rapid Prototyping Journal, 2010. **16**(6): p. 450-459.

191. Taminger, K.M., *Electron Beam Additive Manufacturing: State-of-the-Technology, Callenges & Opportunities*, in *Direct Digital Manufacturing Workshop*. 2010, NASA Langley Research Centre: Solomons, MD.

192. Bendersky, L. and A. Rosen, *The effect of exposure on the mechanical properties of the Ti-6Al-4V alloy.* Engineering Fracture Mechanics, 1984. **20**(2): p. 303-311.

193. Smarsly, W., Y.T. Lee, and G. Welsch, *Microporosity in Hot Isostatically Pressed Ti--6Al--4V Powder Compacts.* Metall. Trans. A, 1985. **16A**(10): p. 1831-1834.

194. ASTM, *ASTM E8M - 04 Standard Test Methods for Tension Testing of Metallic Materials [Metric]*. 2004, ASTM International: West Conshohocken, PA.

195. ASTM, *ASTM E23 - 02a Standard Test Methods for Notched Bar Impact Testing of Metallic Materials*. 2002, ASTM International: West Conshohocken, PA.

196. Herold, H., et al., *Use of Instrumented Charpy Impact Tests for the Determination of Fracture Toughness Values.* Praktische Metallographie-Practical Metallography, 2010. **47**(1): p. 34-44.

197. ASTM, *ASTM B348 - 03 Standard Specification for Titanium and Titanium Alloy Bars and Billets*. 2003, ASTM International: West Conshohocken, PA.

198. ASTM, *ASTM B265 - 03 Standard Specification for Titanium and Titanium Alloy Strip, Sheet, and Plate*. 2003, ASTM International: West Conshohocken, PA.

199. ASTM, *ASTM B367 - 93 Standard Specification for Titanium and Titanium Alloy Castings*. 1997, ASTM International: West Conshohocken, PA.

200. ASTM, *ASTM E140 - 97 Standard Hardness Conversion Tables for Metals Relationship Among Brinell Hardness, Vickers Hardness, Rockwell Hardness, Superficial Hardness, Knoop Hardness, and Scleroscope Hardness*. 1997, ASTM International: West Conshohocken, PA.

201. Toton, J.T., *The Design, Characterisation and Application of an Accelerated Drill Test for Cutting Tool Development*, in *School of Applied Sciences*. 2014, RMIT University: College of Science, Engineering and Health. p. 172.

202. Toenshoff, H.K. and B. Denkena, *Basics of Cutting and Abrasive Processes*. 2013, Springer: Dordrecht.

203. Schajer, G.S., *Practical Residual Stress Measurement Methods*. 2013, Somerset, NJ, USA John Wiley & Sons

204. Josefson, B.L., *Prediction of Residual Stresses and Distortions in Welded Structures.* Journal of Offshore Mechanics and Arctic Engineering, 1993. **115**(1): p. 52-57.

205. Bouchard, P.J. and P.J. Withers, *The Appropriateness of Residual Stress Length Scales in Structural Integrity.* Journal of Neutron Research, 2004. **12**(1): p. 81-91.

206. Holden, T.M., *Tutorial on intergranular strains*. 2010, Northern Stress Technologies: Deep River, Ontario, Canada.

207. Ziara-Paradowska, A., *Investigation of Residual Stress in Welds Using Neutron and Synchrotron Diffraction*, in *Department of Mechanical and Aerospace Engineering*. 2008, Monash University: Clayton, VIC.

208. Ueda, Y., H. Murakawa, and N. Ma, *Welding deformation and residual stress prevention*. 2012, Boston: Butterworth Heinemann.

209. Funderburk, R.S., *Postweld heat treatment.* Welding Innovation Quarterly, 1998. **15**(2): p. 17-18.

210. Milne, I., R.O. Ritchie, and B. Karihaloo, eds. *Comprehensive Structural Integrity*. Vol. Volume 7. Practical Failure Assessment Methods. 2007, Elsevier.

211. Withers, P.J. and H.K.D.H. Bhadeshia, *Residual stress. Part 2 – Nature and origins.* Materials Science and Technology, 2001. **17**(4): p. 366-375.

212. Weiss, I., G.S. Baker, and R.D. Das Gupta, *Vibrational Residual Stress Relief in a Plain Carbon Steel Weldment.* Welding Research Supplement, 1976. **55**(2).

213. Zhao, X., et al., *Simulation of vibration stress relief after welding based on FEM.* Acta Metallurgica Sinica (English Letters), 2008. **21**(4): p. 289-294.

214. Aoki, S., T. Nishimura, and T. Hiroi, *Reduction method for residual stress of welded joint using random vibration.* Nuclear Engineering and Design, 2005. **235**(14): p. 1441-1445.

215. Xu, J., L. Chen, and C. Ni, *Effect of vibratory weld conditioning on the residual stresses and distortion in multipass girth-butt welded pipes.* International Journal of Pressure Vessels and Piping, 2007. **84**(5): p. 298-303.

216. Chataigner, S., et al., *Improving welded joint fatigue life using shot peening or grinding*. 2012, LUNAM Universite: Bouguenais, France.

217. Nur Azida Che, L. and A. Aidy, *Fatigue strength improvement of MIG-welded joint by shot peening.* IOP Conference Series: Materials Science and Engineering, 2011. **17**(1): p. 012001.

218. Kobayashi, M., T. Matsui, and Y. Murakami, *Mechanism of creation of compressive residual stress by shot peening.* International Journal of Fatigue, 1998. **20**(5): p. 351-357.

219. Chen, X., et al., *Investigation of microstructures and residual stresses in laser peened Incoloy 800H weldments.* Optics & Laser Technology, 2014. **57**(0): p. 159-164.

220. Hill, M.R., et al., *Measurement of laser peening residual stresses.* Materials Science and Technology, 2005. **21**(1): p. 3-9.

221. Evans, A.D., et al., *The effect of incidence angle on residual stress state in laser peened Ti-6Al-4V plate*, in *ICSP9 - 9th International Conference on Shot Peening*. 2005: Paris, France. p. 454-459.

222. Luzin, V., K. Spencer, and M.X. Zhang, *Residual stress and thermo-mechanical properties of cold spray metal coatings.* Acta Materialia, 2011. **59**(3): p. 1259-1270.

223. Withers, P.J. and H.K.D.H. Bhadeshia, *Residual stress. Part 1 – Measurement techniques.* Materials Science and Technology, 2001. **17**(4): p. 355-365.

224. Hutchings, M.T., et al., *Introduction to the characterization of residual stress by neutron diffraction*. 2005, Boca Raton, FL: Taylor & Francis.

225. Frankel, P., et al., *Comparison of residual stresses in Ti–6Al–4V and Ti–6Al–2Sn–4Zr–2Mo linear friction welds.* Materials Science and Technology, 2009. **25**(5): p. 640-650.

226. Luckhoo, H.T., T.S. Jun, and A.M. Korsunsky, *Inverse eigenstrain analysis of residual stresses in friction stir welds.* Procedia Engineering, 2009. **1**(1): p. 213-216.

227. Liu, C. and C.-l. Dong, *Internal residual stress measurement on linear friction welding of titanium alloy plates with contour method.* Transactions of Nonferrous Metals Society of China, 2014. **24**(5): p. 1387-1392.

228. Colegrove, P.A., et al., *Microstructure and residual stress improvement in wire and arc additively manufactured parts through high-pressure rolling.* Journal of Materials Processing Technology, 2013. **213**(10): p. 1782-1791.

229. Brice, C. and W. Hofmeister, *Determination of Bulk Residual Stresses in Electron Beam Additive-Manufactured Aluminum.* Metallurgical and Materials Transactions A, 2013: p. 1-7.

230. Knowles, C.R., T.H. Becker, and R.B. Tait, *Residual stress measurements and structural integrity implications for selective laser melted Ti-6Al-4V.* South African Journal of Industrial Engineering, 2012. **23**(3): p. 119-129.

231. Sandvik-Coromant. *Landing gear beam*. Industrial Solutions: Aerospace, Titanium n.d. [cited 2013 September 5]; Available from: http://www.sandvik.coromant.com/en-gb/industrysolutions/aerospace/titanium/Pages/Landing-gear-beam.aspx.

232. Cuiuri, D., *Control of the short-circuit gas metal arc welding process using instantaneous current regulation*, in *School of Electrical, Computer and Telecommunications Engineering*. 2000, University of Wollongong: Wollongong. p. 405.

233. Cuiuri, D. and J. Norrish. *Verstatile welding power source controller for research and product development*. in *Joint International Conference Computer Technology in Welding & Manufacturing (16th) & Mathematical Modelling & Information Technologies in Welding & Related Processes (3rd)*. 2006. Kiev, Ukrane.

234. Balasubramanian, V., V. Jayabalan, and M. Balasubramanian, *Effect of current pulsing on tensile properties of titanium alloy.* Materials & Design, 2008. **29**(7): p. 1459-1466.

235. Wu, M., L. Li, and H. Hao, *Titanium alloy welding method based on arc ultrasonic process*. 2006: China.

236. Kirstein, O., V. Luzin, and U. Garbe, *The Strain-Scanning Diffractometer Kowari.* Neutron News, 2009. **20**(4): p. 34-36.

237. James, J.A., et al., *A virtual laboratory for neutron and synchrotron strain scanning.* Physica B: Condensed Matter, 2004. **350**(1–3, Supplement): p. E743-E746.

238. Ganguly, S., et al., *Automation of a neutron diffractometer for analysis of residual stress inside complex engineering components.* Applied Physics A: Materials Science and Processing, 2010. **99**(3): p. 601-606.

239. Manns, T. and B. Scholtes, *DECcalc - A Program for the Calculation of Diffraction Elastic Constants from Single Crystal Coefficients.* Materials Science Forum, 2011. **681**: p. 417-419.

240. Choi, W.B., et al., *Integrated characterization of cold sprayed aluminum coatings.* Acta Materialia, 2007. **55**(3): p. 857-866.

241. Chang, K.-H. and C.-H. Lee, *Finite element analysis of the residual stresses in T-joint fillet welds made of similar and dissimilar steels.* The International Journal of Advanced Manufacturing Technology, 2009. **41**(3-4): p. 250-258.

242. Teng, T.-L., et al., *Analysis of residual stresses and distortions in T-joint fillet welds.* International Journal of Pressure Vessels and Piping, 2001. **78**(8): p. 523-538.

243. Ueda, Y. and M.G. Yuan, *A Predicting Method of Welding Residual stress Using Source of Residual Stress (Report II) : Determination of Standard Inherent Strain(Mechanics, Strength & Structural Design).* Transactions of JWRI, 1989. **18**(1): p. 144-150.

244. Ueda, Y. and M.G. Yuan, *A Predicting Method of Welding Residual Stress Using Source of Residual Stress (Report III) : Prediction of Residual Stresses in T- and I-joints Using Inherent Strains(Mechanics, Strength & Structural Design).* Transactions of JWRI, 1993. **22**(1): p. 157-168.

245. Ueda, Y., et al., *A Predicting Method of Welding Residual Stress Using Source of Residual Stress (Report IV) : Experimental Verification for Predicting Method of Welding Residual Stresses in T-joints Using Inherent Strains(Mechanics, Strength & Structural Design).* Transactions of JWRI, 1993. **22**(1): p. 169-176.

246. Song, S.P., A.M. Paradowska, and P.S. Dong, *Investigation of Residual Stresses Distribution in Titanium Weldments.* Materials Science Forum, 2014. **777**: p. 171-175.

247. Nishida, M., et al., *Residual Stress Measurement of Titanium Casting Alloy by Neutron Diffraction.* AIP Conference Proceedings, 2008. **989**(1): p. 101-104.

248. Pitt, F., et al., *Postprocessing effect on the ductility and flexural behavior of three titanium alloys under simulated superplastic forming conditions.* Journal of Materials Engineering and Performance, 2004. **13**(6): p. 735-743.

249. Conrad, H., *Effect of interstitial solutes on the strength and ductility of titanium.* Progress in Materials Science, 1981. **26**(2–4): p. 123-403.

250. Liu, Z. and G. Welsch, *Effects of oxygen and heat treatment on the mechanical properties of alpha and beta titanium alloys.* Metallurgical Transactions A, 1988. **19**(3): p. 527-542.

251. ASM. *Titanium Ti-6Al-4V (Grade 5), Annealed*. 2009 [cited 2009 October 12]; Available from: http://asm.matweb.com/search/SpecificMaterial.asp?bassnum=MTP641.

252. ASM. *Titanium Ti-6Al-4V (Grade 5), ELI, Annealed*. 2009 [cited 2009 October 12]; Available from: http://asm.matweb.com/search/SpecificMaterial.asp?bassnum=MTP643.

253. Du, H.L., et al., *Air oxidation behaviour of Ti-6Al-4V alloy between 650 and 850°.* Corrosion Science, 1994. **36**(4): p. 631-642.

254. Pitt, F., *Influence of Grain Size and Microstructure on Oxidation Rates in Titanium Alloy Ti-6Al-4V Under Superplastic Forming Conditions.* Journal of Materials Engineering and Performance, 2004. **13**(6): p. 727-734.

255. Rosen, A., S. Nadiv, and M. Bohrer, *Effect of High-Temperature Exposure on Mechanical and Electrical Properties of Ti-6Al-4V Sheet.* Materials Evaluation, 1975. **33**(6): p. 135-137, 140.

256. Rosen, A. and A. Rottem, *The effect of high temperature exposure on the creep resistance of Ti-6Al-4V alloy.* Materials Science and Engineering, 1976. **22**(0): p. 23-29.

257. Yoshimura, H. and J. Nakahigashi, *Ultra-fine-grain refinement and superplasticity of titanium alloys obtained through protium treatment.* International Journal of Hydrogen Energy, 2002. **27**: p. 769-774.

258. Liu, C.-T., T.-I. Wu, and J.-K. Wu, *Formation of nanocrystalline structure of Ti–6Al–4V alloy by cyclic hydrogenation–dehydrogenation treatment.* Materials Chemistry and Physics, 2008. **110**: p. 440-444.

259. Kahveci, A.I. and G.E. Welsch, *Hardness versus strength correlation for oxygen-strengthened Ti-6Al-4V alloy.* Scripta Metallurgica et Materiala, 1991. **25**(8): p. 1957-1962.

260. Welsch, G. and W. Bunk, *Deformation Modes of the Alpha-Phase of Ti--6Al--4V as a Function of Oxygen Concentration and Aging Temperature.* Metall. Trans A, 1982. **13A**(5): p. 889-899.

261. Henry, S.D., et al., *Fatigue Data Book - Light Structural Alloys*. 1995, ASM International.

262. McCue, D. and B. Irving, *Gast Tungsten Arc Welding: It's Built to Handle Titanium.* Welding Journal, 1991. **70**(11): p. 31-36.

263. Mathers, G. *Welding of titanium and its alloys - Part 1*. 2009 [cited 2011 June 6]; Available from: http://www.twi.co.uk/content/jk109.html.

264. Miller. *Titanium 101: Best TIG (GTA) Welding Practices*. 2010 [cited 2010 March 30]; Available from: http://www.millerwelds.com/resources/articles/TIG-gtaw-titanium-welding/.

265. Bendersky, L. and A. Rosen, *The effect of exposure on fracture of Ti-6AL-4V alloy.* Engineering Fracture Mechanics, 1980. **13**(1): p. 111-118.

266. Xiong, J., et al., *Vision-sensing and bead width control of a single-bead multi-layer part: material and energy savings in GMAW-based rapid manufacturing.* Journal of Cleaner Production, 2013. **41**(0): p. 82-88.

267. Sanchez Roca, A., et al., *Stability analysis of the gas metal arc welding process based on acoustic emission technique.* Welding International, 2009. **23**(3): p. 173-173-180.

268. Sharma, A., et al. *Online Monitoring of Electron Beam Welding of TI6AL4V Alloy Through Acoustic Emission*. 2007: NDT Internet Publishing, Tacheniusweg 8, Herford, D-32052, Germany, [mailto:rd@ndt.net], [URL:http://www.ndt.net].

269. TIMET, *Properties and processing if TIMETAL 6-4*. 2008, Titanium Metals Corporation.

270. Ding, D., et al., *A tool-path generation strategy for wire and arc additive manufacturing.* The International Journal of Advanced Manufacturing Technology, 2014. **73**(1-4): p. 173-183.

271. Sandvik-Coromant. *Pylon Bracket*. Industrial Solutions: Aerospace, Titanium n.d. [cited 2013 September 5]; Available from: http://www.sandvik.coromant.com/en-gb/industrysolutions/aerospace/titanium/Pages/Pylon-bracket.aspx.

APPENDICIES

Appendix A – Process Characterisation

Table A1. Parameter combinations used for experiments to characterise the GTAW additive manufacture process.

Trial	Independent Variables					
	Arc Length	Arc Current	Wire Feed		Travel Speed	Interpass Temp
	mm	amps	ratio	mm/min	mm/min	°C
1	3	100	5	500	100	40
2	3	120	7	1050	150	90
3	3	140	9	1800	200	150
4	3	80	11	2750	250	200
5	3.5	100	7	1400	200	200
6	3.5	120	5	1250	250	150
7	3.5	140	11	1100	100	90
8	3.5	80	9	1350	150	40
9	4	100	9	2250	250	90
10	4	120	11	2200	200	40
11	4	140	5	750	150	200
12	4	80	7	700	100	150
13	5	100	11	1650	150	150
14	5	120	9	900	100	200
15	5	140	7	1750	250	40
16	5	80	5	1000	200	90

Table A2. Measured output variables used as raw data for analysis of variance.

Trial	Output 1	Output 2	Output 3	Output 4	Output 5	Output 6	Output 7	Output 8	Output 9	Output 10	Output 11	Output 12	Output 13	Output 14
	Voltage V	Build Up H	Width W	W/H	Roughness MLT	Roughness STDEV	Hardness HV	Prior β L_β	HAZ Depth D_HAZ	Vol Frac α V_α	α Lath Width W_α	α Lath Length L_α	Aspect Ratio AR	Colony Size L_colony
1	10.7	0.499	8.627	17.279	1.134	0.209	341	2.069	5.3	0.892	0.890	7.965	9.047	3.947
2	11.1	0.826	8.618	10.436	1.426	0.282	330	0.976	4.0	0.845	0.944	8.751	9.408	4.961
3	11.7	0.921	8.577	9.312	1.543	0.246	325	0.989	4.5	0.860	1.103	11.227	10.425	5.427
4	9.5	1.031	6.071	5.887	5.863	0.769	327	0.380	1.5	0.828	0.716	7.190	10.413	3.382
5	11.6	1.073	6.248	5.822	2.338	0.229	327	0.952	3.0	0.814	0.804	7.373	9.343	4.911
6	11.9	0.640	6.590	10.298	3.174	0.184	328	0.672	2.8	0.814	0.901	6.849	7.796	6.274
7	11.8	0.766	11.002	14.356	2.337	0.659	326	1.154	5.4	0.828	1.086	9.481	9.133	6.051
8	9.9	1.193	5.840	4.895	1.159	0.214	326	1.818	3.3	0.807	0.890	7.699	9.291	5.321
9	11.3	1.284	5.231	4.073	1.837	0.362	309	0.926	2.0	0.795	0.921	7.952	9.337	4.443
10	11.7	1.172	7.189	6.131	1.803	0.155	309	1.149	2.7	0.806	0.856	7.988	9.324	4.323
11	12.7	0.514	9.893	19.246	2.236	0.184	328	1.452	5.4	0.811	1.073	9.476	9.012	4.537
12	10.4	0.852	7.744	9.091	1.684	0.087	313	1.531	4.0	0.820	0.978	8.556	9.005	5.698
13	11.4	1.248	7.086	5.679	1.337	0.172	308	2.045	3.0	0.821	0.971	8.299	8.815	5.419
14	12.2	0.816	10.470	12.831	1.071	0.208	318	1.917	5.4	0.830	0.911	8.780	10.376	5.738
15	13.0	0.804	7.177	8.928	1.090	0.167	325	0.833	3.1	0.811	0.826	8.409	10.284	5.196
16	11.0	0.757	4.797	6.338	1.939	0.318	320	1.333	2.0	0.806	0.682	6.684	9.513	4.355

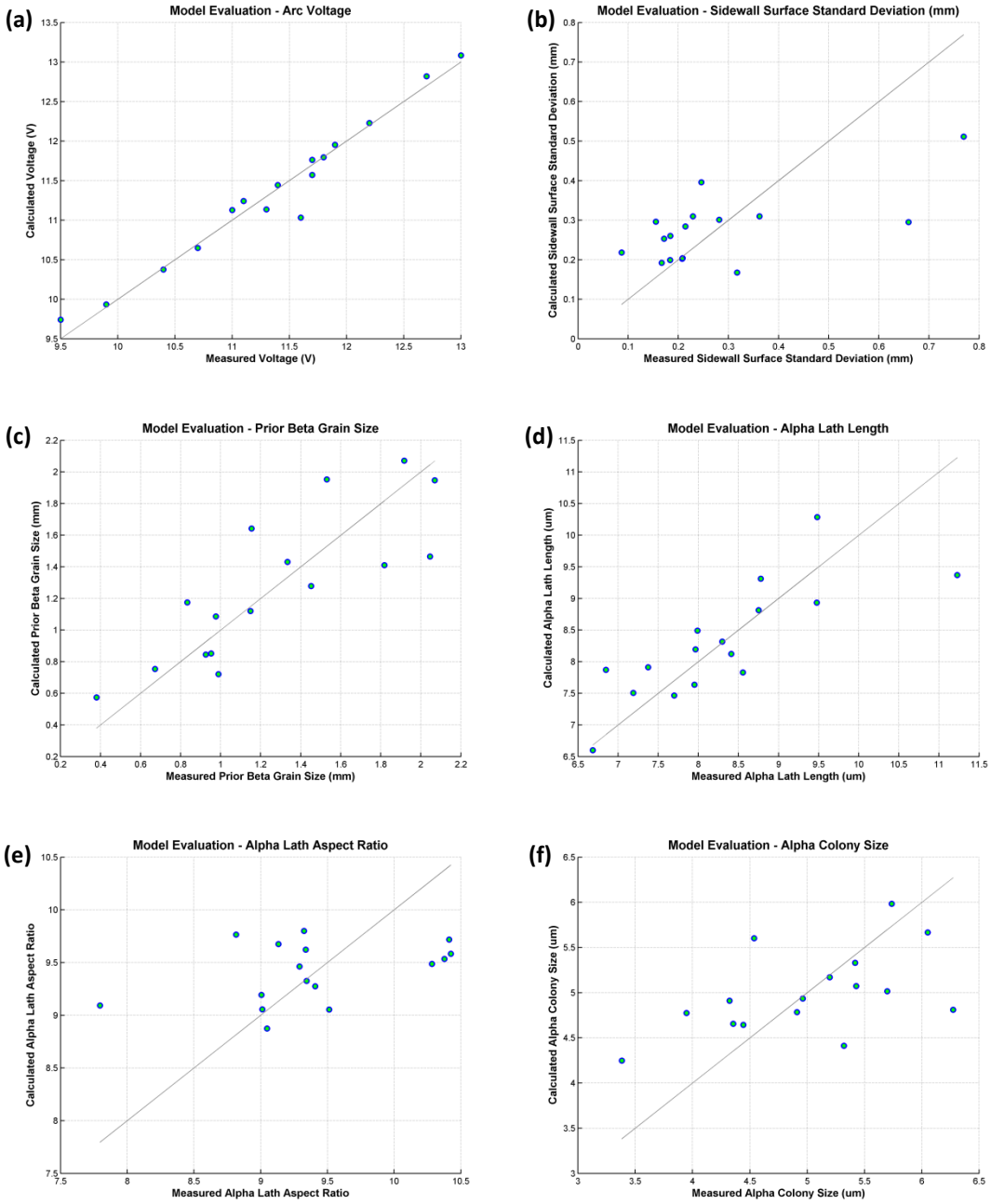

Figure A1 Comparison of measured and calculated values for output variables (a) arc voltage, (b) surface profile standard deviation, (c) prior β-Ti grain size, (d) α-Ti lath length, (e) α-Ti lath aspect ratio and (f) α-Ti colony size.

Appendix B – Mechanical Properties

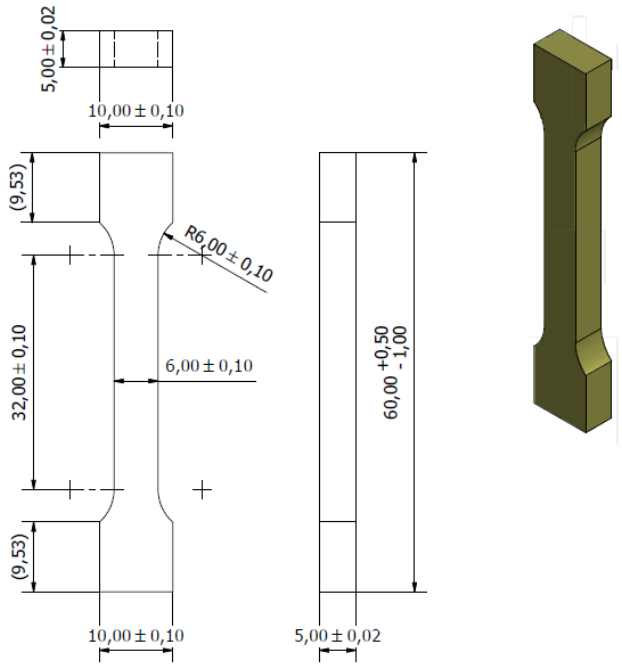

Figure B.1 Geometry of sub-size 'dog-bone' samples used for static tensile testing.

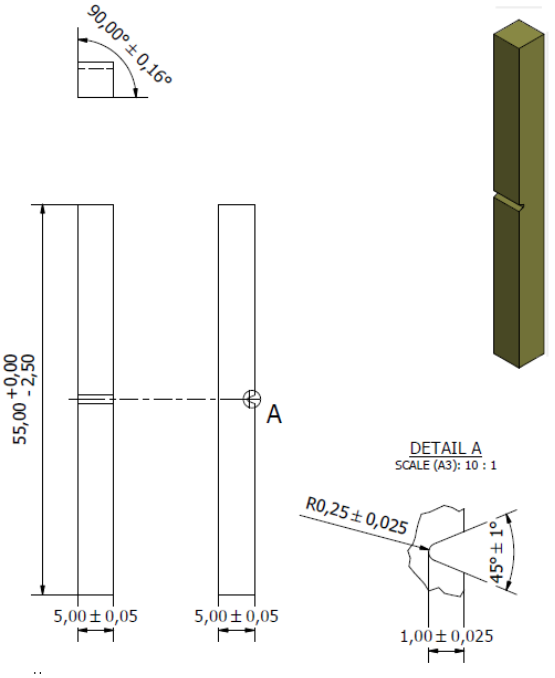

Figure B.2 Geometry of sub-size notched samples used for Charpy impact testing.

Table B.1 Summary of observations from Charpy impact testing of wrought plate and additively manufactured samples. In sample identification the first letter relates to the orientation of the length of the sample with the second letter corresponding to the direction of crack propagation (i.e. from the root of the notch through the sample).

Sample ID	Notch Orientation	Test Temperature (°C)	Energy (J)	Macro Photo	Notes
T-N-B5 (T1A)	A-para.	-40	4		-Planar fracture surface (mostly brittle fracture) -Rolling direction clear from striations (parallel) -Small shear lips, more broad toward notch
T-N-B6 (T2A)	A-para.	-40	5	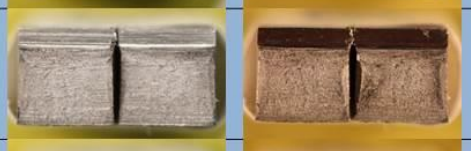	-Planar fracture surface (mostly brittle fracture) -Rolling direction clear from striations (parallel) -Small shear lips, more broad toward notch
T-L-B7 (T3B)	B-perp.	-40	4		-Slightly more fibrous surface (still planar) -Rolling direction clearly running perp to notch -Small shear lips, more consistent width
L-N-B1 (L1A)	A-para.	-40	3		-Planar fracture surface (mostly brittle fracture) -Rolling direction clear from striations (parallel) -Small shear lips, narrower than trans samples
L-N-B2 (L2A)	A-para.	-40	4	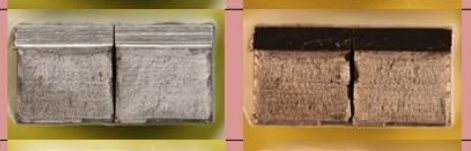	-Planar fracture surface (mostly brittle fracture) -Rolling direction clear from striations (parallel) -Small shear lips, narrower than trans samples
L-T-B3 (L3B)	B-perp.	-40	3	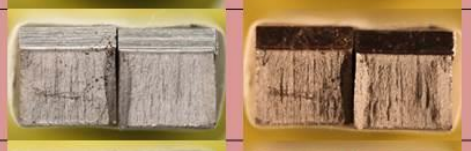	-Slightly more fibrous surface (still planar) -Rolling direction clearly running perp to notch -Small shear lips, more consistent and wider
L-T-B4 (L4B)	B-perp.	-40	3		-Slightly more fibrous surface (still planar) -Rolling direction clearly running perp to notch -Small shear lips, more consistent and wider
L-T-W1 (H1A)	A-para.	-40	6		-Less planar fracture and more fibrous -Larger shear lips arcing in from sides -No indication of texturing or alignment
L-T-W2 (H2A)	A-para.	-40	6		-Less planar fracture and more fibrous -Larger shear lips arcing in from sides -No indication of texturing or alignment
L-N-W3 (H3B)	B-perp.	-40	6		-Less planar fracture and more fibrous (ductile) -Larger shear lips arcing in from sides -No indication of texturing or alignment
L-N-W4 (H4B)	B-perp.	-40	6		-Less planar fracture and more fibrous -Less defined shear lips -No indication of texturing or alignment
N-T-W5 (V1A)	A-para.	-40	6	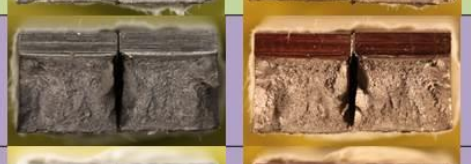	-Faceted fracture surface and more fibrous -Less defined shear lips, ductile drawing in edges -No indication of texturing or alignment
N-T-W6 (V2A)	A-para.	-40	5		-Semi planar fracture surface and more fibrous -Less defined shear lips, not arcing more linear -No indication of texturing or alignment
N-T-W7 (V3A)	A-para.	-40	6		-Semi planar fracture surface and more fibrous -Less defined shear lips, not arcing more linear -No indication of texturing or alignment
N-T-W8 (V4A)	A-para.	+24.4	6	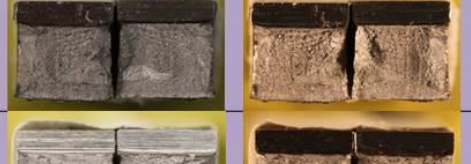	-Semi planar fracture surface and more fibrous -Less defined shear lips, not arcing more linear -No indication of texturing or alignment
N-L-W9 (V5B)	B-perp.	-40	7	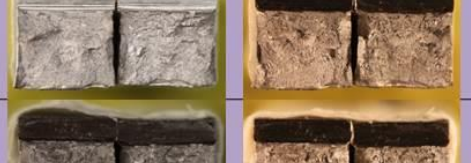	-Semi planar fracture surface and more fibrous -Less defined shear lips, ductile drawing in edges -No indication of texturing or alignment
N-L-W10 (V6B)	B-perp.	-40	6	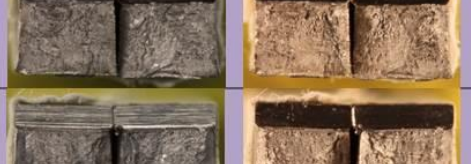	-Semi planar fracture surface and more fibrous -Less defined shear lips, ductile drawing in edges -No indication of texturing or alignment
N-L-W11 (V7B)	B-perp.	+24.4	6		-Semi planar fracture surface and some fibrous -Shear lips arcing inward to interior -No indication of texturing or alignment

Appendix C – Residual Stress

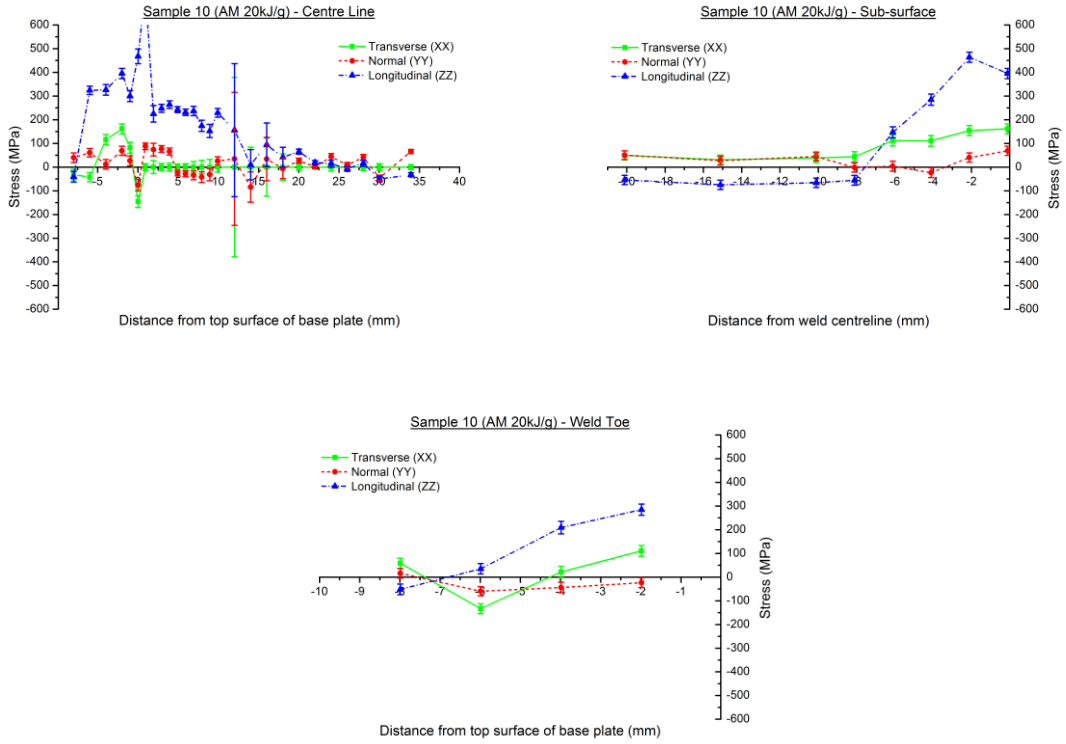

Figure C.1 Distribution of principal residual stresses in Wall_10 (20 kJ/g DCEN).

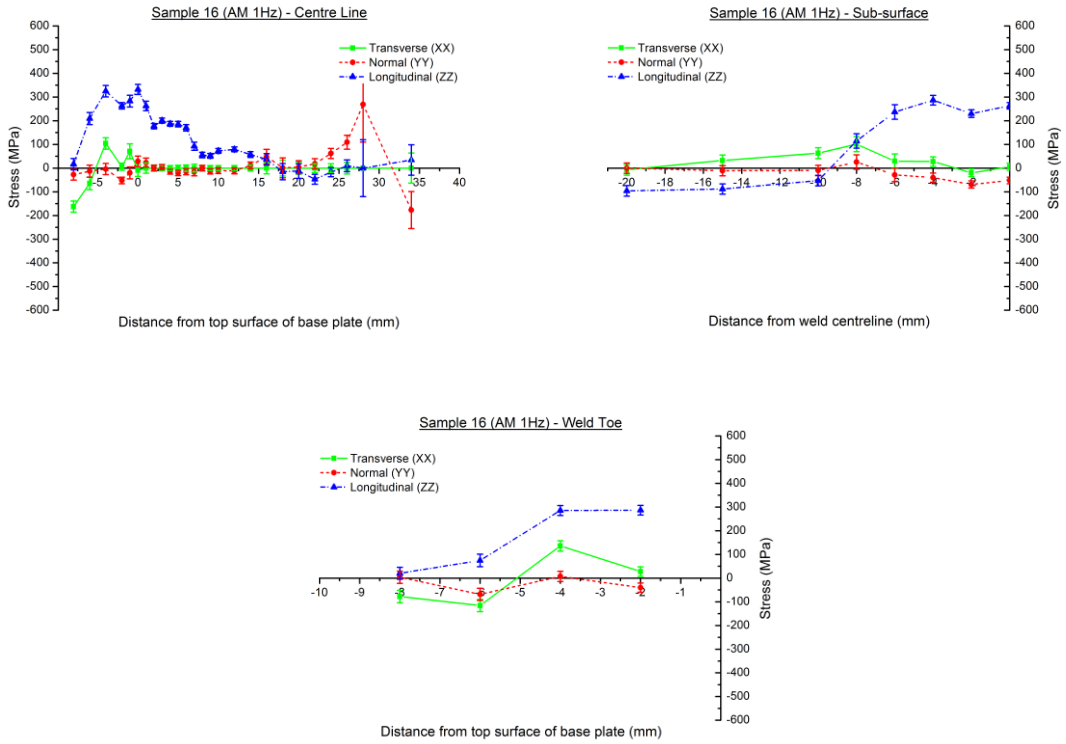

Figure C.2 Distribution of principal residual stresses in Wall_16 (20 kJ/g Pulsed 1 Hz).

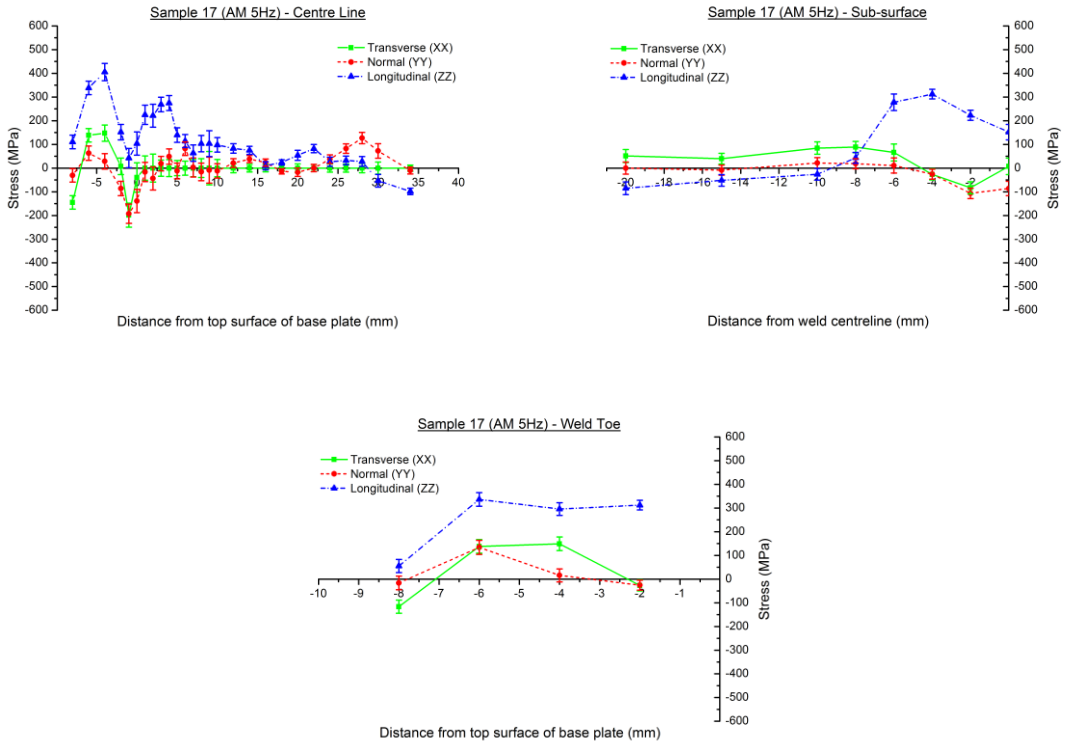

Figure C.3 Distribution of principal residual stresses in Wall_17 (20 kJ/g Pulsed 5 Hz).

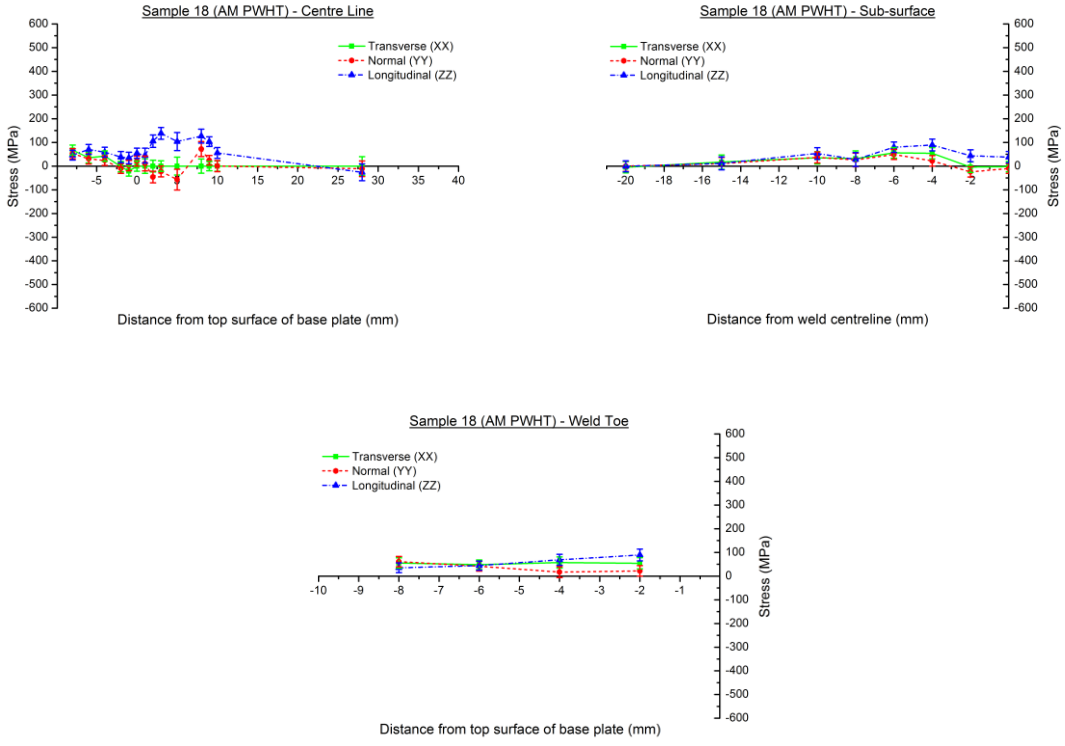

Figure C.4 Distribution of principal residual stresses in Wall_18 (20 kJ/g DCEN, PWHT).

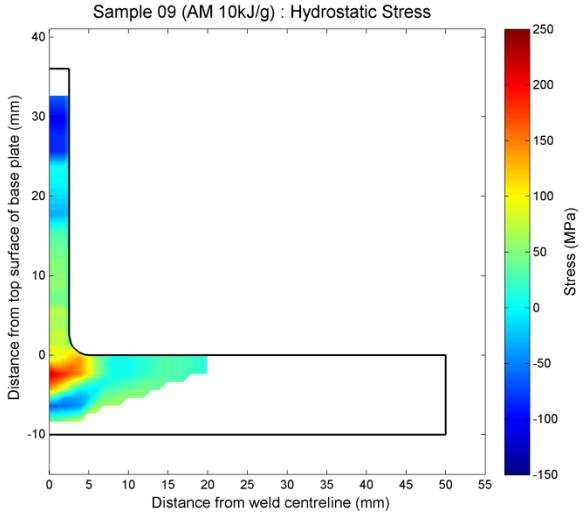

Figure C.5 Distribution of hydrostatic stresses in Wall_09 (10 kJ/g DCEN).

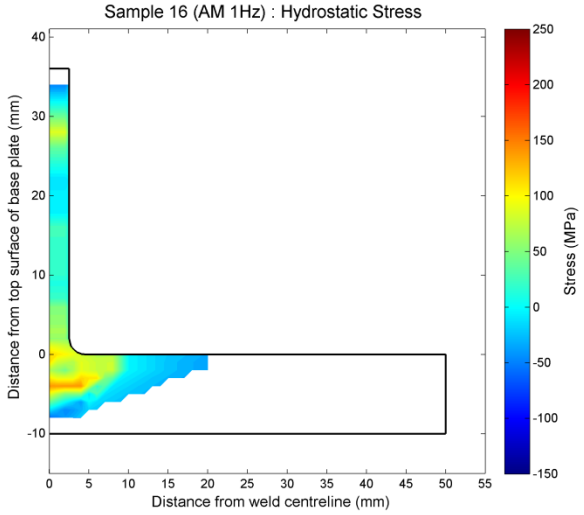

Figure C.6 Distribution of hydrostatic stresses in Wall_16 (20 kJ/g Pulsed 1 Hz).

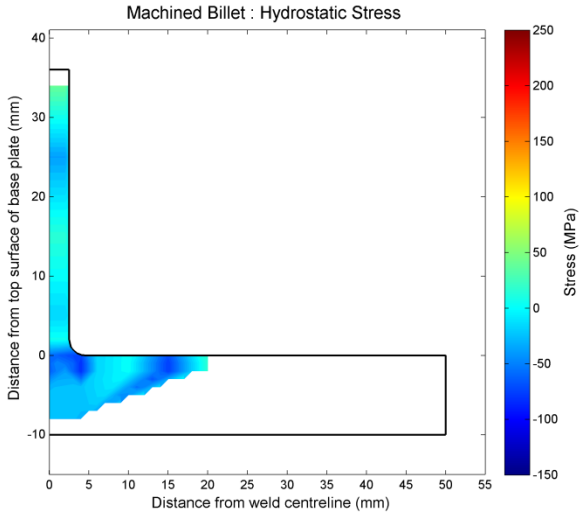

Figure C.7 Distribution of hydrostatic stresses in machined billet.

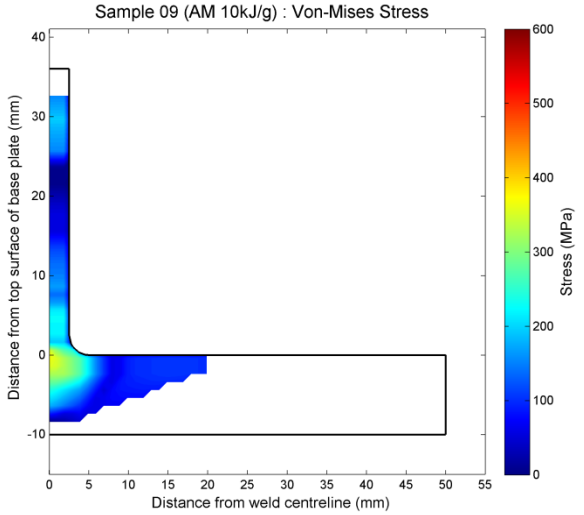

Figure C.8 Distribution of von-Mises equivalent stresses in Wall_09 (10 kJ/g DCEN).

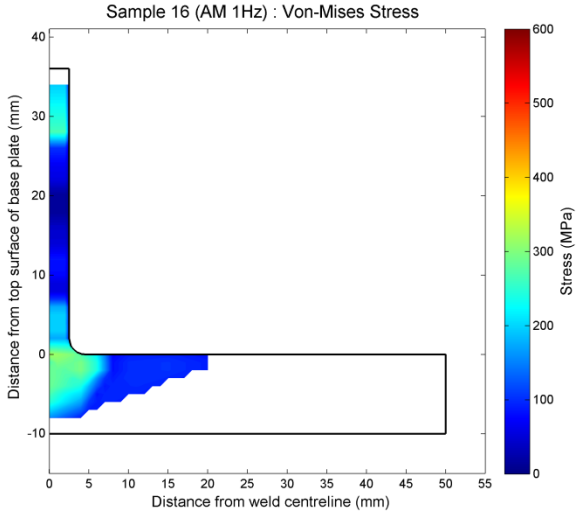

Figure C.9 Distribution of von-Mises equivalent stresses in Wall_16 (20 kJ/g Pulsed 1 Hz).

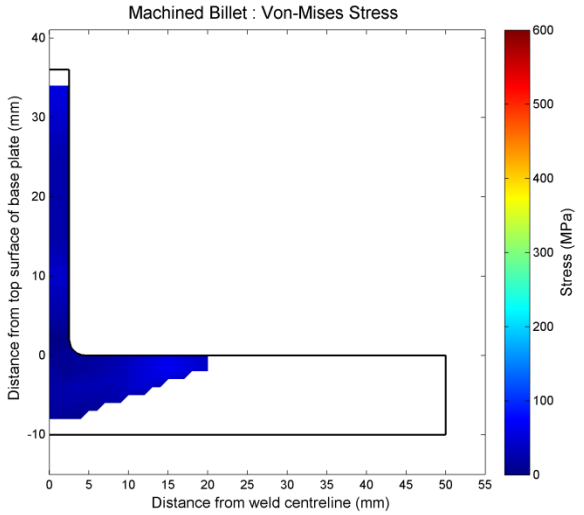

Figure C.10 Distribution of von-Mises equivalent stresses in machined billet.

Appendix D – Atmospheric Contamination

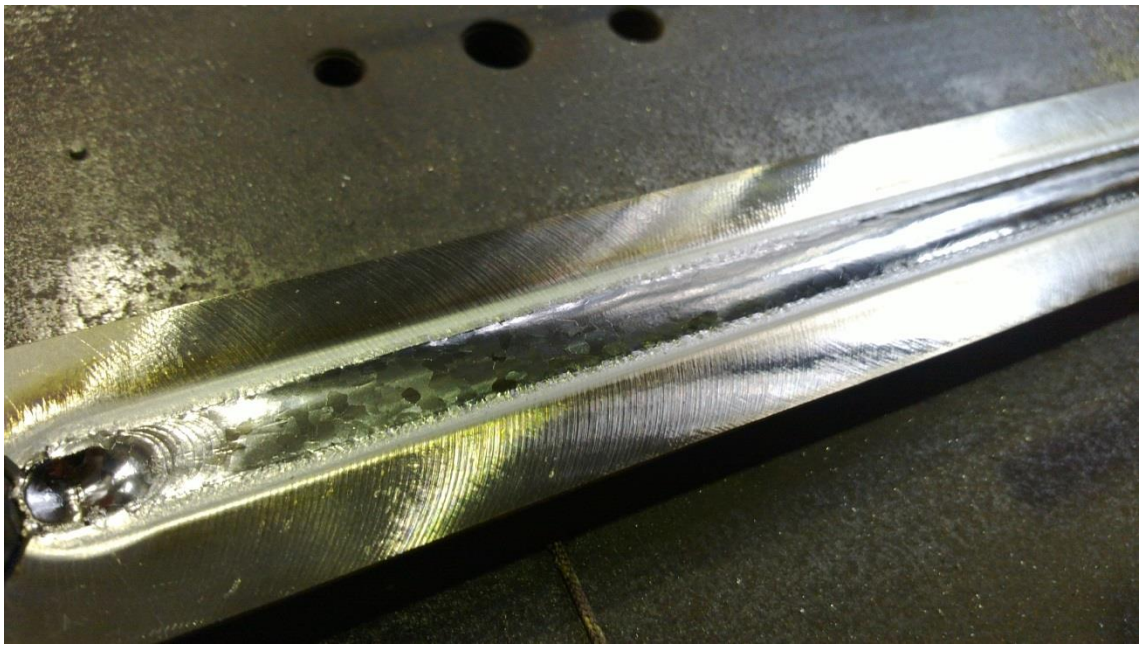

Figure D.1 Photograph of weld bead appearance for bead-on-plate trial E (multi-pass with trailing shielding) after 25 welding passes showing silver bead appearance with large prior β-Ti grains in the fusion zone and reinforcement and accompanying crater at the end of the weld bead.

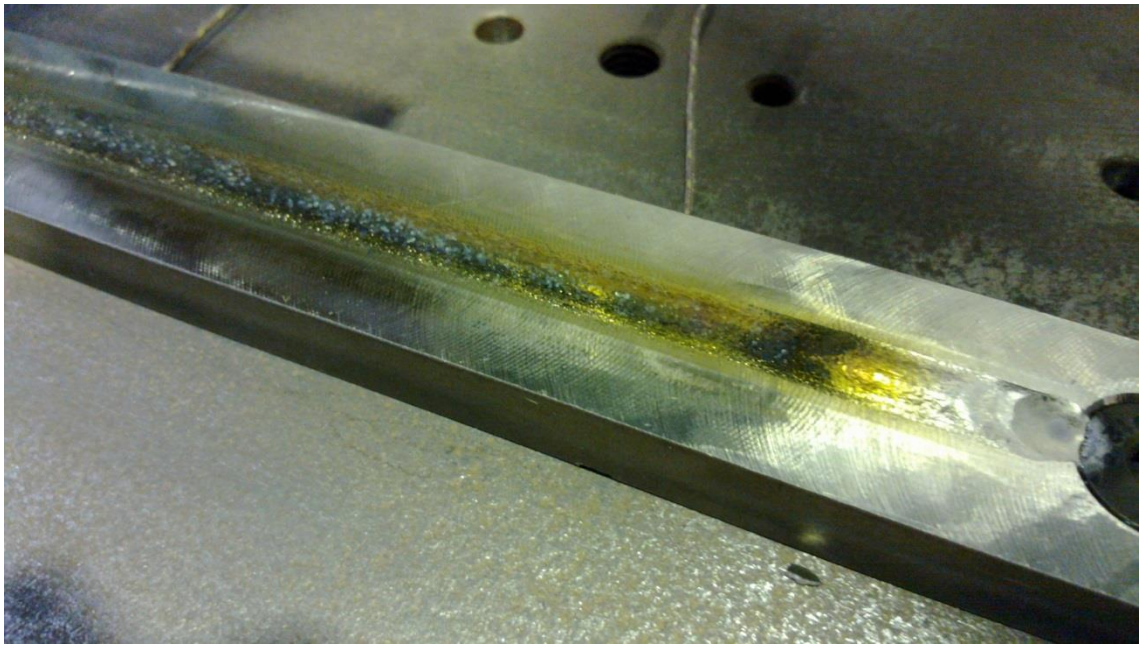

Figure D.2 Photograph of weld bead appearance for bead-on-plate trial D (multi-pass without trailing shielding) after the first welding pass showing straw and blue bead appearance with large prior β-Ti grains in the fusion zone and reinforcement and accompanying crater at the end of the weld bead.

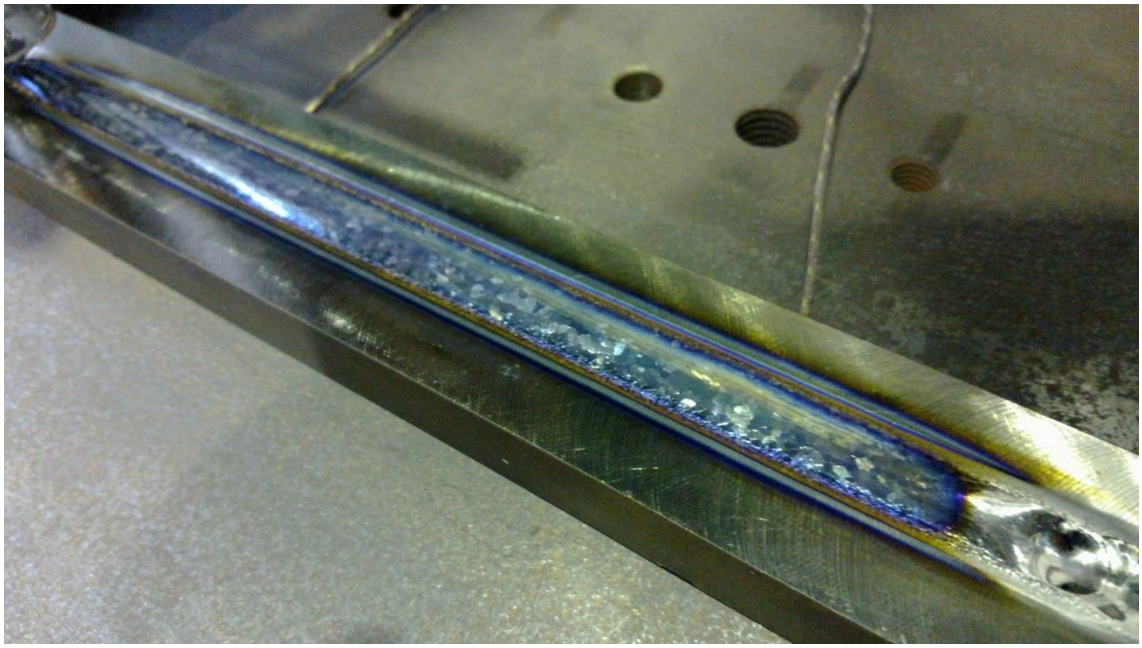

Figure D.3 Photograph of weld bead appearance for bead-on-plate trial D (multi-pass without trailing shielding) after 10 passes welding passes showing blue bead appearance with large prior β-Ti grains in the fusion zone and reinforcement and accompanying crater at the end of the weld bead.

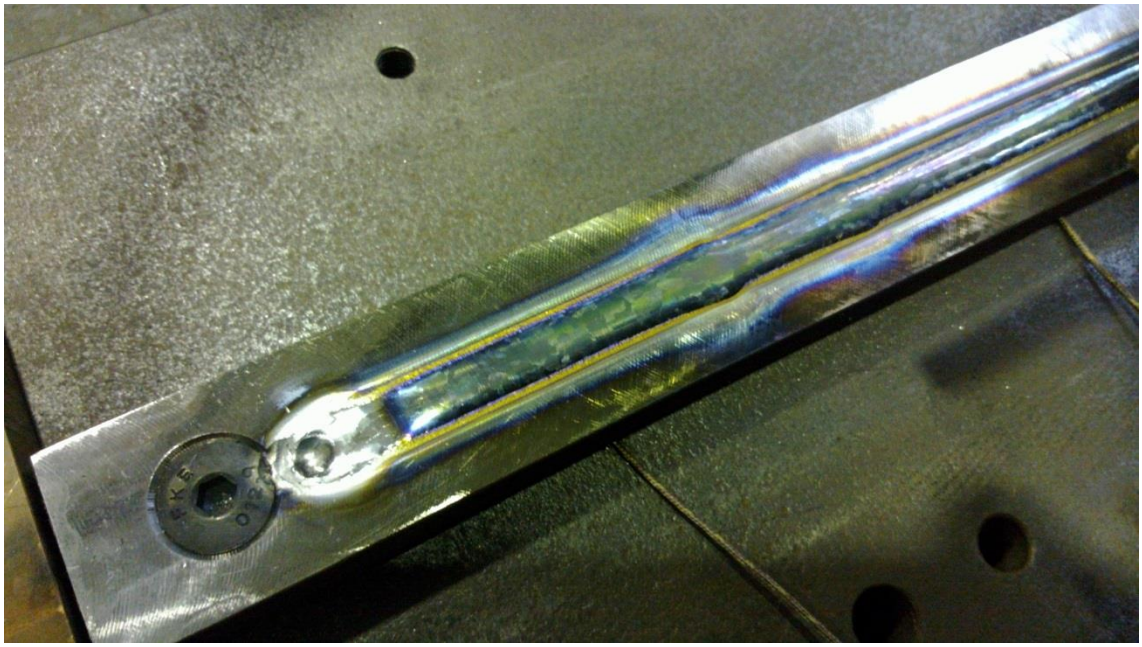

Figure D.4 Photograph of weld bead appearance for bead-on-plate trial D (multi-pass without trailing shielding) after 25 passes welding passes showing strong blue bead appearance with large prior β-Ti grains in the fusion zone and reinforcement and accompanying crater at the end of the weld bead.